Imperial College London

Bioactive glass based fibre mats for wound healing

Xingchen Zhao

Submitted for the degree of Doctor of Philosophy (Ph.D.)

Department of Materials

Imperial College London

2022

Abstract

Wounds are one of the most prevailing healthcare problems. Two of the most common wound types, burn injuries and chronic ulcers, are imposing a great threat to the medical systems due to their high incidence, high morbidity, high cost of treatment, and high likelihood to induce further problems, such as infection, loss of sensory nodes, cell mutation, etc. Burn injuries usually have a damaged epidermis with excessive exudates that can become infected and cause severe inflammation while in the meantime, the sensory nodes, follicles, and glands are fully damaged. Diabetic ulcers, the most common type of chronic wounds, have unepithelialized epidermis that causes biofilm colonization, strong accumulation of cytokines and protease, and neuropathy from diabetes. The most important steps in the regeneration of both wounds are the regeneration of the ECM and vascular network, in order to ensure cell attachment and migration as well as the delivery of oxygen and nutrients to the wound site.

This thesis describes the development of 3D ECM-mimic bioactive glass fibre mats as strategies for the regeneration of both injuries. Bioactive glasses (BGs) are biodegradable materials that have already been widely used as a synthetic bone graft material that can regenerate bone defects and as the active ingredient for remineralizing toothpastes, but now they are finding use as medical devices (scaffolds or matrices) for wound healing applications. BGs degrade into therapeutic ions that promote individual steps in the wound healing cascades, including hemostasis, antibacterial effect, anti-inflammation, appropriate cell proliferation, angiogenesis, re-epithelialization, and extracellular matrix production.

BG fibre mats were obtained through an optimized sol-gel electrospinning approach, in which the electrospinning and material parameters were determined through experimentation. The fabricated fibre mats mimicked the extracellular matrix in the dermis layer and can be easily packed into wound defects.

We synthesized zinc-delivering bioactive glass fibre mats as scaffolds for burn regeneration as the controlled release of zinc ions is thought to be antibacterial, and have anti-inflammation and follicle regeneration properties. In vitro studies confirmed the capabilities of the fabricated fibre mats in ECM deposition and angiogenesis. 3 mol% of Zn incorporation reduced the cytotoxic effect of BGs to fibroblasts and stimulated their expression of growth factors (PDGF, VEGF, bFGF, TGF-β, and HIF-1α) from fibroblasts and endothelial cells for ECM deposition and angiogenesis. Media conditioned with HDFs

that had been precultured with BG dissolution products influenced the proliferation and migration of endothelial cells and their protein expression, which provides insights into understanding the mechanism of BGs in angiogenesis.

We also synthesized borosilicate bioactive glass fibre mats through modified sol-gel electrospinning for diabetic ulcer regeneration. Boron was selected as it promotes epithelialization, tissue granulation, anti-inflammation, ECM deposition, and most importantly, angiogenesis. The incorporation of boron into the BG system stimulated high expressions of angiogenic factors (VEGF, bFGF, HIF-1α) from fibroblasts and promoted the proliferation and migration of endothelial cells.

In vivo studies were conducted in order to investigate the efficacy of silicate and borosilicate BGs in healing diabetic ulcers and to understand the mechanism of them to individual phases of wound healing, including wound closure, epithelialization, anti-inflammation, angiogenesis, tissue granulation, and ECM deposition. The assays included imaging the wound areas through optical cameras, histology analysis and immunohistochemistry analysis. BGs were found to stimulate faster wound healing as they highly promoted all the above-mentioned healing steps. The incorporation of boron into the BG system and processing BGs to fibrous structure both impact the healing effect.

Declaration

Originality declaration

I hereby certify that the work presented in this thesis is the result of my own research and investigations, that was carried out mainly at the Department of Materials, Imperial College London during the period of October 2018 to January 2022. My in vitro studies were conducted at the Department of Surgical Biotechnology, Division of Surgery & Interventional Science, UCL, and State Key Laboratory of High Performance Ceramics and Superfine Microstructure, Shanghai Institute of Ceramics, Chinese Academy of Sciences, and my in vivo studies were conducted at the College of Life and Sciences, Northeastern University. All contributors have been truly and properly acknowledged.

Copyright declaration

The copyright if this thesis rests with the author and is made available under a Creative Commons Attribution Non-Commercial No Derivatives license. Researchers are free to copy, distribute or transmit the thesis on the condition that they attribute it, that they do not use it for commercial purposes and they do not alter, transform or build upon it. For any reuse or redistribution, researchers must make clear to others the license terms of this work.

Covid impact declaration

My original plan was to conduct material synthesis and characterization at Imperial College, and to conduct biological tests at Royal Free Hospital, UCL. However, by the start of 2020, the world suffers from the Covid-19 pandemic, and the national lockdown caused a great interruption of my work. I cannot express my gratitude to my supervisor, Prof. Julian Jones, when he managed to let me carry on my biological studies in China. I also cannot forget the dedicative help from Dr. Gavin Jell, Prof. Chengtie Wu, Prof. Huiling Gao, and their group members. But, despite of this, there has still be a great suspension of my plans. For example, some of the work that I intended to do on borosilicate-chitosan hybrids and borosilicate-PTHF hybrids have to be suspended by the dissolution studies.

Acknowledgments

I would like to thank Prof. Julian Jones for welcoming me to the group and guiding me through this project. My determination to pursue a Ph.D. was inspired by his lecture. Throughout my Ph.D., he guided me in developing my research and lab skills, improving my writing skills on reviews and papers, helping me to gain confidence in teaching and presentations, and giving me suggestions on my future career. In the tough period of the pandemic, he helped me to overcome this interruption by inspiring me to write a review and encouraging me to carry out my in vitro and in vivo studies in China. I owe him a great debt of gratitude as my work would not have been possible without his help and dedication.

I would like to thank Dr. Gavin Jell for welcoming me to his group in the Division of Surgery & Interventional Science, UCL (Royal Free Hospital). He is the enlightener of my cell studies and supported me in helping me undertake my cell work both in UCL and the Shanghai Institute of Ceramics. He also helped me greatly in my in vivo studies. I would not have achieved the results outlined in this thesis without his help and suggestions.

I would like to extend my thanks to Prof. Chengtie Wu from Shanghai Institute of Ceramics, Chinese Academy of Sciences, for enabling me to have an amazing 3-month collaboration in his group. He and his group made my stay enjoyable and had give me a great many inspirations for my research. I am particularly grateful to Dr. Zhai for helping me design the stages of my in vitro studies and guiding my experiment throughout my stay.

I would also like to thank Prof. Huiling Gao from Northeastern University, Shenyang for supporting my animal studies. She was a great teacher and taught me how to conduct animal studies step to step to build my confidence and proficiency in embedding, segmenting, and staining. Her extensive knowledge and experience saved me a lot of time in the designing of animal models and staining the wound tissues.

My work would also not be possible without my lab mates. I am very grateful to Dr. Elizabeth Norris for introducing me to my project and teaching me electrospinning and sol-gel synthesis; to Dr. Francesca Tallia (Fra), Gloria, and Zhijun for their devotion to managing the group; to Joel for his help in designing the initial stage of my cell study;

to Agathe and Xiuyuan for all the lab orders; to Yu-Chien and Haffsah for giving me suggestions in my hybrid synthesis; to Xiaomeng for teaching me the melt-derived approach; and to all of the group for helping and inspiring me during my pursuit of the diploma. I also wish to express my thanks to the amazing members in the department: to Dr. Alessandra Pinna (Ale) for her help with the BET; to Richard Sweeney and Victoria Bemmer for their help with the XRD; to Mahmoud Ardakani and Ecaterina Ware for their help on SEM and EDX; to Ben Chan and Greg Casson for the induction on mechanical testing, ICP, and FTIR; to Dr. Manjula Silva for providing me an amazing opportunity to work as a GTA. I would not have gone this far without you.

I also wish to thank all my friends. You played a pivotal role in supporting me and encouraging me. Every day has been enjoyable with all of you.

At the end of the acknowledgment, I wish to present my deepest gratitude to my family. To my grandma, I fulfilled our promises. To my parents, thank you for your support in the past 23 years. Thank you for allowing me to pursue a Ph.D., and supporting me throughout these years. You brought me up to who I am now and please be looking forward to what I will become.

Table of Contents

Abstract 2

Declaration 4

Acknowledgments 5

Table of Contents 7

List of Figures 13

List of Tables 19

List of Abbreviations 20

1 **Introduction** 21

2 Literature review 25

2.1 The wound healing cascade 25

2.1.1 Hemostasis 26

2.1.2 Inflammation 26

2.1.3 Proliferation 30

2.1.4 Remodeling 32

2.2 Wound types and treatments 32

2.2.1 Burns 32

2.2.2 Chronic wounds 34

2.2.3 Skin cancer 37

2.2.4 Deep wounds 37

2.2.5 Treatments 39

2.3 Introduction of bioactive glass 42

2.4 Methods of bioactive glass synthesis 46

2.4.1 Melt derived 46

2.4.2 Sol-gel derived 47

2.4.3 Mesoporous bioactive glasses 50

2.4.4 Bioactive glass nanofibres 52

2.5 Therapeutic ions from BGs to the wound healing cascade 57

2.5.1 Hemostasis 57

2.5.2 Antibacterial effect 59

2.5.3 Anti-inflammation 74

2.5.4 Angiogenesis 79

2.5.5 Re-epithelialization 93

2.5.6 Extracellular matrix deposition 97

2.5.7 Summary 99

3. Characterization Techniques 103

3.1 Physical analysis 103

3.2 Chemical analysis 103

3.2.1 X-ray Diffraction 103

3.2.2 Fourier transform infrared spectroscopy 104

3.2.3 Inductively coupled plasma atomic emission spectroscopy (ICP-AES) 104

3.3 In vitro analysis 105

3.3.1 CCK-8 assay 105

3.3.2 ELISA assay 105

3.3.3 Transwell assay 106

3.4 In vivo analysis 106

3.4.1 Diabetic wound model 106

3.4.2 Histology analysis 107

3.4.3 Immunohistochemistry 108

4. Zinc-ion-delivery bioactive glass fibre mat for burn regeneration 110

4.1 Introduction 110

4.2 Methods 111

4.2.1 Preparation of sol-gel electrospun Zn-BG fibre mats 111

4.2.2 Preparation and characterization of Zn-BG fibre mats 115

4.2.3 Dissolution study 116

4.2.4 In vitro study on fibroblasts and endothelial cells 116

4.2.5 Statistical analysis 117

4.3 Results and Discussion 117

4.3.1 Morphology of 3D ECM-mimic fibre mats 117

4.3.2 Chemical structure of 3D ECM-mimic fibre mats 119

4.3.3 Dissolution profiles 120

4.3.4 Fibroblast viability 125

4.3.5 PDGF expression from fibroblasts 128

4.3.6 TGF-β expression from fibroblasts 129

4.3.7 HIF-1α expression from fibroblasts 130

4.3.8 VEGF expression from fibroblasts 131

4.3.9 bFGF(FGF-2) expression from fibroblasts 133

4.3.10 Metabolic activity of endothelial cells 134

4.3.11 Migration of endothelial cells 135

4.3.12 Growth factor expressions from endothelial cells 136

4.4 Concluding remarks 138

5 Borate-based bioactive glass fibre mats for the regeneration of diabetic ulcers 139

5.1 Introduction 139

5.2 Methods 141

5.2.1 Synthesis of the borosilicate BG fibre mats 141

5.2.2 Characterization 143

5.2.3 Dissolution profiles 143

5.2.4 Biocompatibility test and protein expression on fibroblasts 144

5.2.5 Proliferation, migration, and protein expression on endothelial cells 144

5.2.6 Statistical analysis 145

5.3 Results and Discussion 145

5.3.1 3D ECM-mimic borate-based bioactive glass fibre mats 145

5.3.2 Chemical structure of 3D ECM-mimic fibre mats 147

5.3.3 Dissolution studies 149

5.3.4 In vitro cytocompatibility assessment on HDF 152

5.3.5 PDGF expression from fibroblasts 155

5.3.6 TGF-β expression from fibroblasts 156

5.3.7 HIF-1α expression from fibroblasts 157

5.3.8 VEGF expression from fibroblasts 159

5.3.9 bFGF (FGF-2) expression from fibroblasts 160

5.3.10 In vitro endothelial cell viability and protein expressions 161

5.3.11 In vitro endothelial cell migration 164

5.4 Concluding remarks 165

6 In vivo analysis of borate-based bioactive glass fibre mat on diabetic rodent model 167

6.1 Introduction 167

6.2 Methods 168

6.2.1 Design of the animal model 168

6.2.2 Wound closure assay 170

6.2.3 Histology analysis 170

6.2.4 Immunohistochemistry analysis 171

6.3 Results and Discussion 172

6.3.1 In vivo wound closure assay 172

6.3.2 Angiogenesis assessment through optical images 174

6.3.3 H&E Staining 175

6.3.4 Masson Trichrome Staining 178

6.3.5 Anti-inflammation immunohistochemistry assessment 181

6.3.6 Angiogenesis immunohistochemistry assessment 185

6.3.7 Alpha-smooth muscle actin immunohistochemistry assessment 191

6.4 Concluding remarks 195

7 Conclusion and future work 197

7.1 Conclusion 197

7.1.1 Sol-gel electrospinning parameters for BG fibre mats 197

7.1.2 BG fibre mats releasing zinc ions for the regeneration of burn injuries..... 198

7.1.3 Borosilicate BG fibre mats for diabetic ulcer regeneration 198

7.1.4 In vivo assessment of BGs in diabetic ulcer regeneration..... 199

7.2 Future work 199

7.2.1 Synergistic effects of multiple therapeutic ions in the BG system..... 200

7.2.2 inorganic-organic hybrid fibre mats for the regeneration of load-bearing tissues 200

References.....202

List of Figures

Figure 2. 1. Schematic diagram of individual phases of wound healing and major cells/proteins involved (A) hemostasis, (B) inflammation, (C) proliferation, and (D) remodeling. Reproduced with permission and modified with permission from [81]. . 25

Figure 2. 2. Time course for individual wound healing stages: hemostasis, inflammation, proliferation, and remodeling, for individual wound healing activities and individual cells & proteins. 27

Figure 2. 3. Schematic diagram of the burn pathology and the histology burns during its healing. Reproduced with permission from [2]. 33

Figure 2. 4. Schematic diagram of the burn regeneration treatment. Reproduced with permission from [2]. 34

Figure 2. 5. Schematic diagram of the chronic wounds. Reproduced with permission from [23]. 35

Figure 2. 6. Schematic of the histology of skin and the hypodermis. Reproduced from https://learnmuscles.com/blog/. 38

Figure 2. 7. Schematic of deep wound regeneration mechanism. Reproduced with permission from [198]. 38

Figure 2. 8. Schematic diagram of the structure of a borosilicate BG with network former (Si and B), network modifier (Ca and Na), and bridging/non-bridging oxygens 43

Figure 2. 9. Schematic of the osteogenic mechanism of bioactive glasses. 44

Figure 2. 10. Schematic of the melt-derived approach of bioactive glass and scaffold production. 46

Figure 2. 11. Schematic of the sol-gel approach of bioactive glass synthesis. 47

Figure 2. 12. Schematic diagram of the structure evolution and alkali ion distribution of sol-gel-based BG synthesized through TEOS and $Ca(NO_3)^2$ during (a) gelling, (b) drying, and (c) stabilization, modified from [284]. 48

Figure 2. 13. (A) A schematic diagram of the structure of MBG particles and their inner ordered mesoporous channel, and (B) The TEM images of calcined hexagonal 80S15C MBG recorded along the [100] directions. Modified from [279, 304, 305]. . 51

Figure 2. 14. (a) Schematic diagram of the electrospinning apparatus in a vertical alignment, reproduced from [319]. (b) Schematic diagram of the propagation of the electrospinning jet reproduced from [313]. (c) Schematic diagram of electrospun fibre structure achieved under low to high voltages (from a to e), Reproduced with permission from [320]. (d) SEM images of the silicate-based sol–gel-derived fibres 70S30C (70 mol% SiO_2, 30 mol% CaO), with diameters of 320 nm, were reproduced from [97]. 53

Figure 3. 1. Schematic of the ELISA process. Adapted from MBL life of Science website (https://ruo.mbl.co.jp/bio/e/support/method/elisa.html) 105

Figure 3. 2. Schematic of a general process of immunohistochemistry staining. Adapted from [794]. (The timing described in the process may vary between protocols). 108

Figure 4. 1. Schematic of zinc-ion-delivering bioactive glass fibre mats as potential burn regeneration matrices 111
Figure 4. 2. SEM images of the 70S27C3Zn fibre mats synthesized under humidity of (a) 24-26%, (b) 35-37%, (c) 42-45%, and (d) 51-55%. 113
Figure 4. 3. (a) Photograph of an electrospun fibrous bioactive glass scaffold; SEM images of the fibre mats with composition 70 SiO_2-30-x CaO-x ZnO, in mol% where x = (b) 0 ; (c) 1 ; (d) 3 ; and (e) 5. 118
Figure 4. 4. XRD patterns of the as-produced 70S30C, 70S29C1Zn, 70S27C3Zn, and 70S25C5Zn bioactive glass scaffolds. 119
Figure 4. 5. FTIR spectra of the as-produced 70S30C, 70S29C1Zn, 70S27C3Zn, and 70S25C5Zn bioactive glass scaffolds. 120
Figure 4. 6. SEM images of the morphology of 70S27C3Zn fibre after being immersed in DMEM for 7 days. 121
Figure 4. 7. Elemental concentration profiles (ICP) of TRIS buffer following immersion of bioactive glass fibre mats 70S30C, 70S29C1Zn, 70S27C3Zn, and 70S25C5Zn over 7 d (a) Ca, (b) Zn, and (c) Si. 121
Figure 4. 8. pH change of TRIS buffer following immersion of bioactive glass fibre mats 70S30C, 70S29C1Zn, 70S27C3Zn, and 70S25C5Zn over 7 d (a) Ca, (b) Zn, and (c) Si. 122
Figure 4. 9. Elemental concentration profiles (ICP) of DMEM following immersion of bioactive glass fibre mats 70S30C, 70S29C1Zn, 70S27C3Zn, and 70S25C5Zn over 7 d (a) Ca, (b) Zn, and (c) Si. 123
Figure 4. 10. pH change of DMEM following immersion of bioactive glass fibre mats 70S30C, 70S29C1Zn, 70S27C3Zn, and 70S25C5Zn over 7 d 123
Figure 4. 11. The effect of the dissolution products of the 70S30C, 70S29C1Zn, 70S27C3Zn, and 70S25C5Zn scaffolds on the metabolic activity (MA) of HDFs on days 1, 3, and 7, represented by the (a) normalized MA against the DMEM control. (*P <0.05, **P<0.01, ***P <0.001,****P <0.0001) 126
Figure 4. 12. The effect of undiluted, 1/2 diluted, and 1/4 diluted dissolution products on MA of HDFs at day (a) 1, (b) 3, and (c) 7, represented by the intensity of absorbance at 450 nm. (*P <0.05, **P<0.01, ***P <0.001,****P <0.0001) 127
Figure 4. 13. PDGF expressed from the HDFs (ELISA assay) cultured with the undiluted and 1/2 diluted dissolution products of the 70S30C, 70S29C1Zn, 70S27C3Zn, and 70S25C5Zn scaffold, for 2 days. (*P <0.05, **P<0.01, ***P <0.001,****P <0.0001) 129
Figure 4. 14. TGF-β expressed from the HDFs (ELISA assay) cultured with the undiluted and 1/2 diluted dissolution products of the 70S30C, 70S29C1Zn, 70S27C3Zn, and 70S25C5Zn scaffold, for 2 days. (*P <0.05, **P<0.01, ***P <0.001,****P <0.0001) 130
Figure 4. 15. HIF-1α expressed from the HDFs (ELISA assay) cultured with the undiluted and 1/2 diluted dissolution products of the 70S30C, 70S29C1Zn, 70S27C3Zn, and 70S25C5Zn scaffold, for 2 days. (*P <0.05, **P<0.01, ***P <0.001,****P <0.0001) 131
Figure 4. 16. VEGF expressed from the HDFs (ELISA assay) cultured with the undiluted and 1/2 diluted dissolution products of the 70S30C, 70S29C1Zn, 70S27C3Zn, and 70S25C5Zn scaffold, for 2 days. (*P <0.05, **P<0.01, ***P <0.001,****P <0.0001) 132

Figure 4. 17. bFGF(FGF-2) expressed from the HDFs (ELISA assay) cultured with the undiluted and 1/2 diluted dissolution products of the 70S30C, 70S29C1Zn, 70S27C3Zn, and 70S25C5Zn scaffold, for 2 days. (*P <0.05, **P<0.01, ***P <0.001,****P <0.0001) 133
Figure 4. 18. (a) Metabolic activity of HUVECs after being cultured with 1:1 mixture of endothelial culture media with control medium (DMEM-HDF), 70S30C-HDF, 70S29C1Zn-HDF, 70S27C3Zn-HDF, and 70S25C5Zn-HDF conditioned media at day 1, 3, and 7. (*P <0.05, **P<0.01, ***P <0.001,****P <0.0001) 134
Figure 4. 19. (a) Cell number and (b-f) images of migrated HUVECs after being cultured for 16 hours in a Transwell assay with (b) the control medium, (c) 70S30C-HDF conditioned medium, (d) 70S29C1Zn conditioned medium, (e) 70S27C3Zn conditioned medium, and (f) 70S25C5Zn conditioned medium. (*P <0.05, **P<0.01, ***P <0.001,****P <0.0001) 136
Figure 4. 20. HIF-1α, VEGF, bFGF (FGF-2), and eNOS expressed from HUVECs (ELISA assay) cultured with the 1:1 mixture of endothelial culture media with control medium (DMEM-HDF) 70S30C-HDF, 70S29C1Zn-HDF, 70S27C3Zn-HDF, and 70S25C5Zn-HDF conditioned media for 48 h. (*P <0.05, **P<0.01, ***P <0.001,****P <0.0001) 137

Figure 5. 1. Schematic of the role of boron released from BG to the cells in the diabetic ulcer regeneration cascade 140
Figure 5. 2. (a) Schematics of 3D borosilicate BG fibre mats (b-h) SEM images of the electrospun bioactive glass fibre mats with composition (70-x) SiO_2-30 CaO-x B_2O_3, in mol% where x = (b) 0; (c) 5; (d) 15; (e) 35; (f) 55; (g) 65; (h) 70; 146
Figure 5. 3. XRD patterns of as-produced 70S30C, 65S30C5B, 55S30C15B, 35S30C35B, 15S30C55B, 5S30C65B, 70B30C bioactive glass fibre mats (along with an indication of the crystallization peaks for calcium borate). 148
Figure 5. 4. FTIR spectra patterns of as-produced 70S30C, 65S30C5B, 55S30C15B, and 35S30C35B bioactive glass fibre mats. 149
Figure 5. 5. Elemental concentration profiles (ICP) of DMEM following immersion of bioactive glass fibre mats 70S30C, 65S30C5B, 55S30C15B, and 35S30C35B over 7 d (a) Ca, (b) B, and (c) Si. 151
Figure 5. 6. pH change of DMEM following immersion of bioactive glass fibre mats 70S30C, 65S30C5B, 55S30C15B, and 35S30C35B over 7 d. 151
Figure 5. 7. The effect of the dissolution products of the 70S30C, 65S30C5B, 55S30C15B, and 35S30C35B fibre mats on the MA of HDFs at days 1, 3, and 7, represented by the intensity of absorbance at 450 nm. (*P <0.05, **P<0.01, ***P <0.001,****P <0.0001) 152
Figure 5. 8. The effect of undiluted, 1/2 diluted, and 1/4 diluted dissolution products on MA of HDFs at day (a) 1, (b) 3, and (c) 7, represented by the intensity of absorbance at 450 nm. (*P <0.05, **P<0.01, ***P <0.001,****P <0.0001) 154
Figure 5. 9. PDGF expressed from the HDFs (ELISA assay) cultured with the undiluted and 1/2 diluted dissolution products of the 70S30C, 65S30C5B, 55S30C15B, and

35S30C35B fibre mats, for 3 days. (*P <0.05, **P<0.01, ***P <0.001,****P <0.0001). 156
Figure 5. 10. TGF-β expressed from the HDFs (ELISA assay) cultured with the undiluted and 1/2 diluted dissolution products of the 70S30C, 65S30C5B, 55S30C15B, and 35S30C35B fibre mats, for 3 days. (*P <0.05, **P<0.01, ***P <0.001,****P <0.0001). 157
Figure 5. 11. HIF-1α expressed from the HDFs (ELISA assay) cultured with the undiluted and 1/2 diluted dissolution products of the 70S30C, 65S30C5B, 55S30C15B, and 35S30C35B fibre mats, for 3 days. (*P <0.05, **P<0.01, ***P <0.001,****P <0.0001). 158
Figure 5. 12. VEGF expressed from the HDFs (ELISA assay) cultured with the undiluted and 1/2 diluted dissolution products of the 70S30C, 65S30C5B, 55S30C15B, and 35S30C35B fibre mats, for 3 days. (*P <0.05, **P<0.01, ***P <0.001,****P <0.0001). 159
Figure 5. 13. bFGF(FGF-2) expressed from the HDFs (ELISA assay) cultured with the undiluted and 1/2 diluted dissolution products of the 70S30C, 65S30C5B, 55S30C15B, and 35S30C35B fibre mats, for 3 days. (*P <0.05, **P<0.01, ***P <0.001,****P <0.0001). 160
Figure 5. 14. Metabolic activity of HUVECs at day 1, 3, and 7 from HUVECs at day 3 after being cultured in the BG-HDF conditioned media, conditioned with 70S30C, 65S30C5B, 55S30C15B, and 35S30C35B fibre mats and the DMEM-HDF conditioned media. (*P <0.05, **P<0.01, ***P <0.001,****P <0.0001). 161
Figure 5. 15. Elisa results of HIF-1α, VEGF, bFGF (FGF-2), and eNOS expressions from HUVECs at day 3 after being cultured in the BG-HDF conditioned media, conditioned with 70S30C, 65S30C5B, 55S30C15B, and 35S30C35B fibre mats and the DMEM-HDF conditioned media. (*P <0.05, **P<0.01, ***P <0.001,****P <0.0001). 162
Figure 5. 16. Cell number of migrated HUVECs after being cultured for 16 hours in a Transwell assay with the DMEM-HDF medium, and 70S30C-HDF, 65S30C5B-HDF, 55S30C15B-HDF medium, and 35S30C35B-HDF medium. (*P <0.05, **P<0.01, ***P <0.001,****P <0.0001) 163
Figure 5. 17. (a-e) images of migrated HUVECs after being cultured for 16 hours in a Transwell assay with (a) the DMEM-HDF medium, (b) 70S30C-HDF conditioned medium, (c) 65S30C5B-HDF conditioned medium, (d) 55S30C15B-HDF conditioned medium, and (e) 35S30C35B-HDF conditioned medium. 164

Figure 6. 1. Schematic of the effect of BG samples on different steps in diabetic ulcer pathology and their corresponding assessment approach 167
Figure 6. 2. Schematics of Histology analysis: Analysis of collagen area and number of cells from Masson Trichrome Staining using Color devolution from ImageJ 171
Figure 6. 3. Schematics of Immunohistochemistry analysis： Analysis of VEGF area in wounds using Color devolution from ImageJ. 172

Figure 6. 4. Images of regenerated wound area taken on days 0, 3, 7, 10, and 13 post-surgery on diabetic C57BJ/6 mice treated with 70S30C (70S) powder, 55S30C15B (55S) powder, and 55S30C15B (55S) fibre. 173
Figure 6. 5. Relative wound area of different treatment groups after 0, 3, 7, 10, and 13 days post-surgery on diabetic C57BJ/6 mice treated with 70S30C powder, 55S30C15B powder, and 55S30C15B fibre. (*P <0.05, **P<0.01, ***P <0.001,****P <0.0001). 174
Figure 6. 6. Blood vessel formation of the sacrificed skin tissue of different treatment groups after 7 and 13 days post-surgery on diabetic C57BJ/6 mice treated with 70S30C (70S) powder, 55S30C15B (55S) powder, and 55S30C15B (55S) fibre. 175
Figure 6. 7. Images of H&E staining of diabetic C57BJ/6 mice wound sections treated with 70S30C (70S) powder, 55S30C15B (55S) powder, and 55S30C15B (55S) fibre on 7 days post-surgery. 176
Figure 6. 8. Images of H&E staining of diabetic C57BJ/6 mice wound sections treated with 70S30C (70S) powder, 55S30C15B (55S) powder, and 55S30C15B (55S) fibre 13 days post-surgery. 177
Figure 6. 9. The length of wound gap derived from H&E staining of diabetic C57BJ/6 mice wound sections treated with 70S30C powder, 55S30C15B powder, and 55S30C15B fibre 7 and 13 days post surgery. (*P <0.05, **P<0.01, ***P <0.001,****P <0.0001). 178
Figure 6. 10. Images of Masson Trichrome staining of diabetic C57BJ/6 mice wound sections treated with 70S30C (70S) powder, 55S30C15B (55S) powder, and 55S30C15B (55S) fibre 7 days post-surgery. 179
Figure 6. 11. Images of Masson Trichrome staining of diabetic C57BJ/6 mice wound sections treated with 70S30C powder, 55S30C15B powder, and 55S30C15B fibre on 13 days post-surgery. 180
Figure 6. 12. The relative area of collagen deposition derived from Masson Trichrome staining of diabetic C57BJ/6 mice wound sections treated with 70S30C powder, 55S30C15B powder, and 55S30C15B fibre 13 days post surgery. (*P <0.05, **P<0.01, ***P <0.001,****P <0.0001). 181
Figure 6. 13. Images of IL-1β immunohistochemistry staining of diabetic C57BJ/6 mice wound sections treated with 70S30C (70S) powder, 55S30C15B (55S) powder, and 55S30C15B (55S) fibre on 7 and 13 days post-surgery. 182
Figure 6. 14. Quantification of IL-1β relative area in percentage derived from IL-1β immunohistochemistry staining of diabetic C57BJ/6 mice wound sections treated with 70S30C powder, 55S30C15B powder, and 55S30C15B fibre on 7 and 13 days post surgery. (*P <0.05, **P<0.01, ***P <0.001,****P <0.0001). 183
Figure 6. 15. Images of IL-10 immunohistochemistry staining of diabetic C57BJ/6 mice wound sections treated with 70S30C (70S) powder, 55S30C15B (55S) powder, and 55S30C15B (55S) fibre on 7 and 13 days post-surgery. 184
Figure 6. 16. Quantification of IL-10 relative area in percentage derived from IL-1β immunohistochemistry staining of diabetic C57BJ/6 mice wound sections treated with

70S30C powder, 55S30C15B powder, and 55S30C15B fibre on 7 and 13 days post surgery. (*P <0.05, **P<0.01, ***P <0.001,****P <0.0001). 185
Figure 6. 17. Images of VEGF immunohistochemistry staining of diabetic C57BJ/6 mice wound sections treated with 70S30C (70S) powder, 55S30C15B (55S) powder, and 55S30C15B (55S) fibre on 7 days post-surgery. 186
Figure 6. 18. Images of VEGF immunohistochemistry staining of diabetic C57BJ/6 mice wound sections treated with 70S30C (70S) powder, 55S30C15B (55S) powder, and 55S30C15B (55S) fibre on 7 days post-surgery. 187
Figure 6. 19. Quantification of relative area of VEGF derived from VEGF immunohistochemistry staining of diabetic C57BJ/6 mice wound sections treated with 70S30C powder, 55S30C15B powder, and 55S30C15B fibre on 7 and 13 days post surgery. (*P <0.05, **P<0.01, ***P <0.001,****P <0.0001). 188
Figure 6. 20. Images of CD31 immunohistochemistry staining of diabetic C57BJ/6 mice wound sections treated with 70S30C (70S) powder, 55S30C15B (55S) powder, and 55S30C15B (55S) fibre on 7 days post-surgery. 189
Figure 6. 21. Images of CD31 immunohistochemistry staining of diabetic C57BJ/6 mice wound sections treated with 70S30C (70S) powder, 55S30C15B (55S) powder, and 55S30C15B (55S) fibre 13 days post-surgery. 190
Figure 6. 22. Number of blood vessels per mm^2 derived from CD31 immunohistochemistry staining of diabetic C57BJ/6 mice wound sections treated with 70S30C powder, 55S30C15B powder, and 55S30C15B fibre on 7 and 13 days post surgery. (*P <0.05, **P<0.01, ***P <0.001,****P <0.0001). 191
Figure 6. 23. Images of α-SMA immunohistochemistry staining of diabetic C57BJ/6 mice wound sections treated with 70S30C (70S) powder, 55S30C15B (55S) powder, and 55S30C15B (55S) fibre on 7 days post-surgery. 192
Figure 6. 24. Images of α-SMA immunohistochemistry staining of diabetic C57BJ/6 mice wound sections treated with 70S30C (70S) powder, 55S30C15B (55S) powder, and 55S30C15B (55S) fibre 13 days post-surgery. 193
Figure 6. 25. The number of vascular smooth muscles per mm^2 derived from α-SMA immunohistochemistry staining of diabetic C57BJ/6 mice wounds sections treated with 70S30C powder, 55S30C15B powder, and 55S30C15B fibre on 7 and 13 days post-surgery. (*P <0.05, **P<0.01, ***P <0.001,****P <0.0001). 194
Figure 6. 26. The relative area of α-SMA derived from α-SMA immunohistochemistry staining of diabetic C57BJ/6 mice wound sections treated with 70S30C powder, 55S30C15B powder, and 55S30C15B fibre on 7 and 13 days post-surgery. (*P <0.05, **P<0.01, ***P <0.001,****P <0.0001) 195

List of Tables

Table 2. 1. Major growth factors involved in wound healing and a summary of their roles. 28
Table 2. 2. Major cytokines and proteases involved in wound healing and a summary of their roles. 29
Table 2. 3. Common BG names and composition (mol%). 43
Table 2. 4. Common microorganisms inhibited by BG. 59
Table 2. 5. Summary of BG glass systems designed to deliver ions with antibacterial properties. MBG = mesoporous (ordered) bioactive glass; Antibacterial ratio = the percentage of bacteria remaining after culture with BG for a certain period; MIC: Minimal inhibitory concentration; MBC = Minimal bactericidal concentration; Inhibition halo = a bacteria-free zone induced by BG powders or scaffolds on the agar plate. 69
Table 2. 6. BG glass system to angiogenic responses. (HUVEC: Human Umbilical Vein Endothelial Cells. EC: endothelial cells other than HUVECs, MSC: Mesenchymal stem cells, DPPSC: Dental Pulp Pluripotent-Like Stem Cell, CAM: Chorioallantoic membrane, AV loop: Arteriovenous loop) 88

Table 4. 1. Sol-gel compositions 70 SiO_2-30-x CaO-x ZnO, in mol% (x = 0,1,3,5) and the quantities of TEOS, nitric acid, ethanol, calcium nitrate tetrahydrate, and zinc nitrate hexahydrate used. 115
Table 4. 2. Fibre diameters of the electrospun bioactive glass scaffolds. 118

Table 5. 1. Nominal sol-gel compositions and the quantities of TEOS, nitric acid, ethanol, calcium nitrate, and triethyl borate used. 143
Table 5. 2. Fibre diameters of the electrospun bioactive glass scaffolds. 147

Table 6. 1. The effect of BG implantation, the effect of boron incorporation, and the effect of fibre VS powder in wound healing steps are derived from the pairwise comparison among wounds treated with nothing (control), 70S30C powder, 55S30C15B powder, and 55S30C15B fibre mats respectively. (Little means no significance, Medium means *0.01 < P < 0.05 of significance, High means **0.0001 < P < 0.01 significance, and very high means ****P < 0.0001 significance) 196

List of Abbreviations

3D	Three-dimensional
bFGF (FGF-2)	Basic fibroblast growth factor
BG	Bioactive glass
CCK-8	Cell counting kit-8
CD31	Cluster of differentiation 31 (marker for endothelial cells)
DMEM	Dulbecco's Modified Eagle Medium
ECM	Extracellular matrix
ELISA	Enzyme-Linked ImmunoSorbent Assay
eNOS	Endothelial nitric oxide synthase
FTIR	Fourier transform infrared spectroscopy
H&E	Hematoxylin and eosin
HDF	Human dermal fibroblast
HIF-α	Hypoxia-induced factor α
HUVEC	Human umbilical vein endothelial cells
ICP-OES	Induced coupled plasma- optical emission spectroscopy
IL-1	Interleukin-1
IL-10	Interleukin-10
MA	Metabolic activity
PDGF	Platelet-Derived Growth Factor
TEB	Triethyl borate
TEOS	Tetraethyl orthosilicate
TGF-β	Transforming growth factor beta
TRIS	Tris(hydroxymethyl)aminomethane
VEGF	Vascular endothelial growth factor
XRD	X-ray diffraction
α-SMA	Alpha-smooth muscle actin

1 Introduction

An increasing need for solutions to burn injuries and diabetic ulcers

Burns are one of the most common household injuries but can lead to some of the most severe consequences [1, 2]. Amongst the estimated 11 million annual cases of burn injuries worldwide, 180,000 of them lead to death [2] because of the massive water loss, pain, and infection after severe burns [3, 4]. Patients suffering from severe burn injuries usually have: (1) damaged epidermis with excessive exudates that can become infected; [5, 6] (2) degraded ECM and necrotic tissues that cause inflammation; [7, 8] (3) follicle loss that leads to function loss and fewer stem cell sources [9, 10]. The ECM and vascular network in the dermis are also usually damaged, making it more difficult to provide nutrients and oxygen to regenerate wounds [11].

With the worldwide surge in diabetic and aging patients, diabetic ulcers are also becoming a greater threat to the national healthcare system [12, 13]. It usually leads to amputation [14, 15] and high mortality, as 60% of patients with diabetic ulcers die within 5 years [16-18]. The cost of diabetic ulcer treatment is more than $50000 and the regenerated tissue never recovers to the structural and functional integrity of the original skin [19]. Diabetic ulcers commonly experience a prolonged inflammation phase where pro-inflammatory cytokines and protease aggregate in the wound side and impair the function of cells, growth factors, and the ECM [16, 20-22]. The neuropathy of diabetics also inhibits keratinocyte migrations which leads to bacteria colonization and biofilm formation at the wound site [23, 24]. Local ischemia has been a major cause of the delayed regeneration of diabetic ulcers, as it inhibits the supply of nutrients and oxygen [25-27].

Grafts are still a common strategy for the two types of conditions, but the transplanted tissues lack important wound regeneration factors including pigments, hair follicles, sweat glands, immune cells, etc. and the whole process also induces the risk of pain, donor site infection, cell death, and more importantly, lack of donor skin [18, 28]. Delivering biomolecules and proteins to wound areas through hydrogels can be therapeutic [1, 29-31], but has limitations in reproducibility and storage. Wound matrices, a 3D matrix that is pressed into the wound defect and degrades while the wound regenerates, are becoming more popular [32], but there have not been ideal matrices that satisfy all the biological requirements in diabetic ulcer regeneration cascades. The high cost and time consumption, difficulty in the sourcing, production, storage, and application of novel

dressings, as well as narrow audience of targeting, are all obstacles in wound matrices development and applications [33-35].

Bioactive glasses as strategies for wound healing

Recently, bioactive glasses have been reported as strategies for wound regeneration [36-38]. Bioactive glasses (BGs) are a type of biodegradable inorganic materials that were commercially successful in osteogenesis [39-42]. Their efficacies in soft tissue repair are due to their biodegradability and their ion delivery capabilities as BG has been reported to incorporate and deliver more than twenty therapeutic elements that are involved in different signaling or stimulation pathways [43-46]. BGs were reported to stimulate hemostasis [47, 48], antibacterial activities [49, 50], anti-inflammation [51, 52], the up-regulation of VEGF and FGF-2 from fibroblasts [53, 54], epithelialization and wound closure [55, 56], as well as endothelial tubule formation in vitro and in vivo [57, 58]. Zn is incorporated into the BG system to ensure a sustained release of Zn ions that stimulates antibacterial, anti-inflammatory, angiogenic, and follicle regeneration properties during the burn regeneration cascades [59-64]. Borate-based and borosilicate BGs are being developed for diabetic ulcer regeneration as boron has been previously proved to stimulate epithelialization, angiogenesis, ECM deposition, anti-inflammation, tissue granulation, etc. [57, 65-73], but the concentration to effect correlation remains unknown.

Development of bioactive glasses fibre mats

Another aspect of the design of ideal wound matrices is the physical structure. The ECM in wounds consists of collagen, proteoglycan, laminin, and fibronectin, in which collagen forms a grid-like inter-crosslinked structure [74]; proteoglycan provides hydration and withstands forces; [75]; laminin stabilizes the architecture of the collagen [76]; fibronectin binds integrins on the cell membrane to the collagen network [77]. Scarring collagen is more oriented than normal collagen in both superficial dermis and deep dermis [78, 79]. To structurally promote the attachment, proliferation, and migration of fibroblasts and endothelial cells, it could be ideal to fabricate biomaterials into a cotton-wool-like structure, which mimics the ECM in the intact skin [80-82]. Recently, the Mo-Sci corporation developed a melt-blowing approach to fabricate BG fibres of different compositions [83-85], but these fibres were high in Na and K, which have adverse effects to wound regeneration (e.g. pain, high local pH) [86-90]. The fibres were heterogeneous in length and diameter, 75% of which contained beading [45, 46, 72, 91]. These beads are usually in tens of micrometers so that greatly affect the degradation and ion release kinetics of the fibre mats, interrupt the structural homogeneity of the fibre mat, and inhibit the attachment of cells.

The sol-gel electrospinning technique is an alternative approach for synthesizing ultrafine BG fibres [92, 93]. Kim *et al.* first applied this technique in synthesizing BG nanofibres [94]. Sol-gel precursors, mixed with the polymer solution, were delivered from a syringe and dragged towards the collector by the electric potential. During the spinning, the sol was gelled into fibres and dried. The diameters of the BG fibres were adjusted by altering the precursor concentration. The voltage used affected fibre morphology, e.g. fibre thickness and level of beading [95]. Poologasundarampillai *et al.* introduced the first binder-free sol-gel electrospinning approach to produce 3D structured (0.5-2 mm compared to conventional 2D mats (< 0.5 mm)) BG fibres (1.5 μm in diameter) [96]. However, the use of polymer binder was later reintroduced to improve the reproducibility of 3D structured BG fibres with diameters of 0.21-0.34 μm [97]. The fibres had no cytotoxicity and stimulated higher VEGF expression from fibroblasts, indicating their potential angiogenic activities.

Outline of the thesis

The general aim of this thesis is to design ECM-mimic bioactive glass fibre mats for the regeneration of burn injuries and diabetic ulcers, to investigate the efficacies of the fabricated samples in vitro and in vivo, and to understand the mechanism of BGs and therapeutic ions to individual steps in the wound regeneration.

The literature review presents an overview of the wound healing cascade, pathologies of abnormal wounds, and current practices used to heal wounds. It describes the development of bioactive glasses and their synthesis, in which the use of sol-gel electrospinning fibres and the parameters influencing the fibre morphology is elaborated in detail. The role of ions released from BGs and their effect on individual steps in the wound healing cascade is introduced and their therapeutic range was estimated as a basis to design novel wound matrices. Chapter 3 summarizes the characterization techniques used in this thesis. The experimental work and results are presented and discussed in Chapters 4 – 6, and conclusions are made in Chapter 7.

In Chapter 4, 3D ECM-mimic Zn-containing BG fibre mats were synthesized to deliver therapeutic zinc ions for burn regeneration, particularly on stimulating angiogenesis and ECM deposition. BG fibres with a composition of 70 mol% SiO_2-(30-x) mol% CaO- x mol% ZnO (x=0, 1, 3, and 5, labeled as 70S30C, 70S29C1Zn, 70S27C3Zn, and 70S25C5Zn respectively) were prepared through the sol-gel electrospinning method **[98-101]**. The effects of Zn incorporation on the physical and chemical structures of BG fibres were assessed through XRD, FTIR, and SEM. The dissolution profiles of the resultant fibre mats

were accessed in TRIS buffer solution and DMEM. The advantages of Zn incorporation to cell proliferation, protein expressions, and angiogenesis were further evaluated on Human Dermal Fibroblasts (HDF) and Human Umbilical Vein Endothelial Cells (HUVECs). Our fibre mats could be used as 3D matrices for burn regeneration underneath more conventional dressings.

Chapter 5 proposes a modified sol-gel approach that enables the synthesis of 3D ECM-mimic borosilicate BG fibre mats without using methoxyethoxides. BG fibres with a composition of (70-x) mol% SiO_2-30 mol% CaO- x mol% B_2O_3 (x=0, 5, 15, and 35, 55, 65, and 70) were prepared through the sol-gel electrospinning method. The fibre mats exhibit a 3D ECM-mimic structure, tailorable degradation, ion-release kinetics, biophysical cues promoting cell attachment and migration, and biochemical cues promoting cell proliferation, protein expression, anti-inflammation, and angiogenesis. The resultant fibre mats were characterized through XRD, FTIR, and SEM, and their dissolution profiles were acquired in DMEM. In vitro studies assessed the role of boron incorporation in the proliferation, migration, and protein expressions of HDFs and HUVECs, which indicates the mechanism of boron in ECM and angiogenesis during wound regeneration.

The efficacy of the fibre mats fabricated in Chapter 5 was further assessed in vivo and the results are summarized in Chapter 6. 70S30C powder, 55S30C15B powder, and 55S30C15B fibre were implanted in diabetic wounds of C57BJ/6 mice and characterized by their capabilities in wound closure, tissue granulation, anti-inflammation, ECM deposition, angiogenesis, etc. through histological and immunohistochemical analysis. This study enables us to understand the effect of BG on all major wound healing steps and provide insight on whether boron incorporation in BG systems or processing BGs into fibre mats benefits the above-mentioned steps.

2 Literature review

2.1 The wound healing cascade

Wound healing is a well-defined physiological process that consists of four consecutive but overlapping phases: hemostasis (sometimes called coagulation), inflammation, proliferation, and tissue remodeling [81] (Figure 2. 1). The average period for normal wound healing is less than 3 weeks but is expected to be longer if the patient suffers from any intrinsic disease states or extrinsic infection. Figure 2. 2 indicates the activation time of individual phases as well as cells or proteins involved [80].

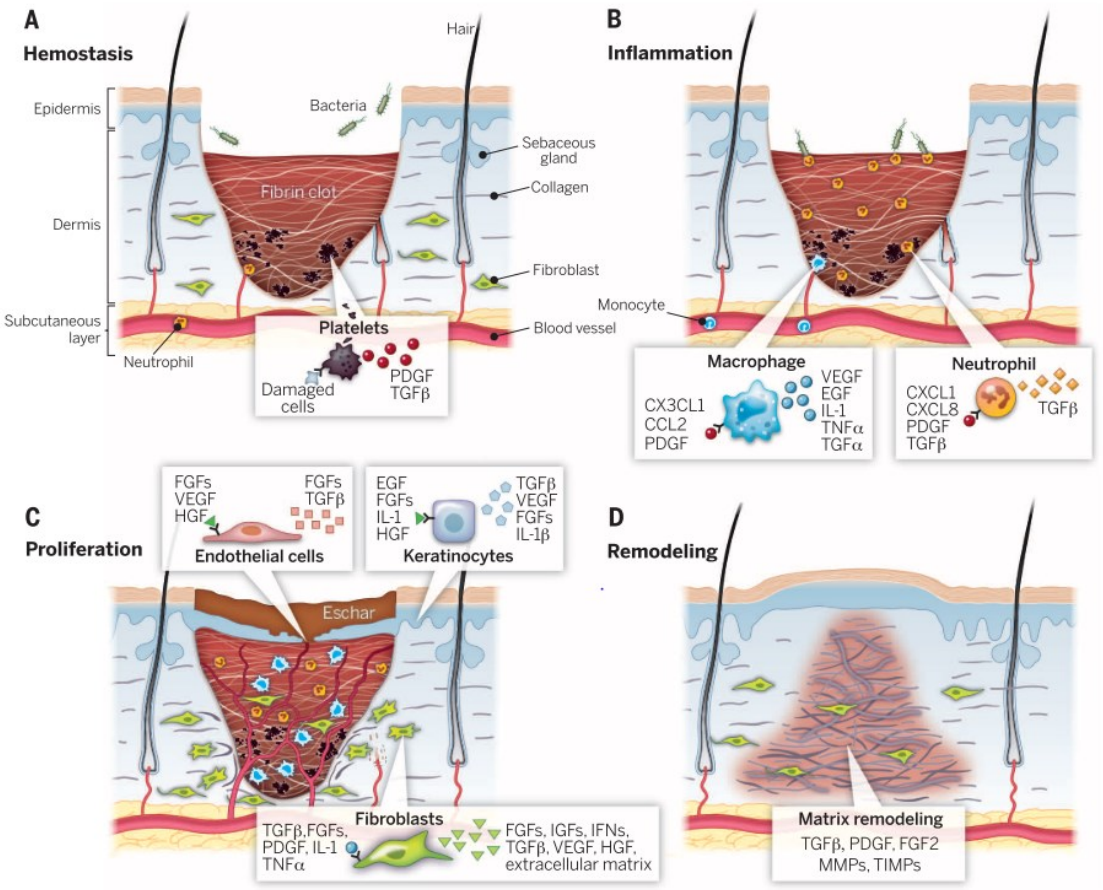


Figure 2. 1. Schematic diagram of individual phases of wound healing and major cells/proteins involved (A) hemostasis, (B) inflammation, (C) proliferation, and (D) remodeling. Reproduced with permission and modified with permission from [81].

2.1.1 Hemostasis

The hemostasis phase is separated into primary and secondary hemostasis. Primary hemostasis is immediately activated after an injury. First, the blood vessels contract (vasoconstriction), to reduce blood outflow. This is followed by the formation of a platelet plug from platelets that aggregate through the blood flow. The plug forms a preliminary barrier to preventing blood loss [102]. Secondary hemostasis contributes to the induction of a fibrin clot covering the platelet plug to fully stop bleeding. The extrinsic coagulation pathway is immediately activated by tissue factors from damaged endothelial cells and stimulates a burst secretion of thrombin. The intrinsic coagulation pathway is also initiated with the activation of Factor XII due to the exposure of endothelial collagen after the endothelial damage and supplies the rest of thrombin release when the extrinsic pathway turns off [82]. Thrombin catalyzes the conversion of fibrinogen to fibrin and the fibrin attaches to the platelet plug [103]. The final clot formed serves as a scaffold for the attachment of immune cells, endothelial cells, fibroblasts attachment, growth factors, and cytokines [80].

2.1.2 Inflammation

By the end of the hemostasis phase, approximately 24-48 hours after wound formation, the early stage of the inflammation phase is activated. Clot formation causes vast migration of leukocytes, primarily neutrophils, to blood vessels in the wound [12]. Then, significant vasolidation occurs to increase vascular permeability and allow leukocytes to infiltrate into the clot [103, 104]. Neutrophils co-function with some monocytes to encapsulate and destroy foreign pathogens and particles, turning them into exudate. They also stimulate the release of protease and reactive oxygen/nitrogen species (ROS/RNS) to further degrade damaged tissues and ECM [80]. This stage serves to produce a natural scaffold for cell migration and proliferation. The digestion behaviour further results in chemotaxis for cell migration, proliferation, and protein expression.

Common reactive oxygen species (ROS) occurring in wounds are: hydroxyls OH^-, superoxide anion O_2^-, hydroperoxyl radical HO_2, and hydrogen peroxide H_2O_2. They commonly arise from different oxygen uptake activities including ATP production in mitochondria, lipid/protein synthesis in the endoplasmic reticulum, and digestion from oxidoreductases [105]. During inflammation, the digestion of pathogens by leukocytes greatly increases the ROS level through the secretion of NADPH oxidase, which reduces molecular oxygen to ROS, termed the respiratory burst [106]. ROS level dramatically modulates cellular responses, for example:

1. A ROS level lower than basal concentration inhibits the proliferation of most cells, including macrophages, fibroblasts, and endothelial cells;
2. Increased ROS level induces several transcription factors to stimulate inflammatory response through immune cell chemoattraction;
3. Excessive ROS level leads to cell apoptosis through the generation of pro-apoptotic proteins, and eventually cellular necrosis [105, 107, 108].

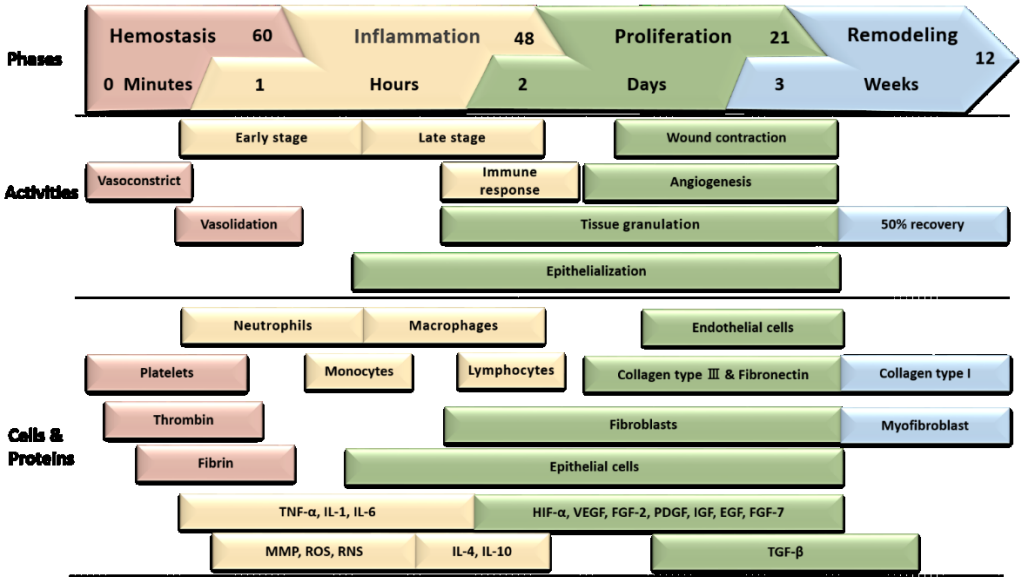


Figure 2. 2. Time course for individual wound healing stages: hemostasis, inflammation, proliferation, and remodeling, for individual wound healing activities and individual cells & proteins.

Reactive nitrogen species (RNS), such as nitrogen oxide (NO), are also released during growth factor activities and are associated with similar functions to ROS but they do not regulate vasoconstriction [105]. At the later stage of inflammation, macrophages, differentiated from monocytes, substitute neutrophils' role in clearing the debris and induction of protease and ROS/RNS [103]. Macrophage activity causes up-regulation of many cytokines and growth factors for further inflammatory or proliferative responses [109]. The details of their biological responses are summarized in

In the anti-inflammatory phase, macrophages favour phenotype M2, and the level of inflammatory cytokines is reduced with an increase in anti-inflammatory cytokine levels. Furthermore, fibroblast proliferation is promoted by macrophage activities and fibroblasts become an alternative source for cytokines and growth factors. This later stage serves to generate an environment rich in growth factors and low in cytokines, for the proliferative activities in the proliferation phase.

Table 2. 1 and Table 2. 2 [12, 80, 81, 110]. Late-stage inflammation is separated into two steps, distinguished by the phenotype of macrophages [111]. In the inflammatory step, macrophages favour the phenotype M1 and more inflammatory cytokines are generated for the digestion behaviour.

In the anti-inflammatory phase, macrophages favour phenotype M2, and the level of inflammatory cytokines is reduced with an increase in anti-inflammatory cytokine levels. Furthermore, fibroblast proliferation is promoted by macrophage activities and fibroblasts become an alternative source for cytokines and growth factors. This later stage serves to generate an environment rich in growth factors and low in cytokines, for the proliferative activities in the proliferation phase.

Table 2. 1. Major growth factors involved in wound healing and a summary of their roles.

Growth factor	Cell source	Ref.	Summary of role
Transforming growth factor α (TGF-α)	Macrophages Platelets	[112, 113]	Induces the formation of granulation tissue Stimulates keratinocyte and fibroblast proliferation
Transforming growth factor β (TGF-β)	Macrophages Platelets Neutrophils Fibroblasts	[114-116]	Activates fibroblasts and fibroblast chemotaxis Differentiates fibroblasts into myofibroblasts Promotes collagen synthesis and matrix construction Induces re-epithelialization Stimulates angiogenesis Promotes wound contraction Stimulates TIMP and downgrades MMP Stimulates other growth factor expression Modulates scarring
Platelet-derived growth factor (PDGF)	Macrophages Platelets Keratinocytes Fibroblasts Endothelial cells	[80, 117-119]	Activates immune cells and fibroblasts Promotes collagen synthesis and ECM deposition Stimulates TIMP and downgrades MMP
Vascular endothelial growth factor (VEGF)	Neutrophils Platelets Keratinocytes	[120, 121]	Stimulates endothelial cell migration and proliferation Stimulates angiogenesis and neovascularization
Fibroblast growth factors (FGF)	Macrophages Endothelial cells Fibroblasts	[122, 123]	Stimulates endothelial cell proliferation Induces keratinocyte proliferation and migration Induces fibroblast migration and proliferation Stimulates angiogenesis and neovascularization Induces ECM deposition and re-epithelialization
Keratinocyte growth factors (KGF(FGF-7))	Macrophages Endothelial cells Fibroblasts	[124, 125]	Induces keratinocyte proliferation and migration Induces re-epithelialization

basic Fibroblast growth factors (FGF-2)	Macrophages Endothelial cells Fibroblast	[126]	Stimulates endothelial cell migration and proliferation Stimulates angiogenesis and neovascularization
Insulin-like growth factor (IGF)	Macrophages Neutrophils Fibroblasts Liver Keletal muscle	[127, 128]	Induces keratinocyte proliferation Induces fibroblast proliferation Promotes collagen synthesis Stimulates endothelial cell proliferation Stimulates angiogenesis and neovascularization Induces keratinocyte proliferation and migration Induces ECM deposition and re-epithelialization Promotes cell metabolism
Epidermal growth factor (EGF)	Macrophages Keratinocytes Fibroblasts	[113]	Induces keratinocyte proliferation and migration Stimulates endothelial cell proliferation Induces ECM deposition and re-epithelialization
Connective tissue growth factor (CTGF)	Endothelial cells Keratinocytes	[129, 130]	Mediates action of TGF-β on collagen synthesis
Thromboxane A2 Serotonin	Platelets	[131]	Accelerates vasoconstriction Accelerates platelet aggregation Increases vascular permeability
Prostaglandin E2 (PGE2)	Macrophages Keratinocytes Endothelial cells	[132, 133]	Accelerates vasoconstriction Accelerates platelet aggregation Increases vascular permeability Leads to pain and fever

Table 2. 2. Major cytokines and proteases involved in wound healing and a summary of their roles.

Cytokines		Ref.	Cell source	Summary of role
Inflammatory cytokines	Tumour necrosis factor α (TNF-α)	[134, 135]	Macrophages Neutrophils Monocytes	Inhibits carcinogenesis and viral replication Increases protease secretion Increases expression IL-1, IL-6, and KGF Stimulates collagen synthesis Induces ECM deposition and re-epithelialization Promotes ROS release
	Interleukin-1 (IL-1)	[135, 136]	Macrophages Keratinocytes Endothelial cells	Induces fibroblast and keratinocyte chemotaxis Increases protease secretion Increases expression of KGF Stimulates collagen synthesis Promotes keratinocyte migration Promotes cell metabolism
	Interleukin-2 (IL-2)	[137]	T-lymphocytes	Increases fibroblast infiltration and metabolism
	Interleukin-6 (IL-6)	[138, 139]	Macrophages Neutrophils Fibroblasts	Induces fibroblast and keratinocyte proliferation Chemoattracts PMNs

	Interleukin-8 (IL-8)	[140]	Macrophages Fibroblasts	Activates as macrophage and neutrophil chemotaxis Induces keratinocyte maturation Promotes MMP secretion
	Interferon γ (IFN-γ)	[141, 142]	T-lymphocytes Macrophages	Activates macrophage and granulocytes maturation Inhibits collagen synthesis and cross-linking Increases collagenase formation Promotes ROS release
Anti-inflammatory cytokines	Interleukin-4 (IL-4)	[143]	T-lymphocytes Basophils Mast cells	Inhibits the expression of TNF-α, IL-1, and IL-6 Induces fibroblast proliferation Stimulates collagen synthesis
	Interleukin-10 (IL-10)	[144, 145]	T-lymphocytes Macrophages Keratinocytes	Inhibits the expression of TNF-α, IL-1, and IL-6 Induces fibroblast proliferation Stimulates collagen synthesis
	Lipoxins	[146]	Platelets Leukocytes	Inhibits neutrophil activation
Proteases	Elastase	[147]	Fibroblast Leukocytes	Degrades collagen Digests growth factors
	Matrix metallo-proteinase (MMP)	[148, 149]	Fibroblast Leukocytes	Degrades elastin Digests growth factors
	Tissue inhibitor of metallo-proteinase (TIMP)	[150]	Fibroblast Leukocytes	Inhibits MMP activities

2.1.3 Proliferation

The proliferation phase is activated when the wound is debris-free and a new matrix is available for fibroblast attachment [151], so it initiates during hemostasis as platelets secrete growth factors, attracting fibroblasts and overlaps the inflammation phase as growth factors and cytokines are released from macrophages. The whole proliferation phase spans three weeks, involving three major proliferation actions:

1. angiogenesis, induced through the migration and proliferation of endothelial cells, repairing of broken blood vessels, and generating new ones;
2. re-epithelialization, induced through the migration of epithelial cells, mainly keratinocytes, closing the wound to prevent infection and create an environment suitable for cells living and growth;
3. ECM deposition, induced through the activities of fibroblasts, synthesizing ECM proteins such as collagen, elastin, and fibronectin, leading to further tissue granulation and wound contraction.

All the above reactions are stimulated by the up-regulation of proliferative genes. Angiogenesis is commonly induced under a hypoxia environment, causing significant enhancement in Hypoxia-inducible Factor-1α (HIF-1α) expression [152]. This environment induces the further stimulation of angiogenic factors such as VEGF and FGF-2. Both proteins serve to modulate the migration and proliferation of endothelial cells and induce capillary formation. Other factors or cytokines including TGF, KGF, PDGF, and TNF-α also indirectly enhance angiogenesis. Excess in TGF-β induces VEGF secretion by affecting the HIF-α pathway [153, 154]. PDGF could co-function with hypoxia to further increase VEGF secretion and also stimulate the differentiation pericyte, a cell that stabilizes vascular [110, 154, 155]. Moreover, as VEGF and FGF-2 are mainly secreted from fibroblasts, factors relevant to fibroblast proliferation, such as TNF-α, indirectly increase the VEGF and FGF-2 secretion.

Re-epithelialization starts as epithelial cells proliferate at the non-wounded edge and then migrate to form a complete sheet that covers the wound [12]. A moist and antibacterial environment is more favoured for re-epithelialization [103]. EGF plays an important role in re-epithelialization as it serves as a mitogen for keratinocyte proliferation and migration. KGF is a protein expressed from fibroblast and can only bind to the keratinocytes or hair follicles in order to promote the proliferation, migration, and morphogenesis of epithelial cells [156]. Some have also reported that it stimuates the secretion of a urokinase-type plasminogen activator, an important protease in neovascularization in the basal membrane [157]. TGF-β is known to shift keratinocytes to a more migratory phenotype and thereby enhances the kinetics of wound closure [158, 159]. Insulin and IGF can also enhance the migration of keratinocytes [160]. PDGF, IL-1, and IL-6 up-regulate the production of EGF, TGF, and IGF and thus indirectly enhance re-epithelialization [110].

Fibroblasts are activated and migrate to the wound area in the first 2-3 days through TGF-β and PDGF derived from platelets [80]. In response to PDGF, they secrete collagen type III, fibronectin, and other ECM proteins, including hyaluronan, fibronectins, and proteoglycans. By the end of the inflammation phase, a provisional matrix is formed to replace the initial clot, termed granulation tissue, which has different collagen species (collagen type III instead of type I) and alignment compared to unwounded tissues and has low strength. As the matrix matures, TGF-β peaks and collagen type III reabsorbs to form collagen type I, along with the increase of matrix strength [82]. In addition, fibroblasts differentiate into myofibroblasts, smooth muscle cells that accelerate tissue granulation and initiate wound contraction [103, 161]. Wound contraction usually starts about seven days after injury [12]. Its rate is dependent on the shape and status of the wound. The end

of the wound contraction marks the end of the proliferation phase. The disorder of this phase could lead to tissue deformity and fibrosis [162, 163].

2.1.4 Remodeling

The remodeling phase is activated after the initial wound closure while ECM production and differentiation of myofibroblasts are ongoing. ECM production is balanced by the degradation of impaired ECM, apoptosis of fibroblasts, and removal of the initial capillaries [80]. Collagen and other ECM molecules continue to rearrange into a more aligned structure and eventually, thorough wound regeneration is achieved. However, wounds never reach the same level of strength and function as normal tissues. Wounds merely have 50% recovery in 3 months and around 60-70% in the long-term [12, 18]. In addition, scarring can occur due to the excessive formation of fibrous connective tissues. One of its main contributors is the excessive TGF-β secretion from macrophages or fibroblasts [164], while other factors such as CTGF, PDGF, and IL-4 also directly or indirectly lead to scarring [165]. Scars could be differentiated into hypertrophic scars (scars with the same collagen arrangement as normal tissues and good vascular network and regress in 6 months) and keloids (scars with different collagen arrangement and bad vascular network and grow instead of regress), and both of them exhibited a high-stress field in tissue [23, 166]. Both scars are poorly functional and vulnerable to repeated trauma, viral infection, or carcinogenesis.

2.2 Wound types and treatments

2.2.1 Burns

Burns is one of the most common household injuries but can lead to some of the most severe consequences [1]. They can be caused by not only the heat from fire or hot objects, but also friction, cold, radiation, chemical, or electric sources [2, 167]. Amongst the estimated 11 million annual cases of burn injuries worldwide, 180,000 of them lead to death [2]. Severe burns can be fatal due to the massive water loss, pain, and infection after the injury [3, 4]. By the depth of wounds, burn injuries can be classified as superficial burns (first degree, on the epidermis), partial or intermediate burns (second degree, partially penetrating the dermis), full-thickness burns (third degree, fully penetrating the dermis to the hypodermis), and fourth-degree burns (damage down to the muscle or bone) [2]. Burn wounds usually have a damaged epidermis with excessive exudates that can become infected (Figure 2. 3); [5, 6]. This leads to severe inflammation with massive infiltration of macrophages and high expressions of cytokines and protease, which cause

degraded ECM and necrotic tissues [7, 8]. Besides, follicles were lost in burn injuries and could hardly be regenerated leading to function loss and fewer stem cell sources [9, 10]. The ECM and vascular network in the dermis are also usually damaged, making it more difficult to provide nutrients and oxygen to regenerate wounds [11].

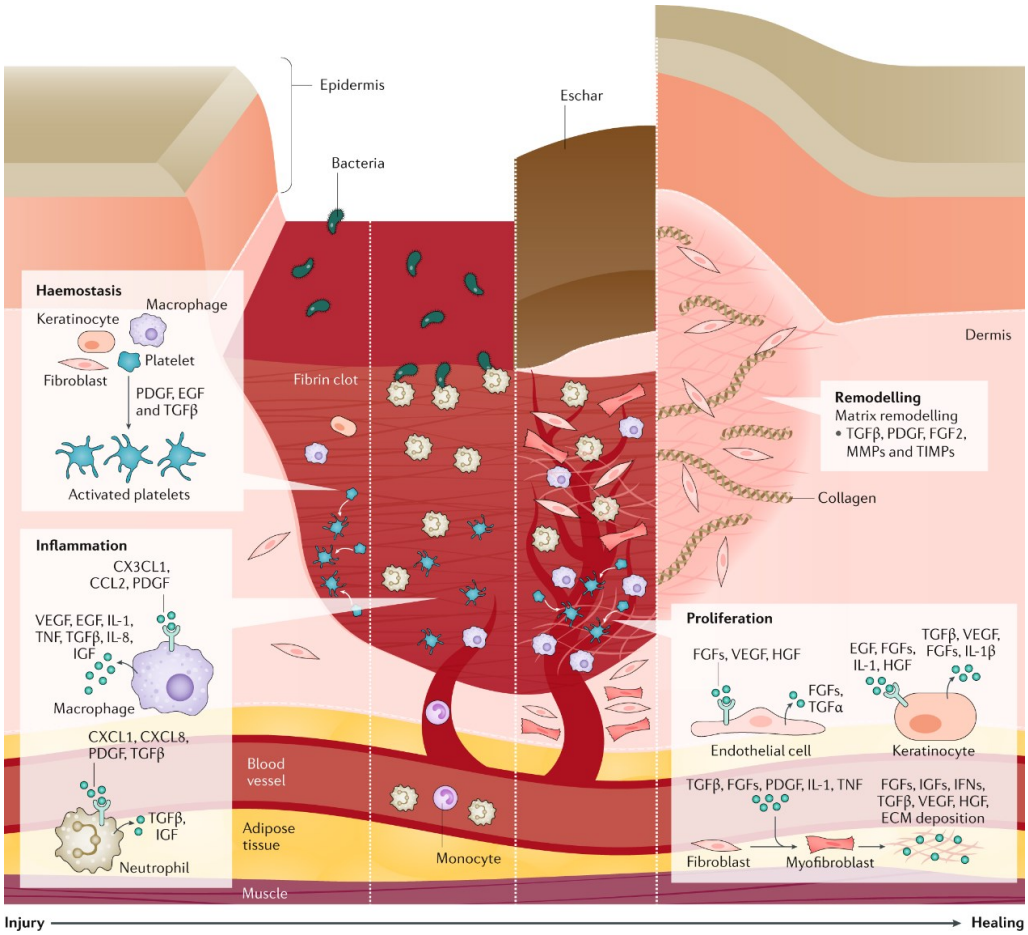


Figure 2. 3. Schematic diagram of the burn pathology and the histology burns during its healing. Reproduced with permission from [2].

The wound healing cascade for burn regeneration was similar to that of normal wound regeneration, but severe burns must need treatments to prevent the death of the patients. The regeneration of severe burns usually requires fluid resuscitation, preventing water loss immediately after the burn is stopped (Figure 2. 4) [168]. The follows the surface antibacterial treatment and wound excision, to prevent death from infection and remove debridement and necrotic tissue, leaving an open wound. Then, wounds were covered with grafts, dressings, or 3D wound matrices for improved healing.

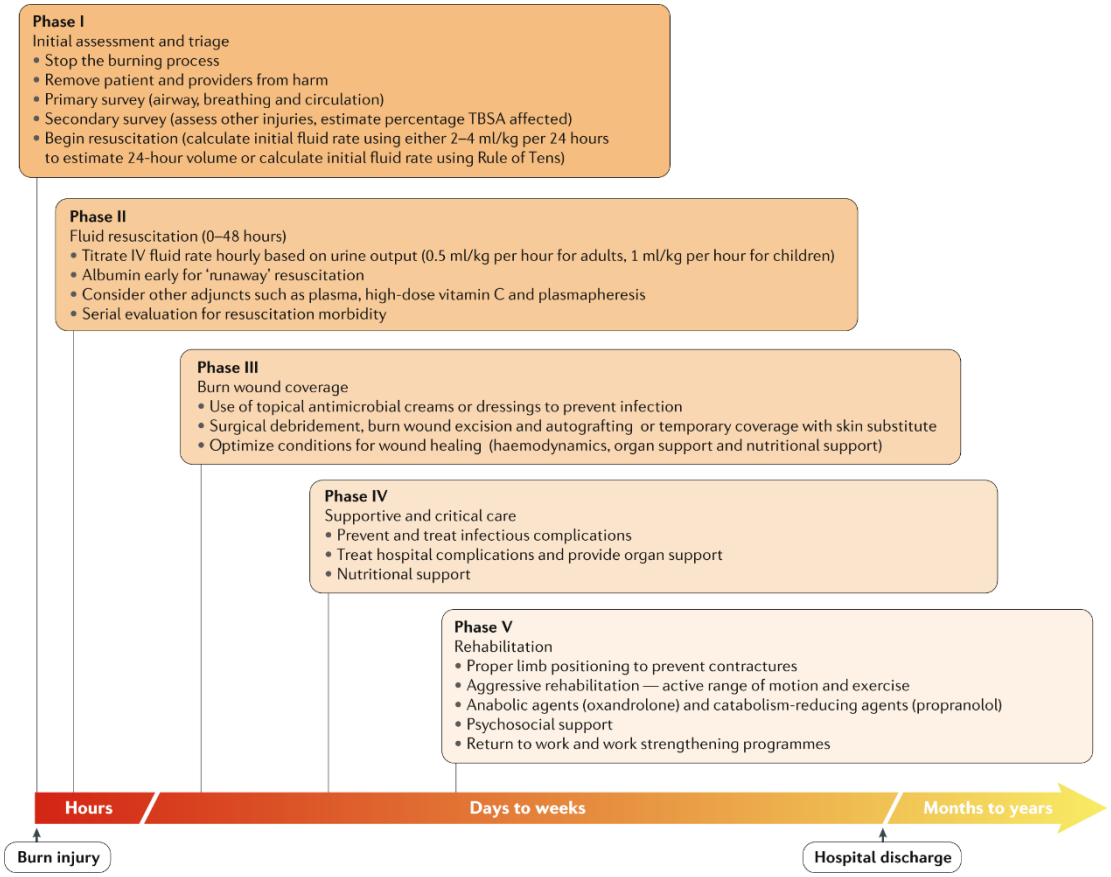


Figure 2. 4. Schematic diagram of the burn regeneration treatment. Reproduced with permission from [2].

2.2.2 Chronic wounds

Chronic wounds do not heal through this well-defined process and will not regenerate the structural and functional integrity of the injured tissue. The healing process stalls in the 'inflammation' phase and could last for more than 3 months. In chronic wounds, the level of inflammatory cytokines will keep on elevating and will not peak in a given period, while the levels of growth factors were significantly reduced [16, 20-22, 169]. The prolonged inflammation resulted in ECM degradation and tissue necrosis (Figure 2. 5). Neuropathy in some chronic wounds may highly stimulate keratinocyte proliferation but hinders their migration, which therefore resulted in infection. Besides, lack of blood supply, or ischemia, is one of the most important problems for all types of chronic wounds.

Chronic wounds can be due to both internal and external factors. As examples of internal factors, either low or excessive oxygenation would impair wound healing. Infection and foreign materials would greatly prolong inflammation and delay wound closure [13]; defective, damaged, or senescent cells would impair inflammatory response and lead to

an increase of cytokines [80]. Vascular insufficiency or local ischemia has been the greatest problem for all types of chronic wounds, as they the inhibited supply of oxygen and nutrition that fuels cellular activities [25-27]. For instance, calories and sugar are essential for cellular metabolism, Vitamin A is essential for inflammation, cellular differentiation, and re-epithelialization; Vitamin C and E are antioxidants and necessary for controlling inflammation and deposition of ECM [170-172]. External factors include repeated trauma, medication, bad wound treatment environment that would all aggregate wound inflammation and could cause severe infections [12, 173]. Stress, aging, and chronic diseases, especially diabetes, are three major factors of chronic wounds. They lead to three main categories of chronic wounds: pressure ulcers, venous leg ulcers (VLUs), and diabetic foot ulcers (DFUs),

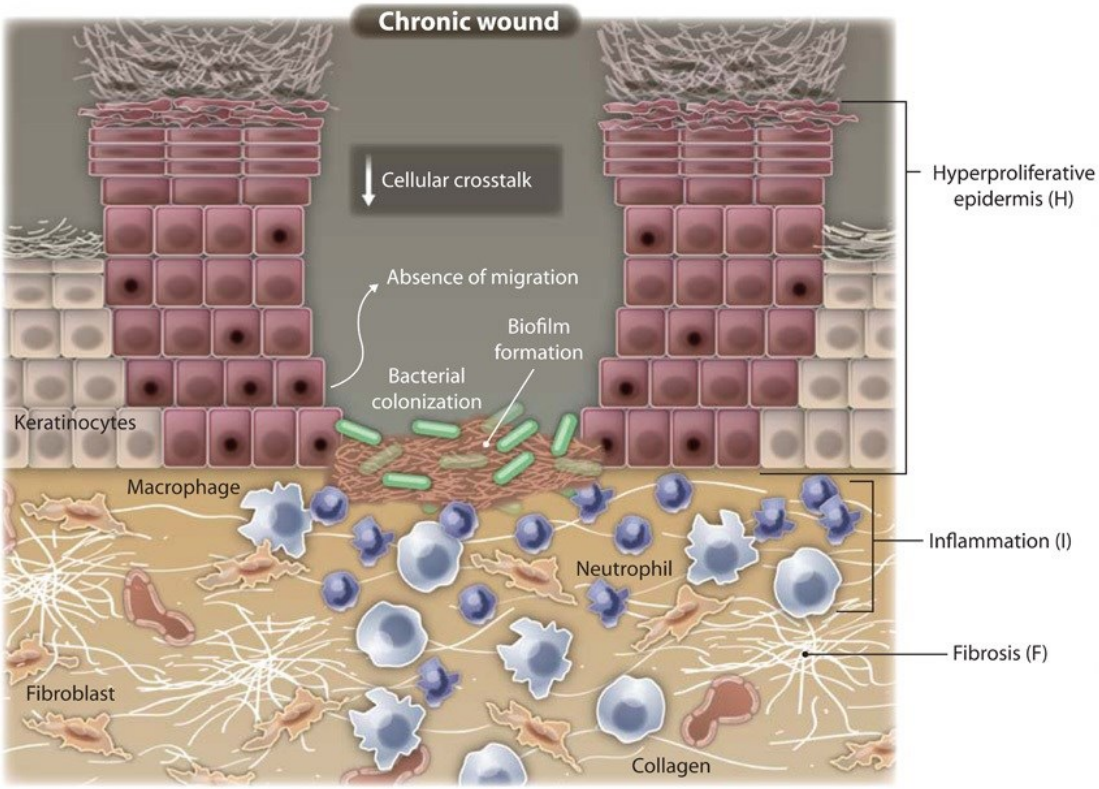


Figure 2. 5. Schematic diagram of the chronic wounds. Reproduced with permission from [23].

2.2.2.1 Pressure ulcers

Pressure ulcers are derived from undissolved pressure, shear, friction, and moisture on soft tissues [23, 174]. They are common for the elderly and immobile patients and the in-hospital mortality rate is 20-33% [175]. The pressure exerted between the external source and cortical bone occludes blood flow and causes tissue ischemia. Continuous pressure

results in chronic tissue damage in the dermis and hypodermis (termed stage 3) or even deep down the muscles (stage 4) which do not heal normally due to the impaired vascular network. Shear stress exerted between the skin and the cortical bone (for example, when sliding down the beds) makes it even easier for the occlusion. The surface skin may eventually be destroyed by the friction or moisture to initiate a wound. Young patients were rich in elastin and collagen in their wound ECM so they were much more tolerable than old patients. Pressure ulcers could also be exaggerated by external factors such as poor nutrition, diabetes, neuro damages, etc. [176, 177].

2.2.2.2 Venous leg ulcers

Venous leg ulcers are the most severe type of chronic venous disease and have up to a 3 to 4% incidence rate among all elderly patients [23]. In capillaries, venous valves are forced open by blood flow, and little blood reflux is needed to close the valve [178]. Venous leg ulcers are usually caused by chronic venous insufficiency, which causes superficial venous reflux, particularly in the ankle region of the lower legs. This results in hypertension for endothelial cells and obstructed local blood supply, which leads to persistent inflammation, lipodermatosclerosis, inhibited keratinocyte migration, and skin ulceration [179, 180]. Incompetent venous valve obstructed venous blood flow, obesity, and leg immobility are major reasons for chronic venous hypertension and were usually found in elder people [179]. Venous leg ulcer patients may also be associated with impaired gene signaling and microRNA expression [181, 182].

2.2.2.3 Diabetic ulcers

Diabetic ulcers are the most common type of chronic ulcer and have been becoming a greater threat to patients and national healthcare systems with the increasing worldwide prevalence of diabetes [12, 13]. Type 2 diabetes patients cover 6.4% of the world population and are expected to increase up to 8% in 2030, in which 15% of them would suffer from DFU throughout their lifetime [183, 184]. It usually leads to up to an 84% amputation rate [14, 15] and high mortality, as 60% of patients with diabetic ulcers die within 5 years [16-18]. The cost of diabetic ulcer treatment is more than $50000 and the regenerated tissue never recovers to the structural and functional integrity of the original skin [19]. The neuropathy of diabetes disrupts the metabolism of the cells and promotes the synthesis of ROS instead of NO, which induces prolonged inflammation [185]. For instance, the high glucose level in the blood disrupts the enzymatic activities between protein and sugar [186]. The impaired nerve system also inhibits signals for chemotaxis

and growth factors in the wound area, leading to impaired phagocytosis, keratinocyte migration, angiogenesis, and anti-inflammation [187].

2.2.3 Skin cancer

Skin cancers were usually induced when cells in the epidermis mutate under somatic changes from viral or chemical irritation [188, 189]. The type of the mutated cells determines the type of cancer, for example, basal cells mutate into basal cancer cells, keratinocytes mutate into squamous cancer cells, while melanocytes mutate to form melanoma. Chronic wounds and burn injuries are easily subjected to carcinoma, especially squamous cancer [190, 191] [192]. This is because the defected wounds have impaired immune system and vascular network, high ROS levels and oxidative stress that damages DNA, and excessive cytokines and protease. Besides, after the removal of a malignant tumour, neoplastic cells hide among normal epidermis cells but retain their cancerous potential for months, and oncogene factors may not be fully removed so that there is a high risk of recurrence [193]. Tumourigenesis greatly prevents wound healing. For instance, DNA alteration/mutation disables tumour suppressor genes, over-expression of oncogenes, and the production of new oncogenes. Tumour cells have a much higher uptake of growth factors and cytokines than normal cells, so they proliferate and migrate (metastasis) much faster while reducing the growth of normal tissues. Tumour cells or tumour-associated leucocytes and platelets also create their own pathway in producing more factors for ongoing proliferation [194, 195].

2.2.4 Deep wounds

Deep wounds are a type of wound that penetrates the hypodermis layer, or even down to the muscle layer. As shown in Figure 2. 6, the hypodermis layer is around 7 mm in thickness, consisting of two different layers [196, 197]. Both layers were pillared by fibres consisting of connective tissues, but in a different arrangement and filled with fat tissue. The superficial fascia separates the two layers while the deep fascia separates the hypodermis to the muscle.

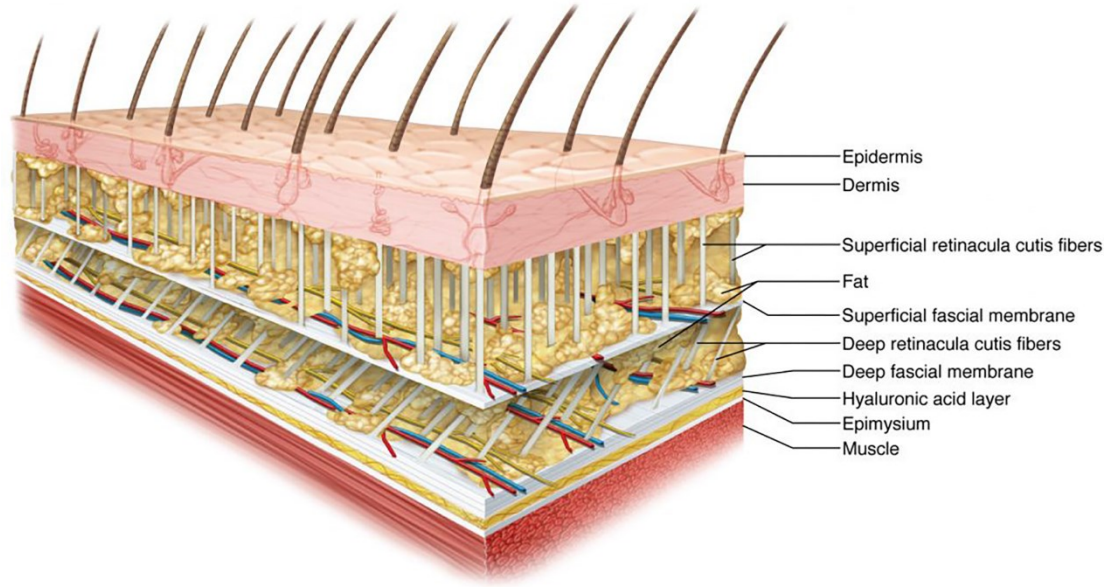


Figure 2. 6. Schematic of the histology of skin and the hypodermis. Reproduced from https://learnmuscles.com/blog/.

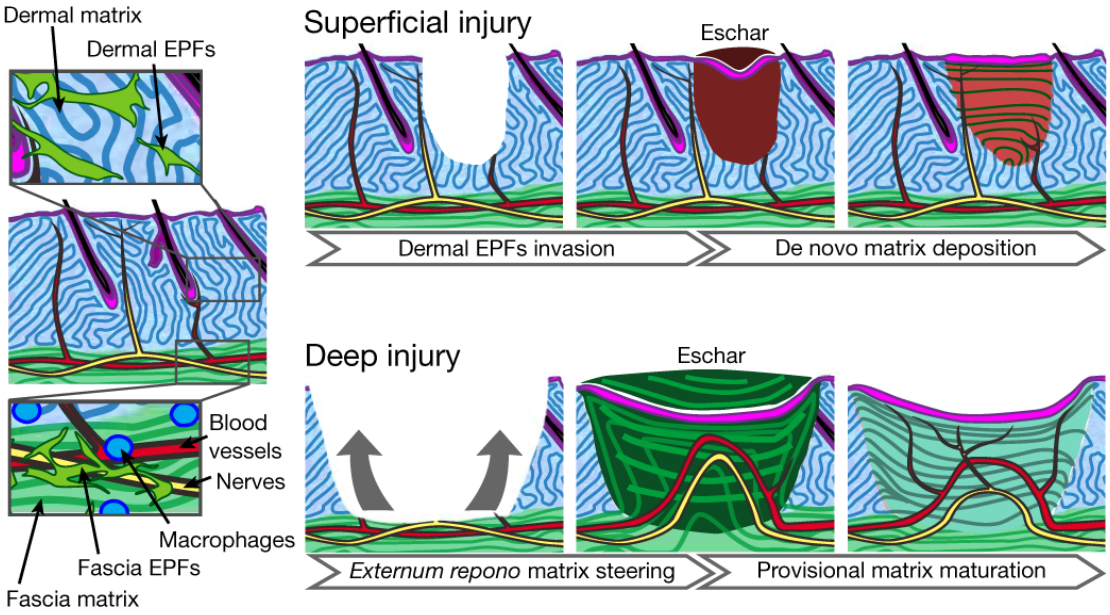


Figure 2. 7. Schematic of deep wound regeneration mechanism. Reproduced with permission from [198].

Deep wounds are prevailing, because the epidermis layer is only 0.05 mm thick and the dermis layer is 2 mm thick so injuries may easily penetrate into the hypodermis, but are not receiving much scientific attention. Recently, Correa-Gallegos *et al.* reported that the mechanism of deep wounds was distinct from that of normal wounds [198]. Figure 2. 7 indicated that in superficial injuries, dermis fibroblasts migrated to the wound site and fill up the wounds, and dermis endothelial cells

migrate to form blood vessels, while for deep wounds, the predominant fibroblasts sources are the fascia and the initial blood supply was from the hypodermis as well. Once a clot was formed in the deep wounds, capillaries grow on the infiltrated blood vessels and the infiltrated vessel only disappears when a full granulated tissue and vascular network is formed.

To design wound matrices for chronic deep wound regeneration, biological cues are needed to stimulate the migration of fibroblasts and endothelial cells from the fascia. Physical cues are also required to mimic the hypodermis environment (parallel ECM load-bearing fibre) and to provide pathways for cell attachment and migration.

2.2.5 Treatments

Wound care is extremely important in preventing the rise of chronic wounds or other morbidities. The removal of debris and necrotic tissue is the first step in wound treatment in order to prevent infection and produce a clean area for cell attachment and proliferation [104]. The surgical approach of physical debridement is the most common approach but could lead to pain and bleeding [199]. The enzymatic approach involves covering the wound by occlusive dressing to stimulate the expressions of protease, mainly collagenase and papain, to degrade the ECM [200, 201]. This method is safe and effective but may not infiltrate into devitalized tissues. A biosurgical approach may also be feasible where surgeons apply maggots to digest wounds mechanically while secreting helpful protease to kill pathogens, up-regulate growth factors and promote fibroblast proliferation [202, 203].

Infection protection is another indispensable step in wound healing. Bacteria are commonly deposited on the skin and would easily cause infection as they reach a threshold of 105 per gram of tissue [204]. Multiple ions have been applied for antibacterial effect, including silver, zinc, copper and etc. (detailed in later sections), or nanoparticles containing Au or Pt [205, 206]. These elements have been successfully incorporated into dressings or wound matrices but for antibacterial effects before grafting, ointment and cream were commonly used.

2.2.5.1 Grafting

It has been proposed that autologous grafts (full-thickness of keratinocyte grafts) have been one of the most successful treatments against chronic wounds [190, 207]. The conventional approach involves transplanting the epidermis and/or a part of the

dermis from the donor site to the wound area, named split-thickness autograft [208]. If the wound is small, a full-thickness autograft, in which the epidermis and all of the dermis were removed and implanted, is possible. On both occasions, it is expected that transplanted cells survived in a new area and the donor site would heal through re-epithelialization, but cells from the donor site may not be fully compatible [209]. The lack of donor skin has been the greatest challenge, especially considering that only a few cells on autograft would proliferate. Besides, the risk of pain, donor site infection and cell death during grafting all make grafting an imperfect treatment option.

Keratinocyte grafting is a recent grafting approach as keratinocytes are expected to secret their own mitogenic factors. However, an adult keratinocyte will not proliferate when transplanted to the wound media [208]. Therefore, keratinocytes harvested from donor epithelia need to be cultured in an environment similar to that of the wound site so that the mature skin graft could permanently replace wound skin. But there may be a higher chance of infection and irritation, as the preparation time of keratinocyte grafting is up to 3-4 weeks [210, 211]. In addition, growth factors dysfunction and senescent cell are two risks associated with aging patients [212, 213].

2.2.5.2 Dressing and wound matrices

Dressings of all types promote wound healing and prevent further infection or morbidity. The most traditional form of dressing is gauze, which builds a protective layer on the wound but may cause further damage when removed due to its dryness. Modern dressings are commonly occlusive to retain moisture in wounds and lead to local hypoxia to promote inflammation and proliferation [81]. Semipermeable films are the most common dressings type. They allow permeation of water vapour and oxygen while forbidding microbial invasion and are also flexible and could fit in the wound without additional tapping [214]. For exudative wounds, high absorbent and moisture-retaining foam dressings are used to prevent the over-soaking of tissue in exudate, but they need to be changed at least every 3 days [215]. Hydrogel dressings are extremely useful in dry wounds because their water retaining capabilities promote exudate absorption and moisture-retaining, but the risk of overhydration and low mechanical properties are their drawbacks [214]. Hydrocolloid dressings consist of two layers: an inner gel-like layer and an outer semi-permeable layer. It would moderately absorb exudate and has better mechanical properties to be long lasting [216]. The most suitable dressing depends on the targeting wound types.

Advances in biomaterials stimulate the development of wound matrices. These matrices were implanted in the wound area and induced biological cues to stimulate wound healing. Collagen matrices are commonly used and specifically useful in re-epithelialization and chronic wounds [18]. Though these matrices do not replace tissue collagen directly, they facilitate cell attraction and deplete negative factors including protease and ROS [217]. The implanted collagen will be digested by protease into metabolites to form human collagen. Other ECM components, such as hyaluronic acid, fibrin, and fibronectin could be used alone or with collagen to stimulate cell attachment, migration and proliferation, angiogenesis, and anti-inflammation [218-220]. Chitosan promotes platelet adhesion and fibrinogen adsorption, and has antimicrobial properties so that they activate macrophage, fibroblast and keratinocyte activities [221, 222]. Alginate dressings have unique fibrous structure that makes them highly absorbent but not moist retaining [215]. It is also highly antimicrobial and could stimulate the growth of inflammatory cells and cytokines through the release of multiple therapeutic components [223, 224]. Other materials for wound matrices include cellulose, gelatin, and various synthetic polymers which will be introduced in later sections.

2.2.5.3 Others

Implementing drugs or growth factors to wound through hydrogels, collagen matrices, or mesoporous inorganic materials is becoming more popular in recent years [225-228]. Yet, PDGF-BB (Platelet-Derived Growth Factor BB) is approved in the US, but not in the UK [18, 110]; FGF-2 is being permitted in Japan and China [229]; injectible EGF is also being developed in Cuba [230]. Stem cell therapies in the skin are also getting more attention in recent years [231, 232]. Wound stem cells such as the epidermis stem cell, follicle stem cell, endothelial stem cell, mesenchymal stem cell, etc. can be derived into wound cells through preculture with target genes and proteins [231, 232] But since the stem cells are usually autologous, the problem of sourcing and compatibility between the donor cite and wound has been the greatest problem. The above-mentioned strategies were challenged by the time consumption of the process, the storage of proteins/cells, target delivery, etc.

Bioactive glasses are a group of biodegradable materials that have been commercially successful as products for bone regeneration [43, 46, 233-236]. Their release of therapeutic ions and surface affinity to both hard and soft tissue make them emerge as leading candidates for healing chronic wounds [233, 237, 238]. The

remaining sections of the review chapter aim to summarize the modern advances in BGs and the mechanism of therapeutic ions in wound healing.

2.3 Introduction of bioactive glass

Glass is a non-equilibrium, non-crystalline state of matter that exhibits a glass transition behaviour in which the material has the same microstructure as a supercooled liquid but will reach the equilibrium crystallized state given an infinite time [239]. When temperature raise above the glass transition temperature Tg, the glass will change from a brittle 'glass state' into a 'viscous' state where glass begins to flow [240]. Glass properties are characterized by the role of cations in its structure. Constituent oxides are classified into network formers and network modifiers [241]. Network formers are oxides that build up the glass structure and are indispensable for glass. Examples of them are SiO_2, B_2O_3, and P_2O_5. Network modifiers are oxides that disrupt and terminate the connecting network. Examples are Na_2O and CaO. Intermediates are oxides that possess the properties of both network former and network modifiers. Examples are Al_2O_3 and ZnO [242]. Oxygen atoms are also classified into bridging and non-bridging oxygens. Bridging oxygens are those connecting two network formers while non-bridging oxygens are those attracted by doped modifying cations and thus connecting one network former with one network modifier [243]. Q^n structure is an important way to summarize the number of bridging oxygen in the glass. Q^n stands for a structure with 'n' surrounding bridging oxygen around them. The network connectivity% can be defined by:

$$NC' = \frac{4*(M_f)-2(M_2^1O+M^{II}O)+6(M_{P_2O_5})}{M_f} \quad (2.1)$$

where M_f is the molar fraction of the network forming oxide, e.g. Si, and M_2^1O and $M^{II}O$ are the respective molar fractions of the mono and divalent modifier oxides within the glass. This equation is founded on the hypothesis that phosphate forms its own orthophosphate network.

Different compositions will change the inter-bonding between oxygen and cations [242]. This is because of the interaction of the cation fields of different elements. Cation field strength is closely related to the dissolution rate, bioactivity, bonding strength, network connectivity, and even coordination in glass [244-247].

The first bioactive glass (BG) was introduced by Hench in 1969, with a composition of $46.1SiO_2$-$24.4Na_2O$-$26.9CaO$-$2.6P_2O_5$ (mol%), and was termed 45S5 or Bioglass® [248]. It was the first inorganic material that exhibited tight chemical bonds with the bone and

soft tissues [249]. The mechanism of bone-bonding was attributed to the deposition of hydroxycarbonate apatite (HCA) layer, derived from glass dissolution products, on the surface of the glass, which thereby interacts with collagen fibrils and integrated with host bones [248]. The term 'bioactive' was then associated with the formation of the HCA layer. Now "bioactivity" is associated more with a material provoking a positive biological response from the in vivo environment.

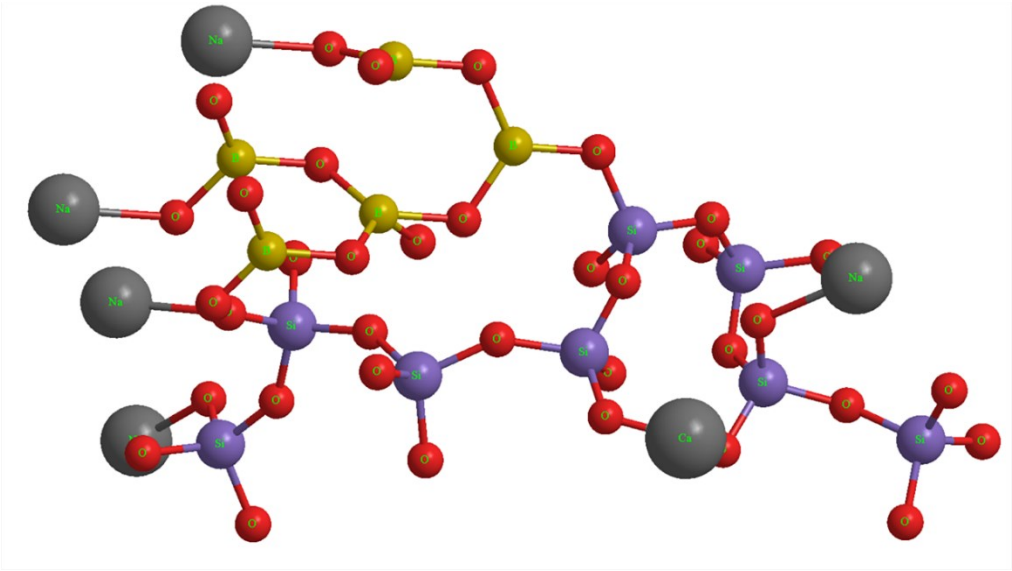


Figure 2. 8. Schematic diagram of the structure of a borosilicate BG with network former (Si and B), network modifier (Ca and Na), and bridging/non-bridging oxygens.

The original 45S5 composition has remained the most commonly used composition, but other compositions have been investigated for different applications. Common compositions are listed in Table 2. 3. There are three main types of BG that can be classified according to their network formers (ions that form glass networks through bridging oxygen bonds): silicate-based glass, borate-based glasses, and phosphate-based glasses. Borate and phosphate-based glass generally dissolve faster than silicate-based glass [45]. Different network modifiers (cations that disrupt the connecting network) include Na, Ca, Ag, K, and Cu. Intermediates that possess the properties of both network former and network modifier, include Al, Zn, and Co [242]. A schematic diagram of the BG structure is presented in Figure 2. 8.

Table 2. 3. Common BG names and composition (mol%).

Names	SiO_2	CaO	P_2O_5	Na_2O	B_2O_3	MgO	K_2O	CuO	ZnO	SrO	CaF_2
45S5	46 .1	26.9	2.6	24.4	0	0	0	0	0	0	0
S53P4	53.85	21.77	1.72	22.65	0	0	0	0	0	0	0
58S	60	36	4	0	0	0	0	0	0	0	0

77S	80	16	4	0	0	0	0	0	0	0	0
1393	54	22	2	6	0	8	8	0	0	0	0
1393-B1	36	22	2	6	18	8	8	0	0	0	0
1393-B2	18	22	2	6	36	8	8	0	0	0	0
1393-B3	0	22	1.75	6	54.65	7.9	7.7	0	0	0	0
1605	0	23.91	1.89	6.49	49.69	8.32	8.54	0.34	0.82	0	0
0601	51.3	24.8	1.74	5.87	0	8.41	7.85	0	0	0	0
0601-B1	39.2	25.3	1.77	5.97	11.3	8.56	7.99	0	0	0	0
0601-B2	26.58	25.74	1.8	6.08	22.9	8.71	8.14	0	0	0	0

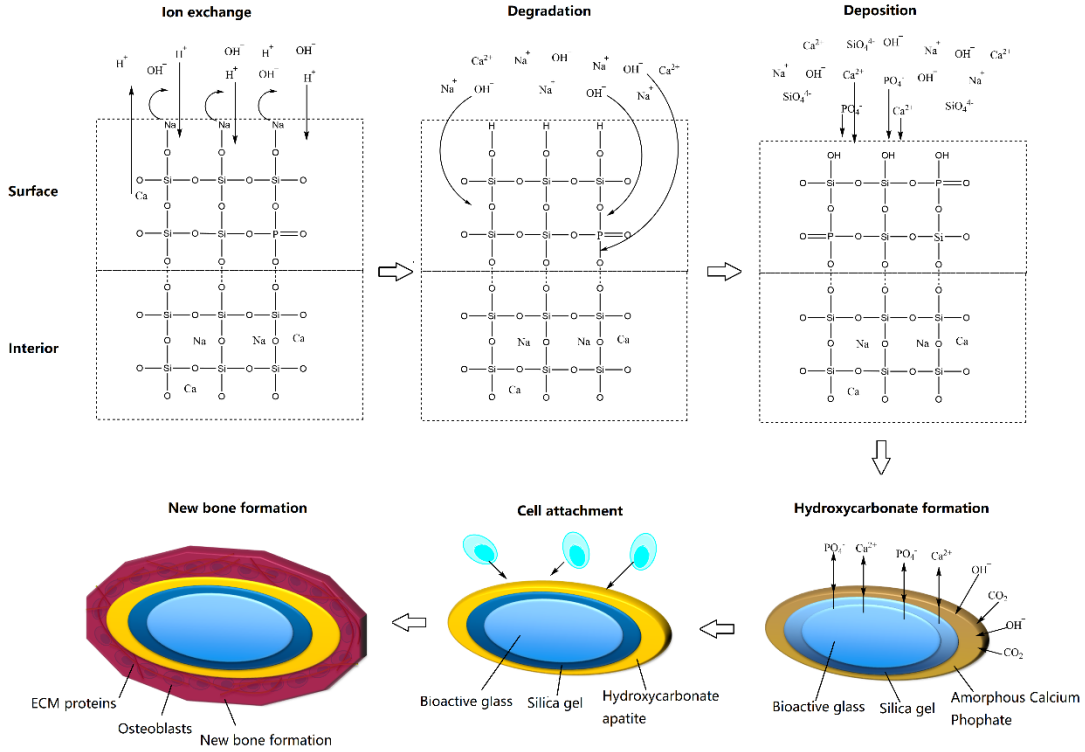


Figure 2. 9. Schematic of the osteogenic mechanism of bioactive glasses.

The most successful application of BG is the regeneration of hard tissues, including bone, dentine, or spinal fusion [46]. Their osteogenic properties are attributed to the cellular responses of therapeutic ions including Si, Ca, and P species in the up-regulation of osteoblast activities and, in the case of Sr-containing glasses, down-regulation of osteoclast behaviour [250-252]. The mechanism of the above properties was summarized as:

1. Ions (Na, Ca, P) at the BG surface dissolve into body fluid causing the reduction of H^+ in body fluid and thereby increase local pH.
2. As pH exceeds 9, OH^- ions attack the O-Si-O bond and lead to SiO_4^{4-} release.
3. Body fluid is over-saturated with Ca and P ions so that ion precipitation initiates in the exposed OH^- group and calcium phosphate film forms on the surface of the glass.

4. Calcium phosphate incorporates OH^- and carbonate group and crystallizes into HCA.
5. Collagen fibrils from host bone interact with the HCA layer via cellular processes to form a strong bond [248].

The effect of the dissolution ions of BG on cells enlightened its potential in soft-tissue engineering [253]. The therapeutic ion released from BG was stimulative to wound healing capability. For instance, silicon species (thought to exist in the form of SiO_4^{4-}) induce endothelial cell homing, differentiation, and migration and thus sprout neovessel formation [254, 255]. Boron and boric acid have long been known as antibacterial and anti-inflammatory reagents while also stimulating angiogenesis [65, 256-258]. Phosphate ions up-regulate the forkhead box protein C2 and VEGF secretion and therefore stimulate HUVEC migration and tubule formation [259, 260]. Ca^{2+} ions contribute greatly to hemostatic behaviour [261-263], but also promote keratinocyte and endothelial cell proliferation and motility in protein expression (PDGF, TGF-β, EGF, bFGF, IGF) and angiogenesis [264, 265]. Cu^{2+} ions exhibited multiple effects including antibacterial capabilities [266, 267], simulation of hypoxia, modulation of angiogenic factors and cytokines [268, 269], and stimulation of endothelial cell migration and proliferation to form neo-vessels [270, 271]. Co^{2+} ions also stimulate hypoxia-induced factors and thus stimulate the secretion of angiogenic factors and angiogenesis [272, 273]. Zn^{2+} ions are antibacterial, anti-inflammatory, and stimulative to angiogenesis through their interplay with macrophages in the secretion of growth factors [63, 274-277]. All the above ions can be incorporated into the BG structures and are sustained and released during glass dissolution, inducing therapeutic effects. Combined with the biodegradable, porous, flexible, and commercializable features of BGs, it has been confirmed that BGs exhibited great potential as promising wound healing devices.

Wilkinson *et al.* further investigated the role of genes regulated by different metallic ions (Ca, Mg, Cu, Mn, Fe, Al, and Co) to wound healing cascades [278]. Upon injury, the level of Ca increases to the highest level from day 1 to day 3 and then goes down on day 7; the levels of Fe, Cu, Mg start increasing on day 2, reach the highest concentration on day 7, and only start going down after the remodeling phase (> day 14). In comparison, the levels of Al, Co, and Mn merely start to increase by day 7 and reach the highest level on day 14. The role of ions in differentially expressed genes of different wound healing cascades was also determined. For example, Ca-specified genes are highly involved in cell proliferation and ECM deposition, while also involved in others, such as inflammation, angiogenesis, keratinization, etc.

2.4 Methods of bioactive glass synthesis

The melt-derived and sol-gel-derived approaches, as detailed in Figure 2. 10 and Figure 2. 11, are the basis of the synthesis of novel BGs with specific structures. Scaffolds of different morphology have been synthesized depending on their intended application [46]. Mesoporous bioactive glasses (MBGs) with highly ordered mesoporous channels with diameters between 2 and 50 nm were proposed by Yan *et al.* in 2004 [279]. The resultant highly-porous texture favours the delivery of drugs and therapeutic ions as well as enables cell infiltration and activation [280]. BG nanoparticles (NPs) ranging from 50 to 200 nm were synthesized for tissue engineering [281]. BG nanofibres spun into ECM-mimicking structures were found to encourage cell attachment, differentiation, and proliferation, which thereby promote angiogenesis and wound closure [97, 238].

2.4.1 Melt derived

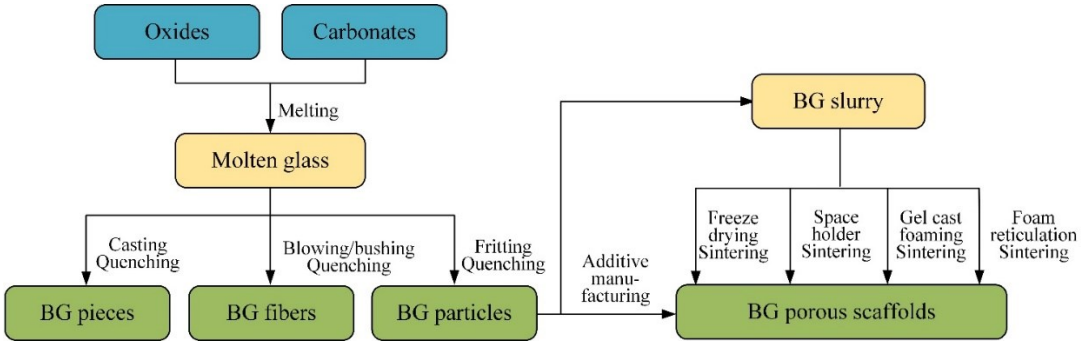


Figure 2. 10. Schematic of the melt-derived approach of bioactive glass and scaffold production.

The melt-derived approach involves the melting of silicon dioxide, calcium carbonate, sodium carbonate, and phosphorus pentoxide in a platinum crucible to more than 1300 ℃ [46]. Other metallic oxides or carbonates can be added to the melt for the incorporation of trace elements [250]. The resultant molten glass is quenched in either a graphite mold to maintain a specific shape or water (frit) to acquire particulate glass with ongoing grinding and sieving process. Fibres can be drawn from the melt before quenching, as detailed in Section 2.6.1 [282]. The melt-derived approach is commonly applied to commercial production due to its easiness of manufacturing and cheap manufacturing cost. But the main drawback of this approach is that the Na_2O must be incorporated to decrease the melting point, which makes the control of BG composition as well as the corresponding ion release kinetics difficult [250]. Excessive (>25%) Na^+ ions would not lead to therapeutic effects but induced a toxic alkaline environment. The precursors were usually

melted at 1300-1500 ℃ and the overall time taken for the melt-derived approach is less than 1 days (longer if the ingredients were mixed overnight).

2.4.2 Sol-gel derived

The sol-gel derived approach generally consists of a transformation from a precursor into a silica gel followed by drying to form dry gels and sintering to form BGs [283]. The overall process consists of hydrolysis and condensation, (casting), gelation, aging, drying, stabilization, and sintering. Figure 2. 12 illustrates the structural evolution during each step and their characterization techniques [284]. The precursor for silicon is TEOS ($Si(OC_2H_5)_4$) and the precursor for metallic ions are their chlorides or nitrates.

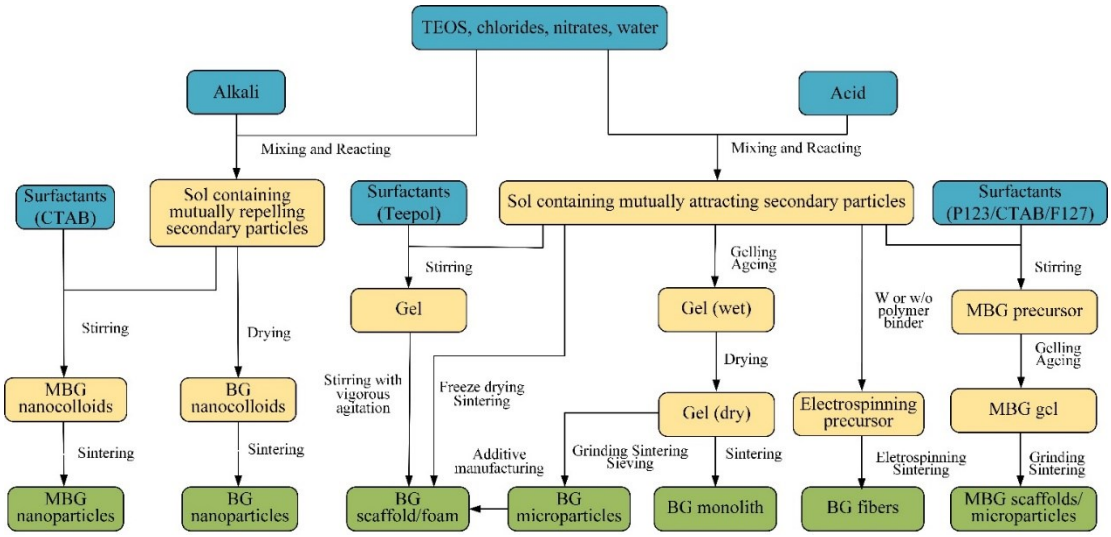


Figure 2. 11. Schematic of the sol-gel approach of bioactive glass synthesis.

In comparison to the melt-derived approach, the sol-gel process enables the formation of BG with Si content more than 70 mol% and does not require Na_2O as a modifier [284]. The synthesis temperature of the sol-gel process is also lower than the crystallization temperature of the glass, leading to no crystallization. Furthermore, sol-gel BGs are innate with mesopores from 6-17 nm and this greatly enhances the surface area of the glass [285, 286]. The surface area of sol-gel BG particles of 1-32 μm is 70-130 m^2g^{-1} while that of similar composition melt-derived BGs is 2.7 m^2g^{-1} [287]. In addition, sol-gel BGs have more OH^- groups and lower network connectivity than theoretical values. Unfortunately, sol-gel-derived glasses are more costly and time-consuming to synthesize. The first sol-gel-derived product was the 58S composition, used for bone regeneration.

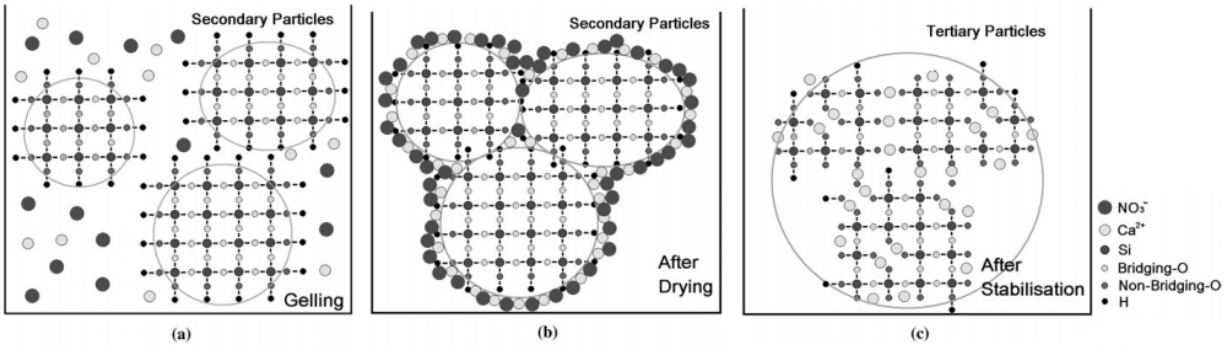


Figure 2. 12. Schematic diagram of the structure evolution and alkali ion distribution of sol-gel-based BG synthesized through TEOS and $Ca(NO_3)^2$ during (a) gelling, (b) drying, and (c) stabilization, modified from [284].

2.4.2.1 Hydrolysis and Condensation

In the presence of acidic catalysts, TEOS hydrolyzes into $Si(OH)_4$ and ethanol for condensation. During condensation, Si-O-Si siloxane bonds are formed and primary particles begin to bond with each other to form secondary particles. Reactions taken place are:

$$\text{Hydrolysis: } Si(OC_2H_5)_4 + 4H_2O \rightarrow Si(OH)_4 + 4C_2H_5OH \quad (2.2)$$

$$\text{Condensation: } Si(OH)_4 + Si(OH)_4 \rightarrow (HO)_3Si - O - Si\text{-}(OH)_3 + H_2O \text{ (Aqueous)} \quad (2.3)$$

$$\text{Condensation: } Si(OH)_4 + Si(OH)_4 \rightarrow (HO)_3Si - O - Si - (OH)_3 + OH^- \text{ (as R-OH)} \quad (2.4)$$

2.4.2.2 Gelation

The product after hydrolysis and condensation is the solution (Sol) containing silica nanoparticles with diameters around 2 nm, which consists of several silicon tetrahedra [46]. The gelation phase is activated when a 3D network is formed from colloidal particles. In this phase, viscosity increases dramatically, eventually forming a gel. During the gelation phase, the glass can be processed into nanofibres, as demonstrated in Section 2.6.2 [95]. One of the key factors influencing the kinetics of hydrolysis and condensation is the sol pH value. The reaction kinetics are lowest near the isoelectric point, which is approximately pH=2.2 [288]. Both acidic and alkaline environments accelerate the synthesis of silanols owing to the increase of free H^+ or OH^- ions, but their mechanisms are slightly different [283].

When treated with strong acids, H^+ is involved as the catalyst:

$$Si_nO_a(OH)_b + Si(OH)_3O^- + H^+ \rightarrow Si_nO_a(OH)_{(b-1)} - O - Si(OH)_3^+ + H_2O \quad (2.5)$$

When treated with alkali or weak acids, OH^- is involved as the catalyst:

$$Si_nO_a(OH)_b + Si(OH)_3^+ + OH^- \rightarrow Si_nO_a(OH)_{(b-1)} - O - Si(OH)_3^+ + H_2O \quad (2.6)$$

where $Si_nO_a(OH)_b$ is the surface hydrolyzed silica particles and 'n', 'a' and 'b' are integers [289]. Acids are commonly used as catalysts in the majority synthesis of BG microparticles, monoliths, fibres, or foams [46]. Alkaline catalysts induce a slower increase in the kinetics compared to acid and are commonly applied in the synthesis of BG nanoparticles, as detailed in Section 2.5 [283].

The stoichiometric ratio (R) of water/TEOS is another important factor during sol-gel hydrolysis and condensation. The alkalinity of water destroys proton activity and thus modulates hydrolysis behaviour [290]. When R<2 the alcoholic condensation is favoured while when R>2 the aqueous condensation is favoured [291]. Furthermore, R=2 is the optimum value for fibres to be drawn– in the induction of viscosity around 1-10 pa.s [292, 293]. Water content also regulates the porosity in BGs as their removal creates more holes when stabilizing [294]. Moreover, the incorporation of other solvents including dioxane, ethanol, and acetone during synthesis alters the rate of hydrolysis and condensation [283]. Though the hydrolysis, condensation, and gelation reactions are still ongoing during the aging phase, it usually takes 1 day to stir the precursors before putting them into the aging oven. The gelation process for the sol-gel electrospinning process is described in later sections.

2.4.2.3 Aging

After gelation, the gel contains liquid with delocalized ions, as shown in Figure 2. 12 (a), and the aging phase initiates. The aging phase consists of 4 steps: continued polycondensation, syneresis, phase transformation, and coarsening [291]. Polycondensation reactions are the continuation of the gelation phase as secondary particles cross-link to form larger networks and the strength of the gel continues to increase. The growth of particle size spontaneously causes gel shrinkage and liquid expulsion, termed syneresis. Phase transformation occurs when the degree of cross-linking is high enough to proceed with the gel into a solidified wet gel. Coarsening initiates when localized dissolution and reprecipitation induce large pores to grow at the expense of small ones, termed Ostwald ripening [291]. A high necking level of secondary particles is achieved as the product of the aging phase. The aging usually takes 3 days under 60 ℃.

2.4.2.4 Drying

Drying removes liquid from the surfaces and pores to form a dry gel or xerogel. Only after sufficient aging time, when small pores with higher capillary forces are removed, can the drying phase begin, as otherwise cracking of the structure is easily induced [288]. Another

important parameter during the drying phase is the rate of drying, which can be controlled by the addition of surfactant, a hypercritical drying process, or reducing the surface energy by producing monodispersed pore size by controlling the rate of hydrolysis and condensation [283]. After drying, ions precipitate on the surface of secondary particles, as shown in Figure 2. 12 (b). The drying temperature rises from 80 to 130 ℃ and the process takes around 3-4 days.

2.4.2.5 Stabilization

Stabilization involves the removal of chemically active groups that make the glass unstable under room temperature including OH^- and unreacted silanols. Stabilization is usually achieved by heat treatment at around 500 ℃ and simultaneously leads to the relaxation of the glass structure due to rehydration [289]. In addition, NO_3^- groups from cation sources are removed during stabilization. Conventional NO_3^- groups decompose under 561 ℃ [295]. But the BG system, there requires a higher temperature for complete eradication of NO_3^-. For instance, Arcos *et al.* observed that 700 ℃ removed 95% of NO_3^- while 800 ℃ removed 100% of NO_3^- in two individual BG systems [296]. Another role of stabilization is to incorporate Ca into the network [286]. After stabilization, tertiary particles are formed from the clusters of secondary particles and precipitated ions, which is the final structure in glass, as shown in Figure 2. 12 (c).

While a high stabilization temperature is ideal to remove chemical groups, a much higher temperature affects other properties of glass. Sintering BG above its glass transition temperature causes the elimination of nanopores and following reduction of BG porosity and surface area [284]. For instance, 58S glass stabilized at 800 ℃ induces a significant reduction in porosity and surface area [296]. This is because high temperature activates viscous flow and diffusion of the glass mesopores to a state with lower interfacial energy [291]. In addition, HA may be formed around 800-900 ℃ dependent on the composition [297]. The stabilization time can take around 1 day.

2.4.3 Mesoporous bioactive glasses

Yan *et al.* developed a novel generation of BGs in 2004 [279]. These resultant BG microparticles had highly ordered mesoporous channels with diameters between 2 and 50 nm and were termed mesoporous bioactive glasses (MBGs). MBGs possess much higher surface areas and pore volumes than conventional BG particles or monoliths from both melt-derived and sol-gel approaches.

MBGs can only be synthesized through the sol-gel approach by the mixing of the inorganic precursor with surfactants during the 'hydrolysis and condensation' phase. The majority of MBGs exist in a form of microparticles or scaffolds and are commonly synthesized in an acidic environment. In the alkaline environment, MBG nanoparticles (NPs) are synthesized in a similar approach as BG NPs, which is detailed in Section 2.5.2.

The surfactants are the major factor influencing the morphology of MBGs. They exhibit structure-directing capabilities and are removed through sublimation at high temperatures, leaving a structure with plenty and interconnect mesopores, as detailed in Figure 2. 13. P123 and F127, block polymers of $EO_{20} - PO_{70} - BO_{20}$ and $EO_{106} - PO_{70} - BO_{106}$ respectively, are commonly applied as surfactants to induce MBGs (EO is poly(ethylene oxide), PO is poly(propylene oxide), and BO is poly(butylene oxide)). The majority of MBGs formed using P123 had surface areas around 278-400 m^2g^{-1} and pore volume around 0.4-0.5 cm^3g^{-1} [279, 298, 299]. While increasing the ratio of P123 to inorganic composition, MBGs with a surface area of 499 m^2g^{-1} and pore volume of 0.7 cm^3g^{-1} were fabricated [300]. In addition, synthesizing MBGs using F127 leads to an average surface area of 520 m^2g^{-1} and pore volume of 0.51 cm^3g^{-1} [301]. Cetrimonium bromide (CTAB), a quaternary ammonium surfactant, is another common surfactant of MBG and induces an even higher surface area and pore volume up to 1040 m^2g^{-1} and 1.54 cm^3g^{-1} respectively [302, 303].

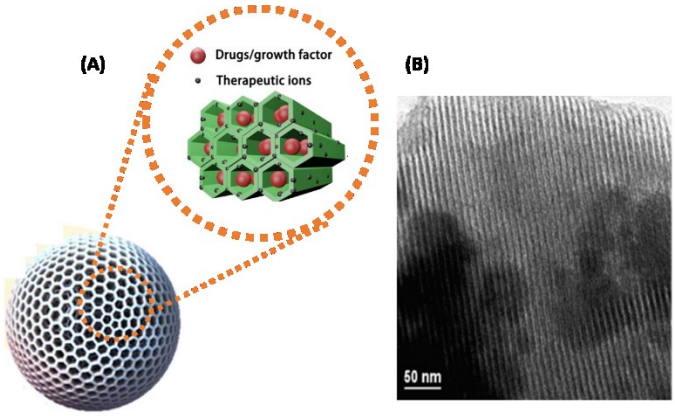


Figure 2. 13. (A) A schematic diagram of the structure of MBG particles and their inner ordered mesoporous channel, and (B) The TEM images of calcined hexagonal 80S15C MBG recorded along the [100] directions. Modified from [279, 304, 305].

One of the main applications of MBGs is the delivery of drugs or biomolecules. The size of mesopores in MBGs is around 6-20 nm [305]. In comparison, the size of most drugs is the size of a few Benzene rings, which are a few hundreds of pm (10^{-12}). They can easily

fit in the mesopores and bind with the walls during drug loading while being released when immersed in a dissolution medium.

2.4.4 Bioactive glass nanofibres

BG nanofibres mimic the collagen and fibronectin fibrils in the ECM and favour the attachment, proliferation, differentiation, and migration of cells [306, 307]. BG nanofibres could be fabricated from both the melt-quenching approach and sol-gel derived approach.

2.4.4.1 Melt derived

Jung *et al.* from Mo-Sci (Rolla, Missouri) patented an approach to retrieving BG fibres directly from the melt during quenching [83]. Similar to the synthesis of melt-derived BG, oxides, and carbonates are melted in Pt crucible at under 900 to 1500 ℃, and fibres are pulled out either by hand or through bushing by a rotating drum [308]. However, the fibre diameters are difficult to control, the fibres are short and the fibre yield is low (~25%) compared to the overall glass produced, while the remaining are beads. In a modified fibre retrieving method proposed by Zhou *et al.*, high pressure (0.35 MPa) airflow can be applied in retrieving longer and thinner fibres [84].

BG fibres can be also synthesized through processing melt-quenched monolith. Quintero *et al.* proposed the laser spinning approach to form uniformly long and cylindrical BG fibres with diameters around 200-300 nm [309]. This approach can be applied to multiple BG compositions with therapeutic ion incorporation such as Mg, Zn, Sr, etc. [310]. However, the fibres may not be homogeneous, as they range from tens of to 5000 nm [311]. They also only have a low yield (25% fibres while the remaining are beads and colloids).

2.4.4.2 Sol-gel derived

In sol-gel derived approach, electrospinning is commonly applied to produce ultrafine fibres. For sol-gel derived glasses, electrospinning of the sol can produce long ultrafine fibres (Figure 2. 14 (d)). A sol-gel solution is whipped into long and homogeneous fibres as it passes from a syringe needle, under high voltage, to an earthed collector [312, 313]. Process variables such as applied voltage, humidity, temperature, sol cation content, viscosity, and distance to the collector and collector type affect fibre morphology [97, 314, 315].

Electrospinning is an approach to producing ultrafine fibres by injecting a solution under high voltage. This technique was patented in 1934 by Formhales but has gained

much attention only by the start of this century [313], but the idea originates from the 1600s. Electrospun fibres perfectly mimic the ECM fibrils, such as collagen and fibronectin, which had a diameter from 100 to 700 nm [316], which makes them structurally favourable for cell attachment, proliferation, and migration. Polymers are the common material being electrospun as they are generally processable and soluble in organic solvents [307, 317, 318].

The electrospinning apparatus usually consists of four components, a syringe with spinneret, a syringe pump, a grounded collector, and a high voltage power supply, as presented in Figure 2. 14 (a) [316]. The solution undergoes the following steps into long and homogeneous fibres (Figure 2. 14 (b)), including:

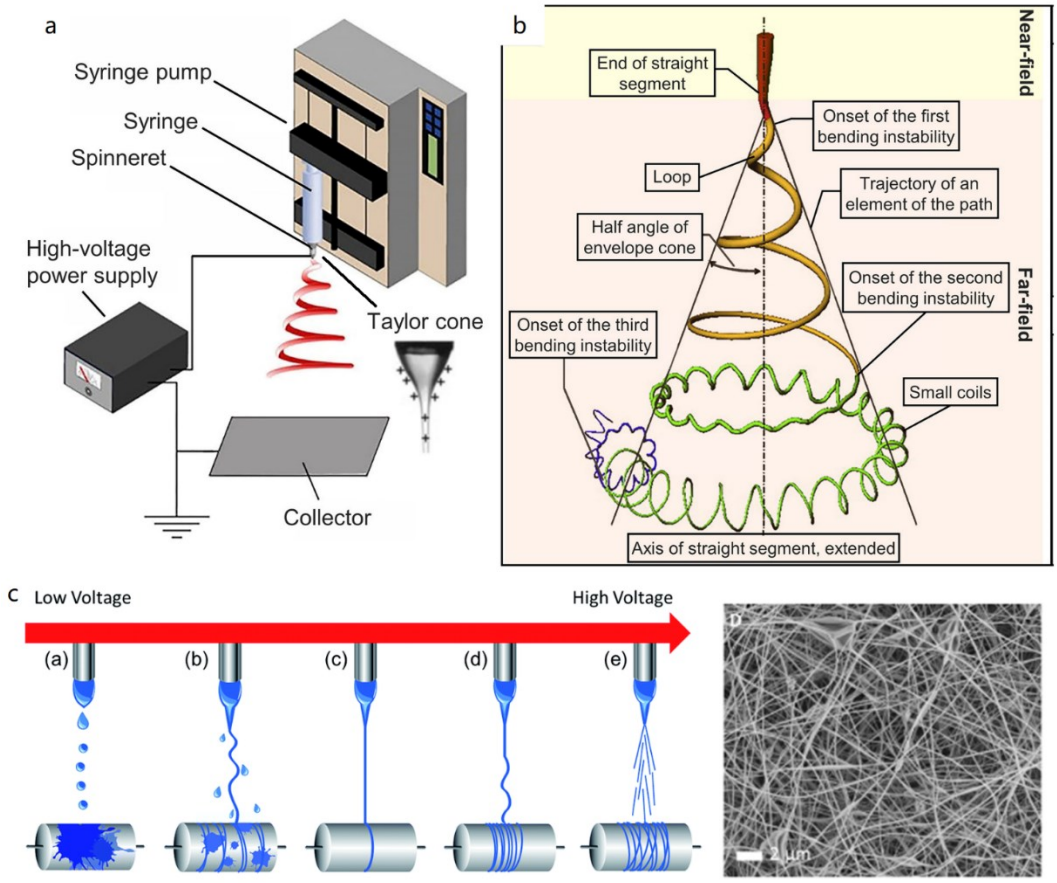


Figure 2. 14. (a) Schematic diagram of the electrospinning apparatus in a vertical alignment, reproduced from [319]. (b) Schematic diagram of the propagation of the electrospinning jet reproduced from [313]. (c) Schematic diagram of electrospun fibre structure achieved under low to high voltages (from a to e), Reproduced with permission from [320]. (d) SEM images of the silicate-based sol–gel-derived fibres 70S30C (70 mol% SiO_2, 30 mol% CaO), with diameters of 320 nm, were reproduced from [97].

Taylor cone formation

During electrospinning, the liquid from the spinneret was extruded and exist as droplets due to the surface tension. While the electric potential reaches a critical value, the electrostatic force and the surface tension reach an equilibrium, and the droplet forms into a Taylor cone. The critical value depends on the physicochemical properties of the solution, but the Taylor cone is a cone with a semi-verticle angle around 49.3° regarding less of the solution property or the electrospinning parameters [312].

Jet propagation

When the voltage reaches the critical limit, the solution overcomes the surface tension and a jet is created from the tip of the cone [313]. The jet is straight until reaching the bending instability. The jet decelerates during its propagation because the surface tension and viscoelastic force of the solution are opposite to the propagation direction [321]. The force also thins the jet due to the speed difference between the surface and center of the jet. When the acceleration is zero, any small perturbation of the jet stops its straight movement, which leads to bending instability. The critical length of the straight segment depends on the surface charge, flow rate, electrical conductivity of the fluid, density of the fluid, the strength of the electric field, current passing through the jet, and initial radius of the jet and the jet velocity is around 1-15 m/s [322].

Bending (whipping) instability

The entry of the first bending instability relates to far-field electrospinning. The jet quickly bends by 90°, and the trajectory evolves into a series of loops that propagates around the original direction. The coil consists of one continuous, looping, spiraling, and whipping action so that the bending instability is the most important step for the elongation and thinning of the jets [315]. There are different types of bending instability. Rayleigh instability is an axisymmetric bending that is dominated by the surface tension but suppressed by high electric potential. The second type of bending is also axisymmetric, but it is dominated by strong electric potential. The third type is non-axisymmetric resulting from the electrostatic repulsion among the jet surfaces. The aerodynamic instability and the “lateral electrostatic force” exert a long wavy perturbation to the jet. The dominant type depends on the electroconductivity of the jet, external electric field, physicochemical properties of the liquid, and other electrospinning parameters [314]. The jet then forms a much smaller coil as the secondary bending instability, in which the whipping and thinning were even faster. The jet can be elongated up to 10,000 times within a short period of 0.05 s or less [319].

Solidification and deposition

The cross-section of the fibres decreased by around 1300 times during the bending instability and the jet solidifies before its deposition on the collector. The complex fibre mat structures also merit the bending instability. Most charges of the fibre mat will dissipate during the deposition, but due to the low conductivity of the fibres, a little charge may still remain [323, 324].

The first silica electrospun fibres were produced with diameters from 200-400 nm [325] and alumina-borate oxide fibres had diameters of about 550 nm [93]. Electrospinning of other glass compositions followed [94, 95, 326], with a 7-11 kV voltage thought to be optimal for fibre production [95]. Kim *et al.* reported that the application of a polymer binder, such as polyvinyl butyral (PVB), resulted in a favoured viscosity and surface tension of the solution for the spinning to commence [94].

The conventional electrospinning approach mostly generated 2D fibre mats. Poologasundarampillai *et al.* produced the first 3D electrospun BG scaffold, of the 70S30C composition [96], with thicker non-woven mats (0.5-2 mm) compared to conventional 2D mats (<0.5 mm). This unique 3D structure was formed through the branching effect and the compilation of branched fibres due to the mutual repulsion of conductive ions (Ca^{2+}) and the solution viscosity. Ca^{2+} incorporation also stimulated the stretching of the jet and bending of the fibres. While the Ca^{2+} was initially thought to be critical for the 3D structure, Norris *et al.* found that humidity was more important and calcium-free fibres could also be spun into a 3D format. They synthesized 3D fibre mats with fibre diameters matching that of the collagen fibrils by using PVB as a binder [97]. The 70S30C fibres synthesized were ~340 nm in diameter with a surface area of 43.1 m^2g^{-1}.

Voltage

The voltage supply for electrospinning is usually a static DC supply. The polarity of the voltage (positive or negative) depends on the solution properties as some materials, especially electrolytes, can only be electrospun under one polarity [327, 328]. The strength of the electric potential affects the number of charges carried by jet and the magnitude of electrostatic repulsion among both internal and external electric fields [329]. In general, at low voltage, the surface tension will not be overcome so only beads will be formed from the solution. The increasing voltage will create continuous fibre, but the further increase results in more fluid ejaculation time for fibre stretching and evapouration thus thicker and non-homogeneous fibre [320]. For some solutions, such as the sol-gel precursor, branching occurs while the voltage reaches a critical value and fibre diameters becomes even thinner but their length also reduces [316]. However, Poologasundarampillai *et al.*

were able to produce long fibres through branching and therefore developed the first 3D electrospun scaffold (non-woven fibre mat thickness > 0.5 mm) [96].

AC power supply commonly introduces alternating segments of positive and negative in fibres. This decreases the electrostatic repulsion and thus suppresses bending instability [330]. The frequency of the AC determines the length of the segments, as well as the bundling effect due to the attraction of positive and negative segments during the bending instability.

The electroconductivity of the solution is an important factor influencing the critical voltage applied and the fibre structures. Solution with higher electrical conductivity would lead to the production of thinner fibres [315]. This is because there were more charges in the solution so the electrostatic force at the thinning step was higher.

Viscosity and surface tension

Viscosity implies the jet's ability in dragging the solution. Low viscosity induces solution 'dropping' towards the collector with no continuous fibres, but high viscosity usually in high surface tension, inhibits the jet formation and induces the formation of beads as well as thicker and non-homogeneous fibres due to its instability [331]. But in polymeric solutions, the control of concentration and molecular weight may not change viscosity while reducing surface tension. For example, chitosan dissolved in 90% ethanol had much lower surface tension than chitosan in water, but similar viscosity [332]. Both viscosity and surface tension also affects the thinning and effect during electrospinning.

Others

An increase in the flow rate increases the amount of solution extruded from the spinneret, so it wound generally enlarges the fibre diameter, but a critical flow rate is required to ensure the formation of the Taylor cone. Working distances determine the stages of bending instability. In general, longer working distances stimulate better solidification of the fibres [313]. Fibres also become thinner with the increase of working distance until a certain point, while further increases do not affect fibre diameters. Fibre diameters also increase with the increase of needle diameter. Ambient parameters, including humidity and temperature, also influence the morphology of the resultant fibre mat [97].

2.5 Therapeutic ions from BGs to the wound healing cascade

2.5.1 Hemostasis

While bioactive glasses are relatively new to wound healing applications, other silica-based inorganic materials have been used for some time. Aluminum silicate (hydrated Al_2O_3 $2SiO_2$, Kaolin clay) impregnated gauze has been used to stop massive bleeding for more than a decade, e.g. QuikClot® [333, 334]. In addition, silica nanoparticles [335-337] and mesoporous silica [338-341] and silicate clay [342, 343] have been used as hemostats. Soluble silicate ions can be a major factor in its success. Silicates induce platelet aggregation through the MMP2 and adenosine diphosphate pathways [344, 345], and exhibit excellent absorption capabilities to condense coagulation factors and generate $Si{-}O^-$ functional groups on the surface of the glass that activate factor XII of the intrinsic pathway [48, 346-348]. However, QuikClot® poorly biodegrades and leads to an exothermic reaction that causes some tissue necrosis, foreign-body reactions, and even thrombosis [349-351]. Thereby, their applications have been limited by the Food and Drug Administration (FDA) [352].

Ostomel *et al.* created a hemostatic BG using SiO_2-CaO-CaP sol-gel microspheres reported their potential in increasing the rate of clot initiation and growth, as well as improve the ultimate clot strength [47]. Other studies also reported that the incorporation of calcium improved the clotting kinetics of silica in vitro and in vivo in femoral artery and rabbit artery models [337, 339]. Ca^{2+} ions are enrolled in the coagulation cascade (factor IV) of thrombin regeneration and the ions stimulate platelet chemotaxis and adhesion, enzyme activation (factor X, protein kinase C, mitogen-activated protein kinase), and protein formation (factor XII, factor VII, and factor XIII) [341, 353-355]. The inclusion of Ca^{2+} in the silicate network of a sol-gel glass increases pore size and surface area, resulting in an enhanced absorption ability [286], e.g. mesoporous $SiO_2 - CaO$ particles (150-200 nm) soaked in rabbit blood for 60 minutes increased clot stiffness by 33%, and platelet aggregation number compared to SiO_2 particles [349]. Similarly, mesoporous silica xerogels containing 10 mol% Ca^{2+} induced a 50% reduction of PT and APTT compared to Ca-free xerogels both in vitro and in vivo in rabbit femoral artery injury [356, 357]. However, as Ca^{2+}ions reach a critical level, they led to a negative hemostatic effect due to induction of apatite formation. For example, the faster Ca^{2+} release from the 58S MBG

led to faster HCA precipitation and thereby resulted in a decreased coagulation rate compared to that of 77S [358].

BGs release therapeutic Si species and Ca^{2+} ions, resulting in the reduction of activated partial thromboplastin time (APTT) in the intrinsic pathway for coagulation and prothrombin time (PT) for extrinsic pathways for coagulation, as well as the acceleration of platelet aggregation and thrombus protein expressions [47, 358, 359]. BGs can also be processed into structures with high surface area and porosity to absorb blood, clotting factors, and platelets [341]. MBGs have been invented to have a 3-5 fold increase of both the surface area and the porosity of BGs and thereby exhibit much higher potential in hemostasis compared to conventional BGs. For example, 15 mg of 77S MBG reduced clotting time from 10.9 minutes to 2.9 minutes while that for conventional BG particles was 3.5 minutes [358]. Further evidence proved that MBGs reduced APTT and bleeding time to 33-50% of that of conventional BG particles both in vitro [48] and in vivo [360]. MBG nanofibres also have high surface areas and porosity, e.g. electrospun Eu/Tb doped MBG fibres using PVP+P123+CTAB had an average diameter of 100-120 nm, surface areas of 171-188 m^2g^{-1}, and pore volumes of 0.186-0.246 cm^3g^{-1} [361]. They are analogous to the mesh structure of fibrin protein that further promotes platelet aggregation and clot formation. Saha *et al.* found that BG nanofibres stimulated the fibrin clot structure and promoted platelet aggregation [362].

BG are also potential platforms for a broad spectrum of therapeutic ions that promote hemostasis. Among them, gallium has the most outstanding hemostatic effect. Ga-containing compounds, especially gallium nitrate, have been patented for the enhancement of early-stage hemostasis [363-365]. Although the exact mechanism of gallium remains unknown, researchers have proved that the Ga^{3+} reduce clotting time due to activation of the intrinsic pathway or platelets [363]. In addition, Ga-containing BGs have a higher surface area and porosity than Ga-free BGs [100, 366]. Pourshahrestani *et al.* found that 1 mol% Ga-MBG stimulated much more thrombin generation, thrombus formation, and platelet aggregation compared to Ga-free MBGs [48], although increasing the Ga content to 3 mol% reduced the levels back to those seen for Ga-free MBG. The 1 mol% Ga-MBGs were further proven to be 3-5 times more efficient in sprouting hemostasis compared to two commercial hemostats in vitro: Advanced Clotting Sponge Plus™ and Celox™ [367]. Tantalum (TA) is another element that was recently reported hemostatic in BG system [368], as 5 mol% of TA induced a 50% reduction of APTT [369, 370].

Other trace elements that have been commonly incorporated in BGs retain the potential for sprouting hemostasis. For example, Cu^{2+} and Ni^{2+} have high affinity with FXII factor, FXI factor, and high molecular weight kininogen [371]. Zn^{2+} ions stimulate the formation of fibrin fibres and thus increase the rate of thrombus formation either by itself or by co-functioning with the chitosan scaffold because Zn^{2+} induce both the activation of FXII factor and high molecular weight kininogen [372]. In addition, the lack of Zn^{2+} results in decreased platelet aggregation, T-cell numbers, and the response of T-lymphocytes to phytomitogens [373]. Co^{2+} and Fe^{3+} exhibit an indirect stimulation of hemostasis [374]. Mg^{2+} level has also been reported as crucial to hematoma volume and growth [375], but others reported that Mg^{2+} have a slight impairment to coagulation [376]. The above-mentioned evidence on the hemostatic behaviour of BGs and their released therapeutic ions confirmed the potential of BGs in the hemostasis phase of wound healing.

2.5.2 Antibacterial effect

BGs are antimicrobial to a large spectrum of bacteria, as listed in Table 2. 4. Eight different types of BGs, including S53P4 and 13-93, have been reported to exhibit strong antibacterial properties to 29 common pathogens within the BG dose from 6.25-100 mg mL^{-1} [49]. The antibacterial effects of BGs are attributed to two separate mechanisms. First, the dissolution of Na^{+} and Ca^{2+} increases the local pH value to more than 9, which exceeds the normal living pH of microorganisms (around 7.2), and can kill them [377]. For example, 5 g of particulate 45S5 in 10 mL of nutrient broth, artificial saliva, and DMEM induced a pH level of more than 10 which killed more than 90% of 6 different bacterial within 3 hours [50], while when reducing the pH to 7.2 using HCl, only 30% of microbes were killed. However, a pH rise can lead to general cytotoxicity. Secondly, the silicate ions dissolved inhibit bacteria growth [378]. This mechanism could be supported by the success of other silica-based materials such as disinfectants [334, 379]. However, antibacterial studies of 50 mg mL^{-1} of six different types of BGs in 13 pathogens revealed that the effect of silicate ions was negligible compared to that of pH [380].

Table 2. 4. Common microorganisms inhibited by BG.

	Full name	**Abbreviation**	**Presence**
Gram-positive bacteria	*Staphylococcus aureus*	*S. aureus*	Normal Flora, Skin, Respiratory tract, model microorganism
	Staphylococcus epidermidis	*S. epidermidis*	Normal Flora, Skin
	methicillin-resistant S. aureus	MRSA	Infection (’Superbug’)
	Streptococcus mutans	*S. mutans*	Oral Cavity
	Streptococcus gordonii	*S. gordonii*	Saliva

	Streptococcus sanguis	*S. sanguis*	Gum
	Streptococcus pyogenes	*S. pyogenes*	Skin
	Enterococcus faecalis	*E. faecalis*	Gastrointestinal tracts
	Bacillus subtilis	*B. subtillis*	Gastrointestinal tract
	Listeria monocytogenes	*L. monocytogenes*	Infection (Lethal)
	Clostridium difficile	*C. difficile*	Gastrointestinal tract
Gram-negative bacteria	*Escherichia coli*	*E. coli*	Normal Flora, Lower intestine, Model microorganism
	Pseudomonas aeruginosa	*P. aeruginosa*	Normal Flora, Skin
	Klebsiella aerogenes	*K. aerogenes*	Gastrointestinal tract
	Klebsiella pneumoniae	*K. pneumonia*	Gum, Skin, Intestines
	Porphyromonas gingivalis	*P. gingivalis*	Oral cavity, Gastrointestinal tract,
	Prevotella intermedia	*P. intermedia*	Gum
	Aggregatibacter actinomycetemcomitans	*A. actinomycetemcomitans*	Gum
Fungi	*Candida albicans*	*C. albicans*	Normal flora, Gut
	Trichophyton rubrum	*Tr. rubrum*	Dead skin
	Trichophyton violaceum	*Tr. violaceum*	Dead skin

Even though BGs seem superior in killing some bacteria, such as some facultative bacteria in root canal systems (S*. mutans*, *P. aeruginosa*, *E. faecalis,* etc.) the anti-microbial properties of common BG compositions are inferior to clinical disinfectants, such as calcium hydroxide [381]. The anti-microbial effects of BGs can be improved in three aspects: increasing BG surface area to pursue faster dissolution; adding antibiotics/disinfectants; introducing antimicrobial trace elements into glass structure for ion delivery [382]. Increased surface area stimulates faster dissolution of ions leading to a quicker formation of a high-pH and ion-rich environment that inhibit bacteria growth. For example, MBGs were ideal to be more antibacterial than non-mesoporous BGs: 10 mg of $50SiO_2 - 20CaO - 26Na_2O - 4P_2O_5$ MBGs in 1 mL of 10^3 CFU/mL bacterial suspension for 24 hours inhibited 99% of *E. coli* and 66% of *S. aureus* within 24 hours while 50 mg of MBG had full inhibition to both bacteria [383]. Similarly, BG NPs induce significant enhancement to the antimicrobial capability compared to conventional BG particles. Mortazavi *et al.* reported the potential of BG NPs (20-100 nm) of various compositions in inhibiting *E. coli*, *P. aeruginosa*, *Salmonella typhi* (*S. typhi*), and *S. aureus* above 50 $\mathrm{mg\,mL^{-1}}$, below the cytotoxic concentration to fibroblasts [384]. Increased dissolution rate can lead to toxicity and many articles do not report dose effects on eukaryotic cells.

Delivery of ions can exhibit antibacterial effects. Antibacterial ions that have been loaded in BGs include Ag^+, Zn^{2+}, Cu^{2+}, Ga^{3+}, $Ce^{3+/4+}$, which are released with the degradation of glass. Using borates or phosphates as the glass network former can

increase the antimicrobial effect. Therapeutic ions could also co-function with antimicrobial drugs to further increase the antibacterial capability of BGs. For instance, Ag^+ loaded BG (Ag-BG) not only exhibited a significant antibacterial ability to MRSA above 2.5 mg mL^{-1}, but also recovered the antibacterial activity of antibiotics including oxacillin, fosfomycin, vancomycin, etc. [385]. The effects of trace elements containing BG in antibacterial effects were summarized in Table 2. 5. The antibacterial capabilities of BGs are commonly quantified in three approaches. The first is by their minimum inhibitory concentration (MIC) or minimum bactericidal concentration (MBC). The second is by the diameter of the bacteria-free zone induced by BG powders or scaffolds on the agar plate, termed as inhibition halo diameter. The third is the antibacterial ratio, the percentage of bacteria remaining, after culture with BG for a certain period.

2.5.2.1 Silver

Mechanism: Since ancient times, silver has been known to inhibit food spoilage induced by a broad range of microorganisms. Today, silver remains to be the commonest and most bactericidal source against both gram-negative and gram-positive bacteria [386]. The most profound effect of silver is that it binds with thiol(sulfhydryl) groups of cysteine residues, fuel for many enzymatic activities, and thereby deactivates enzymatic functions of bacteria [387]. In addition, silver forms S-Ag bonds with disulfide and sulfhydryl groups blocking respiration and electron transfer of the surface proteins on microbial surfaces. This interrupts the rescue mechanisms, reducing the resurrection of cells after external damage, and causes the collapse of the proton motive force that de-energizes the microbial membrane and eventually leads to their death [388, 389]. Furthermore, silver can rupture the bacterial membrane and would induce further damage through interaction with cytoplasm, nucleosides, and phosphate groups of nucleic acids [386, 390]. Finally, the introduction of silver would raise the level of local ROS that eradicate external microbial through immunization [391, 392].

BG: The first Ag-BG was prepared by Bellantone *et al.* with 0.8 mol% Ag incorporation [393]. The incorporation of Ag^+ in the BG network greatly enhanced the BG's antibacterial properties, as the *E. coli* concentration after 20-hour treatment with Ag-BG was 96% lower than that of Ag-free BG. The antibacterial effects increased with an increased dose of Ag-BG. The MIC of the resultant BG was 0.2 mg mL^{-1} [393] and MBC value was 1 mg mL^{-1} [394, 395] but the cytotoxicity to eukaryotic cells was not investigated. Similar antibacterial effects were observed against *P. aeruginosa* [394], *S. aureus* [394], *S. mutans* [396], and MRSA [397]. The release of Ag^+ ions were the main reason for the antibacterial activities. Ag^+ ions were consumed when killing bacteria, as a decrease of Ag^+ level was observed,

which was proportional to the inhibition of MRSA [397]. In general, Ag^+ release to 50-70 mg L^{-1} was sufficient to kill every bacteria [396, 398]. However, when ensuring cell viability, the Ag^+ level shall be maintained at about 3.5 mg L^{-1}, which still exhibits an antibacterial effect and is not cytotoxic to osteoblast [399]. Sol-gel BG nanofibres (500-900 nm) with 0.1 mol% of Ag_2O, 2 mol% of B_2O_3, 68-69 mol% of SiO_2, and 29-30 mol% CaO were proved to have better antibacterial ability compared to a model aminoglycoside antibiotic, tobramycin at MIC dose (15 mm compared to 9 mm in diameter in halo test) [362]. Releasing around 4 mg L^{-1} of Ag, the fibre was non-toxic to GM00637 fibroblasts but promoted its migration. Similar results were found for 2 mg L^{-1} doses of BG fibres with 1.84 mol% Ag (1000-2000 nm) (87.48 SiO_2, 10.68 CaO), which was non-toxic to osteoblasts and reduced *S. aureus* number from 10^{11} to 10^4 in 12 hours [400].

Similar effects were observed in Ag-containing borosilicate [399, 401] and borophosphate BG [402, 403]. For example, 0.05, 0.5 and 1 mol% Ag_2O-containing 1393-B2 BG scaffolds inhibited *E. coli* and *S. aureus* within 24 hours (from 80% to 90% when composition increase from 0.05 to 1 mol%) [399]. In addition, a relevant report claimed that $3Ag_2O$-$97[1.5B_2O_3$-SiO_2-CaO] BG system caused further inhibition effect to *E. coli* (316 times reduction after 1 hour and 10^4 times after 2 hours) and *S. aureus* (100 times reduction after 6 hours) [401]. Melt-derived $59.5B_2O_3$-$2P_2O_5$-9.5CaO-$9CaF_2$ -(20 - xNa_2O)-xAg_2O (mol%, x=0.25, 0.5 and 0.75) induced an increased antibacterial effect to *E. coli* and *S. aureus* [404]. 0.5 mol% of Ag_2O reduced the MIC for *E. coli* and *S. aureus* from 1 and >1 mg mL^{-1} to 0.25 mg mL^{-1}.

In general, the antibacterial effect of Ag-BGs increases as silver increases in the composition, for both silicate and borosilicate/borophosphate glasses [402]. The surface area or texture also influences the rate of release of Ag [252, 398]. But for Ag-containing phosphate glasses [405], the antibacterial effect against *Listeria monocytogenes* (*L. monocytogenes*) increased when Ag_2O composition increased from 0.2 to 1 mol%, but then decreased beyond 1.5 mol%. This was explained by the excess silver forming silver nanoparticle clusters in the glass, which could neither form Ag-S bonding nor penetrate the bacteria membrane. Silver nanoparticles were also observed within sol-gel silicate glasses when imaged under TEM and through neutron diffraction [406], although silver was also incorporated in the silicate network as a network modifier. The Ag nanoparticles may be present in many of the sol-gel glasses reported, but their formation was undetected as TEM or diffraction studies were not carried out. The efficacy and reproducibility of glasses containing silver in their composition are difficult to maintain due to the induction of silver metal nanoparticles, which will affect free silver ion release and can also cause

an increase in connectivity of the silicate network as silver is no longer acting as a network modifier.

Yet, the cytotoxic effect of silver and that silver has no other stimulative effect in tissue engineering makes it emerging non-favourable compared with other therapeutic ions. For example, Zn-BG had a lower antibacterial effect than Ag-BG but hardly induced any cytotoxicity [407, 408]. 2 and 4 mol% Zn-BG had slightly higher MBC to *E. coli* compared to Ag-BG of similar composition (0.3 and 0.1 mg mL^{-1} respectively) [409]. But Ag-BGs exhibited a strongly negative effect on bone cell viability and alkaline phosphatase (ALP) expression.

2.5.2.2 Copper

Mechanism: Copper is another commonly used antimicrobial ion and is also an important micronutrient for multiple metabolic activities [410]. There are several mechanisms for its antimicrobial effect. Similar to Ag^{+}, Cu^{2+} ions bind with sulfhydryl groups in cysteines or glutathione etc. and de-energize respiration and metabolic activities of microbial [411]. In addition, Cu^{2+} ions damage lipopolysaccharide patches on membrane walls and therefore disrupt the membrane integrity, transport protein activity, and ion permeability [412]. Another study has also proved that Cu^{2+} ions replace Fe^{3+} in iron-sulfur clusters and substitute Zn^{2+} or other important ions from their binding sites on proteins located on microbial membranes [413]. The most profound antibacterial mechanism of copper is its alternations between redox states Cu^{+} and Cu^{2+} [414]. Through either bonding with sulfhydryl groups or its activity with Cu-containing enzymes, Cu^{2+} ions change their states by generating a voltage potential of 200 to 800 mV and hydrogen peroxide as by-products. Further redox reaction with Cu^{+} induced the generation of hydroxyl radicals that cause detrimental damage to cellular molecules through oxidation of functional groups in proteins and lipids [415]. Of course, this also means too much Cu can also cause general cell toxicity.

BGs: Though Cu^{2+} has been incorporated in different biodegradable glass systems before [416], the first investigation of antibacterial Cu-BG was on melt-derived P_2O_5-Na_2O-CaO glass [417]. In 24 hours, phosphate BGs with 1, 5, and 10 mol% Cu exhibited 0, 7.5, and 30 times reduction of *Streptococcus sanguis* (*S. sanguis*) colony reduction. The effect was due to the increased Cu composition in BGs, which increases Cu^{2+} release and the BG's solubility. Similarly, 2, 4, and 6 mol% of Cu-containing calcium phosphate glass induced 15, 25, and 40 mgL^{-1} of Cu^{2+} release respectively and their inhibitory effects

against *S. aureus* from day 1 to 7 increased correspondingly to their release concentration of Cu^{2+} [418]. The glass containing 2 and 4 mol% CuO exhibited a progressive reduction of microorganisms number 100-1000 times on day 7, while 6 mol% Cu-BG kills 10^8 times of antibacterial effect on day 3. The same trend applies to SiO_2-Na_2O-CaO-P_2O_5 sol-gel BGs as the 24 h inhibition halos induced by glasses containing 0, 3, and 6 mol% CuO were 0, 3, and 9 mm against *E. coli*, respectively, and 2, 5 and 16 mm against *S. epidermidis* [419]. However, Palza *et al.* determined that the MBCs for *E. coli* and *S. mutans* when treated with glasses containing 2.87 mol% and 6.58 mol% CuO in 24 hours were 5-10 mg mL^{-1} [396]. This was because the MBC of Cu^{2+} was 50 mg L^{-1} and more Cu^{2+} in media would not have further improvement in antibacterial effects.

Novel approaches have been proposed to improve the antibacterial efficacy of Cu-BGs. One of them was to promote the shift from Cu^{+} to Cu^{2+} in the BG system as the existence of Cu^{+} in BG reduced the antibacterial activity of Cu-BG [420]. It is not only Cu content in the glass that is important but the rate of release. For example, Gross *et al.* replaced Al_2O_3 with K_2O, B_2O_3 and P_2O_5, keeping Cu content the same, and the resulting increased Cu release rate caused a much higher inhibition against *S. aureus*, *P. aeruginosa*, *K. aerogenes,* and *E. coli* colonies, and >99.9% reduction against all bacteria within 2.5 hours. Chemical treatments, such as the use of tannic acid, ascorbic acid, and NaOH, can promote the reduction of Cu^{2+} to Cu^{0} NPs within BG powders, which further enhance their antibacterial effects [421].

Increasing the ratio of Na: Ca in the BG composition is an alternative approach to increase dissolution rate and Cu release [422]; 5 mol% Cu-containing SiO_2-Na_2O-CaO with a lower Ca/Na ratio had bactericidal effects against *S. aureus* (a halo of 1 mm) while the one with a higher ratio merely exhibited bacteriostatic effects. Cu and Mg were co-loaded into a sol-gel 58S BG [423] (some CaO replaced with MgO) and the glass's antibacterial effect on MRSA increased as MgO increased in the composition to 5 mol%, but as the MgO content increased further, the release kinetics of Cu^{2+} decreased, probably due to Mg switching its role in the glass network, increasing network connectivity over a certain mol%.

2.5.2.3 Zinc

Mechanism: Zinc is the second most abundant element in the human body and is involved in more than 300 enzymatic reactions [373]. During the wound healing process, zinc localizes in the ECM of epidermal and dermal tissues and helps to stabilize the cell membrane during mitosis, migration, and maturation [274]. As an antimicrobial agent, zinc should be regarded as Zn^{2+} ions and ZnO separately. Zn^{2+} ions have an innate

antibacterial effect in the water. They function as other heavy metals that impair bacteria enzymatic activities through bonding [424]. ZnO is a non-toxic agent that is bactericidal to a wide range of pathogenic bacteria which also release Zn^{2+} ions for antibacterial effects [425, 426]. But beyond this, ZnO particles easily interrupt the stabilization mechanism of the microbial membranes and thereby make them more permeable and vulnerable to being ruptured [59, 427, 428]. ZnO particles also exhibited semiconductive properties to induce a high level of ROS, which is its most profound antibacterial mechanism [60]. The stimulated ROS further penetrate bacteria and damage their DNA, RNA, and proteins, especially gram-negative bacteria, whose lipid bilayer membrane is more sensitive than the peptidoglycan protective layer in gram-positive bacteria [429].

BG: The initial reason why zinc was incorporated into the BG system was due to its improvement in bioactivity, the rate of HCA formation, due to the formation of zinc hydroxide precipitates [430-433]. The release of Zn^{2+} from the glass usually increases with the increase of Zn composition in BGs. For instance, 1.32 mol% ZnO incorporation in phosphate BGs stimulated a higher antibacterial effect on *S. mutans* [434]. SiO_2-CaO-SrO-MgO BG containing 2-5 mol% ZnO also had an increased killing effect on *S. epidermidis* with the increase of Zn incorporation [435]. Similar effects were found for a borate glass (13-93B3) containing just 0.83 mol% ZnO against *S. aureus* and *E. coli* [436].

However, while increasing Zn content in the composition increases the Zn^{2+} release from BG, it can significantly reduce the release of other ions, such as Na^{+} or Ca^{2+}. For example, the antibacterial effect against *S. epidermidis*, *S. aureus*, *S. pyogenes*, *B. subtilis,* and *K. lebsiella* of Zn-free BG was similar to that of 15.53 mol% Zn-BG, which had much higher ZnO in its compositions than many Zn-BGs [437]. Wajda *et al.* compared the antibacterial effect of melt-derived and sol-gel-derived Zn-containing SiO_2-CaO BGs [438]. Melt-derived 2 mol% Zn-BG and sol-gel derived Zn-free and 4 mol% Zn-BG had noticeable antibacterial effects. This was because that sol-gel derived BG had a much faster (>2 times) release of SiO_4^{4-} and Ca^{2+} ions but a slower release of Zn^{2+} ions compared to that of melt-derived BG. In addition, the increase of zinc composition from 2 to 4 mol% hardly enhanced Zn^{2+} release kinetics in sol-gel derived Zn-BGs as Zn promoted the formation of Si-O-Si bonding in sol-gel BGs and makes them harder to dissolve.

The antibacterial effect of Zn was also assessed in glasses that also released a range of other therapeutic ions, including Cu [436], Ti [439], Nb [440], Ag [408], F [434], Mg, and Sr [435], and Zr [441]. The complexity of the compositions makes it difficult to determine whether Zn is the only active ion for these compositions, but in general, the effect of Zn

was negligible when co-doped with other strong antibacterial ions. For example, while Zn helped kill bacteria in Cu-free BGs, the addition of Cu hardly promoted the antibacterial effect, although, in this particular system, Zn did not change the release kinetics of any elements [436]. Replacing Ag with Zn in the SiO_2-CaO-SrO-P_2O_5 system, reduced the antibacterial ability towards *E. coli*, but promoted osteoblast proliferation [408]. On the other hand, while Zn and F both significantly enhance the antibacterial effect of calcium phosphate glass, co-doping of both had much worse killing effect against *S. mutans* compared to Zn and F-free glasses [434]. For others, the increase in Zn composition promoted antibacterial effect until reaching a critical value of ZnO content, and then a decreased trend was observed [435, 440-442].

2.5.2.4 Boron

Mechanism: The dissolution products of borate/borosilicate glasses are borate groups that exist in the form of boric acid in solution and in blood. Boric acid has been reported as a bactericide and fungicide since the 1860s against a broad spectrum of microorganisms, including *S. aureus*, *Aeromonas hydrophila*, *P. aeruginosa*, *Brucella melitensis Rev1,* and field isolates of *Vibrio anguillarum*, *Aeromonas hydrophila*, *Yersinia ruckeri*, *P. aeruginosa*, *Lactococcus garvieae*, *K. pneumoniae*, *Brucella abortus*, *Aspergillus niger* and *C. albicans* [65, 443]. The MIC of all the above-mentioned bacteria ranges from 0.385 to 7.5 $\mathrm{mgmL^{-1}}$, depending on the type of microorganisms. Boron inhibits protein activities on the membrane of the bacteria cell membranes that fuels bacteria metabolism and molecule uptake [444]; borate groups bind with hydroxyl-rich compounds such as phospholipids, lipopolysaccharides, and glycoproteins in microbial membranes, inducing changes to membrane functional activities and membrane-bound enzymes [445]. Borate groups are small non-polar molecules that can penetrate through microbial membranes and are involved in a variety of enzymatic activities inside the cells [446, 447]. Such activities inhibit microbial enzymatic activity thus leading to an antimicrobial effect. Borate glasses tend to undergo more rapid dissolution compared to silicate glasses with similar amounts of network former and thereby induce faster release of antibacterial ions [45, 448]. For instance, 13-93B3 BG with 0.82 mol% Zn and 0.34 mol% Cu was reported to have a significant inhibition of 4 common biofilm microorganisms including *P. aeruginosa*, *C. albicans*, *S. aureus,* and *Acinetobacter baumannii* compared to 13-93B3 and 45S5 glass [449].

Polymeric hydrogels, fibre, or nanocomposites containing boron also exhibited antimicrobial effects against *E. coli*, *S. aureus*, *P. aeruginosa,* and *C. albicans*, although the effect was half the efficacy of antibiotics [450-452]. Glycerol hydrogel based on boron

was reported to have antimicrobial activity against *E. coli*, *S. aureus,* and MRSA, and antifungal activities against *T richophyton rubrum* and *Tr. violaceum* [453]. However, the effect of borosilicate glass was highly dependent on the doses of BG to bacteria. For example, the antibacterial effects of borosilicate BGs at 5 $\mathrm{mgmL^{-1}}$ (87%) were less than that of silicate BGs (90%), but the effects at 10 $\mathrm{mgmL^{-1}}$ were higher G (> 97.5% than > 92.5%) [454]. It was further concluded that a minimum concentration of 10 $\mathrm{mgmL^{-1}}$ was necessary for borosilicate BG to exert significant bactericidal effects.

2.5.2.5 Others

BGs containing other cations have also been reported to exhibit antibacterial effects. Gallium is an antibacterial reagent that has also had a strong suppressive effect on bone resorption and some cancerous behaviour [455, 456]. Ga also enters microbes through an iron transport mechanism and disrupts the DNA and protein synthesis of the microbes [457]. BG containing 3 mol% of Ga_2O_3 produced an inhibition halo five times larger than that of Ga-free BGs for *S. aureus* [458] and induced 20 times reduction to *P.gingivalis* [459], without inducing cytotoxic effects. But the increase of Ga composition in BG does not always lead to an increased effect. In a separate phosphate glass system, increasing Ga_2O_3 composition from 1 mol% to 5 mol% resulted in decreased Ga^{3+} release and thus a reduced antibacterial effect against various bacteria [460]. The increase in Ga_2O_3 composition also inhibited the release of other ions. For example, in a study of Ga-containing Zn-BG, the increase of Ga_2O_3 composition from 2.5 to 15 mol% replacing B_2O_3 led to a drastic reduction of Zn^{2+} release from 0.46 to 0.24 mg L^{-1} and a decreased inhibitory effect against *S. epidermidis* and an increased effect against *P. aeruginosa*, as Zn^{2+} had more effect on Gram-positive bacteria while Ga^{3+} had more effect on Gram-negative bacteria [461]. The release kinetics was relevant to the composition of other elements in the BG system. For example, phosphate BG with the lowest Ca/Na ratio (14/38) released Ga^{3+} at a higher rate (80 mg L^{-1}), while those with higher ratios induced 20 mg L^{-1} Ga^{3+} release [462]. The synthesis approach affects the antibacterial effect by influencing the release of both Ga^{3+} and other cations. In the SiO_2-CaO system, melt-derived Ga-BG with the highest Ga_2O_3 composition (4 mol%) and sol-gel Ga-free BG exhibited the highest antibacterial effect compared to other counterparts [463]. SiO_4^{4-} and Ca^{2+} ions released from sol-gel BG were more than twice that from melt-derived BGs but melt-derived glasses had a faster release of Ga^{3+} ions. In general, the antimicrobial effect of melt-derived Ga-BG was more dependent on Ga^{3+} release and that of sol-gel-derived Ga-BG was more dependent on the alkaline environment. Ga-MBGs had much higher surface areas compared to Ga-BGs and a stronger antibacterial effect. Pourshahrestani

et al. found that increasing Ga_2O_3 composition from 1 mol% to 3 mol% in SiO_2–CaO-P_2O_5 MBGs increased Ga^{3+} release from 0.1 to 0.3 mg L^{-1} leading to an increased reduction of *E. coli* and *S. aureus* viability from 80% to 99% within 12 h [48]. In MBG scaffolds, increasing Ga_2O_3 composition from 5 to 10 mol% (xGa_2O_3-(100-x)SiO_2–CaO-P_2O_5) significantly increased the antibacterial effect on MRSA and *E. coli* without exhibiting a cytotoxic effect to osteoblasts [464]. The increase in Ga composition also decreased the surface area and porosity of MBGs and increased the crosslinking in the MBG system [48] so that beyond certain compositions, an increase in Ga composition leads to a decrease in Ga^{3+} level and decreased antibacterial effect [100, 465]. For example, Salinas *et al.* found that 3.5 mol% Ga_2O_3 induced very little Ga^{3+} release in SiO_2–CaO-P_2O_5 MBGs and thus had a little antibacterial effect [465]. This is because Ga_2O_3 incorporation significantly reduced the surface area of the MBGs (from 515 to ~380 m^2g^{-1}).

Cerium is the most common lanthanide element and has reported antibacterial effects against a broad spectrum of microorganisms. Cerium has two states in glass composition as Ce^{3+} to Ce^{4+} [242]. Ce^{4+} can switch to Ce^{3+} through redox reaction with the release of oxygen. Both ions have antibacterial capabilities. First, as a heavy metal ion, Ce^{4+} can raise the ROS level that causes severe damage to bacteria membranes, proteins, and DNA [466, 467]. In addition, bacteria could uptake Ce^{4+} which would impair their cellular respiration, oxygen uptake, and glucose metabolism [468]. The incorporation of a small amount of cerium makes little difference to BG structure and degradation kinetics [469]. Therefore, Ce-BGs were not investigated until the development of Ce-loaded MBGs (Ce-MBGs) or Ce-BG NPs [100]. For instance, 10 mg mL^{-1} of 5 and 10 mol%, Ce-loaded SiO_2-CaO-P_2O_5 MBGs caused >99.9% inhibition of *E. coli* while MGS with 0-1 mol% CeO_2 hardly possessed any effects [470].

Mg is an essential element that involves in the enzymatic activities, cellular signaling, and stabilizing cell components of all organisms [471, 472] and it can donate two electrons for ROS generation [473, 474]. The mechanism may involve the binding of Mg^{2+} to bacteria membranes [475] and the ions may also penetrate the cells, making them more vulnerable to leakage and membrane rupture [476, 477]. Mg^{2+} ions also prevent the formation of biofilms by generating a protective layer on the surface of materials to prevent bacteria adhesion [478], and the disruption of cyclic di-GMP, a second messenger for signal transduction in bacteria [475, 479, 480]. The antibacterial effect of Mg-BG first increases with the increase of Mg composition and then decreases as the increase of Mg composition slowed down the release kinetics of Ca^{2+} ions and hardly increased Mg^{2+} concentration [481, 482]. For the $55SiO_2$-$10K_2O$-(35-*x*)CaO-*x*MgO (*x* = 0, 5, 15, 25, 35

mol%) system the growth inhibition on *S. aureus*, *Salmonella,* and *C. albicans* [483] increased as the Mg increased in the glass composition until it reached 15 mol% the glass's efficacy on *S. aureus* and *Salmonella* started decreasing, while that of *C. albicans* further increased to >99.9% inhibition. Similarly, in the SiO_2-P_2O_5-CaO system, the glasses were effective on MRSA until Mg composition reached 5 mol%, after which further increase of magnesium in the composition led to adverse effects [481]. The reason is that increasing Mg in the composition reduced the release of other therapeutic ions, both because Ca content in the composition decreased, but also because Mg can take the role of network intermediate. For example, in BGs co-loaded with Cu and Mg, the increase in magnesium composition slowed down Cu^{2+} release and thus had an adverse antibacterial effect [423]. The same results were observed in BG co-loaded with Zn and Mg [484].

Fluoride has been reported to inhibit a broad spectrum of microorganisms, particularly in dental care [485], and fluoride-containing bioactive glass was reported antimicrobial against *S. mutans* biofilm [486] with increasing fluoride composition having a more pronounced inhibitory effect against both *P.gingivalis* and *A.actinomycetemcomitans* [487]. However, S53P4 glasses doped with 2.4, 6.4, and 8.8 mol% fluorides were found to have less effect than fluoride-free BG against *E. coli* unless the dose of BG exceeded 20 $\mathrm{mg\,mL^{-1}}$ [488] and increasing the fluoride composition resulted in decreased antibacterial behaviour.

Strontium was an important element in bone regeneration. It contributes to the stimulation of type I collagen, the proliferation of osteoblast, and the inhibition of osteoclast differentiation [489-491]. BGs with Sr replacing Ca from 0 to 39 mol% were found to increase the antibacterial effect against *P. gingivali* and *A.actinomycetemcomitans* [492]. In addition, Sr-BG (SiO_2-CaO-P_2O_5-Na_2O) containing gelatin scaffold was found antibacterial to *S. aureus* while the gelatin with Sr-free BG had no effect [493]. A Sr and F co-loading BG was incorporated into bone cement and reduced *S. aureus* and *S. faecalis* viability by 3 orders of magnitude [494]. The effect increased with the increase of Sr incorporation (replacing Ca) until reaching a critical point (2.5 mol% for *S. faecalis* and 10 mol% for *S. aureus*), after which a decreased trend occurred. This was because the incorporation of Sr decreased the relative release of both Sr^{2+} ions and F^- ions in the medium as Sr-O bonding is more stable than Ca-O bonding.

Table 2. 5. Summary of BG glass systems designed to deliver ions with antibacterial properties. MBG = mesoporous (ordered) bioactive glass; Antibacterial ratio = the percentage of bacteria remaining after culture with BG for a certain period; MIC: Minimal

inhibitory concentration; MBC = Minimal bactericidal concentration; Inhibition halo = a bacteria-free zone induced by BG powders or scaffolds on the agar plate.

Ion	Microorganism	Synthesis	Ion comp. (mol%)	Ref.	Key points
Ag	*E. coli*	Melt-derived	0.8	[393] [394]	MIC = 0.2 mg mL^{-1} MBC = 1 mg mL^{-1}
			3	[401]	10000 times reduction in bacteria number
			0.05 - 1	[399]	Antibacterial ratios were 80 to 90% with concentration increases
			2	[402]	Large inhibition halo increases with the decrease of the P/(Ca+Na) ratio
			0.25, 0.5, 0.75	[404]	0.5 mol% of Ag reduced the MIC from 1 mg mL^{-1} to 0.25 mg mL^{-1}
		Sol-gel	5	[395]	Antibacterial ratio > 99% at 1 mg mL^{-1}
			1.48, 2.85	[396]	MBC = 0.3-0.5 mg mL^{-1}
		MBG	0.54	[495]	Inhibition halo of 1.5 cm at > 8 mg L^{-1}
			0.5	[360]	Antibacterial ratio was 99%
			3.1, 5.29	[496]	Antibacterial ratio was 88% and 100%
		NPs	0.27 - 2.9	[497]	Inhibition halo of 2 cm
			2, 4, 6	[498]	Inhibition halo of 9.3, 21, and 19.3 mm respectively
			1.39	[499]	Inhibition halo of 11.75 (non-modified) and 10.75 mm (modified)
			10	[500]	Significant but not quantified antibacterial effect
	S. aureus	Melt-derived	0.8	[394]	MBC = 0.5 mg mL^{-1}
			2	[401]	Large inhibition halo increases with the decrease of the P/(Ca+Na) ratio
			3	[399]	100 times reduction in bacteria viability
			0.25, 0.5, 0.75	[404]	0.5 mol% of Ag reduced the MIC from > 1 mg mL^{-1} to 0.25 mg mL^{-1}
		MBG	0.54	[495]	Inhibition halo of 1.5 cm at >8 mg L^{-1}
			0.016	[501]	MBC = 0.1–0.5 mg mL^{-1}
			3.1, 5.29	[496]	Antibacterial ratio was 86.2% and 100%
		NPs	0.27 - 2.9	[497]	Inhibition halo of 2 cm
			2, 4, 6	[498]	Inhibition halo of 16, 20.6, and 19 mm respectively
			0.05M	[502]	Antibacterial ratio was >90%
			1.39	[499]	Inhibition halo of 17.5 (non-modified) and 9 mm (modified)
			10	[500]	Significant but not quantified antibacterial effect
		Sol-gel fibre	1×10^{-3}	[362]	Inhibition halo of 15 mm
			1.84	[400]	Reduced *S. aureus* number from 10^{11} to 10^4
	P. aeruginosa	Melt-derived	0.8	[394]	MBC = 0.5 mg mL^{-1}
			2	[401]	Large inhibition halo increases with the decrease of the P/(Ca+Na) ratio
		Sol-gel	5	[395]	Antibacterial ratio was > 99% at 1 mg mL^{-1}
			0.1 M	[398]	Inhibition halo of 2 mm
		NP	0.05M	[502]	Antibacterial ratio was >90%

	S. mutans	Sol-gel	1.48, 2.85	[396]	MBC = 0.5-2 mg mL $^{-1}$
	MRSA	Sol-gel	2.1	[397]	1000 times reduction in bacteria number
	S. sanguis	Melt-derived	1, 5, 10	[403]	30, 180 and 600 times reduction in bacteria number respectively
	L. monocytogenes	Melt-derived	0.2, 1, 1.5	[405]	Effect of 1 mol% Ag > that of 1.5 mol% Ag
	E. faecalis	MBG	0.1 M	[503]	Antibacterial ratio was 99%
Cu	*E. coli*	Melt-derived	3, 6	[419]	Inhibition zone of 5 and 16 mm
			2, 4, 6	[418]	MBC = 0.5 mg mL $^{-1}$
			20	[420]	Antibacterial ratio was >99.9%
		Sol-gel	2.87, 6.58	[396]	MBC = 5-10 mg mL $^{-1}$
		MBG	1.56	[495]	Inhibition halo of 2 cm at >8 mg L^{-1}
			5	[504]	Antibacterial ratio was 99% after 7 days
			0.5, 1.5, 2.5	[505]	Complete suppression at all Cu compositions
			5	[506]	MIC and MBC = 50 mg mL $^{-1}$
		NPs	2	[304]	The antibacterial ratio was 70-75%
	S. aureus	Melt-derived	2, 4, 6	[418]	MBC = 0.5 mg mL $^{-1}$
			20	[420]	Antibacterial ratio was >99.9%
		Sol-gel	2, 4, 6	[418]	10^3, 10^4, and 10^8 times reduction in bacteria number
		MBG	1.56	[495]	Inhibition halo of 2 cm at >8 mg L^{-1}
			0.5, 1.5, 2.5	[505]	Complete suppression at 1.5 and 2.5 mol%
		NPs	2	[304]	The antibacterial ratio was 70-75%
	P. aeruginosa	MBG	20	[420]	Antibacterial ratio was >99.9%
			0.5, 1.5, 2.5	[505]	Complete suppression at 1.5 and 2.5 mol%
		Ion exchange	5	[422]	Inhibition halo of 1 mm
	S. mutans	Sol-gel	2.87, 6.58	[396]	MBC = 5-10 mg mL $^{-1}$
	MRSA	Sol-gel	5	[423]	Antibacterial ratio decreases with Mg incorporation
	B. subtillis	MBG	0.5, 1.5, 2.5	[505]	Complete suppression at 1.5 and 2.5 mol%
	S. sanguis	MBG	1, 5, 10	[417]	0, 6, and 30 times reduction in bacteria number
	S. epidermidis	Melt-derived	3, 6	[419]	Inhibition zone of 5 and 16 mm
		NPs	2	[304]	The antibacterial ratio was 50%
	E. faecalis	Sol-gel	0.5, 1.5, 2.5	[505]	Composition dependent inhibition halo
	K. aerogenes	MBG	20	[420]	Antibacterial ratio was >99.9%
	C. albicans	Melt-derived	0.5, 1.5, 2.5	[505]	Composition dependent inhibition halo
Zn	*E. coli*	MBG	2, 4	[409]	MBC = 0.2 mg mL $^{-1}$
		Melt-derived Sol-gel	2, 4	[438]	Composition and synthesis-dependent antibacterial effect
	S. aureus	MBG	4	[465]	The antibacterial ratio was 70%
			4, 7	[507]	Antibacterial ratio was 70% and 90%

		Melt-derived Sol-gel	2, 4	[438]	Composition and synthesis-dependent antibacterial effect
	P. aeruginosa	Melt-derived	0 - 15.53	[437]	Composition dependent inhibition halo width up to 36.1 mm
		MBG	5	[508]	Inhibition halo of 0.41 cm
			3, 5	[509]	Antibacterial ratio was 89.4%
	S. mutans	Melt-derived	1.32	[434]	Viability decrease from 10^{6-7} to 3.68 x 10^4 CFU/mL
	B. subtilis	MBG	3, 5	[509]	Antibacterial ratio was 91.3%
		Melt-derived	0 - 15.53	[437]	Only 15.53 mol % induce inhibition halo of 12 mm
	S. epidermidis	Melt-derived	2, 3.8	[435]	Dose and composition-dependent antibacterial effect up to 90%
			3, 5	[509]	Antibacterial ratio was 91.3%
			0 - 15.53	[437]	Composition dependent inhibition halo width up to 21.7 mm
	P.gingivalis	Sol-gel	5	[510]	Higher antibacterial effect than Zn-free BGs
	S. pyogenes	Melt-derived	0 - 15.53	[437]	Composition dependent inhibition halo width up to 68 mm
	A.actinomycetemcomitans	Sol-gel	5	[510]	Higher antibacterial effect than Zn-free BGs
	P. intermedia	Sol-gel	5	[510]	Higher antibacterial effect than Zn-free BGs
	K. pneumonia	Melt-derived	0 - 15.53	[437]	Only 15.53 mol % induce inhibition halo of 11.9 mm
Ga	*E. coli*	Melt-derived	1, 3, 5	[460]	Decreased antibacterial effect with composition due to decreased Ga release
			1, 5	[511]	Slight antibacterial effect
		MBG	1, 2, 3	[48]	Antibacterial ratio increases with Ga composition up to 80%
		Melt-derived Sol-gel	2, 4	[463]	Only melt-derived BG with 4% Ga and sol-gel BG with 0% Ga had
	S. aureus	Sol-gel	3	[458]	Inhibition halo of 30 mm
		Melt-derived	1, 5	[511]	Slight antibacterial effect
		MBG	1, 2, 3	[48]	Antibacterial ratio increases with Ga composition up to 99%
	MRSA	Melt-derived	1, 3, 5	[460]	Only 1% exhibited a little effect
	C. difficile	Melt-derived	1, 3, 5	[460]	Only 1% exhibited a little effect
	P.gingivalis	Melt-derived	3	[512]	$10^{5.4}$ times reduction in bacteria number
			3	[459]	16 times more inhibition compared to Ga-free BG
	P. aeruginosa	Melt-derived	1, 3, 5	[460]	Decreased antibacterial effect with composition due to decreased Ga release
			3	[462]	The highest effect at the lowest Ca and highest Na (14/38) was 7.2 times that of the control

			0 - 15	[461]	Inhibition halo decreased from 31.3 to 21 mm
		MBG	5	[513]	Ga^{3+} ions released were 100 times as the 90% inhibition concentration
	S. epidermidis	Melt-derived	0 - 15	[461]	Inhibition halo increase from 0 to 29 mm
	S. gordonii	Melt-derived	3	[512]	100% inhibition while Ca composition was the lowest (10%)
Ce	*E. coli*	MBG	1, 5, 10	[470]	Strong and composition-dependent effect up to > 99.9%
			1, 3, 5	[511]	Slight antibacterial effect
		NPs	2	[514]	Slight more antibacterial effect than Ce free MBG
	S. aureus		1, 3, 5	[511]	Slight antibacterial effect
		NPs	2	[514]	Slight less antibacterial effect than Ce free MBG
	P. aeruginosa	NPs	2	[514]	Slight less antibacterial effect than Ce free MBG
	B. subtilis	NPs	2	[514]	Slight less antibacterial effect than Ce free MBG
Mg	*S. aureus, Salmonella, C. albicans*	Melt-derived	0 - 35	[483]	Antibacterial ratios were > 99.9% beyond 15%
	MRSA	Sol-gel	0 - 10	[481]	No obvious effect below 5%
Sr	*P. gingivali*	Melt-derived	0 - 39	[492]	Increase slightly when replacing Ca with Sr
	A. actinomycetemcomitans				
	S. aureus	Melt-derived	0 - 50	[494]	30 times reduction in bacteria number
	S. faecalis	Melt-derived	0 - 50	[494]	303 times reduction in bacteria number
Mn	*E. coli, B. subtilis, P. aeruginosa, S. aureus*	MBG	0 - 7	[515]	5 mol% exhibited a significant antibacterial effect
Rb	*E. coli, S. aureus*	MBG	1, 2, 5	[516]	Antibacterial ratio increases with Rb composition up to >90%
Bi	*E. coli*	MBG	0.13 - 1.13	[517]	Composition dependent antibacterial ratio
Zr	*MRSA*	Sol-gel	5, 10	[518]	5 mol% zirconium-containing 58S BG particles had 50% higher antibacterial capabilities to MRSA compared to Zr-free BGs
Ta	*E. coli, S. aureus*	Sol-gel	0.2 - 1	[519]	Increased antibacterial abilities with the increase of Ta composition
F	*E. coli*	MBG	2.4, 6.4, 8.8	[488]	0 mol% exhibited significant antibacterial effect
	A. actinomycetemcomitans	Melt-derived	0 - 7	[487]	Composition dependent antibacterial effect up to 80%
	P. gingivalis				Composition dependent antibacterial effect up to 50%

Manganese-loaded MBG was proved to have a significant antibacterial effect against *E. coli*, *B. subtilis*, *P. aeruginosa,* and *S. aureus* compared to control and Mn-free glasses [515]. 58S BG particles containing 5 mol% zirconium had 50% higher antibacterial capabilities to MRSA compared to Zr-free BGs [518]. Similar 58S BG particles containing 1 mol% Ta reduced the viability of *S. aureus* and *E. coli* to 10% of that of Ta-free BGs [519]. MBG scaffolds containing 1-5 mol% of Rubidium were also found to have an inhibitory effect against *E. coli* and *S. aureus* [516]. A glass containing 5 mol% Rb gave 10% more inhibition of *E. coli* and *S. aureus* and a BG containing 0.1 -1 mol% bismuth oxide was more bactericidal to *E. coli* compared to Bi-free BG [517].

In general, Cu, Zn, and B are common therapeutic ions incorporated into the BG system. Besides, Mirragen, a borate-based BG product with Cu and Zn incorporation (1605 as described in Table 2.3), has been proved successful as commercial product for chronic ulcers. It is of particular interest to investigate the antibacterial effect of Cu, Zn, and B to wound healing.

2.5.3 Anti-inflammation

There has been a contradictory view of the anti-inflammatory effects of BGs. Sol-gel-derived $SiO_2 - P_2O_5 - CaO$ BGs and bioactive glass-ceramics have been reported to induce inflammation due to the stimulation of macrophage proliferation [520, 521]. For example, Bosetti *et al.* reported that 45S5 BG induced an increased regulation of TNF-α and TNF-α-mRNAs from peritoneal macrophages and monocytes [522]. Besides, the HCA that formed from the dissolution products of BGs can further induce inflammation by up-regulating the expressions of IL-1, TNF-α, IL-6, and IL-8 [523-525]

Recently, 45S5 was found to be anti-inflammatory. For example, Day *et al.* reported a significant down-regulation of IL-6 from macrophages and monocytes when treated by 45S5, with negligible changes in the amount of TNF-α and IL-10 [526]. 45S5 BGs were reported to activate macrophages towards the M2 phenotype [51]; more M1 phenotypes (represented by marker iNOS) transformed into M2 phenotypes (represented by marker ARG) when treated with BG extracts than when treated with a control medium. 45S5 also induced a significant decrease in IL-1 and TNF-α expression and a significant increase in IL-10, VEGF, FGF-2, and TGF-β. The stimulation of the macrophage phenotype switch is highly dependent on the BG dose, which too much glass proves an inflammatory response. 20 $mg\ L^{-1}$ of 58S BG particles stimulated RAW (a macrophage cell line) proliferation and promoted the switch from M1 to M2 phenotype, but 100 $mg\ L^{-1}$ of particles led to a significant inflammatory response with a significant decrease in cell number [527]. In

addition, RAW cells treated with 100 mg L^{-1} BG leads to a significant increase in iNOS, IL-1, and IL-1ra while those with 20 mg L^{-1} had a down-regulation in all pro-inflammatory factors. Gomez *et al.* reported that the dissolution products of 1 mg mL^{-1} MBGs ($75SiO_2$-$20CaO$-$5P_2O_5$), following conditioning in DMEM for 24 hours, reduced the number of macrophages while maintaining the percentage of M1 phenotypes [528].

Although the precise mechanism for the anti-inflammatory responses of BG has not yet been identified, its effect can be attributed to the release of soluble silica. Silicon-based materials, such as coral sand, calcium silicates, and sodium metasilicate, have been widely applied in the treatment of diabetic ulcers, glomerulopathy, and other inflammatory diseases [529-532]. For example, silicic acid and sodium metasilicate exhibited a broad spectrum of anti-inflammatory behaviour including the down-regulation of TNF-α and several antioxidant enzymes such as copper superoxide dismutase (CuSOD), manganese SOD (MnSOD), catalase, and glutathione peroxidase (GPx) [531, 532]. Calcium may also lead to anti-inflammatory responses through calcium influx [533].

Zhao *et al.* investigated the effect of dissolution products of BG scaffolds (SiO_2:CaO:P_2O_5 = 80:15:5) on RAW cells and IL-4 treated RAW cells (representing the inflammatory and anti-inflammatory state) [52]. In both conditions, the cells expressed significantly high levels of IL-1, IL-6, and Arginase (anti-inflammatory gene) and a decrease in IL-10 and TNF-α. Similarly, for alginate hydrogels containing SiO_2-CaO-P_2O_5 BG, an increase in M2 macrophage phenotype was observed, with the down-regulation of inflammatory cytokines and up-regulation of anti-inflammatory cytokines [235]. The anti-inflammatory behaviour leads to a paracrine effect that can promote the regeneration of tissues, including fibroblast proliferation and migration, growth factor expression (VEGF, FGF-2, and TGF-β), angiogenesis, etc. [52, 235]. Both the anti-inflammatory effect and the paracrine regenerative effects were confirmed in vivo in diabetic rat models [52, 527], and in normal and macrophage-depleted mice [235].

2.5.3.1 Copper

Mechanism: Cu is a well-known anti-inflammatory agent; Cu complexes have been commonly used as non-steroidal anti-inflammatory drugs enhancing the effect while reducing the toxicity of their uncomplexed parent drug [534-536]. The Cu is thought to enroll in the metabolism of free radicals through redox reaction and relieve oxidative stress during wound healing. Cu serves as catalytic components to MMPs, hydroxylases, and oxidases that lyse down detrimental ROS and prevent inflammation [537]. Though Cu may also induce the formation of OH free radicals that promote inflammation, recent evidence

proved that Cu complexes with specific OH-inactivating ligands inactivate OH groups once they are formed [538]. Besides, Cu mimics cupriprotein superoxide dismutase and destroys superoxide anions which disable them [534, 539]. The level of ceruloplasmin, the commonest transporter of Cu that binds with 70-80% plasma Cu, upregulates with the increase of Cu level and generates a protective role under inflammatory conditions [540, 541]. The proposed mechanism was proved by investigation of copper levels in the metabolism of both acute and chronic inflammatory conditions where its deficiency favours the pro-inflammatory state [542].

BGs: $80SiO_2 - 15CaO - 5P_2O_5$ and $80SiO_2 - 10CaO - 5P_2O_5 - 5CuO$ MBGs were detected in their macrophage phenotype concentration through their respective markers CCR7 and CD163 signalings [543]. Cu-MBGs exhibited a high stimulation of macrophage migration and provoked a switch of M1 to M2 phenotype. Cu-MBG also induced a slight increase in IL-1 and IL-1ra expression. Further investigations during in vivo tests revealed that Cu-MBG induced low inflammatory response and increased angiogenic effect. In addition, Lin *et al.* found similar effects for $75SiO_2 - 15CaO\text{-}5CuO - 5P_2O_5$ BGs [544]. The scaffolds induced a marked decrease of TNF-α and IL-18 and a marked increase of IL-10 within a concentration of 0.5-16 mg L^{-1}. A down-regulation of M1 marker iNOS and an up-regulation of M2 marker CD206 were also observed.

2.5.3.2 Zinc

Mechanism: The role of zinc as an anti-inflammatory ion is due to its regulation of zinc transporter mRNA [545] and the capability of zinc as an antioxidant. Zinc is known to: (1) inhibit the NADPH enzyme; (2) induce the production of metallothioneins; (3) prevent the production of hydroxyl radicals from iron and copper by competing with them to bond to the cell membrane; (4) reduce the production of cytotoxic cytokines; (5) promote the proliferation of enzyme superoxide dismutase (SOD) in order to change superoxide radical back to hydroxy peroxide [61, 62]. Zinc strongly prevents the apoptosis and tumourigenic of both epithelial and endothelial tissues. It stimulates the anti-inflammatory responses with nutrients and proteins as by-products to further stimulate healing behaviour [274, 546]. The deficiency of zinc leads to an adverse effect on cytokine function and secretion and thereby impairs the function of the basic messengers of the immune system [547, 548]. It is argued that the chemotaxis of leukocytes and ROS production are also inhibited during zinc deficiency [549]. This impaired behaviour is a sign of prolonged inflammation as a longer period was required for sufficient secretion of cytokines, ROS, and macrophage chemotaxis, thereby indicating the potential of zinc for anti-inflammatory effect [373, 545]. Zinc regulates inflammatory cytokines for an anti-inflammatory response, e.g. Zn-

containing HA was capable of decreasing the TNF-α concentration in the THP-1 cell line [550].

BGs: A phosphate BG containing zinc had a similar effect on IL-6 down-regulation and IL-10 up-regulation as that of 45S5, but 45S5 was much more toxic to lipopolysaccharide (LPS) treated RAW cells [526]. In borosilicate glasses in the xZnO-(100-x)[5MgO-40B_2O_3-34SiO_2-5P_2O_5-16CaO] (mol% x = 0, 1.5 and 5) system, 5 mol% Zn incorporation induced the smallest M1/M2 ratio for THP-1 cells [551]. It also promoted the highest expressions of ARG and IL-10 and the paracrine effect to stimulate growth factor expressions from hBMSCs. Similar effects were found for chitosan-alginate hydrogels containing 58S BG NPs (50-100 nm) with 5 mol% ZnO, where pro-inflammatory factors were down-regulated in vivo with stimulated wound closure and angiogenesis [552]. Compared with Cu-BGs of the same composition, Zn-BG was more anti-inflammatory, for example, 11 mol% sol-gel Zn-BG induced a higher decrease in TNF-α and a higher increase in IL-10 compared to Cu-BG of the same composition, much more than that from Zn-free BGs and the control [553].

2.5.3.3 Boron

Mechanism: Borate and borosilicate glasses are potent anti-inflammatory agents, although hardly any research was imposed in this field. Demirci *et al.* presented the anti-inflammatory effect of boric acid and sodium pentaborate pentahydrate on various inflammatory factors [65]. Boron had inhibitory effects on two important inflammatory mediators, iNOS and COX-2, at all concentrations. In addition, decreased NO concentration was induced from LPS treated RAW cells when treated with >100 mg L^{-1} boron, indicating the potential of boron in anti-inflammatory activities at high concentration. Dietary boron was also reported to significantly enhance the production of erythrocyte superoxide dismutase and therefore stimulated the ROS metabolism [554].

Although the anti-inflammatory effects of borate BGs were not widely studied, their fast dissolution kinetics made them promising platforms for the delivery of therapeutic ions and drugs. For example, boron-containing MBG scaffolds have been reported to incorporate biomimetic anti-inflammatory nano-capsule-gold nanocages that were enveloped by LPS treated macrophage cell membranes coated with cytokine receptors and loaded with resolving D1 as M2 polarization inducer [67]. The resultant scaffold blocked pro-inflammatory cytokines TNF-α and IL-6, and promote M2 polarization both in vitro and in vivo on femoral bone defects.

2.5.3.4 Others

BGs containing other cations have also been reported to exhibit anti-inflammatory effects. Ce-BGs have been reported to induce inflammatory effects. The conversion of Ce^{4+} to Ce^{3+} induces oxygen vacancies that act as auto-regenerative free radical scavengers in inhibiting inflammatory mediators such as NO or ROS [555, 556]. Another study reported that cerium exhibits superoxide dismutase-mimic properties by reacting with superoxide to form hydrogel peroxide [557, 558]. These reactions result in alleviated oxidative stress and reduced inflammatory responses [559]. As a result, cerium oxide has been commonly used as an anti-oxidants in diminishing oxidative disruption of the cell membrane and protecting cells from ROS-induced damages [169, 560, 561]. In addition, while scavenging superoxide decreases the attraction of macrophages and neutrophils in inflamed tissues, nanoceria has been applied as promising anti-apoptotic and anti-inflammatory drugs in vivo [562-565]. SiO_2-CaO MBG NPs (100-300 nm) containing 2.8 mol% CeO_2, promoted significantly lower expressions of oxidative stress-related genes (NOS2, PTGS2, NRROS, and MMP9) compared to Ce-free MBGs at 1 mg mL^{-1} [566]. They also promoted fewer cytokine expressions (IL-1, TNF-α, IL-6, and tryptophan 5-monooxygenase activation protein zeta).

Ag reduced inflammatory effects in a porcine dermatitis model [567-569] and in wound dressings [570-572]. 58S Ag-BG microparticles with 1 mol% Ag_2O replacing Ca were characterized by their anti-inflammatory effects on human PMNs and peripheral blood mononuclear cells (PBMC) [573]. Below the cytotoxic level, Ag-BG was capable of decreasing intra- and extracellular ROS levels when assessed with opsonized zymosan, a compound that induces oxidative burst by activation of NADPH-oxidase through binding to complement receptors [574]. This was because the dissolution products from BGs interrupted the balance of oxidative status, inhibited the binding of zymosan, and reacted with free radicals as superoxides scavengers. In addition, Ag-BGs induced higher IL-4 in PBMC compared to the control. However, the cytotoxicity of Ag-BGs made them an unwelcoming candidate as anti-inflammatory ions [573, 575]. For example, although Ag-containing 46S6 BG induced anti-inflammatory properties by preventing IL-1 and IL-6 excretion from a differentiated THP-1 cell line, its LC50 (concentration that leads to 50% cell death) was 20 times less than that of Cu-BG and 10 times less than that of Cu-Zn-BG [575].

Sr incorporated materials have been reported to have anti-inflammatory potential through the down-regulation of TNF-α and IL-1β and up-regulation of IL-10 [576-578]. A recent

report also indicated the synergistic effect of Sr and Zn in inducing M2 polarization [579], but it was not conclusive whether both ions contributed. Zhao *et al.* reported the anti-inflammatory effects of 58S microspheres containing 10 mol% SrO inducing M2 polarization [580]. The ratio of M1:M2 in Sr-BG was 42.33: 51.85 while that in Sr-free BG is 45.85: 38.23 and that in control is 48.52: 45.33. This was further confirmed by lower expressions of inflammatory cytokines including IL-1, IL-1ra, TNF-α, and IL-6, and higher expressions of anti-inflammatory cytokines IL-10 and Arginase compared to those of control and Sr-free BGs. The resultant media after the anti-inflammation were rich with growth factors, such as VEGF, PDGF-BB, FGF-2, SDF, and Angiogenin, for further angiogenic activities in vitro and in vivo. Similarly, Zhang *et al.* observed that 6 mol% Sr-containing 58S BG induced a higher increase in M2 phenotype and a further decrease in the expressions of IL-6 and IL-1 compared to Sr-free BG and the control [581].

Ce or Ag are not good candidates to be incorporated in BG fibres as cerium significantly reduces the degradability and Ag may induce a cytotoxic effect during the fast degradation of BG fibres. Strontium hardly affects soft tissue engineering while its major application is in bone regeneration. Cu, Zn, and B have been widely studied and BG products consisting of these ions are successfully commercially in reducing inflammatory effects during diabetic ulcer regeneration. It would have a higher impact to study the mechanisms.

2.5.4 Angiogenesis

The first few investigations of the angiogenic effect of BGs were assessed for bone regeneration [45, 46, 582, 583]. For example, the first report on BG in angiogenesis reported its synergistic effect with recombinant human bone morphogenetic protein-2 (rhBMP-2) in sprouting angiogenesis in bone [582, 584]. rhBMP-2 containing BG up-regulated Flt-1 and KDR, two receptors of VEGF in vitro, and a 2-fold increase in bone vascularization. The same cell types and proteins are involved in angiogenesis in the wound. Endothelial cells were stimulated by BGs, BG dissolution products, or BG dissolution products pre-cultured with cells (bone cells, fibroblasts, keratinocytes, or macrophages) for enhanced proliferation, migration, and protein expressions (VEGF, FGF-2), and vessel formation both in vitro and in vivo. The angiogenic effects of BGs are summarized in Table 2. 6.

Day *et al.* first reported the role of 45S5 BG in angiogenesis, which significantly increased VEGF [53] and FGF-2 [54] expressions from CCD-18CO fibroblasts in the dose range of 0.01-0.1 w/v %. Similarly, 45S5 had similar stimulations to fibroblasts and enhanced vessel density when a BG-fibroblast skin graft was implanted in a full-thickness defect in a mouse

[55]. 45S5 also induced increased pro-angiogenic factor expressions including VEGF, HGF, PIGF, angiopoietin, and angiogenin in MSCs [58]. When loaded into collagen sponges, 45S5 up-regulated VEGF and tubule formation from endothelial cells [585], promoted vessel formation on quail chorioallantoic membrane [586], and induced vessel formation in a calvarial defect [587]. Similar effects were observed when loading 45S5 into hydrogels, where increased angiogenic effects were observed compared with BG-free materials [588-591].

The optimal dose of S53P4 to induce the highest VEGF expression from fibroblasts was also 0.01-0.1 w/v % [592]. Chitosan-silk fibroin containing 58S BG (10 wt%) also enhanced fibroblast proliferation, ECM deposition, and vascularization, and reduced inflammation in vivo [593]. $70SiO_2$-$25CaO$-$5P_2O_5$ BG in a PDLLA electrospun membrane promoted a 3-fold increase in CD31 expression (markers on the endothelial cells in blood vessels) in vivo and a 2-fold increase in new blood vessel formation in a diabetic wound model relative to PDLLA alone [594]. Alginate hydrogel containing BG also promoted angiogenesis through stimulating anti-inflammation in macrophages in vivo in normal and macrophage-depleted mice [235].

A recent study revealed a co-culture of BG with another cell stimulated angiogenesis. For example, S53P4 treated dental pulp pluripotent-like stem cells (DPPSCs) up-regulated VEGF and endothelial markers like vWF, FLK-1, and CD31 in HUVEC, and stimulated in vitro tubule formation [595]. In addition, 45S5 glass-ceramic 3D scaffolds stimulate angiogenesis in vitro on HUVEC and on CAM angiogenesis assay when co-cultured with human adipose tissue-derived stem cells [596].

The unique structure of BG fibres provides a network for the attachment, proliferation, and migration of endothelial cells. Melt-derived silicate-based BG fibres stimulated the blood vessel formation in vitro on HUVEC and fibroblasts and in vivo, which was patented Mo-Sci corporation (Rolla, Missouri, patent number US7745682B2, US-8535710-B2) [83, 597]. Sol-gel-derived 3D electrospun 70S30C BG nanofibrous scaffold also promoted VEGF expressions from fibroblasts [97].

The release of SiO_4^{4-} ions can be the main reason for the angiogenic effect of BG [598-600]. For example, silicates significantly increased the node number, circle number, and tube length of in vitro HUVECs tubules. This was supported by an assessment on HUVEC migration and homing (migration to its original tissues), where significant activity was observed in soluble silicate treated cells compared to non-treated cells. Li *et al.* and Zhai

et al. reported that SiO_4^{4-} ions at a concentration of 1.9 - 4.9 mg L^{-1} promoted angiogenesis in a co-culture system of fibroblasts and endothelial cells due to the endothelial NO and NO synthase production, which promoted vascular endothelial cadherin in the cell junction areas to facilitate vessel formation [600, 601]. Even beyond 20 mg L^{-1}, SiO_4^{4-} ions still up-regulated the expression of hypoxia-induced factor 1α (HIF-1α) and stabilized it by blocking HIF-prolyl hydroxylase 2 in endothelial cells [602, 603]. The up-regulation of HIF created a hypoxia-mimic environment in wounds and promoted the expressions of angiogenic factors in endothelial cells, including VEGF and FGF-2, along with their receptors, kinase inserts domain receptor (KDR, also called VEGFR-2), and FGF-2R. HIF up-regulation also stimulated the expressions of endothelial NOS (eNOS), an isoform of NO, in endothelial cells that promotes further proliferation of endothelial cells, adhesion of leukocytes, and platelet aggregation, leading to complete new blood vessel formation [604].

Ca release also stimulated angiogenesis of BG. An increase in calcium levels surrounding cells leads to calcium intake, which opens specific channels in the plasma membrane and generates calcium signaling. Calcium levels are closely related to the signaling pathways of various proteins, including PDGF, EGF, IGF-I, FGF-2, and VEGF [605-609]. In particular, calcium levels increase with the binding of FGF-2 and VEGF to their respective receptor tyrosine kinases in the endothelial cells [605]. Calcium signaling activities were also reported in fibroblast, which involves cell proliferation and expression of VEGF [610].

2.5.4.1 Boron

Mechanism: The role of boron in cellular activities can attribute to its binding to cis diol groups, which enable them to cross the cell membrane and involves in RNA activities, due to the presence of cis diol groups in RNA ribose moieties [611, 612]. 0.25% (w/v) of boric acid in fibroblast growth medium stimulated two times the increase in TNF-α mRNA from HDFs, which boric acid stimulated early state angiogenesis from since the inflammation phase [258]. Borate groups have also been shown to stimulate VEGF and TGF-β mRNA translation in endothelial cells, which thereby promote the expressions of VEGF and TGF-β [611]. In addition, NaBC1, an ion channel that regulates boron metabolism, is stimulated by borate ions and promotes angiogenesis via PI3k-independent pathways [613, 614].

HUVEC proliferation and tubule formation has been reported to accelerate as borate dose (boric acid) in the culture medium increased [57, 615, 616]. 60 mg L^{-1} of boric acid increased the proliferative response of HUVECs through the activation of the mitogen-activated protein kinases (MAPK) pathway, a pathway involved in signal communication

from the growth factor receptors at cell surfaces to cell DNA [57]. The ERK phosphorylation levels, which represent angiogenic mitogenic signals, in HUVECs were also up-regulated correspondingly to the increase of boron dose from 3 to 60 mg L^{-1}. Besides, Li *et al.* found that 45 mg L^{-1} of BO_3^{3-} stimulated the proliferation, migration, and tubule formation of endothelial cells [617].

BG: 45S5 BG（45S5.2B）containing ~2 mol% borate induced a higher HUVEC proliferation, migration, and in vitro tubule formation compared to that of 45S5, 45S5 loaded with VEGF, and 45S5 loaded with FGF-2 [57]. Further investigation revealed that the ERK phosphorylation levels in HUVECs were higher when treated with 45S5.2B and a positive correlation of this level occurred with increasing concentrations of boron. A similar finding was observed in the chorioallantoic membrane of quail embryos wherein 45S5.2B exhibited 26% higher FGF-2 production compared to 45S5 over 2 days of culture and thus higher new vessel formation [618].

PCL film containing 30 wt% 13-93B1 particles promoted higher VEGF expression from MSCs and increased CD31, CD144, KDR, and VEGF expression from hy926 endothelial cells compared with BG-free PCL [619]. 13-93B3 glass microfibres, with fibre diameters ranging from 0.5 to 1 μm, induced a two-fold stimulation of in vivo angiogenesis in a Sprague Dawley (SD) rat model compared to 13-93 silicate glass fibres with similar morphology [84]. 13-93B3 BG fibres were also commercially proved to promote angiogenesis in patients with diabetic venous stasis ulcers, a disease that is unable to heal through other treatments [282, 620].

BGs with the same components as 13-93B1 glasses but different compositions, named '01-06B1' (37.5 SiO_2-22.6 CaO-5.9 Na_2O-4.0 P_2O_5-12.0 K_2O-5.5 MgO-12.5 B_2O_3), induced three-fold higher VEGF expressions in osteoid in vivo than 45S5 [621]. In addition, the ionic dissolution product (1 wt/vol%) of 01-06B1 and 01-06B2 (2 and 7 mg L^{-1} BO_3^{3-}, respectively) increased VEGF secretion in MSCs (ST2), which was 3-fold and 2-fold of the VEGF expression stimulated from 13-93B3 (40 mg L^{-1} BO_3^{3-}) respectively and >20 fold of that of 13-93 [622]. Another borate BG system, GL1550, up-regulated the expressions of CD31, HIF-α, KDR, and VEGF from zoledronate treated endothelial cells, which mimics the angiogenic environment in osteonecrosis of the jaw, and promoted a 4-fold increase in endothelial migration and a 5-fold increase in tubule formation in vitro [623].

The addition of aluminum to borate BGs was found more stimulative to VEGF, IGF, and CX43 on mouse muscle myoblast cells (C2C12s), and the conditioned media from BGs

pre-cultured in C2C12 cells induced HUVEC migration and tube formation [68]. In vivo studies in volumetric muscle loss regeneration further proved that these novel borosilicate BGs exhibited higher angiogenic capability compared to silicate-based glasses. Besides, $50.6B_2O_3 - 23.7CaO - 6.43Na_2O - 8.24MgO - 8.46K_2O - 2.57SrO$ BGs promoted higher expressions of VEGF, FGF-2, and PDGF from 3T3-L1 cells in vitro and a 2-fold increase in blood vessel formation 14 days after the surgery on wounds of rodent model in vivo [66].

2.5.4.2 Phosphate

Mechanism: Phosphate-based glasses have also been documented for their potential for angiogenic activities [233]. Phosphate ions could induce various protein signalings in both human and mouse mesenchymal stromal cells, especially that of VEGF and FGF [259]. For example, phosphate causes an increase in VEGF expression of HUVECs and stimulates migration and tubule formation [260].

BGs: BG with 6.33 mol% phosphate induced higher VEGF stimulation in MC3T3-E1 and human osteosarcoma cell line MG63 compared to phosphate-free BGs and the control [487]. In vivo studies further determined that $44.5P_2O_5$-44.5CaO-$6Na_2O$-$5TiO_2$ BGs induced high vascular formation on endothelial lineage in rats in PLA scaffolds than in pure PLA scaffolds [624]. Yet, the main characteristics of phosphate-based BGs in sprouting angiogenesis are their delivery of therapeutic ions, as phosphate BGs degrade much faster than silicate ones [625, 626]. For instance, phosphate-based BGs delivered Co to induce higher VEGF secretion in MG63 and osteoblasts [272, 627]. However, the fast release of ions may also lead to toxicity. For example, Cu-loaded phosphate-based BGs were reported to inhibit the metabolic activity and proliferation of HUVEC [628].

2.5.4.3 Copper

Mechanism: Copper is widely known to trigger angiogenesis. Cu-containing diet, Cu-based NPs, and $CuSO_4$ promote sprouting angiogenesis [271, 629, 630]. It also promotes angiogenesis in tumours, so chelating Cu has been a common solution to suppress tumour angiogenesis [631, 632]. The angiogenic mechanism of Cu attributes to its induction of a hypoxia-mimicking environment in wounds. Cu functions in angiogenesis through the activation of the EGFR/ERK/c-fos transduction pathway and thereby the up-regulation of HIF-1α expressions [269]. These activations induce a simulated hypoxia environment and lead to the secretion of angiogenic factors such as VEGF, FGF-2, fibronectin, angionectin, TNF-α, IL-1, prostaglandin E-1, etc. [269]. It then fuels the activities of VEGF and FGF-2 through the angiogenic cascade [271]. In addition, Cu is also necessary for the HIF-1α

transcriptional complex formation and fuels the interaction with the hypoxia-responsive element in target genes [633].

Cu interacts with the MAPK signaling pathways to increase the survival of both endothelial cells and fibroblasts and sprout angiogenesis [634]. It also binds with the mRNA of SPARC, a transiently expressed ECM-binding protein that regulates endothelial cell proliferation [635]. Besides, its anti-inflammatory activities also stimulated the paracrine angiogenic factor expressions from macrophages [534, 539].

BGs: In vivo results have shown contradictory results of the angiogenic capability of Cu-BG. Bi *et al.* reported that the incorporation of 0.34 mol% Cu in 13-93B3 BG stimulated the increase of blood vessel formation in the rat calvarial model from 4.0% to 4.3% (cross-section are percentage in the defect) [636]. Wang *et al.* observed a similar trend that 2.5 mol% Cu in 13-93B2 stimulated higher in vivo vascularization than its Cu-free counterparts in the same animal model [637]. However, Lin *et al.* demonstrated that 1.57 mol% of Cu in 13-93 was toxic to MC3T3-E1 cells and that the non-toxic doses (0.31, 0.62 mol%) induced little stimulation in blood vessel formation was observed in vivo evaluation in rat calvarial [638].

In vitro, 45S5 BG scaffolds containing 1 mol% CuO were assessed for their angiogenic effect on an arteriovenous loop built from the rat groin [639]. The mean vessel density, mean vessel area, and mean vessel size of Cu-BG were 12.27 mm^2, 0.16 mm^2 , and 0.7 mm^2, while those from Cu-free counterparts were 8.98 mm^2, 0.07 mm^2, and 0.3 mm^2 respectively. On the contrary, 45S5 BG containing 2.5 mol% CuO was found to impair the formation of capillary-like networks on SVEC4-10 endothelial cells [640]. But this effect was later determined irrelevant to the incorporation of Cu in BGs, as $CuCl_2$ solution which induces the same Cu^{2+} concentration (12 mgL^{-1}) as that from BG extracts exhibited no obvious inhibition.

When loaded to organic scaffolds, Cu-BGs were generally stimulative to angiogenesis. For example, collagen scaffolds containing 58S BG particles with 2 mol% CuO stimulated VEGF expression from MSCs and tubule formation of HUVECs in vitro and ex vivo angiogenesis in chick embryo ex vivo model [641]. SiO_2-CaO-SrO-CuO BG also promoted in vivo angiogenesis in cranial bone when incorporated into PLGA-collagen-gelatin fibre mats [642]. Eggshell membrane coated with Cu-BGs ($75SiO_2$-(25-x)CaO-xCuO-$5P_2O_5$ (x=2, and 5)) induced a higher release of angiogenic factors from HUVECs compared to that coated with Cu-free BGs and uncoated BGs [643].

13-93B3 microfibres with 0.34 mol% Cu incorporation significantly enhanced in vivo microvascular density in the skin of SKH1 mice [644]. A 2.5-fold increase of vascular density was induced by Cu-BG fibres compared to the empty defect, while that of 13-93B3 fibre was 1.6-fold and that of 45S5 was 1.3-fold, in correspondence to the significant increased VEGF mRNA in tissues with Cu-BG compared to Cu-free BG. Similarly, 13-93B3 glass microfibres with 2.47 mol% Cu, with diameters ranging from 0.4 to 1.2 μm exhibited a 3-fold increase in VEGF, 8-fold increase in FGF-2, and a 10-fold increase in PDGF from fibroblasts compared to Cu-free 13-93B3 fibres and thereby increased HUVEC proliferation, migration, and tubule formation [85]. In vivo evaluations in the rodent skin defect model further proved that the resultant Cu-BG promoted blood vessel formation better than Cu-free BGs and the control (40, 30, and 15 blood vessels/mm^2, respectively). Furthermore, Weng *et al.* reported that Cu-doped SiO_2-CaO-SrO-P_2O_5 electrospun BG fibres induced in vitro tubule formation through the up-regulation of VEGF from HUVECs [645].

2.5.4.4 Zinc

Mechanism: Zinc promotes angiogenesis through its interplay with ROS, which is capable of sprouting angiogenic factors including FGF-2 and VEGF [63]. In addition, the interaction of Zn^{2+} and ROS had also been reported to induce the migration and proliferation of endothelial cells, as well as the formation of blood vessels [646]. Another report emphasized that Zn induced VEGF from osteoblast by enhancing the p44/p42 MAPK pathway [647]. ZnO is one of the common angiogenic agents. For example, ZnO nanoflowers have been reported to induce new vessel formation [648] and its incorporation in PCL electrospun dressing improved angiogenesis both in vitro and in vivo [63, 649, 650]. Zn-containing ointments have also been proved to promote blood vessel formation in vivo [651, 652]. However, contradictory views had been posed claiming that zinc also exhibited anti-angiogenesis properties [603]. Zinc was found to bind with and energize Endostatin, a potent angiogenesis inhibitor, and induced an anti-angiogenic activity [653]. Zinc was also reported to reversely modulate the expression of hypoxia indicating genes such as HIF-1 and HIF-2 [64]. Furthermore, zinc as a thiol-reactive metal would reduce the activities of NF-κB and AP-1, as well as the MMP proteins [654, 655]. In general, the role of Zn on angiogenesis remains uncertain.

BGs: In most cases, another element (such as Cu) was co-loaded with Zn in the BG, e.g. 0.34 mol% of CuO and 0.82 mol% ZnO in 1393-B3 BG nanofibres, which was later termed as 16-05, gave a sustained release of BO_3^-, Cu^{2+}, Zn^{2+} ions that stimulated better cell proliferation and migration, protein expressions, angiogenesis, and wound

healing in vitro and in vivo [91]. Chen *et al.* found that 16-05 fibres induced a much higher VEGF secretion in fibroblasts, compared to that of 13-93B3 fibres and 45S5 fibres, in dynamic tests with a flow rate of 1.0 mL h^{-1} [72]. In addition, when loaded in PDLLA scaffolds, 1 mol% of Zn and Cu co-loaded $60SiO_2$-$25CaO$-$11Na_2O$-$4P_2O_5$ BG exhibited much higher VEGF secretion than BGs with Cu incorporation only and control [656].

Alginate/chitosan hydrogels containing Zn-BG (58S containing 5 mol% ZnO) NPs (50-100 nm) provoked sprout angiogenesis in vivo in SD rats [552]. Much higher CD31 and α-SMA immunohistochemical signals were observed from hydrogel containing Zn-BG NPs compared to a positive control (gel with epidermal growth factor (EGF)), gel-only control, and empty control. Zn-BG NPs also had a synergistic effect with EGF to further promote additional angiogenesis.

2.5.4.5 Cobalt

Mechanism: Cobalt is another angiogenic agent that promotes blood vessel formation by generating a hypoxia-mimicking environment [273]. Co modulates the expression of HIF-1 and HIF-2 in a variety of cells, including BMSCs [272, 657-659], fibroblasts [660-662], and endothelial cells [663, 664], and induces an up-regulation of various hypoxia-responsive factors such as VEGF, FGF-2 and TGF-β [665]. Co-containing materials have been widely tested in angiogenesis in bone and cartilages [661, 665-668].

BGs: Various papers had indicated the potential of Co-containing silicate-based BG scaffolds in bone angiogenesis both in vitro and in vivo [669-673]. For example, 0.75 mol% of Co incorporation of both 45S5 and 2/10 mol% B_2O_3 containing 45S5 induced significantly higher VEGF secretion from MSCs, indicating its high potential for angiogenesis [671]. In addition, Co-containing $SiO_2 - CaO$ and $SiO_2 - CaO - SrO$ BGs stimulated higher VEGF secretion in HUVECs and neovessel formation on a defect of rabbit distal femur compared to their Co-free counterparts when seeded with human umbilical cord perivascular cells [673].

58S Co-BG (2.5 mol% CoO) stimulated a 2-fold increase in HIF-1α and a small but significant increase in VEGF from HUVECs and promoted tubule formation in vitro [674]. In vivo study on the skin of Wistar rats witnessed the promoted tissue infiltration and neovessel formation (vessels with VEGFA) and the HIF-1α stimulated by Co-BG in vivo was 3-4 times than that by 58S [672, 674].

While the abrupt release of Co^{2+} may hinder fibroblast proliferation, Co-BGs were initially proposed for angiogenesis in bone. Composites containing Co-BGs were proposed for wound angiogenesis. Collagen–glycosaminoglycan composites with 45S5 particles containing 4 mol% CoO (10 mg L^{-1} Co^{2+}) further promoted proliferation, migration, and in vitro tubule formation of HUVECs through increasing HIF-1α and VEGF [675]. Similar trends were found for PCL nanofibres with Co-BGs of $SiO_2 - CaO - Na_2O$ and $SiO_2 - MgO - K_2O - Na_2O$ systems (10 mg L^{-1} Co^{2+}) [676]. HIF-1α expressions in fibroblasts more than doubled when increasing the Co composition in BG from 0 to 2 mol% and from 2 to 5 mol%. Both 2 and 5 mol% of Co incorporation promoted a 5-fold increase in VEGF expression from fibroblasts than BG-free BGs, but increasing from 2 to 5 mol% did not make a significant difference.

2.5.4.6 Others

Other trace elements have been reported potential to stimulate angiogenesis in BG. Strontium is an element that is thought to produce an angiogenic effect, but mainly in the fields of bone regeneration [677-681]. The incorporation of Sr is expected to increase VEGF expression from endothelial cells [679, 680, 682], enhance migration of endothelial cells [680, 683, 684], and promote in vitro tubule formation [680, 683, 685]. 3D printed 58S MBGs containing 10 mol% SrO promoted blood vessel formation on critical-sized rat calvarial defects compared to Sr-free MBG [686]; the blood vessel area and blood vessel number in the group treated with Sr-MBG scaffolds were 24.67% and 73, compared to 16.33% and 38% for the Sr-free glass and 3.67% and 6 for the empty control group. When loaded in a gelatin scaffold, $SiO_2 - CaO - P_2O_5$ glass with 15 mol% SrO promoted more microvasculature development in rat calvarial defects than Sr-free BG [687]. The in vivo responses were supported by in vitro observations, for example, 13-93 BG NPs with 3.06 mol % Sr (30-35 nm) induced more than 10-fold VEGF expression from MSCs (at a concentration of 100 gcm^{-2}) compared to that of Sr-free BG [688]. Sr-BGs were also found to promote angiogenesis through their anti-inflammatory responses by stimulating the switch of macrophage to M2 phenotypes. 58S and 58S containing 10 mol% were investigated for their angiogenic effects on RAW macrophages and HUVECs [580]. The Sr-BG had better anti-inflammatory effects and promote higher angiogenic factor expressions from macrophages compared to Sr-free BG and the control. Sr-BG also stimulated higher angiogenin, FGF-2, and stromal cell-derived factor (SDF) expression in HUVECs. The paracrine angiogenic effect was further improved by incorporating this Sr-BG in the IFN-γ-doped PLGA scaffold, where the synergistic effect promoted higher angiogenesis in bone repair in vivo [689].

Lithium is involved in the activation of Wnt/β-catenin and inhibits glycogen synthase kinase (GSK)-3β signaling pathways, a pathway required for NF-κB suppression, TNF-induced activation of IκBα kinase, p44/p42 MAPK and Akt activation [690, 691]. Lithium also increases PAI-1 and MMP-1 levels in endothelial cells, which was relevant to IL-8 and Wnt/β-catenin levels [692, 693]. Both mechanisms contributed to an increased protein level of VEGF in Li-treated endothelial cells [694]. Sol-gel 45S5 containing 5 mol% Li_2O that was pre-incubated with M199 fibroblasts cells induced an enhancement to the proliferation and migration of HUVECs in comparison to those treated with M199 and M199+45S5 [695]. Similarly, the dissolution of a melt-derived Li-BG of the SiO_2-CaO-P_2O_5 system was reported to induce more endothelial cell proliferation and migration, remarkably higher than both Li-free BG extracts and control medium [696]. Li-BGs also induced up-regulation of HIF-1α expression and thus the up-regulation of VEGF, ANG-1, KDR, and PDGF of HUVECs and stimulate more blood vessel formation on SD rats in vivo. The resultant effects were mainly due to the Li^+ release from BG, as the LiCl which had the same Li^+ release as Li-BGs exhibited a similar level of proliferation and migration, in correspondence to previous literature [697]. In vitro endothelial tubule formation from Li-BGs was 2 times that of Li-free BGs [696] and similar to that from BG+LiCl and positive control (BG+FGF-2) [695]. The release of Li^+ ions are also not the only factor for the role of Li-BG in angiogenesis. With the presence of quercetin, an inhibitor of the Wnt/β-catenin canonical pathway, 92% of inhibition of proliferation occurred on LiCl treated cells while only 37% occurred on Li-BG treated cells [695]. One of the mechanisms could be due to the release of other therapeutic ions in BGs that stimulate protein expressions in other cells, such as MSCs [696].

Table 2. 6. BG glass system to angiogenic responses. (HUVEC: Human Umbilical Vein Endothelial Cells. EC: endothelial cells other than HUVECs, MSC: Mesenchymal stem cells, DPPSC: Dental Pulp Pluripotent-Like Stem Cell, CAM: Chorioallantoic membrane, AV loop: Arteriovenous loop)

Ion	Synthesis	Cell type	Assay	Ref.	Effect of angiogenic responses
Si-Ca	Melt-derived	Fibroblasts	Proliferation	[53]	Increased proliferation below 0.1-0.2 % w/v and significant inhibition beyond 0.2 % w/v
			VEGF	[53]	Increased expression with the increase of BG dose within the non-toxic range
			FGF-2	[54]	
		HUVECs	Proliferation	[54]	Increased proliferation with the increase of BG dose until 1% w/v
			Migration	[51]	Dilution-dependent enhancement of migration
			Tubule formation	[58]	Dose and composition-dependent numbers and circles formed

		MSCs	VEGF, HGF, PIGF, Angiogenin, Angiopoietin	[58]	Dose and composition-dependent pro-angiogenic factor secretion from MSCs
		DPPSCs	VEGF	[595]	Slight up-regulation of VEGF compared to BG-free cells
			vWF, FLK-1, CD31		Enhanced expression in BG treated cells compared to BG-free cells
	NPs	HUVECs	VEGF, FGF-2, and eNOS	[698]	Significant up-regulation of VEGF, FGF-2, and eNOS
			Proliferation, Tubule formation	[699]	HUVEC proliferation, in vitro tubule, and in vivo vessel formation in rat subcutaneous tissue
			Tubule formation	[700]	In vitro tubule formation and in vivo vessel formation
	Nanofibres	HUVECs	Proliferation, Migration, Tubule formation	[83, 597]	Increased proliferation, migration, and tubule formation in vitro and in vivo compared to the control and BG particles
		Fibroblasts	VEGF	[97]	Up-regulation of VEGF compared to BG-free cells
B	Melt-derived	HUVECs	Proliferation, Migration, VEGF, IGF, CX43, FGF-2, TGF-β, EGF, Tubule formation	[57]	BGs with slight B incorporation exhibited higher effects compared to control and silicate-based BGs, corresponding to the enhancement of increasing B concentration in media until the concentration reaches 10.8 $\mathrm{mg\,mL^{-1}}$.
				[68]	A novel BG induces a more sustained B release (20 $\mathrm{mg\,mL^{-1}}$) and lower pH exhibited a better effect compared to silicate-based BG and borate BG that release B up to 120 $\mathrm{mg\,mL^{-1}}$.
			Protein kinases, ERK phosphorylation	[57]	A strong dose-dependent increase of both signals contributes to HUVEC proliferation and migration respectively
		CAMs	Tubule formation	[618]	BGs with slight B incorporation induced a higher extent of tubule formation until B concentration in the medium reaches 1.62 $\mathrm{mg\,mL^{-1}}$
		MSCs	Proliferation	[622]	Dose-dependent proliferation as B position below 11.3 mol% induces proliferation while beyond 11.3 mol% exhibited inhibition.
			VEGF		Expression increases with the dose of BG within the non-toxic range
	Nanofibres	HUVECs	Proliferation, Migration, Tubule formation	[282, 620] [84]	Increased proliferation, migration, and tubule formation in vitro and in vivo compared to Si-based BG fibres.
P	Melt-derived	Fibroblasts	Proliferation	[626]	The effect of phosphate BG was not as strong as its capability in the fast release of ions
		Osteosarcoma cell	VEGF	[272]	Phosphate BG up-regulated slight VEGF, but much less than Co-loaded phosphate BG

		MC3T3-E1	VEGF	[487]	BG with 6.33 mol% P induced slight up-regulation, but much less than F containing BG
Cu	Melt-derived	ECs	Proliferation	[640]	1.6 $\mathrm{mg\,mL^{-1}}$ Cu-BG was non-toxic and 6.4 $\mathrm{mg\,mL^{-1}}$ Cu-BG was toxic
			Tubule formation	[640, 641]	No significant increases were observed, and the decreased effect occurred when the Cu-BG dose went beyond 1.6 $\mathrm{mg\,mL^{-1}}$
		MSCs	Proliferation	[656]	Decreased viability with the increase of Cu-BG dose
			VEGF	[641, 656]	Cu-BG exhibited higher VEGF expression compared to Cu-free BG, but decrease with the increase of Cu-BG dose
		CAM	Tubule formation	[641]	Cu-BG induced more tubule formation compared to Cu-free BGs
	MBG	AV loop	Tubule formation	[639]	Higher tubule formation induced by Cu-BG compared to Cu-free BG
		MSCs	Proliferation	[504]	Dose (extract dilution)-dependent on decreased cell viability, but controversial in its significance
			HIF-1α	[504]	Insignificant increase in HIF-1α expression but high dose (extract dilution)-dependent increase of relative HIF-1α
			VEGF	[504]	Significant dose (extract dilution)-dependent increase of protein expression but a significant dose-dependent decrease in protein expression beyond toxic doses.
			KDR, PDGFR-α, angiopoietin-1	[543]	A general increase in protein receptor-dependent on the level of extract dilution
		HUVECs	Migration Tubule formation	[543]	Increased migration and tubule formation of Cu-MBGs compared to Cu-BGs
		ECs	Proliferation, migration	[701]	Insignificant influence of Cu-MBGs on proliferation and migration compared to MBGs
		Zebrafish	Subintestinal vessels	[701]	Higher subintestinal vessels induced by Cu-MBGs compared to MBGs
	Nanofibres	Fibroblasts	VEGF, FGF-2, PDGF	[85, 644]	3 fold increase in VEGF, 8 fold increase in FGF-2, and 10 fold increase of PDGF from fibroblasts compared to Cu-free 1393-B3 fibres
		HUVECs	Proliferation, Migration, Tubule formation	[85, 645]	Increased proliferation, migration, and tubule formation in vitro and in vivo compared to Cu-based BG fibres.
Co	Melt derived	HUVECs	VEGF	[673, 675] [676]	Co-BG exhibited much higher VEGF release compared to Co-free BGs
			HIF-1α	[675] [676]	Increased HIF-1α expression with the incorporation of Co

			Tubule formation	[675]	Co-BG induced more tubule formation compared to Co-free BGs
		Osteosarcoma cell	Proliferation	[272]	No obvious influence on cell viability
			VEGF	[272]	Dose and composition-dependent effect of protein secretion
		MSCs	Proliferation	[671]	No obvious influence on cell viability
			VEGF	[671]	Co-BG exhibited higher and dose-dependent VEGF release compared to Co-free BGs
	MBG	MSCs	Viability	[702]	Decreased viability with the increase of Co composition in MBGs
			HIF-1α, VEGF	[702]	Increased expression with the increase of Co composition in MBGs
		HUVEC	Migration	[703]	Increased migration in Co-MBGs compared to Co-free MBGs
Zn	Sol-gel	MSCs	Proliferation	[656]	Decreased viability with the increase of Zn-BG dose
			VEGF	[656]	Zn-BG exhibited higher VEGF expression compared to Zn-free BG, but decrease with the increase of the Zn-BG dose
	Nanofibres	Fibroblasts	VEGF	[72, 91]	Zn-containing Cu-BG exhibited higher VEGF expression compared to Zn-free Cu-BG.
S	Sol-gel	HUVECs	Proliferation, HIF-1α, VEGF, KDR, eNOS	[681]	Dose-dependent effect of cell proliferation and protein secretion
	NPs	MSCs	VEGF	[688]	More than 10 folds of collagen type I and VEGF secretion
		HUVECs	Proliferation	[704]	Stimulate HUVEC proliferation
Li	Sol-gel	HUVECs	Proliferation, Migration, Tubule formation	[695]	Increased proliferation, migration, and tubule formation than Li-free BG, which is similar to the effect of Li+ ion of the same concentration as Li-BG dissolution product.
			IGF1, TGF-β	[695]	Increased protein up-regulation in Li-BG compared to Li-free BG
			VEGF	[695]	Only at high Li concentration up-regulated VEGF
	Melt-derived	ECs	Proliferation, Migration, Tubule formation	[696]	Increased proliferation, migration, and tubule formation than Li-free BG.
			Wnt/β-catenin, AKT, NF-κB pathways	[695]	Proof that Li+ is an important but not the only reason for the angiogenic effects of Li-BG
			HIF-1α, VEGF, ANG-1, KDR, PDGF	[696]	Li-BG induced higher protein expression compared to Li-free BG
Ga	Melt-derived Sol-gel	Osteosarcoma cells	Proliferation	[463]	Insignificant difference in cell viability against dose, composition, and synthesis
			VEGF	[463]	Decreased Ga^{3+} ion release with the

					increase of Ga composition leads to a decreased effect with an increase of Ga composition. Dose, composition, and synthesis approach dependent on up-regulation
F	Melt-derived	MC3T3-E1	Proliferation	[487]	Decreased cell viability with an increase of F composition in BG
			VEGF	[487]	Increased VEGF expression until F composition peak at 3-6 mol%, and then followed by decreased expression
Nb	Melt-derived	MSCs	VEGF	[705]	Dose and composition-dependent protein up-regulation
Rb	MBG	MSCs	HIF-1α, VEGF,	[516]	Increased VEGF expression with an increase in Rb composition

Niobium-releasing BG was also been reported to be angiogenic in vitro, for example, the dissolution products of 0.5 and 1.0 mol% Nb loaded 45S5 induced higher expressions of VEGF on fibroblasts at 0.01 % w/v compared to 45S5 and the control [705]. Rubidium was reported to induce hypoxia through the stimulation of HIF-1α [516]. Rb-containing MBGs were reported to induce higher expression of HIF-1α and thus higher expression of VEGF. The stimulative effect increases corresponding with the increase of rubidium composition in BG from 1 to 5 mol%. 55 mol% Ti containing SiO_2-CaO BG stimulated angiogenesis in vivo when incorporated in alginate hydrogels [706]. The number of blood vessels increased by 2-fold compared with BG-free hydrogel. Sol-gel-derived Au containing SiO_2-CaO-P_2O_5 BGs also promoted in vivo angiogenesis in dorsal scapular regeneration [707].

Some antibacterial ions can be inhibitory to angiogenesis. For example, Ga and V incorporation in 13-93 prevented in vivo angiogenesis [511]. Ga in both melt-derived and sol-gel-derived 70S30C led to a decrease in VEGF proliferation from MG-63 cells [463]. F-BGs were non-toxic when applied to MC3T3-E1 cells and stimulated VEGF secretion until the fluoride composition exceeded >9.3 mol% [708]. Beyond this concentration, a negative correlation occurred between cell viability and VEGF expression, and fluoride composition. 1393-B3 BG particles and 13-93 fibres containing ceria promoted angiogenesis in rat subcutaneous model in vivo [511, 709]. SiO_2-CaO-P_2O_5 BG containing 5mol% CeO_2 promoted in vitro migration and tubule formation of HUVECs and in vivo angiogenesis in diabetic rats [710]. In addition, Ag-BG nanofibre exhibited a stimulative effect on in vitro endothelial cell proliferation and migration at low doses [362]. But it was uncertain whether the angiogenic effect was due to F/Ag incorporation or common BG components such as Si or Ca.

To design ideal wound matrices that stimulate angiogenesis, it is important to ensure the release of therapeutic ions. Common angiogenic ions such as Cu, Zn, and B have been

more widely studied and their mechanism has been explored. For BG with other ions, it was sometimes uncertain whether the angiogenic effect was due to their incorporation or common BG components such as Si or Ca. Further investigations are needed to explore the mechanisms of new therapeutic ions.

2.5.5 Re-epithelialization

Epithelialization was commonly assessed through the proliferation and migration of epithelial cells, mainly keratinocytes. In wound healing, the extent of epithelialization can be assessed by the rate of wound closure. The first study of BG in re-epithelialization was in the gingival epithelium [711]. The efficacy of BGs in epithelial cell proliferation was assessed and compared with that of a bioabsorbable membrane. The baseline PCNA-proliferative index of the BG group and bioabsorbable membrane group was similar (13.20 and 11.64 respectively). But after 12 weeks of post-operation, the BG group induce a more significant increase in the index (28.76) compared to that of the bioabsorbable membrane group (18.36).

Mossvi *et al.* first investigated 45S5 powder on wound epithelialization [712]. A co-culture system was constructed using intestinal epithelial cell monolayers (Caco-2) and subepithelial fibroblasts CCD-18Co cells to mimic the healing environment. 45S5 induced an obvious epithelialization as the wound closure reached 600% when the BG dose was 0.1% w/v. Very little epithelial cell proliferation occurred, indicating that the re-epithelialization was achieved by migration and restitution of original epithelial cells. Yu *et al.* cultured human dermal fibroblasts on 45S5 dissolution products and found a significant increase in EGF secretions which indicated the potential of BG in re-epithelialization [55]. Furthermore, a skin graft synthesized from BG extracts and fibroblasts significantly improved the wound closure kinetics in vivo.

The release of calcium ions is the main cause of BGs in epithelialization. Various papers reported that Ca^{2+} regulates the growth and differentiation of epidermal cells and Ca^{2+} promoted [713-716]. The epidermis consists of a distinctive Ca^{2+} gradient where the basal layer has the lowest and the stratum granulosum had the highest. Ca^{2+} concentration as low as 2-4 mg L^{-1} started promoting keratinocyte proliferation and Ca^{2+} concentration at 50 mg L^{-1} induced keratinocyte differentiation [713]. Ca^{2+} levels were also key for loricrin, filaggrin, and involucrin, essential keratins that promote epithelialization [715] and involves in lamellar bodies (tubulovesicular secretory organelles of epithelial cells related to lysosomes) secretion responses [717]. Silicates were also reported to promote EGF expressions from keratinocytes [718, 719]. BG also stimulated connexin 43 [56], a protein

affecting gap junction intercellular communication between cells in wound healing processes to promote epithelialization [720]. Connexin 43 expressions were markedly increased in vitro in the BG treated HUVECs, and in vivo in a full-thickness wound model in rats. After 6 days of culture, the initial formation of a new epidermis was found underneath the eschar in BG treated wounds, whereas no new epidermis was formed in non-BG counterparts.

BGs also stimulated epithelialization through their interplay with macrophages. 45S5 stimulated anti-inflammatory effects and promoted the up-regulation of TGF-β in macrophages [51]. The paracrine effect enabled an accelerated wound closure in vivo on excision lesions in rats. Similarly, mice treated with BG (SiO_2-CaO-P_2O_5) containing alginate hydrogels had anti-inflammatory effects in vivo to promote wound closure [235]. It was further found that macrophages are necessary for re-epithelialization as much slower wound closure occurred in macrophage-depleted mice compared to normal mice. Moreover, BG could promote the barrier functional behaviours of keratinocytes to promote epithelialization [721]. Extracts of 58S BG promote keratinocyte differentiation through the formation of tight junctions, and intracellular adhesion complexes in the epidermis that control paracellular molecular permeability [722]. 58S extracts increased claudin-1 (a tight junction protein), altered the subcellular location of four major TJ proteins (claudin-1, occludin, JAM-A, and ZO-1), and increased the expressions of keratinocyte differentiation markers (K10 and involucrin) that eventually stimulated keratinocyte differentiation and migration.

Vaseline containing 45S5 and 58S BGs containing exhibited a faster wound closure compared to BG-free Vaseline in vivo on full-thickness wound rats and sol-gel 58S had better efficacy than melt-derived 58S than melt-derived 45S5 [723]. Fish-collagen submicron fibres (~0.5 μm) containing BG ($80SiO_2$-$15CaO$-$5P_2O_5$) stimulated in vitro epithelialization on human epidermal keratinocytes (HaCaTs) and in vivo wound closure capabilities [724]. Similarly, increased wound closure was observed for collagen and PCL fibrous scaffold containing BG-NPs (100 nm) [725] and BG containing agarose-alginate composite [590]. PDLLA electrospun membrane containing $70SiO_2$-$25CaO$-$5P_2O_5$ BG had 2-times the wound healing rate than the BG-free membrane in diabetic mice [594]. A novel injectable self-healing polypeptide-based 58S BG NPs (300 nm) containing F127--poly-L-lysine hydrogel led to a 94% reduction of the tumour cells and a 91.7% of wound closure was observed in vivo on mice with A375 tumour xenografts [726]. Recently, SiO_2-CaO-P_2O_5 based MBGs were mixed with quaternized chitosan to form a shape memory cryogel to induce faster wound closure in SD rats [727].

2.5.5.1 Boron

The incorporation of boron in the BG system promotes its re-epithelialization effects. For example, the percentage of wound area recovered when treated with 45S5 BGs containing 2 wt% borates was significantly higher (around a 2-fold increase) than that treated by pure 45S5 or with 45S5 with FGF-2 growth factors [57] because borate ions promoted keratinocyte activities and protein expressions for epithelialization. Borate salt was previously found to promote the migration of keratinocytes and exhibited a non-inhibitory effect on keratinocyte proliferation [728]. 100 mgL^{-1} boric acids were also found stimulative to a series of growth factors including G-CGF, GM-CGF, FGF-7, and TGF-β in HaCaT [65].

The role of 45S5 and $50.6B_2O_3 - 23.7CaO - 6.43Na_2O - 8.24MgO - 8.46K_2O - 2.57SrO$ BG in epithelialization was investigated in in vivo skin defects in rodent models [66]. The length of damaged tissues for those treated with borate-based BGs was 1 mm after 21 days of surgery while those of 45S5 and the control were around 2 mm. 13-93B3 BG fibre mat also induced a higher wound closure rate than 45S5 mats and the control in vivo on the SD rat model [84].

2.5.5.2 Copper

Cu promotes keratinocyte migration through the modulation of keratinocyte integrins including α_3, α_6, α_v, and β_2 [729]. They also increase the proliferating cell nuclear antigen (PCNA) and p63 positivity in cells [730]. Cu-based SOD regulates genes in keratinocytes to sprout keratinocyte proliferation and migration [731-733]. The paracrine effect of anti-inflammation stimulated expressions of EGF and IGF [734].

Cu-BG fibres exhibit an ECM-mimic structure and thereby promote the migration of epithelial cells and wound closure [85, 91, 644]. For example, 0.82 mol% Cu-doped 1393-B3 glass microfibres (0.4-1.2 μm) also induced a 10-fold increase in PDGF expression compared to Cu-free BGs [85]. The resultant BGs significantly accelerated wound closure in vivo in the rodent model compared to Cu-free BGs and the control. A similar effect was found on Cu-BG microfibres (229-457 nm) in vitro on tubule formation of HUVECs [645].

Cu-BGs were more commonly loaded to scaffolds or hydrogels in promoting wound closure in vivo [643]. For example, Cu-containing SiO_2-CaO-P_2O_5 BG nanocoating (40-50 nm thickness) promoted diabetic wound closure and epithelialization compared to Cu-free BGs nanocoating in PEGDA-alginate hydrogel [735]. Eggshell membrane coated with Cu-

BGs ($75SiO_2$-$(25-x)CaO$-$xCuO$-$5P_2O_5$ (x=2, and 5)) stimulated faster wound closure in C57BJ/6 mice compared to that coated with Cu-free BGs and uncoated BGs [643]. Cu-containing 1393-B2 also co-functioned with Vitamine E in PLGA scaffolds to promote wound closure in full-thickness in SD rats [736].

2.5.5.3 Zinc

Like Cu, Zn also up-regulates α_3, α_6, α_v, and β_2 integrins in keratinocytes [729, 737] and its SOD regulates genes to promote keratinocyte proliferation and migration [731-733]. Besides, Zn transporters such as ZIP2 and ZIP10 proteins, promoted keratinocyte differentiation [738, 739]. Zn-BG has been reported to induce the proliferation of keratinocytes [740, 741]. Aagren *et al.* proved the enhancement of re-epithelialization by application of 1.4 wt% zinc oxide to wound dressing [275]. Wound healing was improved by 33% in 64 hours when the dressing is gauze and by 76% when the dressing is a collagen sponge. Zinc was also reported to be associated with the increased release of EGF and IGF in porcine wounds, which indicates its potential for wound closure [742].

5 mol% Zn-58S BG NPs (50-100 nm) containing chitosan-alginate hydrogels induced faster wound closure compared to those with Zn-free BGs in SD rats [552]. Recent studies tend to incorporate Zn in Cu-BGs for enhanced wound healing capabilities but made it more difficult to determine the exact effect of Zn on the epithelialization of BGs. 1605 BG fibres, or Mirragen, incorporated 0.34 mol% of ZnO and 0.82mol% CuO in 1393-B3 for increased wound closure effect [72, 91]. Ma *et al.* also co-loaded ZnO and CuO in chitosan-gelatin nanofibres to promote wound closure in G/C-xBG rats [743].

2.5.5.4 Others

Ag-containing borate-based ($60B_2O_3$-$36CaO$-$(4-x)P_2O_5$-xAg_2O) BG promoted the proliferation and migration of HaCaTs [744]. Migration increased with the increase of Ag composition from 0 to 0.5 mol% and decreased beyond 0.5 mol%. Recently, there have also been several studies on PCL fibres with silicate or borate-based BGs with different ion incorporation, such as Co, Mg, Sr, and Zn, which were also potential for promoting wound closure in vivo [745-747].

BGs also had a synergistic effect with some therapeutic molecules. For example, the synergistic effect of SiO_2-CaO BG and desferrioxamine induced the fastest wound closure rate in hydrogel when applied to the diabetic wound splinting model than BG or desferrioxamine alone [748]. SiO_2-CaO-P_2O_5 BG and exosomes derived from MSCs were

loaded to decellularized small intestinal submucosa and significantly improved diabetic wound healing in mice [749].

2.5.6 Extracellular matrix deposition

The ionic products of BGs were reported to induce higher expressions of collagen type I from fibroblasts compared to that of other bioceramics such as biphasic calcium phosphate [750]. BG was also reported to induce the secretion of MMP1, a protein marker indicating ECM deposition, from MSCs [751]. Besides, many had revealed the potential of BG in collagen deposition, but most of these researches focused on the proliferation of collagen in bone [686, 752-755]. Recent studies also elaborated on the role of BG in collagen formation by chondrocytes, where the 13-93B3 glass was reported to be stimulative to collagen type II formation both in vitro and in vivo [756]. Furthermore, significant formations of Collagen type II and Collagen type X were observed when Li-BG was applied to chondrocytes while no significant increase was observed in collagen type I [757]. In addition, it was further explained that the resultant BG up-regulated TGF-β was the necessity in the formation of collagen fibre and the on-going chondrogenesis.

The ions released from BG, such as SiO_4^{4-} and Ca^{2+} stimulated collagen and fibronectin production for ECM formation in the skin. 45S5 BG in PGA mesh promoted collagen deposition on soft tissues both in vitro and in vivo [53]. 45S5 dissolution products also significantly induced the migration of HDF when co-cultured with macrophages [51]. The co-culture system significantly induced the expression of elastin, collagen I, and fibronectin from HDF. Similar results were found on dilutions of 45S5 dissolution products on fibroblast migration, collagen deposition, and fibronectin deposition, and in vivo assessment further proved a significant proliferation of fibroblasts as well as an increased collagen I deposition in the ECM of a full-thickness wound model on nude mice [55]. Another research proposed that BG could improve the secretion of tenascin-C, another common protein involved during ECM remodeling [758]. On the contrary, down-regulation of collagen type I, collagen type III, and fibronectin were observed in $90SiO_2$-$6CaO$-$4P_2O_5$ BGs [758]. Myofibroblast differentiation along with proteins and molecules involved (TGF-β receptor I and Smad2) were also down-regulated. This can be due to the lack of adhesion of sol-gel BGs to ECM proteins [759].

In vivo analysis commonly determine the deposition of ECM proteins through H&E/Masson Trichrome staining, and some also done immunohistochemistry on particular proteins such as collagen type 1 or fibronectin. An abundant ECM deposition was observed in various systems containing BGs compared to those without, including Vaseline [723], fish collagen

fibre mats [724], peptide-based hydrogel [726], quaternized chitosan-based shape-memory cryogel [727], and agarose-alginate hydrogel [590], etc. but in general, few papers presented the enhanced ECM deposition in quantification. 58S NPs (100 nm) induced attachment and proliferation of endothelial cells and up-regulated Col-1 and α-SMA expressions in a collagen-PCL nanofibre system and promoted ECM deposition in vivo [725]. Similarly, 70SiO_2-25CaO-5P_2O_5 BG in a patterned PDLLA electrospun membrane promoted a 3-fold increase in collagen type 1 and collagen type 3 expressions in diabetic wound model of mice than BG-free PDLLA [594].

2.5.6.1 Boron

Boric acid and sodium pentaborate stimulated the deposition of laminin and fibronectin, two ECM proteins, from fibroblasts [65]. Borate-based BGs high potential in promoting ECM deposition owning to their fast dissolution and release of therapeutic ions [45, 46, 238]. In bone regeneration, borate/borosilicate BGs with a non-cytotoxic B release outplayed silicate-based BGs in collagen deposition [68, 622, 760-762]. Borate-based fibres exhibited an ECM-mimic structure which provides pathways for the migration and deposition of ECM proteins [84, 308]. More collagen was deposited in the 1393-B3 BG treated group compared to the 45S5-treated group and both were significantly higher than the control. Similarly, $50.6B_2O_3 - 23.7CaO - 6.43Na_2O - 8.24MgO - 8.46K_2O - 2.57SrO$ induced a higher level of collagen deposition in skin defects of rodent models than 45S5, which was 2 times that in the control group, in correspondence to its high fibronectin and collagen expressions in vitro on 3T3-L1 cells [66]. Nanosized HCA-coating of the resultant borate BGs induced a further improvement in ECM deposition both in vitro and in vivo.

2.5.6.2 Copper

Cu functions in connective tissue through its binding with the enzyme lysyl oxidase, which lyse down certain lysine and hydroxylysine residues into peptidyl aldehydes which center in the crosslinks of collagen and elastin [763, 764]. Deficiency in Cu down-regulated the collagen synthesis in bone [765, 766]. Besides, all Cu concentration >0.06 mg L^{-1} stabilized fibronectins [767, 768].

Cu containing fibres had structural cues that promote the attachment of ECM proteins, for example, Masson trichrome staining revealed that 0.82 mol% Cu containing 1393-B3 fibres promoted higher collagen deposition and better arrangement in SD rat skin [85]. Cu-BGs were also found to stimulate more collagen deposition and arrangement in vivo in PEGDA-alginate hydrogel [735], on eggshell membranes [643], and on PLLA dressings.

All the above-mentioned studies were not quantified, but the histology studies revealed a dense and more aligned ECM compared to the group treated with Cu-free BGs and the control.

2.5.6.3 Zinc

Zn induces a structural reorganization of the gelatin binding domain of fibronectin, which interrupted the alignment of both fibronectin and collagen in ECM, as collagen assembly is integrated with fibronectin polymerization [769]. Zn also reduces the degradation of collagen through anti-inflammatory behaviour [770] and induces collagen synthesis in bone cells [771]. Some studies reported that Zn also has a negative effect on ECM matrices [772] as Zn induces protease expressions such as collagenase and elastase [773], but in general, zinc inhibits MMP activity and prevents ECM degradation caused by protease [274].

5 mol% Zn-containing 58S BG NPs (50-100 nm) also induced more collagen deposition than those with Zn-free BGs in SD rats when doped in chitosan-alginate hydrogel [552]. Besides, Mirragen, a BG product with a 1605 composition (0.82 mol% of Cu and 0.34 mol% of Zn doped in 1393-B3) was commercially successful in ECM deposition when treating diabetic ulcers [72, 91].

2.5.6.4 Others

Strontium incorporation also significantly increases the capability of BG in the synthesis of collagen. Many pieces of evidence have been drawn from the success of Sr-BG in the stimulation of collagen I deposition in bone [686, 755, 774-776]. In soft tissues, SrO modified silicate and phosphate BGs were reported to stimulate collagen deposition from human gingival fibroblasts [626]. Furthermore, Sr-MBG has been reported to induce a significant amount of collagen deposition without being cytotoxic in L929 fibroblast [777].

The synergistic effect of BG and other molecules also stimulated ECM deposition in vivo. For example, SiO_2-CaO BG and desferrioxamine promoted higher collagen type I and type III deposition when loaded in alginate hydrogel [748]. SiO_2-CaO-P_2O_5 BG and exosomes derived from MSCs also exhibited higher collagen type I and type III depositions in diabetic wound healing in mice when loaded to decellularized small intestinal submucosa [749].

2.5.7 Summary

BGs have invaluable potential in the stimulation of hemostasis, inflammation, and proliferation in the wound healing process. The effect could be due to the release of therapeutic ions during BG dissolution. Ca^{2+} is the most important ion in hemostasis, as it involves in the coagulation pathways promotes the hierarchical behaviour in hemostasis from vascular contraction to platelet aggregation and then to fibrin clotting [354]. The highest clotting rate is acquired when Si: Ca ratio = 2.5 [47, 358]. Ga^{3+} also stimulates a series of hemostatic activities, but its composition in glass shall be minimized (< 1 mol%, or Ga^{3+} release < 0.1 mg L^{-1}) to prevent cytotoxicity [48].

SiO_4^{4-} and Ca^{2+} release from BGs has anti-microbial effects on a broad spectrum of microorganisms [49, 50, 377]. Borate or borosilicate BGs also release antibacterial BO_3^{3-} groups, but their efficacies can be insignificant compared with silicate BGs until BO_3^{3-} reaches a yet unknown critical level [454]. Heavy metal ions bind with thiol groups of bacteria, de-energizing its metabolic activities, and inducing ROS and protease secretion to digest microorganisms. Ag^{+} is the strongest anti-microbial ion but its cytotoxicity appears at 2 mg L^{-1} [399, 778, 779], so the composition of Ag in the BG system and the doses of Ag-BGs are usually low (~1 mol% and ~ 1mg mL^{-1}, respectively). Cu and Zn can substitute the function of Ag in anti-microbial activities without inducing strong cytotoxicity. Some reports stated that the anti-microbial effects of Cu and Zn grew proportionally until their concentrations reached 50 mg L^{-1}, but since Cu and Zn also trigger anti-inflammatory effect and angiogenic effect, the ideal concentration of both ions is < 10 mg L^{-1} [780-783], and their ideal compositions in BG depends on the BG dissolution kinetics (< 5 mol% for BG microparticles and scaffolds, and ~ 1 mol% for BG fibres, BG NPs, and MBGs). Ga^{3+} and $Ce^{3+/4+}$ also, induce antimicrobial activities but their compositions should be < 1 mol% for BGs of all different BG structures, as they significantly reduced the dissolution kinetics of BG so that the increase of their compositions in the BG system beyond 1 mol% may reduce their ion release [460, 465, 511]. In terms of anti-inflammation, the release of SiO_4^{4-} stimulates the expression of superoxide dismutase and anti-inflammatory cytokines to promote anti-inflammatory effects in wounds. The incorporation of Cu (5 mol%, Cu^{2+} = 4 mg L^{-1} dependent on the BG dose) in BG further enhances the anti-inflammatory effect because Cu relieves oxidative stress and removes ROS to prevent inflammation [543, 544]. 5 mol% of Zn incorporation also stimulates the switch of macrophage phenotype from M1 to M2 due to its down-regulation of ROS, anti-inflammatory cytokines, MMPs, and NADPH enzyme [61, 62, 551].

In the proliferation phases, SiO_4^{4-} ions stimulate angiogenesis through the up-regulation and stabilization of HIF-1α in endothelial cells, thereby promoting the angiogenic factor

expressions from endothelial cells [602-604]. Ca^{2+} also stimulates angiogenesis through promoting the expressions of angiogenic factors and their binding with corresponding receptors [605-609]. Boron incorporation in BG further promotes angiogenesis within the ideal range of BO_3^-, 45-60 mg L^{-1}[57, 617]. Cu and Co are two common metallic ions in the BG system that promote angiogenesis through the up-regulation of HIF-1α expressions in fibroblasts and endothelial cells [269, 271, 633, 660-664]. The ideal composition of Cu in the BG system is ~5 mol%, as Cu^{2+} is needed for the range of 7-12 mg L^{-1} in BG system [640, 641, 645], and 0.1-0.2 mg L^{-1} in Cu-BG containing composites [643, 735, 784]. Co is needed for the range of ~10 mg L^{-1} for angiogenesis and its common composition in BG is 1-5 mol%, dependent on the BG morphology [675, 676]. The role of Zn^{2+}, Li^{+}, Mg^{2+}, and Sr^{2+} has also been reported to stimulate the proliferation, migration, and protein expression of endothelial cells and thus the formation of new blood vessels in vitro and in vivo, but further analysis is required to understand the ideal dose of these ions [552]. Ion release from BGs was also stimulative to re-epithelialization (wound closure) and ECM deposition, [712]. SiO_4^{4-} and Ca^{2+} promoted EGF expressions in fibroblasts [55], and the deposition of collagen, elastin, and fibronectin from fibroblasts [51, 55]. The incorporation of other therapeutic ions, such as BO_3^-, Zn^{2+} and Cu^{2+} could further improve the above-mentioned effect, but their therapeutic concentrations or compositions remain unknown.

Research into the cellular response to BGs and their dissolution products has confirmed their potential in promoting wound regeneration and many reports have proved BGs' capabilities in individual steps of wound healing both in vitro and in vivo. From existing publications, it can be deducted that the ideal BG composition for wound healing may be based on Si, B, and Ca, where (Si+B): Ca ratio (mol%) equals 2.5 and B composition not to induce a BO_3^- release > 50 mg L^{-1}. Cu and Zn can be incorporated by up to 5 mol% for improved anti-microbial, anti-inflammatory, and angiogenic effects, but their exact compositions will be dependent on the morphology and degradation kinetics of the BG. Other therapeutic ions, such as Co, Li, Mg, Sr, Ce, or Ag, can be incorporated for a particular use, but the ideal compositions of these ions are yet to be determined according to the physical and chemical structures of BG. Besides, since few articles incorporate more than 3 therapeutic ions in BG, the influence of one therapeutic ion on the release kinetics and biological activities of other ions remains unknown. Future efforts are needed in this field in order to design the best BG composition for wound healing. Efforts are also required to break through the limitation in the application of BGs to commercialized products. For instance, sol-gel-derived BGs need to have a higher yield and lower cost of the ingredients, while the control of morphology, composition, and level of mineralization are required for

melt-derived BGs. It also takes longer for the approval of glass products, especially those with ions that were reported to be cytotoxic (e.g. Co or F) even though they exhibit no toxic effect in ionic form.

In this study, a sol-gel approach was used to synthesize bioactive glass nanofibres although the melt-quenching approach was faster and more cost-efficient. The sol-gel BGs in general are more reactive due to the mesoporous generated during the synthesis. It also has a better composition control (no Na and K are required) and less likelihood to generate crystallization (low-temperature stabilization). The sol-gel electrospinning process in particular generates long and homogeneous nanofibres (100-200 nm, length: width >1000:1) while the melt-blowing approach generates short and nonhomogeneous microfibres (1-4 μm, length: width ~100:1, 75% of the remaining become beads).

The objectives for this thesis are to:

1. Synthesize and characterize Zn-containing BG fibre mats to deliver therapeutic zinc ions for burn regeneration and characterize their ability to stimulate angiogenesis and ECM deposition
2. Develop 3D ECM-mimic borosilicate BG fibre mats as strategies for the regeneration of diabetic ulcers and understand the correlation between therapeutic ion concentration and angiogenic behaviour
3. Access borosilicate bioactive glass fibre mats on mice diabetic wound models and understand the mechanism of both boron incorporation and fibre structure to individual steps in the healing cascade.

3. Characterization Techniques

3.1 Physical analysis

Scanning electron microscopy (SEM) consists of an electron source, condenser lens, apertures, electron acceleration coils, objective lens, sample stages, and electron collectors. SEM characterizes the morphology and topography of specimens' surfaces. Electron beams are concentrated towards the samples through the condenser and the objective lens and secondary ions are excited due to the bombarding of the primary electron beam. Secondary ions are reflected from the target samples and collected to produce images. Backscattered electrons are primary electrons that are reflected by the nucleus in the samples. X-rays are energy released by the excitation and de-excitation of ions. Both contribute to the characterization of the topographical composition of the samples. One of the most widely used technique within the SEM machine is the Energy Dispersive X-Ray Spectrometer (EDX), which characterize the topographical elemental distribution through the X-ray diffraction pattern.

SEM samples should either be conductive or coated with a conductive layer. They also need to be fixed to the platform, otherwise, fibres can detach from the fibre mats and float around the vacuum chamber. So, BG fibres were attached to conductive carbon tape before being coated with chromium. Another challenge is to ensure their flatness while obtaining images that indicate the 3D fibre entwining structures. Rough samples cause blurry or imbalanced brightness or even bad coatings which makes the image quality even worse. Several experiments were needed to find the ideal fibre mat thickness and ideal coating thickness for optimal image quality.

3.2 Chemical analysis

3.2.1 X-ray Diffraction

X-ray diffraction (XRD) is a widely used technique in characterizing the crystallinity of materials. Electrons generated from a hot filament are bombarded towards a material, commonly copper, to generate monochromatic X-ray (usually Cu K-α). Incident X-rays are reflected by the atomic planes within the crystalline structure of the material. The reflected X-rays constructively or destructively interact with each other and generate a pattern at different angles and intensities. The reflection follows the Bragg's Law ($n\lambda = 2dsin\theta$),

where *n* is an integer, λ is the wavelength of the incident X-rays, 2θ is the range of reflections angles and *d* is the spacing of the crystalline structure. The spacing between planes are then matched with the unit cell parameters of different materials at different phase to understand what material, what phase and which plane do individual peak on the XRD pattern stands for.

BG is generally an amorphous material, in which there are no crystallinity and the spacings between planes have a wide distribution. This induces a wide distribution of peaks, which is termed the 'amorphous halo'. In order to find signs of crystallinity in the BG system, sample noises need to be reduced, the scanning time needs to be increased and the number of steps should also be increased.

3.2.2 Fourier transform infrared spectroscopy

Fourier transform infrared (FTIR) spectroscopy is a technique that characterizes the types of bonding in materials. The activities of the bonds, including vibration, stretching, etc., correspond to the energy of infrared of different wavelengths. When beams of infrared with wavelengths of 600 to 4000 cm^{-1} are directed at the samples, infrared absorption occurs at certain frequencies, resulting in an FTIR spectrum. The major bands of Si-O-Si, Si-O-B, and B-O-B reside within 600 to 1400 cm^{-1}, and the area of interest predominantly lies in the 600 to 2000 cm^{-1} region. The peak positions and their representation are described in the later sections.

3.2.3 Inductively coupled plasma atomic emission spectroscopy (ICP-AES)

Inductively coupled plasma atomic emission spectroscopy (ICP-AES) is a technique that characterizes the elemental concentration of a solution. A plasma igniter produces plasma through the ionization of argon gas and the p solution is nebulized above the plasma torch which excites the particles to higher energy states. The de-excitation process involves the emission of waves that were recorded by the optical emission spectrometer as 'counts'. A normalized curve correlates the 'counts' to the elemental concentration in solutions.

The common dissolution products are tris(hydroxymethyl)aminomethane buffer solution (TRIS) or Dulbecco's Modified Eagle Medium (DMEM). During the dissolution studies of the BG fibres, the dissolution products are usually diluted by 5-10 times, as the ideal concentration range lies from 1 $\mathrm{mg\,L^{-1}}$ to 50 $\mathrm{mg\,L^{-1}}$. The dissolution profiles of BGs will

indicate potential cytotoxicity or biological activities when compared with previous research.

3.3 In vitro analysis

3.3.1 CCK-8 assay

CCK-8 assay characterizes cell viability by determining metabolic activities. When incubating the CCK-8 solution with the cells for 2 h, the appearance of orange color indicates the metabolic active cells. The color intensity is characterized under an enzyme-linked immunoabsorbent assay microplate reader (Synergy 2, Bio-TEK) at the absorbance of 450 nm.

There is a general agreement that the increase in metabolic activities indicates increased cell viability and also indicates the proliferation of the cells. But the quantification of cell proliferation requires the total DNA assay. In the total DNA assay, cells are lysed by cycling freezing and defrosting and the exposed DNA is stained with dyes (e.g. Hoechst dye) and then characterized through the plate reader.

3.3.2 ELISA assay

ELISA assay is used to measure the concentration of proteins in the supernatant from cell cultures. The kit is comprised of a 96-well plate with monoclonal antibodies pre-coated onto the base of each well. Proteins from samples, standards, or the controls bind with the antibodies (Figure 3.1). When the remaining supernatant is removed, a secondary antibody (enzyme-labeled antibody) that binds with the measured proteins is added to the wells attached by the measuring protein. After the secondary antibody is removed and washed, a dye that binds with the labeled enzyme is added to characterize the protein concentration by measuring the intensity of the sample and the standards.

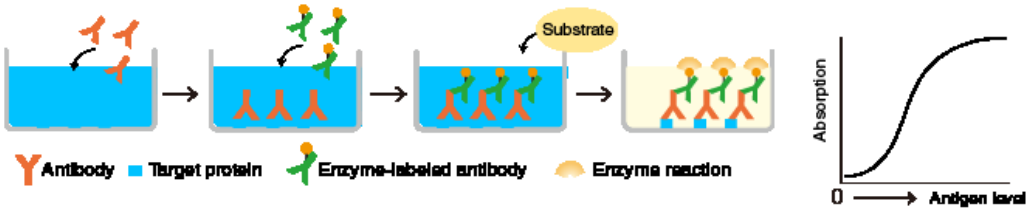


Figure 3. 1. Schematic of the ELISA process. Adapted from MBL life of Science website (https://ruo.mbl.co.jp/bio/e/support/method/elisa.html)

3.3.3 Transwell assay

Transwell assay measures the migration rate of cells. The Transwell consists of the upper compartment and the lower compartment. Cell culture media are added to both compartments and the upper compartment is filled with cells till confluence. The cells could only migrate through the permeable membrane down to the lower compartment. After a certain period (16 hours in this study), the permeable membranes are removed and washed and all cells stuck in between the membranes are labeled with crystal violet. The reason why the cells in the membranes are counted instead of cells at the lower compartment is that cells at the lower compartment may not attach to the well and could be washed away during the washing or the addition of the dye. Then, images are taken and cells are counted.

3.4 In vivo analysis

3.4.1 Diabetic wound model

The animal studies were conducted at Northeastern University, Shenyang, China. Prof. Huiling Gao held the animal license and took charge of the surgery and animal sacrifice. All animal protocols were approved by the Ethical Committee of Northeastern University. C57BL/6J mice (5-6 weeks old, male) were purchased from the Huafukang Animal Center (Beijing, China) and fed for another 2 weeks on a high-fat diet. 48 mice were separated in 16 cages (3 per cage) and were tested for 4 samples at 2-time points (n=6 per group per time point). The nurturing of the animal follows the regulation of animal welfare.

The diabetic wound model is generated based on previous literature [785-787]. Streptozotocin (STZ) or alloxan are the only two drugs that induced diabetes [788, 789]. Recently, STZ is becoming a more popular drug compared to alloxan, as alloxan causes general toxicity and has a narrow diabetogenic dose [790-792]. The common solvent for STZ is 0.1 M citrate buffer (sodium citrate), with a pH of 4.5 [785, 788, 789, 793]. The injection is dependent on the mice type and weight, commonly ranging from 45-70 mg/kg. In general, the diabetic type II model was created by intraperitoneally injecting STZ (Sigma-Aldrich, 50 mg kg^{-1}) to the mice for 7 days. The blood glucose levels were taken from all mice 1 week after injection. All mice had a blood glucose level maintained at 12-15 mmol/L which indicates they are diabetic. Then, a circular full-thickness skin wound was cast on each mouse to mimic the diabetic ulcer. The wound sites were then implanted with 100 mg of the samples accordingly and covered with a transparent dressing

(Tegaderm, 3M) (the control group was only covered with Tegaderm), as the dressing prevents the BG samples loss due to mice movement. The details of the experimental methods are summarized in Chapter 6.

3.4.2 Histology analysis

Hematoxylin and eosin (H&E) staining is the most widely used staining for histology. Hematoxylin stains the nucleus of cells into dark blue color, while eosin stains the extracellular matrix pink and blood vessels as red. The coloration of the staining indicates the distribution of cells, blood vessels, and the ECM in tissues. The epidermis layer consists of blocks of basal cells and keratinocytes so it has the highest cell density. The nuclei of the macrophages are round while that of fibroblasts are elongated, due to the morphology of cells.

Masson Trichrome staining is commonly used to study collagen arrangement and deposition. The three colors are induced by Weigert's iron hematoxylin, Ponceau (red), and Aniline Blue. Cell nuclei are purple as it combines the coloring from all three solutions. The epidermis layer, muscle, and blood vessels are red, while the collagen fibrils are blue. Glacial acid is used to wash the sample after the Ponceau and Aniline Blue stage to differentiate the coloration. On some occasions, green or light green stains are used instead of Aniline Blue.

For histological analysis, the removed skin tissues were fixed in 4% paraformaldehyde for 48 h, embedded in paraffin, and cut into 7 μm sections. The sections were then dewaxed and washed before conducting histological staining. Both H&E and Masson Trichrome staining follows the manufacturer’s instruction. For H&E staining, hematoxylin was dropped to each slice for 1 min. Then, the color of hematoxylin was differentiated from purple to pure blue before being washed under running water for 30 min. Finally, the slices were immersed in Eosin for 20 s before being dehydrated in 90%, 95%, and 100% alcohol and xylene. For Masson Trichrome staining, the slices are incubated with Bouin’s solution overnight. Weigert's hematoxylin was used to stain the nucleus for 2 mins before being differentiated by a combined solution of HCl and ethanol. After being washed, the samples were then immersed in Ponceau Red, Phosphomolybdic acid, and Aniline Blue consecutively, with a 1 min washing with 2% Glacial acid between each stage. The stained sample was dehydrated with a similar approach as the H&E staining.

3.4.3 Immunohistochemistry

Immunohistochemistry (IHC) is a process to study the distribution and quantity of a particular protein or receptor. The process includes antigen retrieval, blocking, the addition of primary and secondary antibodies, addition of Horseradish peroxidase, visualization in DAB, and counterstaining with hematoxylin, as detailed in Figure 3. 2. Antigen retrieval for samples fixed in formalin usually requires heat, an acidic environment, and/or protease. In this study, the samples were boiled in citrate buffer solution (pH = 6) and then cultured with 3% H_2O_2. Though antibodies have preferential avidity for specific antigens, they may also bind with non-specific proteins with binding sites similar to that of the target antigen, leading to a high background staining. Blocking of the samples with a buffer solution deactivates endogenous enzymes or biotin in the site of non-specific proteins, which bind with either the primary or secondary antibodies. 10% BSA in PBS is used in this study as the blocking solution.

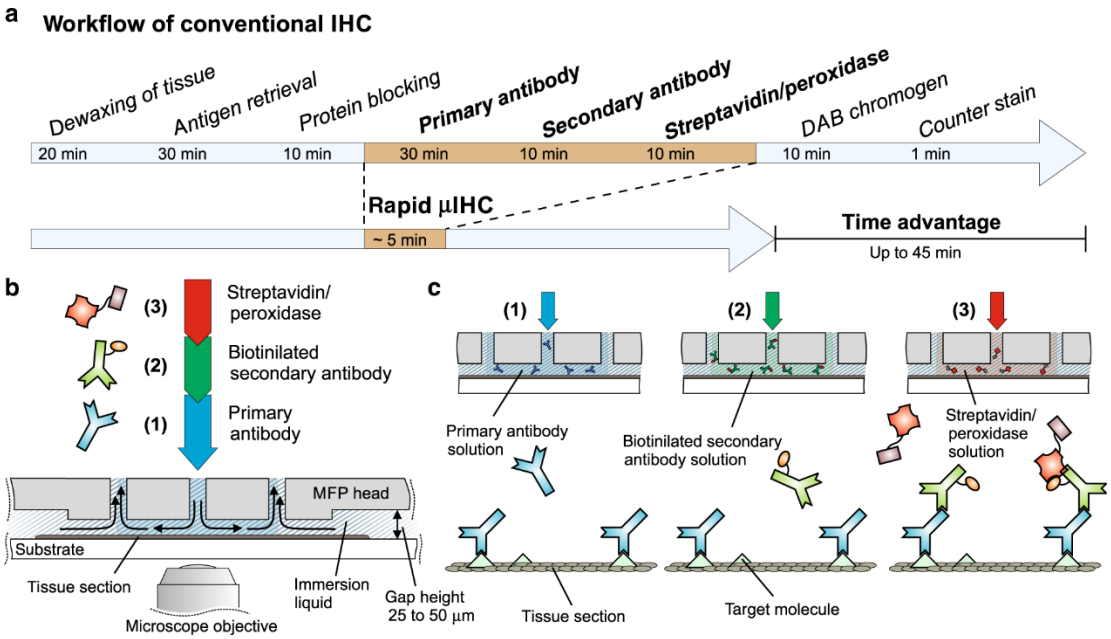


Figure 3. 2. Schematic of a general process of immunohistochemistry staining. Adapted from [794]. (The timing described in the process may vary between protocols).

Primary antibodies can be monoclonal or polyclonal. Monoclonal antibodies respond to a single epitope, antigenic determinant, of the target protein while polyclonal antibodies respond to multiple epitopes. The primary antibodies bind with the target antigen at one end and have enzymes at the other end that bind with the secondary antibodies. The secondary antibody is usually an Immunoglobulin G (IgG) based antibody, which has a high affinity to receptors and enzymes and low affinity with each other and has an end

group for fluorescent labeling (quite similar to that of the ELISA process (Figure 3.1). In some cases, the ‘direct’ method is applied in which the labeling solution is added immediately after the samples are incubated with primary antibodies. In this case, these primary antibodies have a labeling end, but this strategy is much less frequent. Horseradish peroxidase is a common enzyme for labeling and responds with 3,3′-Diaminobenzidine (DAB) to induce a brown color on target proteins. Counterstained hematoxylin enables the visualization of cell nuclei in order to have a better understanding of the distribution of target proteins.

In general, immunohistochemical analysis was performed on CD31 (Abcam), VEGF (Abcam), and α-SMA (Abcam). The dewaxing and washing sessions are similar to that in histology analysis. The slices were then fixed using citrate buffer solution (pH = 6) for 30 min, and then cultured using 3% H_2O_2 for 10 min to retrieve the proteins. Blocking the samples with 10% BSA in PBS for 1 h quenches endogenous biotins or enzymes. The above-mentioned primary antibodies were diluted according to the manufacturer’s instruction and applied to incubate the sections overnight at 4 °C. Then, the sections were further incubated with goat anti-rabbit antibodies and Horseradish Peroxidase for labeling (1.5 h and 40 min respectively). The sections were further visualized using DAB staining (10 min) and the nucleus was highlighted through counterstaining with hematoxylin, as previously described.

4. Zinc-ion-delivery bioactive glass fibre mat for burn regeneration

4.1 Introduction

In this Chapter, the aim was to synthesize 3D ECM-mimicking Zn-containing BG fibre mats to deliver therapeutic zinc ions for burn regeneration and determine their ability to stimulate angiogenesis and ECM deposition through investigating fibroblast cell response in vitro. The first objective was to produce fibres that were based on the 70 mol% SiO_2-(30-x) mol% CaO- x mol% ZnO composition, where x=0, 1, 3, and 5, labeled as 70S30C, 70S29C1Zn, 70S27C3Zn, and 70S25C5Zn respectively. The compositional system was selected based on previous literature that reported 70S30C system stimulates higher VEGF expressions from fibroblasts [98-101]. Zinc was chosen as it stimulates paracrine effects from macrophages and fibroblasts to express angiogenic factors [63, 64], promote endothelial cell activities [795, 796], and stimulate vessel formation in vivo [651, 652]. Zn also induces antibacterial effects through stimulation of reactive oxygen species (ROS) and protease expressions and it interrupts bacterial membrane activities through thiol-group binding [59, 60]; involves Zn-transporter mRNA during inflammation, reducing hydroxyl radicals, stimulating superoxide dismutase expressions, and up-regulating anti-inflammatory cytokines [61, 62]; and promotes the regeneration of follicles [649, 797, 798].

Parameters for electrospinning and the sol-gel synthesis were controlled with the aim of fabricating the Zn-containing BG fibre mats with 3D ECM-mimic structures, in which the fibre mats had a large thickness (0.5-2 mm) and fibres had diameters similar to those of collagen and fibronectin fibrils in the ECM. A second objective was to determine whether the release of ions was within a non-cytotoxic and therapeutic range by investigating the dissolution of the fibre mats in TRIS buffer solution and DMEM.

Fibroblasts are the main cells that populate the wound area and generate a broad spectrum of growth factors for wound closure and angiogenesis [12, 80, 81, 110]. The third objective was to assess the cell viability of Human Dermal Fibroblasts (HDF), one of the most representative types of fibroblasts, when cultured with the dissolution products of the fibre and to understand the effect of the fibre mats on ECM deposition by measuring the levels of PDGF and TGF-β expressed from HDFs. To understand the function of the fibre mats to angiogenesis, the levels of VEGF, bFGF, and HIF-α expressed by HDFs were measured. Endothelial cells are the cells that migrate to form blood vessels. The viability

and migration of HUVECs were characterized in media conditioned with HDF cells cultured with the dissolution products BG fibres, and their relative protein expressions, in order to understand whether the BG dissolution products stimulate the activities of endothelial cells and whether this correlates with the protein expression profiles from both fibroblast and endothelial cells.

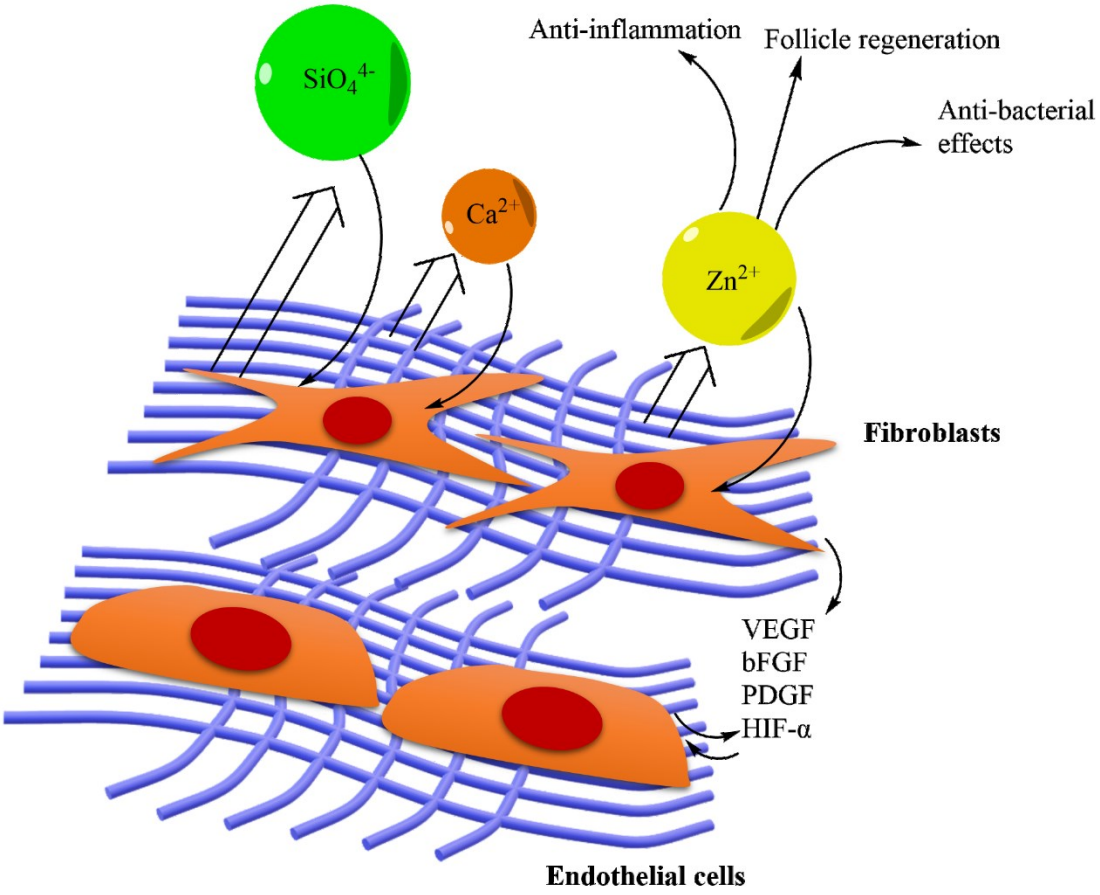


Figure 4. 1. Schematic of zinc-ion-delivering bioactive glass fibre mats as potential burn regeneration matrices

4.2 Methods

4.2.1 Preparation of sol-gel electrospun Zn-BG fibre mats

The sol-gel electrospinning process was applied to synthesize ECM-mimicking BG fibre mats. [283] Tetraethyl orthosilicate (TEOS) and calcium nitrate tetrahydrate ($Ca(NO_3)_2$•$4H_2O$ (g)) were obtained from Sigma Aldrich while zinc nitrate hexahydrate ($Zn(NO_3)_2$•$6H_2O$ (g)) were obtained from Thermofisher. The sol-gel precursors of the Zn-BG fibre mats were prepared through the step-wise addition of TEOS, $Ca(NO_3)_2$•$4H_2O$ (g),

$Zn(NO_3)_2$•$6H_2O$ (g) to a mixture of ethanol, water, and 2 M nitric acid, as illustrated in Table 4. 1 [97, 286]. After being stirred at room temperature for 24 h and then rested for 48 h, the precursor was mixed with a polyvinyl butyral (PVB) binder to acquire the ideal viscosity (0.069 Pa.s) for electrospinning [96]. The viscosity of the sol for fibre mat production was chosen to be 0.069 ± 0.025 Pa.s, as Norris *et al.* found that a viscosity below 0.05 Pa.s resulted in electrospraying of the sol, producing nanoparticles, and a viscosity greater than 0.6 Pa.s halted electrospinning jet formation [97]. Viscosity control was achieved by adding a PVB binder to the sol-gel precursor, which does not incorporate into the BG structure and is burnt out during glass sintering, leaving thin mesoporous BG fibres. The ratio of PVB powder and ethanol in the PVB binder has been previously assessed by Norris *et al.*, who found that increasing the ratio from 1 g/mol (1 g/11.4ml) to 2 g/mol did not significantly influence the viscosity of the binder and therefore did not affect the viscosity when combining with the sol-gel precursor. Therefore, during the synthesis of Zn-containing BG fibres, the ratio of the binder was set as 1 g/mol.

The initial parameter electrospinning parameters followed that proposed by Norris *et al.*, but it was not reproducible at first. The most possible explanation was the difference in the electrospinning environment. The ventilation in the fume hood hugely affected the electrospinning process. The air flow in the fume hood was so strong that it exerted a strong force perpendicular to the jet propagation orientation. If the fume hood was fully closed, the flow reached a maximum so that hardly any fibres landed in the collector. Even at the lowest flow possible, many formed fibres were blown away which made the process much less efficient. It was not possible to obstruct the ventilation of the fume hood as the evaporating solvent would enter the laboratory.

The first idea was to reduce the working distance. This could make the interruption of the air flow less. But, at a fixed voltage, reducing the working distance means the increasing electric potential, so that more solution would be extruded from the spinneret, which can block the needle. Even though the voltage was adjusted correspondingly, the shorter the working distance meant less time for the thinning and solidification of the gel stream so no solid fibre was formed on the collector. Previous literature also reported a general trend of the increase of fibre diameter with the decrease in working distance [313, 316, 799]. Generally, if the working distance reaches a certain minimum level so that near-field electrospinning occurs, the solution never solidifies during propagation and there are usually approaches to guide their patternings, such as the use of a rotating drum or the combining near-field electrospinning with 3D printing [800, 801]. Our collector has a concaved boxed-like shape and the electrode was attached at the back of the box while the aluminum foil for collecting the fibres was at the front. The furthest point of the foil

(edge of the aluminum foil) was around 4 cm away from the electrode plane, while the lowest point of the foil was around 1 cm. Although the reason remains unknown, reducing the distance caused fibre aggregating at the edge instead of the center point. In this case, a very thin layer of fibre was formed, and then the aggregation of fibres at the edges occurred, which usually resulted in blocking.

The second strategy was to use a wind cover on the electrospinning apparatus. A plastic, transparent box was purchased to cover the whole machine, but there were still a few fibres being directed to the collector while most of them were attached to the edge of the box, or the surface of the syringe thruster. A possible explanation of this effect can be that the box was not conductive so it cannot ground the charges. The local charge aggregation was what causes the deviation of the jet.

The last idea was to adjust manually according to the air flow direction and the deviated jet track. Theoretically, this approach may cause the disruption of the electric potential, as the electrodes are not parallel with each other, but has an angle of around 30 degrees. Surprisingly, this was yet to result in a successful fibre collection.

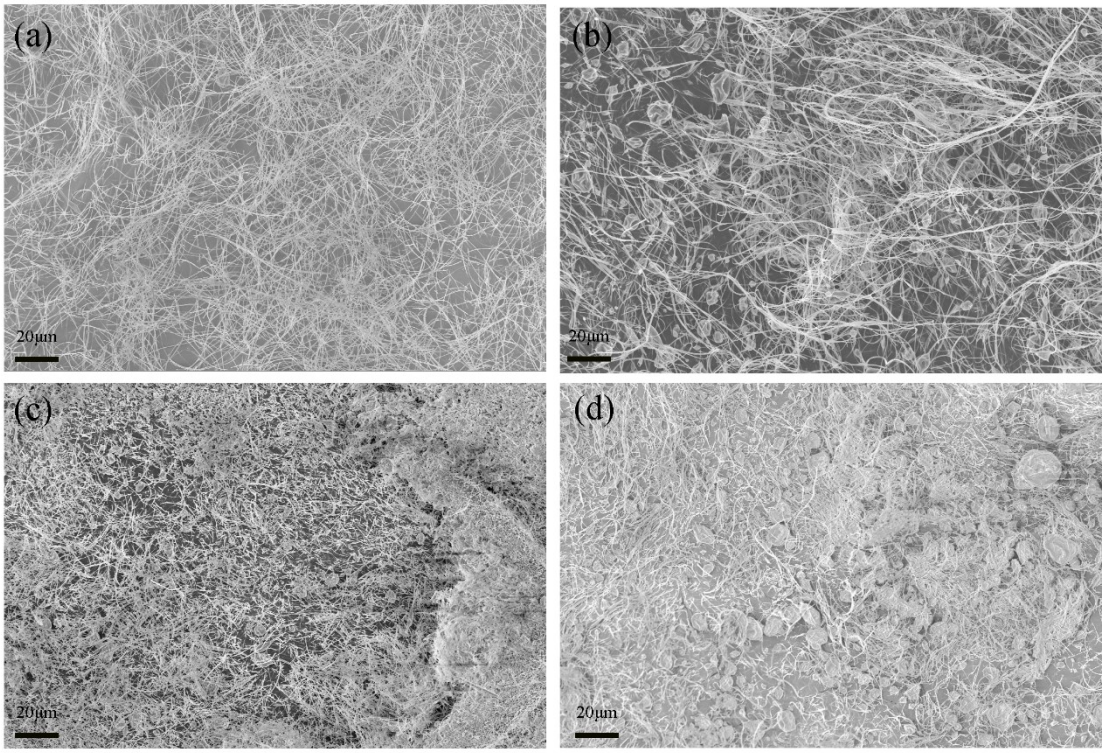


Figure 4. 2. SEM images of the 70S27C3Zn fibre mats synthesized under humidity of (a) 24-26%, (b) 35-37%, (c) 42-45%, and (d) 51-55%.

Even though the ventilation issue was solved, the 3D electrospun fibre was still not being synthesized. The main problem was the effect of humidity, which significantly changes the morphology of the fibre. Previous studies by Norris found that a 2D fibre mat was induced at 27% relative humidity, while 35-55% of the humidity induced 3D fibre mats. Relative humidity of 65% also induced a cotton-wool-like structure, but fibre morphologies were non-uniform in length and diameter with the presence of beads in the fibres [96, 97]. But, this study found that fibres prepared under 25-35% relative humidity were long, thin, and homogeneous (Figure 4. 2 (a)), but those prepared under a relative humidity above 35% are short-branched, thick, and non-uniform (Figure 4. 2 (b, c)), with an increased yield of beads corresponding to the increase in humidity, which disagree with the previous investigations. What was also different was that the lowest the humidity, the better fibre mat morphology it produces, and the thicker is the fibre mat. Beyond 45%, high levels of beading occurred (Figure 4. 2 (d)).

In addition, under high humidity, instead of fibre mat formation, the fibres entwined with each other to form several single strands. This may be because the water molecules in the atmosphere can be charge carriers and makes fibres have more affinities with each other rather than that towards the collector. The existence of ventilation and higher voltage potential makes the ‘stranding’ of fibres even worse.

Other parameters were also investigated while the electrospinning apparatus has been displaced and the humidity influence was re-evaluated. Voltages are adjusted from 6 kV to 18 kV to find the optimal working electric potential. 6 kV was not enough to overcome the surface tension of the solvent. 8 kV yielded 2D fibre mats rather than 3D ones, probably because the electric potential was not enough to stimulate the branching effect between electrospinning jets. 10 kV was selected to be the ideal voltage between the needle and the collector. Higher voltage (>12 kV) could be theoretically more ideal if working at a longer working distance but it yielded thicker BG fibres as more solution was extruded from the spinneret. More importantly, the electrospinning machine was exposed to the ventilation of the fume hood and ambient humidity, so that higher electric potential results in higher free charges in the atmosphere causing deviation of the track of the jet. At a voltage > 14 kV, the free charges became so high that the fibres were not only located on the collector but also on other conductive surfaces.

To find the ideal working distance, BG fibres were electrospun within a spinning range from 8 cm to 20 cm, while 12 cm was chosen as the ideal parameter. Due to the concave shape of the collector, the working distance is determined as the distance between the spinneret to the center point of the aluminum foil. Shorter working distances are not feasible as described in previous sections. The longer the working distance, the longer time for the drying and bending instability. Most electrospinning apparatus has a working distance of around 15 cm [313] because it ensures the occurrence of the secondary bending instability during jet propagation and can very likely induce the third bending instability, which makes the resultant fibres even thinner and longer. However, longer working distances also mean higher chances of deviation of the electrospinning track. If the working distance is beyond 12 cm, the deviation will be so high that it is not even able to collect fibres. The efficiency would also be greatly reduced.

In general, once the gelling was complete, the solution was loaded into a 10 mL syringe with a gauge 22 stainless steel needle. The electrospinning parameters were: electric field strength: 10 kV; flow rate: 0.4 mL h^{-1}; air gap distance: 12 cm; relative humidity: 25%-35%; inner diameter of spinneret: 0.7 mm; room temperature. Then, the resultant fibre mats were heated to 600 °C at a rate of 1 °C min^{-1} with a dwell at 600 °C for 3 h before oven cooling. The sintering process agrees with that of Norris *et al.* and other protocols in sintering silicate-based sol-gel BGs.

Table 4. 1. Sol-gel compositions 70 SiO_2-30-x CaO-x ZnO, in mol% (x = 0,1,3,5) and the quantities of TEOS, nitric acid, ethanol, calcium nitrate tetrahydrate, and zinc nitrate hexahydrate used.

Nominal compositions [oxide mol%]	TEOS [mL]	2 M Nitric acid [mL]	Ethanol [mL]	$Ca(NO_3)_2$• $4H_2O$ [g]	$Zn(NO_3)_2$• $6H_2O$ [g]
70Si-30Ca	15.6	4.2	8	7.12	0
70Si-29Ca-1Zn	15.6	4.2	8	6.84	0.3
70Si-27Ca-3Zn	15.6	4.2	8	6.37	0.9
70Si-25Ca-5Zn	15.6	4.2	8	5.9	1.49

4.2.2 Preparation and characterization of Zn-BG fibre mats

X-ray diffraction (XRD) patterns of the fibre mats were collected from an XRD analyzer (Bruker D2 PHASER) using Cu-Kα radiation (λ = 1.542 Å), with the following parameters: applied voltage: 30 kV; applied current: 10 mA; scanning interval: 10° < 2θ < 70°; step size: 0.035°; time per step: 12 s. Attenuated total reflectance-Fourier transform infrared spectroscopy (ATR-FTIR Nicolet iS10) was used to assess the chemical functional groups in the BG fibre mats under the wavelength of 500–4000 cm^{-1}. The microstructures of the

fibre mats were characterized under the Inlens mode of the LEO-1525 SEM, with 5 kV accelerating voltage and 8 mm working distance. The diameters of the fibres were measured with ImageJ and the average diameters were derived from 10 measurements.

4.2.3 Dissolution study

50 mg of the BG fibre mats were immersed in 75 mL of 5 mM TRIS buffer solution or Dulbecco's Modified Eagle Medium (DMEM) and placed in an incubator shaker at 37 °C and 120 rpm, according to the previously proposed standard protocol [97, 802]. 1 mL of the extracts were collected at each time point (4, 24, 48, 72, 96, and 168 h for TRIS and 4, 24, 72, and 168 h for DMEM), filtered with a 0.2 μm surfactant-free cellulose acetate syringe filters (Corning, USA) and diluted with 9 mL of 1 M nitric acid. The dissolution profile was achieved using an ICP-AES at the wavelengths of 317.9 nm (Ca), 251.6 nm (Si), and 213.8 nm (Zn). The pH change of the media was measured at each time point with a pH meter (Oakton pH 11 m with Oakton general-purpose glass pH probe, Ag/AgCl electrode, and Oakton ATC probe).

4.2.4 In vitro study on fibroblasts and endothelial cells

HDF cell lines were seeded in 96-well plates at a density of 1×10^3 cells cm^{-2} and cultured with 100 μL of DMEM supplemented with 10% (v/v) fetal bovine serum and 1% penicillin/streptomycin (FBS, Thermo Trace Ltd., Melbourne, Australia) for 24 h. BG condition media was prepared by dissolving BG fibres in DMEM for 1 day and the dissolution products were filtered and sterilized before being fed to cells. The supplemented DMEM was then replaced with DMEM conditioned by the BG scaffolds so it contained their dissolution products (6 mg mL^{-1} in supplemented DMEM). The conditioned media was also used diluted with more DMEM (1/2 and 1/4 respectively). HDF cells cultured with supplemented DMEM only were used as the blank control group.

The metabolic activity of fibroblasts was determined on days 1, 3, and 7 through a Cell Counting Kit (CCK)-8 assay (Beyotime) according to the manufacturer's instruction. The metabolic activity was represented as units of optical density (OD) absorbance at 450 nm from an enzyme-linked immunoabsorbent assay microplate reader (Synergy 2, Bio-TEK). The supernatants of the HDFs were extracted on day 3 for the characterization of VEGF, bFGF, PDGF, TGF-β, and HIF-1α through an Elisa assay (Beyotime).

HUVECs were seeded in 96-well plates at a density of 3×10^3 cells cm^{-2} and cultured with the endothelial cell culture medium (Sciencell, USA) with 5% (v/v) fetal bovine serum (FBS,

Thermo Trace Ltd., Melbourne, Australia) and 1% (v/v) endothelial cell growth supplement/heparin kit (ECGS/H, Promocell) for 24 h. HDFs were cultured in BG-conditioned media (6 mg mL^{-1} in supplemented DMEM) for 2 days and the resultant media (BG-HDF conditioned media) was mixed with the endothelial cell culture medium by 1:1. 100 µL of the BG-HDF conditioned media was applied to HUVECs. The metabolic activity (MA) of HUVECs was assessed through the CCK-8 assay and the expressions of VEGF, bFGF, HIF-1α, and eNOS were determined through the ELISA assay on day 3.

The migration of the HUVECs was assessed through a Transwell assay. HUVECs were seeded in the upper layer of the Transwell plate at 3×10^3 cells per well and cultured to confluency. Then, 250 µL of the BG-HDF conditioned media was added to the top layer of the well, while 300 µL of endothelial cell medium was added to the bottom layer. The cells were cultured for 16 h and stained with crystal violet for 1 min. The migrated cells were imaged using an optical microscope (Leica) and counted by a cell counter (bitbucket), according to the manufacturer's instruction [803].

4.2.5 Statistical analysis

The statistical significance of the results was compared using a one-way ANOVA test followed by Dunn's Multiple Comparison. The ANOVA is used comparison among groups with one or two independent variable, given that the data follows a normal distribution. On the other hand, the non-parametric Krustal Wallis test was used instead of parametric ANOVA in asymmetric comparion. The significance was taken between individual component in the in vitro assessment and marked as (*P <0.05, **P<0.01, ***P <0.001,****P <0.0001).

4.3 Results and Discussion

4.3.1 Morphology of 3D ECM-mimic fibre mats

According to Figure 4. 3 (a), the BG fibres entwine and generate a 3D fibre mat. It had a cotton-wool-like structure and had thickness higher than 1 cm. Ideally, this structure can be larger if working at a longer working distance and with no ventilation. This is because when the fibre mat is beyond 1 cm in thickness, the electric attraction at the surface of the fibre mat is lower than that of other conductive surfaces, such as the metal substrate of the syringe thruster. The 3D morphology of the fibres was induced through the branching effect of the electrospun jet, caused by the repulsion of the Ca^{2+} and Zn^{2+} ions. Humidity

may also have an impact on forming 3D structures. 3D fibre mats formed under 35% humidity could be faster than those formed under 25% humidity, but this also came with beads formation.

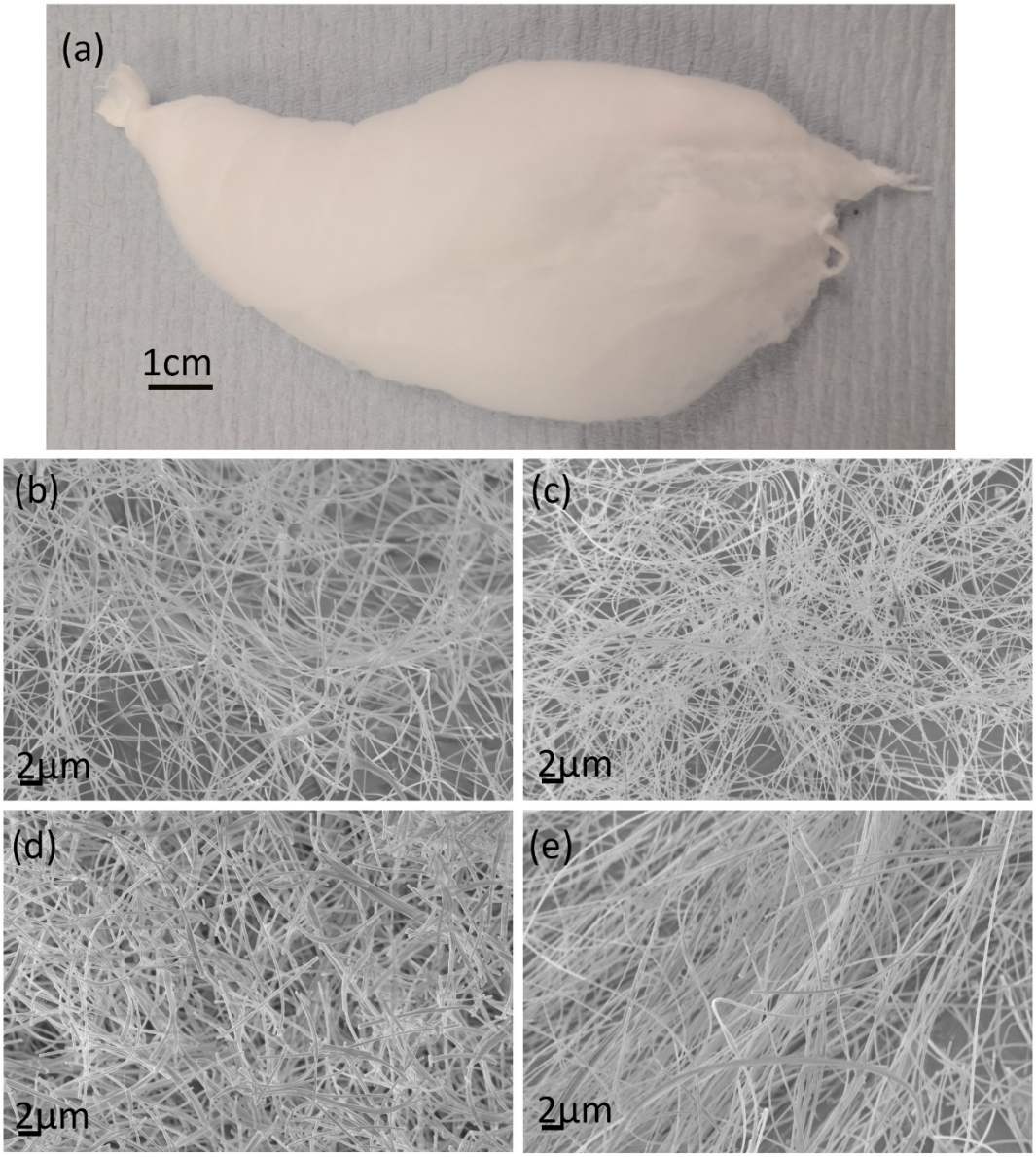


Figure 4. 3. (a) Photograph of an electrospun fibrous bioactive glass scaffold; SEM images of the fibre mats with composition 70 SiO_2-30-x CaO-x ZnO, in mol% where x = (b) 0 ; (c) 1 ; (d) 3 ; and (e) 5.

Table 4. 2. Fibre diameters of the electrospun bioactive glass scaffolds.

Sample	Fibre diameter (µm)
70S30C	0.32±0.07
70S29C1Zn	0.19±0.05
70S27C3Zn	0.23±0.05
70S25C5Zn	0.24±0.05

SEM images (Figure 4. 3 (b-d)) present the microstructure of the fibre mat. The fibres were long, thin, and entangled into an ECM-mimic structure. The diameters of the fibre mats are summarized in Table 4. 2. All BG fibres had a thickness ranging from 160-320 nm, which mimicked the collagen and fibronectin fibrils in the extracellular matrix. The incorporation of zinc did not interrupt the morphology and thickness of the fibres.

4.3.2 Chemical structure of 3D ECM-mimic fibre mats

XRD was used to characterize the crystallinity of materials. BGs are expected to be fully amorphous but calcium silicates, such as Wollastonite, or zinc oxide are the most likely crystal phases that might form in Zn-containing BGs. These crystals correspond to peaks at 29°, 32°, 34°, 37°, and 48° in XRD patterns [97, 804]. All XRD patterns (Figure 4. 4) for BG fibre mats presented amorphous silica halos with wide SiO_2 halos in the range of 20°-34° (2θ). The halo is at low intensity and has no obvious crystal peaks, similar to patterns obtained from mesoporous Zn-containing mesoporous BG powders or scaffolds [805-807]. The incorporation of Zn hardly changed the amorphous state of BGs, as the composition of Zn is little.

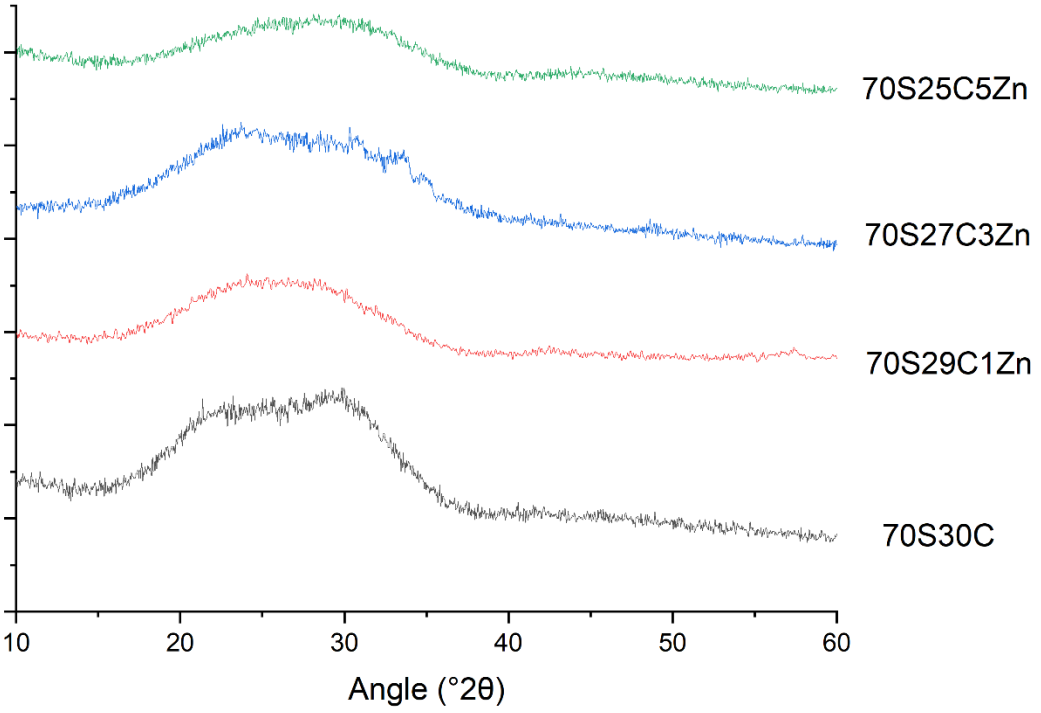


Figure 4. 4. XRD patterns of the as-produced 70S30C, 70S29C1Zn, 70S27C3Zn, and 70S25C5Zn bioactive glass scaffolds.

FTIR (Figure 4. 5) analyzed the bonding presented in BG fibre mats with different Zn compositions. Bands at 1040 and 790 cm^{-1} correspond to the Si-O stretching and the Si-

OH peak, respectively. Bands at 470 cm^{-1} were identified as Si-O-Si rocking vibrations [252, 284, 808], while that at 485 cm^{-1} represents the vibration of Zn-O bonding [809]. No bands presented at 1500, 1420, 1638, and 1300–1500 cm^{-1} indicated no unreacted CO_3^{2-} groups, NO_3^- groups, water, or ethanol remaining in the fibre mats. The incorporation of Zn also hardly affects the types of bonding in the BG system.

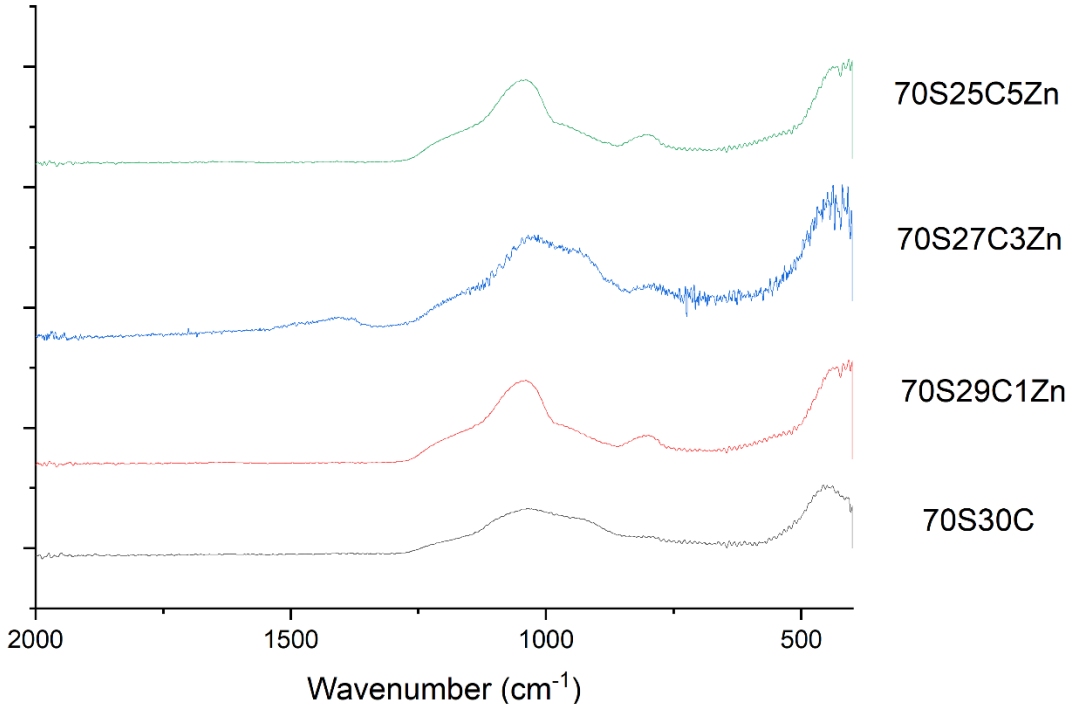


Figure 4. 5. FTIR spectra of the as-produced 70S30C, 70S29C1Zn, 70S27C3Zn, and 70S25C5Zn bioactive glass scaffolds.

4.3.3 Dissolution profiles

While being implanted into the body, the BG samples degrade while releasing therapeutic ions for wound healing activities. The dissolution profiles of Zn^{2+}, Ca^{2+}, and Si (expected to be in the form of SiO_4^{4-}) from BG fibre mats were assessed in both TRIS and DMEM. After 7 days of immersion, the cotton-wool-like fibre structure became shorter-branched fibre pellets, but still with the entwining structure (Figure 4. 6). To understand the possible wound healing activity of the fibre mats, the release of Zn^{2+}, Ca^{2+}, and Si (expected to be in the form of SiO_4^{4-}) upon soaking in TRIS buffer solution for 7 days was measured (Figure 4. 7). A high proportion of Ca^{2+} and Si was released after 24 hours of immersion in TRIS. The concentration of Si released from all fibre mats was similar but the Zn-containing fibre mats released less Ca^{2+}. This can be due to less Ca content (Zn replaced Ca in the composition) but also because Zn^{2+} ions reduce Ca^{2+} ion release kinetics, like that proposed by Aina *et al.* [99], as zinc can take the role of network intermediate.

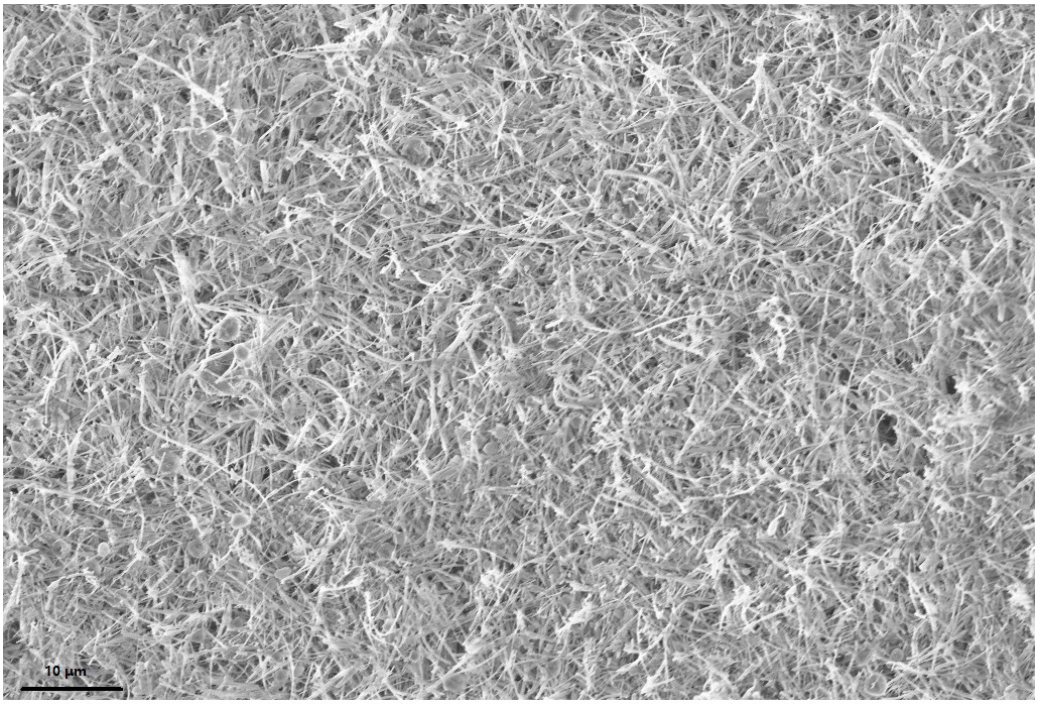


Figure 4. 6. SEM images of the morphology of 70S27C3Zn fibre after being immersed in DMEM for 7 days.

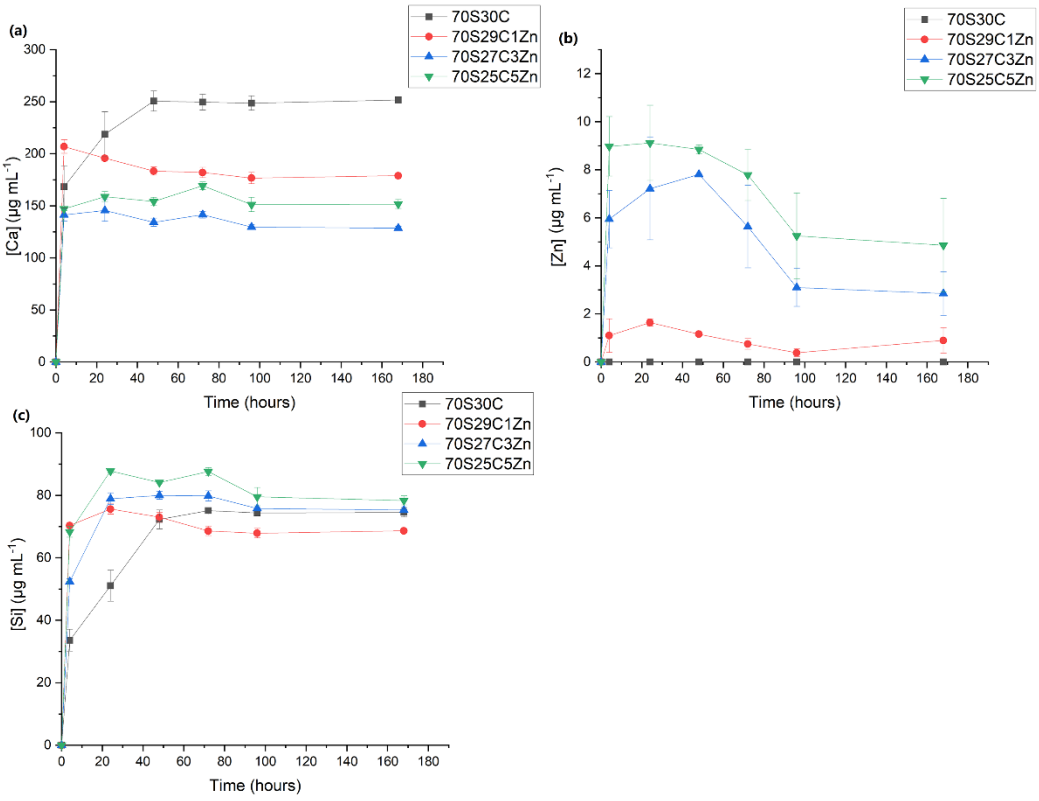


Figure 4. 7. Elemental concentration profiles (ICP) of TRIS buffer following immersion of bioactive glass fibre mats 70S30C, 70S29C1Zn, 70S27C3Zn, and 70S25C5Zn over 7 d (a) Ca, (b) Zn, and (c) Si.

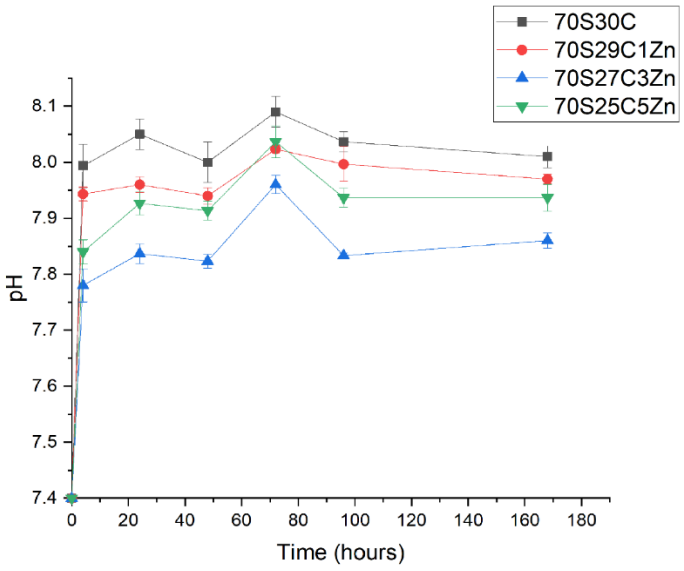


Figure 4. 8. pH change of TRIS buffer following immersion of bioactive glass fibre mats 70S30C, 70S29C1Zn, 70S27C3Zn, and 70S25C5Zn over 7 d (a) Ca, (b) Zn, and (c) Si.

The pH change during BG dissolution followed a similar pattern to the Ca^{2+} release (Figure 4. 8) [284, 810], indicating the ion exchange between the BG fibre mats and H^+ from the ion-rich media. The dissolution study was conducted in a static environment so that the degradation of BGs supports a continuous release of ions and while the ion concentration reached the saturation point, reprecipitation of ions occurred as an equilibrium process. This also explains why SiO_4^{4-} and Ca^{2+} levels stayed constant beyond day 3. The release of Zn^{2+} in TRIS experienced an abrupt peak by day 2 and then decreased, stabilizing by day 4. The decrease of Zn^{2+} might be because of the reprecipitation of the ions. While the supplies for SiO_4^{4-} and Ca^{2+} are excessive, the supply for Zn^{2+} is limited and the majority of Zn is incorporated in the precipitation by day 3. The Zn^{2+} ion levels after 168 h of immersion in TRIS increased as the Zn content in the glass composition increased.

In DMEM, the Si release was similar to that in TRIS, but the Ca^{2+} release was much less (Figure 4. 9). 70S30C fibres still released more Ca^{2+} compared to fibres with Zn in their composition. By day 7, the Ca^{2+} concentration reached approximately 60 μg mL^{-1}, which was similar to the Ca^{2+} concentration reported to be beneficial for fibroblast proliferation (56-64 μg mL^{-1}) [811]. BGs containing Zn still exhibited lower Ca^{2+} release and pH, but the difference was not as significant as it was in TRIS (Figure 4. 10). Interestingly, the Zn^{2+} release increased from 0.5 to 4.5 μg mL^{-1} at day 7 in DMEM and did not increase linearly with the increase of Zn content in BGs , which agrees with the dissolution profiles in TRIS and the observations of Neščáková *et al.* [807]. This is because Zn^{2+} can take the role of network intermediate in the silica network, meaning that ion exchange of Zn^{2+} increases

exponentially with the increase of Zn content in glasses. Keeping the Zn^{2+} release below 7 μg mL^{-1} is likely to prevent cytotoxicity, as Paasche *et al.* found that 7.41 μg mL^{-1} of Zn^{2+} was toxic to fibroblasts [783].

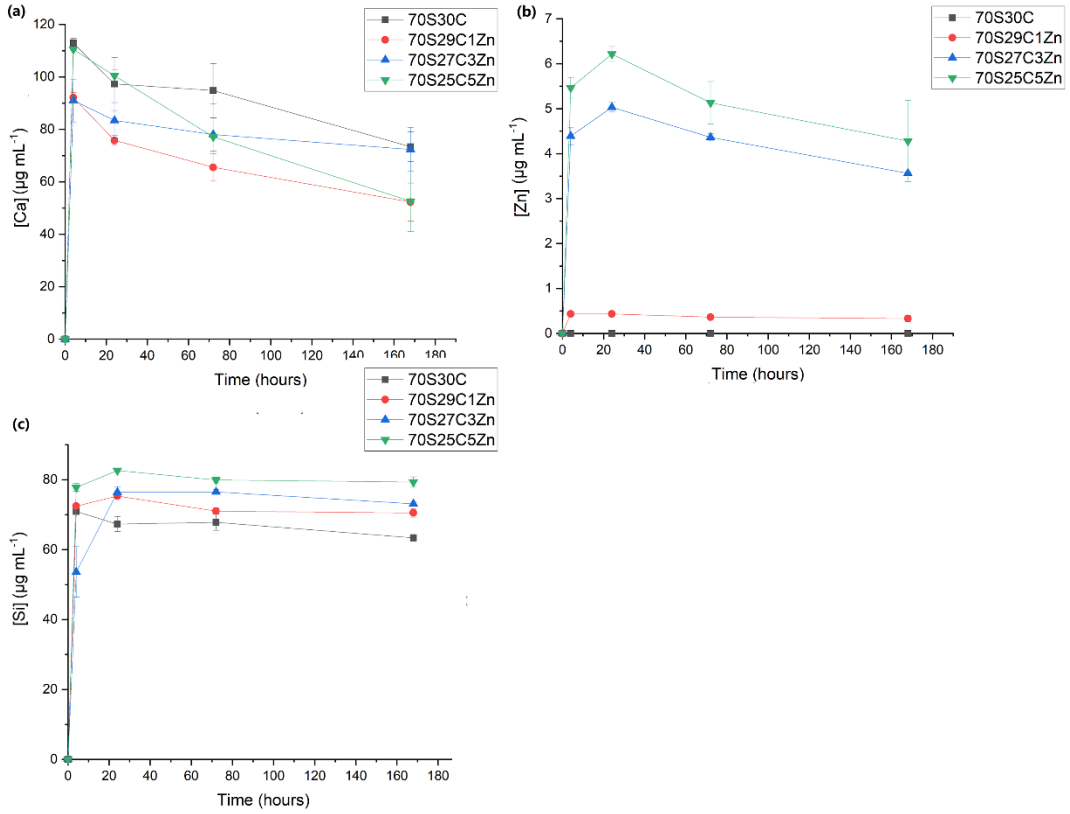


Figure 4. 9. Elemental concentration profiles (ICP) of DMEM following immersion of bioactive glass fibre mats 70S30C, 70S29C1Zn, 70S27C3Zn, and 70S25C5Zn over 7 d (a) Ca, (b) Zn, and (c) Si.

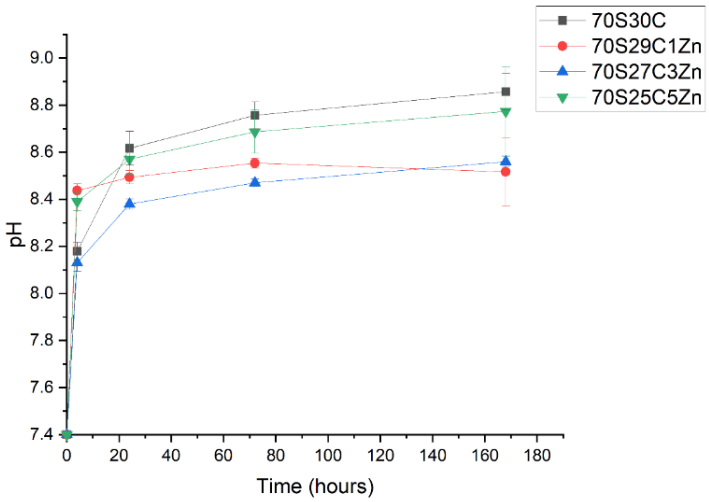


Figure 4. 10. pH change of DMEM following immersion of bioactive glass fibre mats 70S30C, 70S29C1Zn, 70S27C3Zn, and 70S25C5Zn over 7 d

The release of Si and Ca from both Zn-containing BG or Zn-free BG fibre mats were similar to the profiles from previous studies [54, 588, 712], which indicates that this concentration may be therapeutic. Unfortunately, there have not been studies that correlate Si and Ca concentration to their biological effect on wound healing, so their optimal concentration remains unknown. The natural level of silicon in the human body is 0.6 mgL^{-1} in serum and 41 mgL^{-1} in muscle, and slightly more before the generation of new bone [812, 813]. Recent studies that used silica alone, rather than bioactive glasses, indicated that SiO_4^{4-} can stimulate the proliferation of endothelial cells and fibroblasts, but did not mention the dose [814, 815]. Ca^{2+} concentration in tissue is 40 mgL^{-1} in the extracellular environment and 8 mgL^{-1} in the intracellular environment [816]. Considering the role of Ca ions on proliferation without the other bioactive glass dissolution products, Al-Ani *et al.* reported increased keratinocyte and fibroblast division and proliferation by increasing the Ca in the medium [817]. Other studies have further proved the role of calcium in fibroblast proliferation [818, 819] and keratinocyte proliferation [820, 821], with optimal Ca concentration dependent on cell type: <20 mgL^{-1} Ca^{2+} for keratinocyte growth and >56 mgL^{-1} Ca^{2+} for fibroblast proliferation [811].

Our static dissolution assessment proposed that Zn^{2+} release concentration can be within the therapeutic range expected to stimulate antibacterial activities, anti-inflammation, and follicle regeneration, based on results from previous literature. There has been a general agreement that 1-5 mol% of ZnO incorporation in glass stimulates antibacterial effects [409, 434, 435, 438, 822], though the minimum antibacterial concentration of Zn^{2+} released from BGs was 0.05-0.1 μg mL^{-1} [823, 824]. The antibacterial effect increased as Zn concentration increased [805] with 5 μg mL^{-1} killing > 99% of most bacteria [409, 434, 437, 509, 510, 825]. In terms of anti-inflammatory activities, 1 μg mL^{-1} of Zn^{2+} released from BG stimulated the up-regulation of Interleukin-10 (IL-10) and down-regulation of Interleukin-1β (IL-1β) and promoted the switch of macrophage polarisation from inflammatory (M1) to anti-inflammatory populations (M2) [551]. Similar effects were observed in vivo [552] and the anti-inflammation responses were reduced when the released Zn^{2+} exceeded 15 μg mL^{-1} [553]. Zn-releasing inorganic materials were recently found to stimulate follicle regeneration [36, 649]. Zinc chloride was found to stimulate the migration and proliferation of human hair follicle dermal papilla cells and upregulated their expressions of genes (VEGF, BMP-6, KGF, HGF, PDGF-α, PDGF-β, and C-Myc) [36]. Although an accurate range of Zn dose for promoting follicle regeneration has not been confirmed, a range of 2 μg mL^{-1} [826-828] to 13 μg mL^{-1} is suggested [36, 649]. It can be more beneficial to measure the dissolution in a dynamic environment again, as all ions in the static test are saturated within 1 day. In a dynamic environment, there is a constant flow of medium

bypassing the BGs and the ion concentration in the flow is a more precise prediction of the ion-release behaviour of BGs in real life.

pH is also an important factor during wound healing. Intact skins have a pH of 4-6 and wounds that are being healed have a neutral pH [829]. The pH value for acute wounds is 3-5 while that for burns and chronic wounds can reach 9-10 [830]. Our dissolution products generally have a pH around 8.2-8.8 in DMEM, because the silicon network can only break at ph > 9 (induced by the release of metallic ions) but the released silicates (in the form of silicic acid) were acidic. This may indicate that the BG hardly causes a pH-induced cytotoxic effect in real-life burn regeneration. With the healing of the wounds, the pH will reach back to 7.

4.3.4 Fibroblast viability

The in vitro cytocompatibility of the fibre mats was assessed using the CCK-8 assay on the HDF cell line (Figure 4. 11). On day 1, all HDFs cultured with BG dissolution products had higher MA relative to basal DMEM. This can be due to the role of Ca in the proliferation of fibroblasts [817-819]. The increase of Zn incorporation reduced the release kinetics of Ca^{2+} and therefore the corresponding MA. On day 3, the 70S30C fibres caused a reduction in MA relative to basal DMEM, indicating some toxicity, which agrees with the previously reported inhibition effect of calcium-silicate BGs on fibroblasts [53, 54], possibly due to the burst release of Ca^{2+} and the increase in pH in the static culture environment [261, 831]. This is supported by the decrease in MA of the cells cultured 1/2 diluted 70S30C dissolution products (Figure 4. 12), while the 1/4 diluted conditioned media, which had a much lower Ca^{2+} concentration, was not toxic to HDFs.

There has been a controversial view on the effect of BGs on fibroblasts. The first few investigations directly applied BG particles to cells and the role was either insignificant or negative. For example, direct application of <0.1% w/v 45S5 particles to 208F fibroblasts resulted in an insignificant change in cell number and 45S5 doses >0.1% w/v induced significant cytotoxicity, likely due to the toxicity induced by the increase of pH level during the dissolution of 45S5 in a closed vessel [53]. When the same dose of 45S5 was applied to CCD-18Co fibroblasts, even the smallest BG dose (0.01% w/v) induced 30% cell death. The cytotoxic effect may be relevant to the increased pH value in the media [86-89]. For example, the increase in pH value from 7.4 to 8.4 reduced both the migration and the proliferation of human dermal fibroblasts [88]. The natural pH of BG dissolutions in DMEM was around 8-8.5 and could reach>9.3 if Na was incorporated into the BG system [89].

The high pH also reduced the expressions of various proteins, collagen, and promotes protease that further inhibited cell proliferation [832-834].

The surface of BG particles may not be ideal for cell attachment and proliferation and less toxic effects will be found when applying the dissolution products of BG to cells. For example, the ionic products of $SiO_2 - P_2O_5 - CaO - MgO$ BGs that were sintered with different heating temperatures were all stimulative to the proliferation of NIH-3T3 cells [835]. At high dilutions, the stimulated cell proliferation from BGs weakened. For instance, 1/32 to 1/128 diluted 45S5 dissolution products did not stimulate fibroblast proliferation, although still enough to stimulate more protein expressions than the control [55]. Besides, incorporation of either BG or BG dissolution products in the different organic material systems also promoted the proliferation of fibroblasts, keratinocytes, or endothelial cells [235, 721, 722, 724].

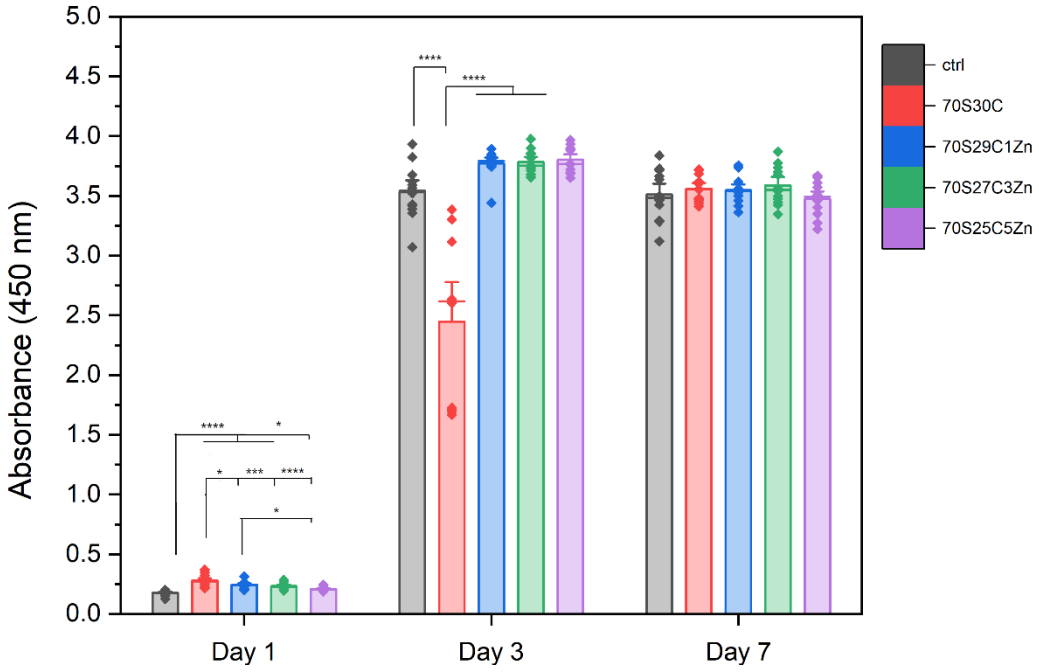


Figure 4. 11. The effect of the dissolution products of the 70S30C, 70S29C1Zn, 70S27C3Zn, and 70S25C5Zn scaffolds on the metabolic activity (MA) of HDFs on days 1, 3, and 7, represented by the (a) normalized MA against the DMEM control. (*P <0.05, **P<0.01, ***P <0.001,****P <0.0001, n=12)

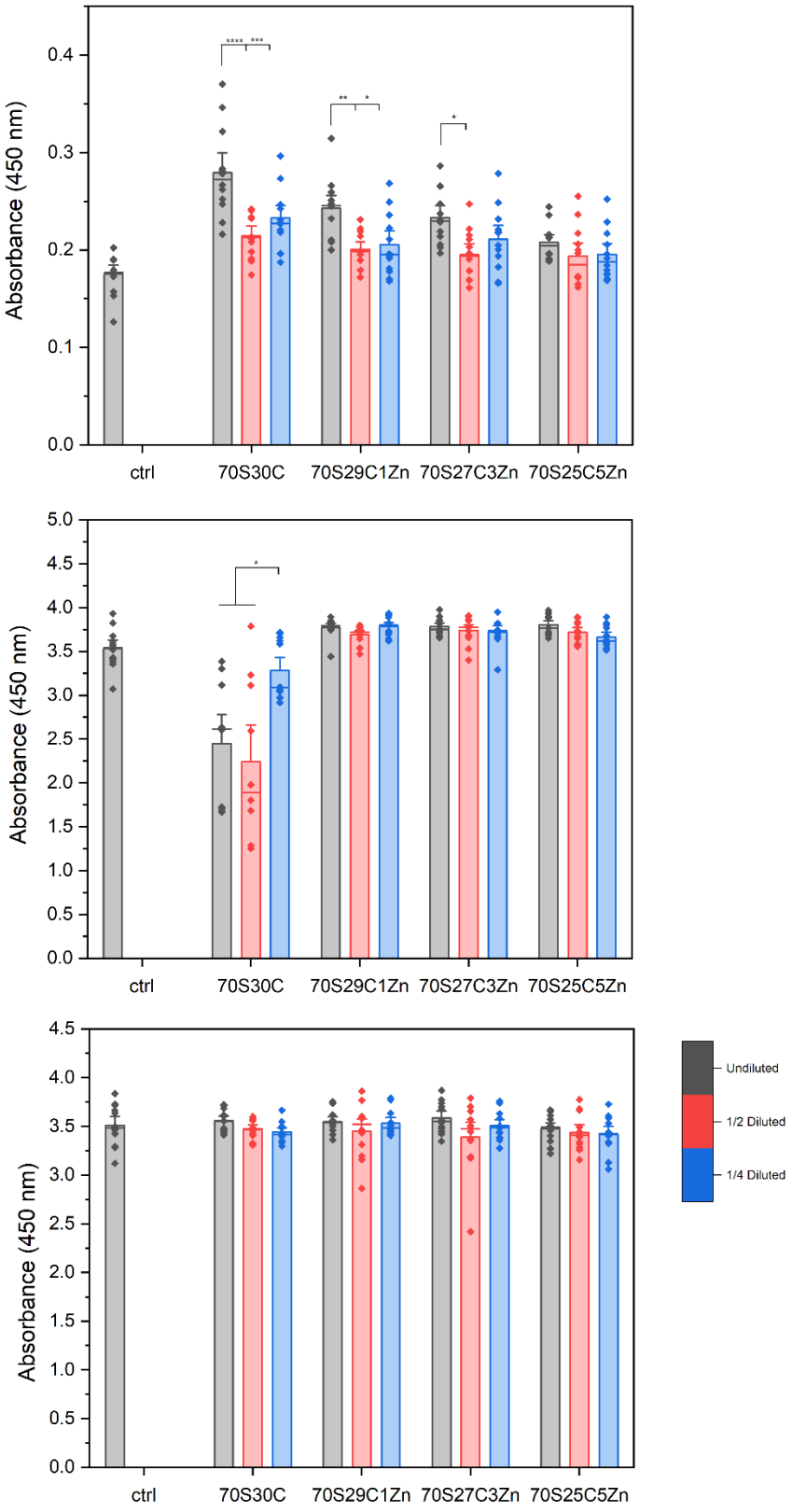


Figure 4. 12. The effect of undiluted, 1/2 diluted, and 1/4 diluted dissolution products on MA of HDFs at day (a) 1, (b) 3, and (c) 7, represented by the intensity of absorbance at 450 nm. (*P <0.05, **P<0.01, ***P <0.001,****P <0.0001, n=12)

Zn-containing BG fibres did not show any cytotoxic effect on fibroblasts, which was expected as the Zn release was below 7 μg mL^{-1} [783, 836], and the incorporation of Zn prevented the abrupt release of Ca^{2+}. Zn reduces extracellular Ca level by interacting with them to stimulate DNA synthesis in fibroblasts [262, 837, 838]; and Zn stimulates the calcium influx in fibroblasts to promote proliferation [839, 840]. There were no significant differences in MA between the cells cultured with basal DMEM and those exposed to BG dissolution products on day 7 as the HDFs were confluent.

4.3.5 PDGF expression from fibroblasts

Platelet derived growth factors (PDGF) are originally expressed from platelets as soon as a wound is cast and platelet aggregates in the wound area to form a clot. They function throughout the wound healing cascade and their source changes from platelets to macrophages at the 'Inflammation' phase, and then to fibroblasts, keratinocytes, and endothelial cells at the 'Proliferation' phase [80, 81]. It was found that having PDGF in wound healing accelerates the healing time by 30% and the wound strength by 50-70% [117]. PDGF is an important protein in the activation of cells. For example, it is a potent activator for cells of mesenchymal origin. It also mediates the 'Inflammation' phase from both the activation of leukocytes to the phenotype change of macrophages (anti-inflammation). Its main function is to stimulate the activation, proliferation, migration, and ECM protein secretion of fibroblasts [80, 118, 119]. PDGF also stimulates angiogenesis as PDGF stimulates the proliferation of endothelial cells and their VEGF expressions, and PDGF promotes pericyte activities to stabilize blood vessels [110, 841-843].

Though there have been few articles reporting the role of BG in PDGF expressions from fibroblasts, we expect that HDF treated with BG should have a higher PDGF expression compared to the control, as previous work that showed Ca^{2+} is essential for PDGF activation and stimulation [844, 845]. All BG fibre mats stimulated therapeutic Ca^{2+} release and therefore up-regulated the PDGF expressions (Figure 4. 13) relative to basal media. Zinc may not have a stimulatory effect on PDGF expressions as when zinc content of the glass increased to 3 and 5 mol%, which also reduced Ca^{2+} content, PDGF expression decreased to values similar to the control. Surprisingly, the 1/2 diluted media of 70S30C, 70S29C1Zn, and 70S25C5Zn induced lower PDGF expressions compared to the control, while the 1/2 diluted media of 70S27C3Zn was similar to that of the control. The mechanism underneath requires further investigation.

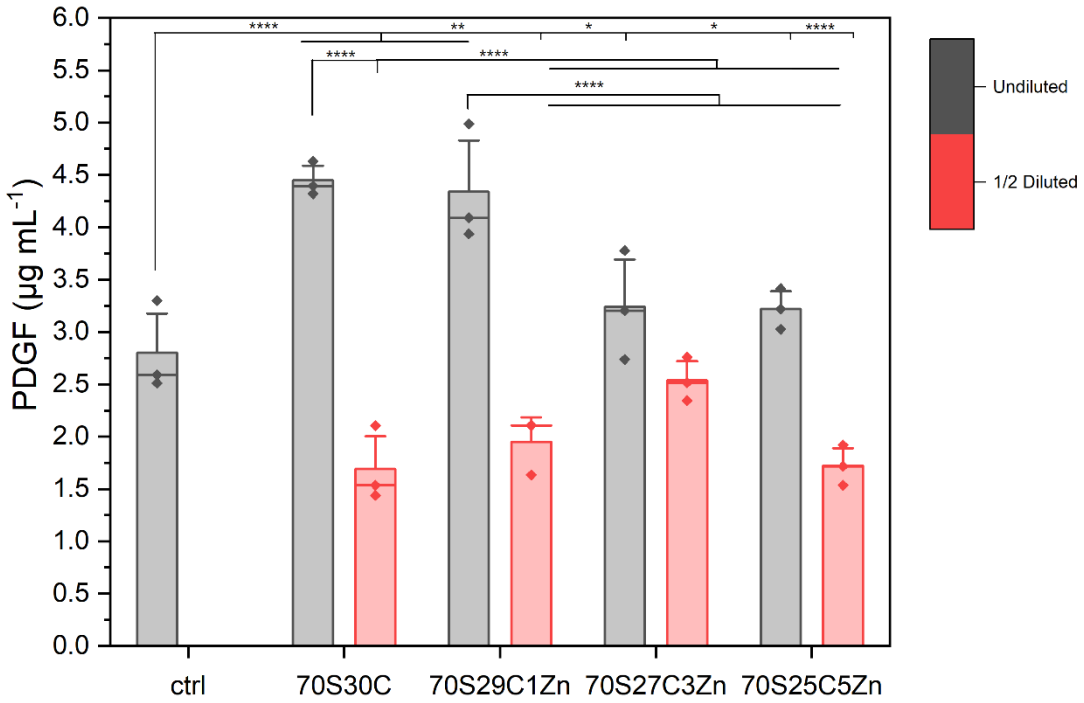


Figure 4. 13. PDGF expressed from the HDFs (ELISA assay) cultured with the undiluted and 1/2 diluted dissolution products of the 70S30C, 70S29C1Zn, 70S27C3Zn, and 70S25C5Zn scaffold, for 2 days. (*P <0.05, **P<0.01, ***P <0.001,****P <0.0001, n=3)

4.3.6 TGF-β expression from fibroblasts

TGF-β is initially secreted from platelets and neutrophils to induce leukocyte chemotaxis. Its activation is an important signal for burn regeneration and contributes to the reduction of inflammation and promotion of angiogenesis [114-116]. During burn regeneration, the TGF-β level in the epidermis should increase, and that in the dermis decrease, in order to promote wound closure but prevent fibrosis [846]. TGF-β is also an important cytokine during the 'Inflammation' phase as it up-regulates metallopeptidase inhibitors while down-regulates matrix metalloproteinase, which is a protease that promotes inflammation [18]. During the 'Proliferation' phase, fibroblasts are a major source of TGF-β as TGF-β provides signals for them to proliferate and differentiate [80, 82]. TGF-β also promotes the aggregation of the total protein, especially that of the ECM proteins, including collagen, elastin, and fibronectin [847].

As shown in Figure 4. 14, the Ca^{2+} and SiO_4^{4-} released from the Zn-free BG fibre mat significantly reduced TGF-β expression from fibroblasts. This can be due to the reduced fibroblast proliferation by Day 3, as TGF-β contributes to the fibroblast chemotaxis in activation and proliferation [80, 82]. The reduced TGF-β may also be due to the interplay

of TGF-β and Ca^{2+}. Ca^{2+} was involved in Factor IV of TGF-β, but excessive Ca^{2+} may obstruct the fibroblast pathway in expressing TGF-β [848, 849]. This is further proved that once treated with diluted BG dissolution products, the TGF-β expressions returned to normal. The incorporation of Zn^{2+} in the BG system resolved the reduced TGF-β expression. This is due to that Zn^{2+} reduces Ca^{2+} release and the interplay of Zn^{2+} and TGF-β through other pathways [850].

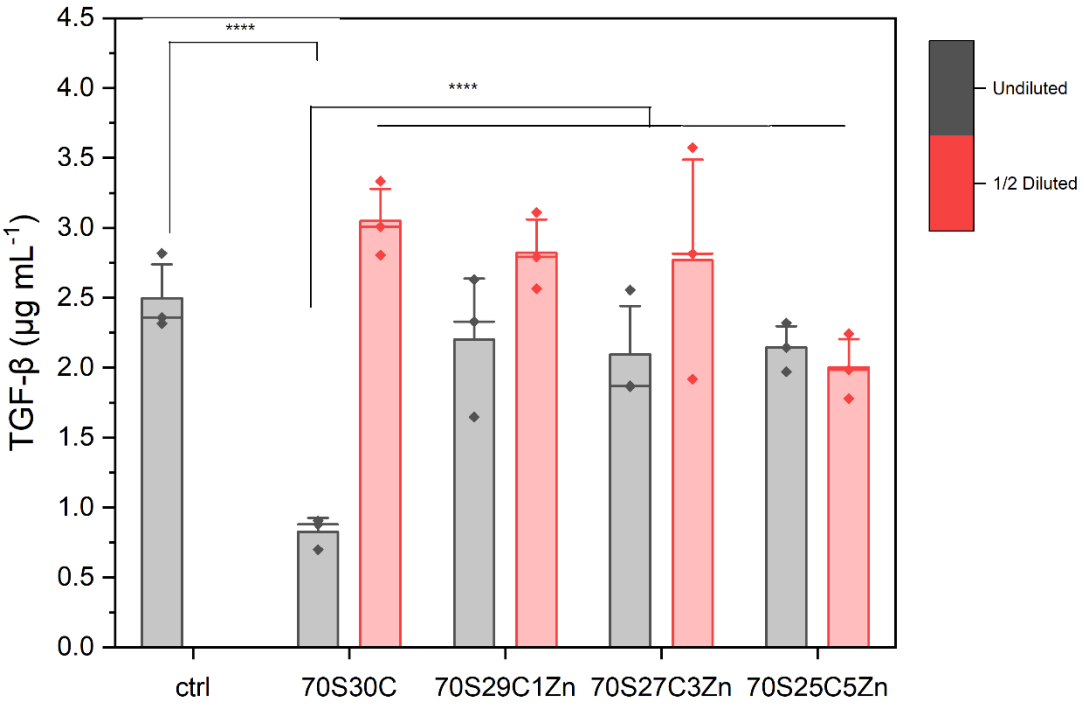


Figure 4. 14. TGF-β expressed from the HDFs (ELISA assay) cultured with the undiluted and 1/2 diluted dissolution products of the 70S30C, 70S29C1Zn, 70S27C3Zn, and 70S25C5Zn scaffold, for 2 days. (*P <0.05, **P<0.01, ***P <0.001,****P <0.0001, n=3)

4.3.7 HIF-1α expression from fibroblasts

Hypoxia-inducible factor 1-alpha (HIF-1α) is a transcriptional regulator of the cellular response to hypoxia, the low oxygen concentration in the body. HIF-1α is activated immediately after a wound is cast for the hemostasis process [851]. In the normal wound healing process, HIF-1α is expressed when there is ischemia induced by a locally broken vascular system and transfer signals to fibroblasts or endothelial cells in the production of angiogenic factors, VEGF and bFGF. Some recent studies provoked up-regulated HIF-1α in wounds to generate a hypoxia-mimic environment in order to promote the expression of angiogenic factors [852, 853].

Figure 4. 15 showed increased HIF-1α expression by the HDFs either increased or was similar to the control when the cells were cultured with the dissolution products of all fibres. This could be due to the role of Ca in the activation of HIF-1α through the upstream of ERK in the hypoxia signal transduction pathway [854, 855]. Calcium signaling also stimulates the translation of HIF-1α to α subunits through the stimulation of classical protein kinase C-α, and the activity of mammalian targets of rapamycin, mTOR [856, 857]. When the conditioned media were diluted, the HIF-1α expressions became even higher than those from the undiluted media. The reason is unknown, but it may be because the Ca concentration is excessive which induces an adverse effect on HIF-1α expression. HIF-1α expressions from Zn-containing BG fibres mats are generally lower than that from 70S30C fibres in both diluted and undiluted media until the Zn composition in BG reached 5 mol%. There is some evidence in the literature that Zn downregulates HIF-1α [858, 859], but others have reported that Zn upregulates HIF-1α [860, 861]. The mechanism needs further investigation.

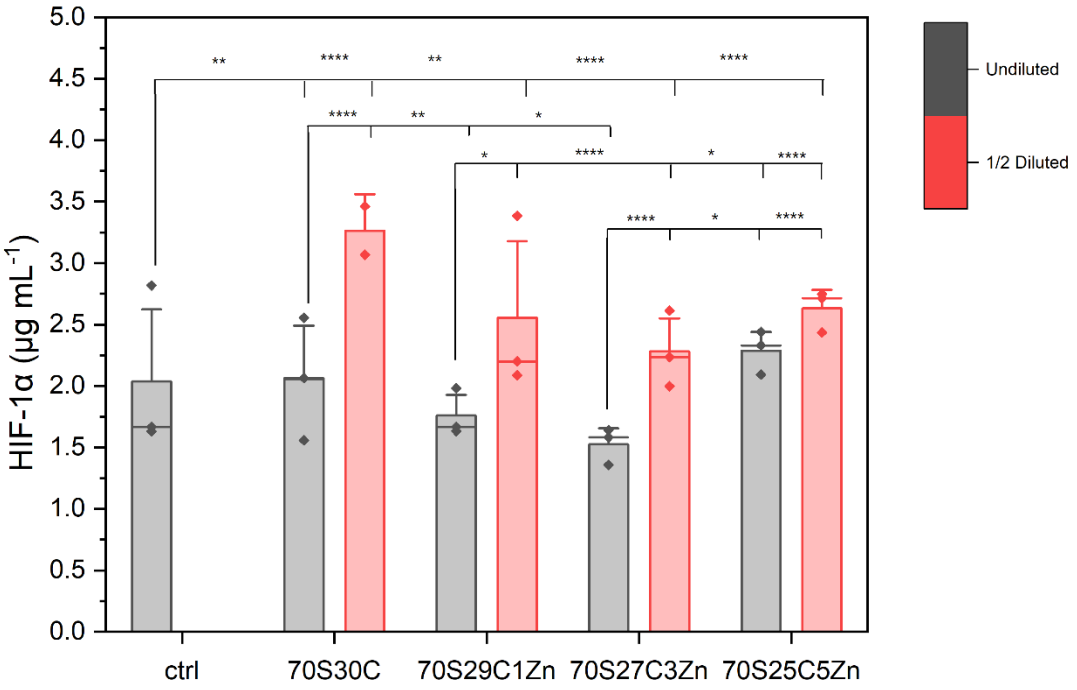


Figure 4. 15. HIF-1α expressed from the HDFs (ELISA assay) cultured with the undiluted and 1/2 diluted dissolution products of the 70S30C, 70S29C1Zn, 70S27C3Zn, and 70S25C5Zn scaffold, for 2 days. (*P <0.05, **P<0.01, ***P <0.001,****P <0.0001, n=3)

4.3.8 VEGF expression from fibroblasts

VEGF is a protein that can be expressed from neutrophils, platelets, keratinocytes, fibroblasts, and endothelial cells. It is also stimulated when a wound is cast to promote blood vessel infiltration to the dermis layer from the hypodermis [862, 863]. Some also reported that it promotes monocyte chemotaxis [121] and induces colonization of macrophage progenitor cells before their activations [864, 865]. Its major function is to ensure the survival of endothelial cells and stimulate their migration and proliferation in order to stimulate angiogenesis [120, 121].

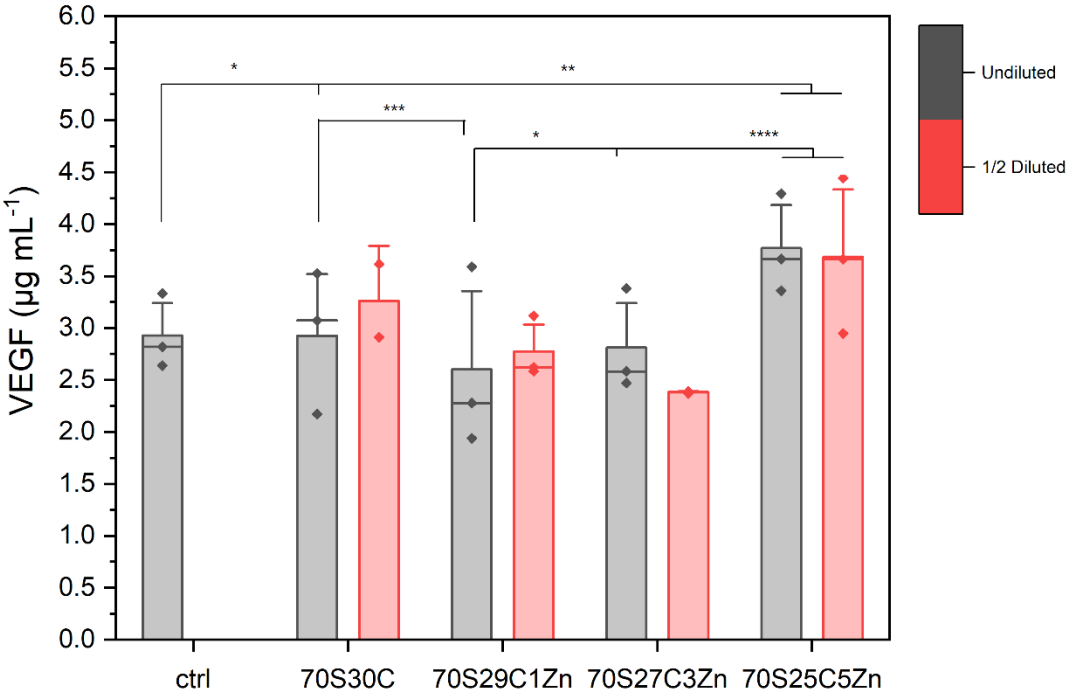


Figure 4. 16. VEGF expressed from the HDFs (ELISA assay) cultured with the undiluted and 1/2 diluted dissolution products of the 70S30C, 70S29C1Zn, 70S27C3Zn, and 70S25C5Zn scaffold, for 2 days. (*P <0.05, **P<0.01, ***P <0.001,****P <0.0001, n=3)

Through their interplay with HIF-1α, Ca^{2+} from the dissolution products of BG fibres upregulated the VEGF expressions from fibroblasts (Figure 4. 16). This agrees with the result of Norris *et al.*, where SiO_2-CaO based BG fibres stimulated VEGF from HDF cell line, with the glass with the highest Ca composition provoking more VEGF expression [97]. The incorporation of Zn reduced the release of Ca^{2+} and little Zn^{2+} so that the 70S29C1Zn fibres induced fewer VEGF expressions (similar to that of the control), but the dissolution products of 70S27C3Zn and 70S25C5Zn upregulated VEGF expressions. In previous studies, Zn-containing materials have been reported to stimulate the expressions of VEGF and endothelial tubule formation in vitro [63, 649, 650, 866], and angiogenesis in vivo [651,

652]. Although the mechanism of Zn in VEGF expressions mainly contributes to its paracrine effect during anti-inflammation, Zn is reported to interact with HIF-1 and HIF-2 to stimulate VEGF expressions [64]. But the correlation between concentration and function remains unknown.

4.3.9 bFGF(FGF-2) expression from fibroblasts

bFGF, or FGF-2, has a similar role in angiogenesis as VEGF but it is not expressed at the start of the wound healing cascade. The major source of bFGF is fibroblasts, while a few of them are expressed in endothelial cells and macrophages [867]. It also has functions that are similar to other factors from the FGF family, including the promotion of fibroblast proliferation and migration, the formation of the ECM, wound closure and re-epithelialization, etc. [868]. Recent studies also reported that bFGF could reduce the scarring effect in wounds [869, 870], especially for scarring in a burn [871].

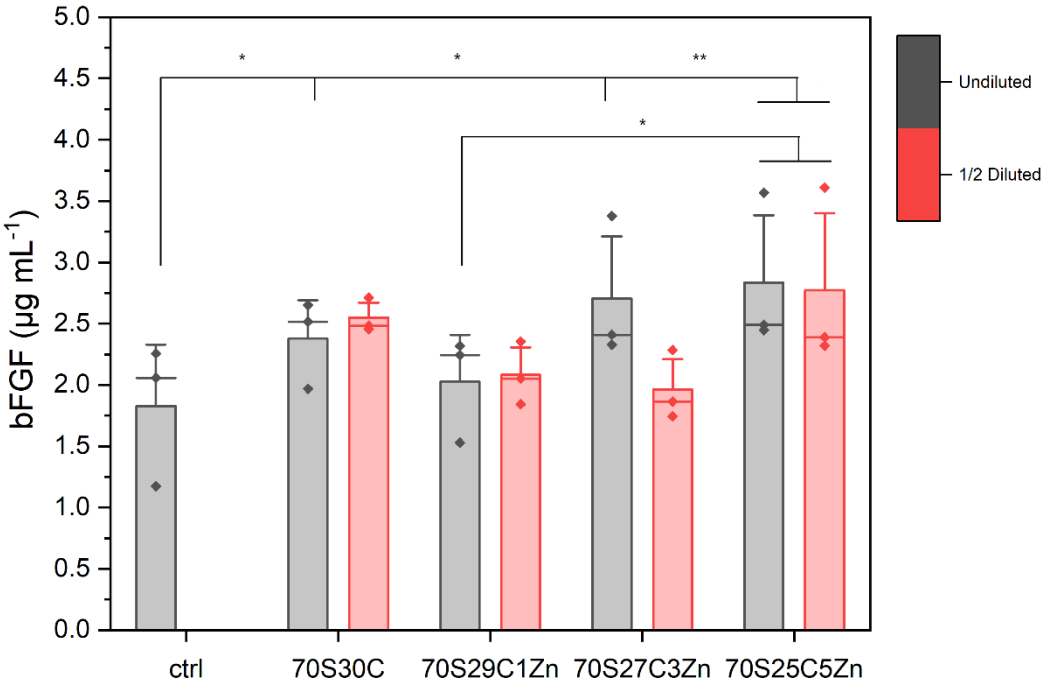


Figure 4. 17. bFGF(FGF-2) expressed from the HDFs (ELISA assay) cultured with the undiluted and 1/2 diluted dissolution products of the 70S30C, 70S29C1Zn, 70S27C3Zn, and 70S25C5Zn scaffold, for 2 days. (*P <0.05, **P<0.01, ***P <0.001,****P <0.0001, n=3)

The bFGF expression profiles from HDF are similar to that of VEGF. The dissolution products of the 70S30C also upregulated bFGF expressions compared to the blank medium, as the interplay of HIF-1α and Ca^{2+} also up-regulates bFGF. The incorporation of

Zn instead of Ca, however, does not reduce the bFGF expressions (Figure 4. 17). Further addition of Zn to 3 and 5 mol% induced higher bFGF expressions. This may be because that Zn has a stronger stimulation to bFGF than Ca [651, 652]. For instance, bFGF expressions increase in media with higher Zn ions [872], but there has been no evidence to correlate the concentration of Ca to bFGF expressions.

4.3.10 Metabolic activity of endothelial cells

BG fibres signal fibroblasts to release growth factors for the activation, proliferation, and migration of endothelial cells. Endothelial cells also have their own pathway of growth factor expression to support their own activities, which may also be enhanced by the ion released from BG. In vitro analysis using BG-HDF media better mimics the environment that endothelial cells undergo in in vivo wound healing.

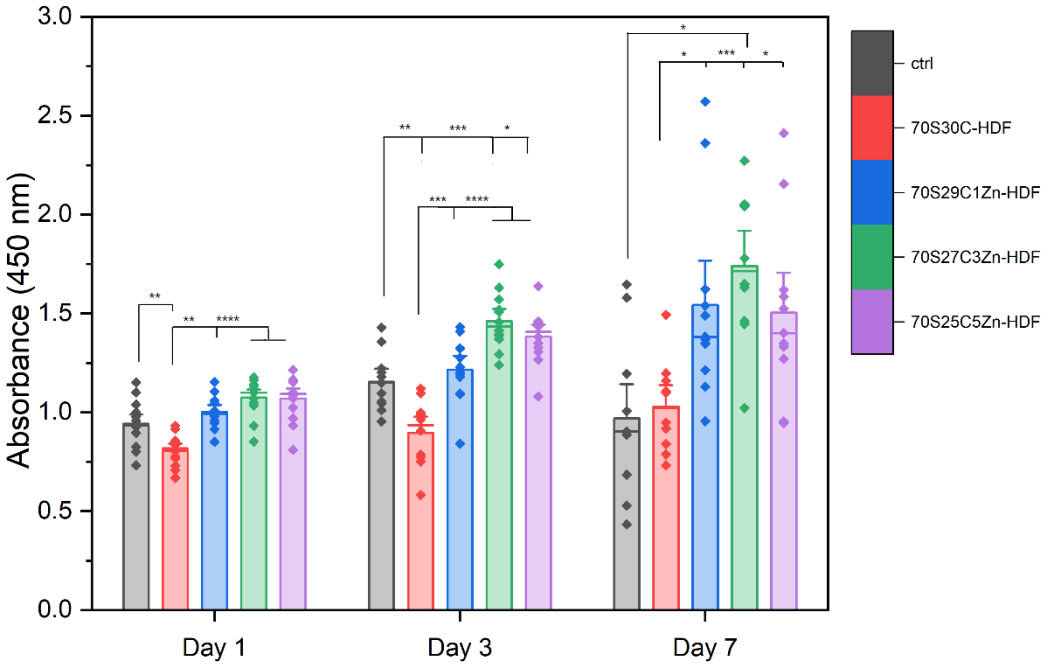


Figure 4. 18. (a) Metabolic activity of HUVECs after being cultured with 1:1 mixture of endothelial culture media with control medium (DMEM-HDF), 70S30C-HDF, 70S29C1Zn-HDF, 70S27C3Zn-HDF, and 70S25C5Zn-HDF conditioned media at day 1, 3, and 7. (*P <0.05, **P<0.01, ***P <0.001,****P <0.0001, n=12)

After being cultured with fibroblasts for 2 days, the BG-HDF conditioned media were further assessed for their role in stimulating angiogenesis regarding the proliferation (MA) and migration of endothelial cells. Though containing more HIF-1α and VEGF, the

70S30C-HDF medium inhibited the proliferation of HUVECs at all time points (Figure 4. 18). This disagrees with Midha *et al.*, who found that the media of 70S30C particles and HDFs promoted the metabolic activities of HUVECs [873]. BGs of other compositions, such as the original 45S5 Bioglass, were also found stimulative to endothelial cell proliferation after pre-incubated with fibroblasts [54, 588]. A possible reason for this was due to the difference in morphology which leads to different ion release kinetics as there was excessive Ca^{2+} in the BG-HDF media. According to Day *et al.*, only small doses (0.01-0.1 w/v % which generated ion concentration below a critical level) of BG stimulated HUVEC proliferation while large doses were cytotoxic [53, 54, 588]. All Zn-containing BG fibres promoted the proliferation of HUVECs, in agreement with previous findings. For example, Aina *et al.* have reported that BG with 5 wt% Zn incorporation significantly enhanced the proliferation of endothelial cells [99].

4.3.11 Migration of endothelial cells

Endothelial cell migration is a key process in angiogenesis involving 6 sequential steps [874]. Endothelial cells migrate to areas with higher concentrations of angiogenic factors as that is the area with ischemia and local hypoxia. The activation makes them protrude and attach to ECM fibrils. They then form stress fibres (actins) within the cells to move their rear part forward. VEGF and bFGF are two major chemotaxes driving the process, that involve integrin activation [875] and provide signaling when binding with their receptors [876], etc.

All BG-HDF media stimulated the migration of endothelial cells (Figure 4. 19), which was in accordance with the expressions of VEGF and bFGF from fibroblasts (Figure 4. 16, Figure 4. 17). Existing literature proved that BG in the form of nanoparticles or nanofibres promoted endothelial cell migration [543, 698, 724] and hence angiogenesis in vivo [91, 552]. There was not much difference between Zn-BG fibres and Zn-free BG fibres except for the one with the highest Zn incorporation. This may be because that Zn has its own pathway in stimulating the migration of endothelial cells other than its up-regulation of angiogenic factors from fibroblasts. Further evidence is needed to understand the mechanism.

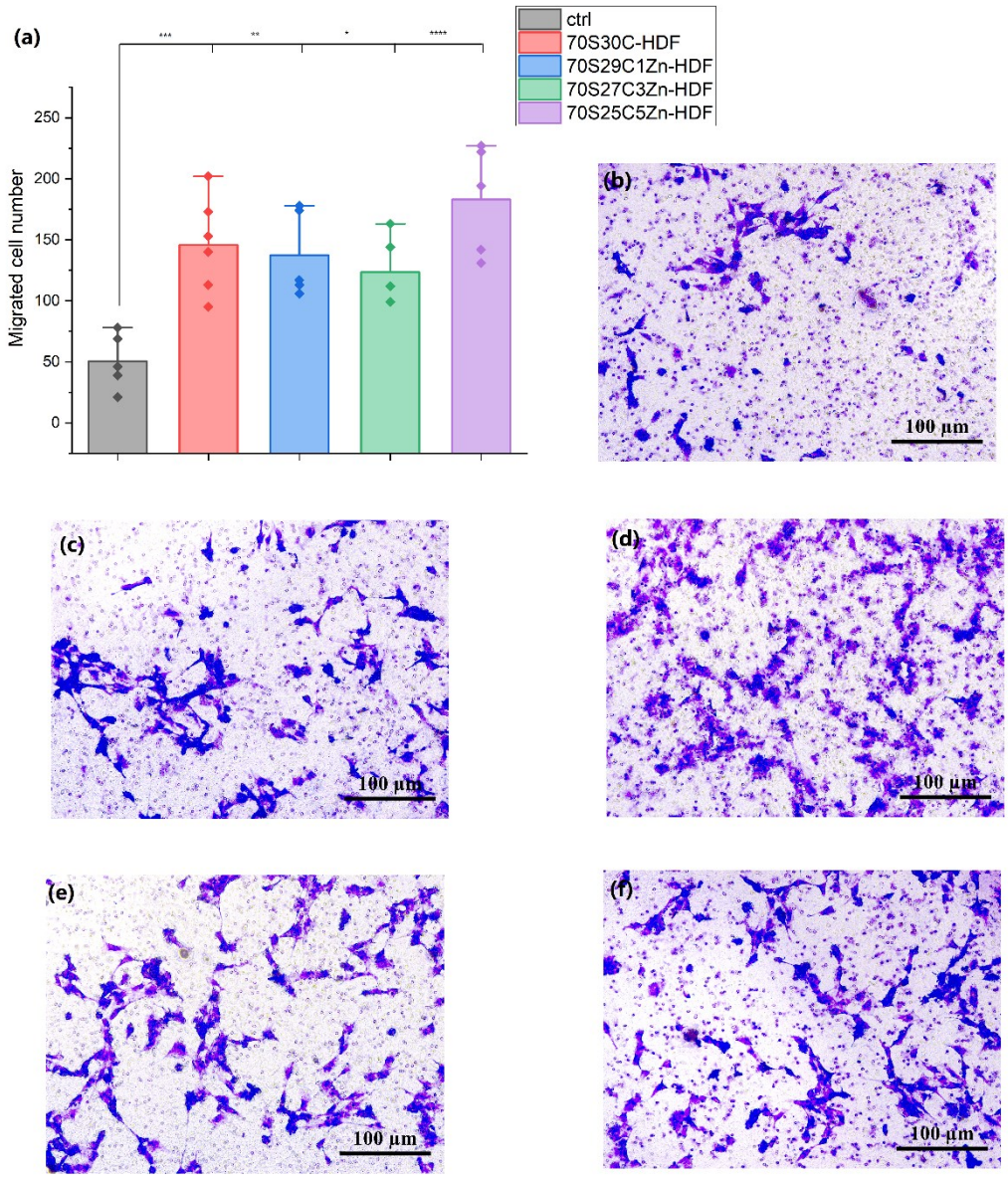


Figure 4. 19. (a) Cell number and (b-f) images of migrated HUVECs after being cultured for 16 hours in a Transwell assay with (b) the control medium, (c) 70S30C-HDF conditioned medium, (d) 70S29C1Zn conditioned medium, (e) 70S27C3Zn conditioned medium, and (f) 70S25C5Zn conditioned medium. (*P <0.05, **P<0.01, ***P <0.001,****P <0.0001, n=6)

4.3.12 Growth factor expressions from endothelial cells

We also assessed the role of BG-HDF media in regulating the expressions of angiogenic factors of endothelial cells. The ELISA results showed angiogenic factors are those remaining from BG-HDF media and those newly expressed through the interplay between

ions and endothelial cells. Though it is unsure the exact quantity from both parts, this study can indicate the actual growth factor level to be uptaken by endothelial cells in real life. Similar to that of fibroblasts, the HIF-1α expression of cells exposed to 70S30C-HDF conditioned media was much higher than that of the other counterparts (Figure 4. 20 (a)), but the VEGF and bFGF expressions were much less (Figure 4. 20 (b, c)) than control. These may attribute to that excessive Ca^{2+} level affects endothelial cell activities in different aspects, such as the ligand-receptor interaction to produce inositol triphosphate [877], mediation of the protein kinase C expressions [878], induce permeability and NO expressions [879], generation of intracellular second messengers [880], etc., but the concentration-to-effect mechanism remains unknown. The incorporation of Zn reduced the HIF-1α expression similar to that of the control and increased the VEGF and bFGF expressions from endothelial cells. The reduced Ca^{2+} release and the inhibition of calcium signaling can be two possible reasons, but further investigations are needed.

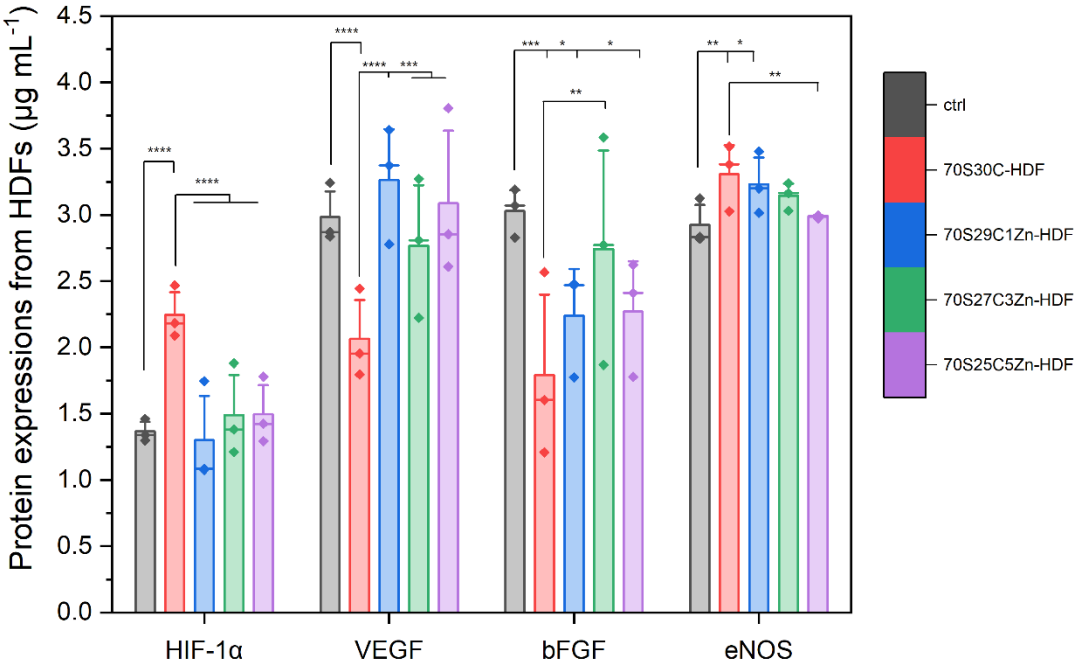


Figure 4. 20. HIF-1α, VEGF, bFGF (FGF-2), and eNOS expressed from HUVECs (ELISA assay) cultured with the 1:1 mixture of endothelial culture media with control medium (DMEM-HDF) 70S30C-HDF, 70S29C1Zn-HDF, 70S27C3Zn-HDF, and 70S25C5Zn-HDF conditioned media for 48 h. (*P <0.05, **P<0.01, ***P <0.001,****P <0.0001, n=3)

eNOS is an enzyme indicating the level of synthesized nitric oxide in vascular endothelium and is another major regulator of cell migration and angiogenesis [881]. For example, mice with eNOS knockout had impaired angiogenesis under ischemia [882, 883]. eNOS is a

Ca^{2+}/calmodulin-dependent enzyme [884]. Brouet *et al.* reported that on exposure to VEGF and Ca^{2+}, eNOS in endothelial cells were upregulated, so eNOS is commonly used as an indicator of angiogenesis [885]. Our results proposed (Figure 4. 20 (d)) that VEGF and Ca^{2+} from the BG-HDF medium were stimulative to eNOS expressions. The decrease of Ca^{2+} as Zn increased reduced the eNOS expression back towards that of the control, but since the difference in Ca^{2+} release is not very significant among BG fibres, the decrease of eNOS with the increase of Zn incorporation is not very significant. Combined with the ELISA results from HDFs (Figure 4. 13) and HUVECs (Figure 4. 20), this study may have revealed the mechanism of BG fibres to angiogenesis. Growth factors released from fibroblasts remained in the BG-HDF media and were depleted through binding to the receptor site in endothelial cells, which stimulates the activity of endothelial cells. Endothelial cells also maintain the angiogenic factor levels in media similar to that of the fibroblasts for sustained angiogenic activities. Further assessments are required to examine the role of each part separately.

4.4 Concluding remarks

We synthesized zinc-delivering bioactive glass fibre mats as scaffolds for burn regeneration. The resultant wound matrix mimicked the ECM environment to stimulate cell attachment and migration and facilitate a controlled release of Zn^{2+}, Ca^{2+}, and SiO_4^{4-} which are in the doses thought to be suitable for antibacterial activities, anti-inflammation, angiogenesis, and follicle regeneration. 3 mol% of Zn incorporation reduced the cytotoxic effect of BGs on fibroblasts and stimulated their expression of growth factors (PDGF, VEGF, bFGF, TGF-β, and HIF-1α) for ECM deposition and angiogenesis. This chapter also reported, for the first time, how media conditioned with fibroblasts that had been precultured with BG dissolution products influenced the proliferation and migration of endothelial cells and their protein expression, which may allow us to understand the actual growth factor level to be uptaken by endothelial cells in real life. In a summary, the Zn-containing BG fibre mats can be the potential strategy for burn regeneration. Further in vitro assessments of in vivo assessment are needed to assess its characteristics in other aspects of burn regeneration, such as their antibacterial, anti-inflammatory follicle regeneration capabilities.

5 Borate-based bioactive glass fibre mats for the regeneration of diabetic ulcers

5.1 Introduction

Diabetic ulcers are causing a great threat to the social healthcare system as it has high occurrence, high mortality, and high cost of treatment. The healing cascade of diabetic ulcers consists of a prolonged inflammation phase where pro-inflammatory cytokines and protease aggregate in the wound side and impair the function of cells, growth factors, and the ECM [16, 20-22]. The neuropathy of diabetics also inhibits keratinocyte migration and impairs chemotaxis, which leads to bacteria colonization and biofilm formation, dysfunctional proteins, and senescent cells at the wound site [23, 24]. Local ischemia has been a major cause of the delayed regeneration of chronic ulcers, as it inhibits the supply of nutrients and oxygen [25-27].

In this chapter, we aim to synthesize 3D ECM-mimic borate-silicate-calcium bioactive glass (defined as borosilicate BG in later sections) and BG fibre mats as strategies for the regeneration of diabetic ulcers, especially in the stimulation of ECM deposition and angiogenesis. Borate and borosilicate BGs are of particular interest in the regeneration of soft tissues [45, 46]. While the degradation of conventional silica-based glasses is two-set and involves the formation of a silica-rich layer, borate-based glasses undergo total dissolution [46, 84]. Borate ions released during BG dissolution are also involved with the 4 most important cell types during chronic wound regeneration cascade, as summarized in Figure 5. 1, and stimulate various regeneration phases. For example, boron incorporation stimulates wound closure and epithelialization, as 2 wt% of B incorporation in the BG system stimulated a 2-fold increase in in vitro wound closure assay [57]. Borate ions also stimulate higher collagen, laminin, and fibronectin deposition in the demis layer [65, 66]. Demirci *et al.* reported the anti-inflammatory effect of boric acid and sodium pentaborate pentahydrate on various inflammatory factors, such as the level of inducible nitric oxide synthase (iNOS) and cyclooxygenase-2 (COX-2) [65]; Yin *et al.* further reported that boron-containing MBG scaffolds down-regulated pro-inflammatory cytokines TNF-α and IL-6, and promoting M2 polarization [67]. Furthermore, various reports proved the capability of borate ions in sprouting the proliferation, migration, and tubule formation of endothelial cells, as well as the expression of growth factors such as VEGF and FGF-2 of fibroblasts, all revealing their potential in angiogenesis [57, 68-73].

Conventional sol-gel processing is only suitable for synthesizing BGs with low boron content (< 15%). This is because the stabilization temperature of the BG (600 °C) exceeds the crystallization temperature of calcium borate (450 °C) [289, 295, 296]. The use of calcium methoxyethoxide as an alternative calcium source exempts the stabilization process but is not ideal for the sol-gel electrospinning process as the process generates much water and ethanol as byproducts [886-888]. This study proposes a modified sol-gel approach in synthesizing borosilicate BGs, in which TEB is thoroughly mixed with TEOS to ensure that individual borate group locks among a few silicate groups, in order to prepare BG fibres with a composition of (70-x) mol% SiO_2-30 mol% CaO- x mol% B_2O_3 (x=0, 5, 15, and 35, 55, 65, and 70, labeled as (70-x)S respectively) through the sol-gel electrospinning method. The fibre mats are electrospun with a > 2 mm thickness, which was determined as the 3D structure as conventional mats have < 0.5 mm thickness. SEM, XRD, and FTIR characterizations were conducted to understand the effect of boron incorporation on the morphology of BG fibres and the chemical structures of BGs. The dissolution study was also conducted to assess the ion released from BG fibres, in order to understand whether they were cytotoxic or therapeutic for wound healing activities.

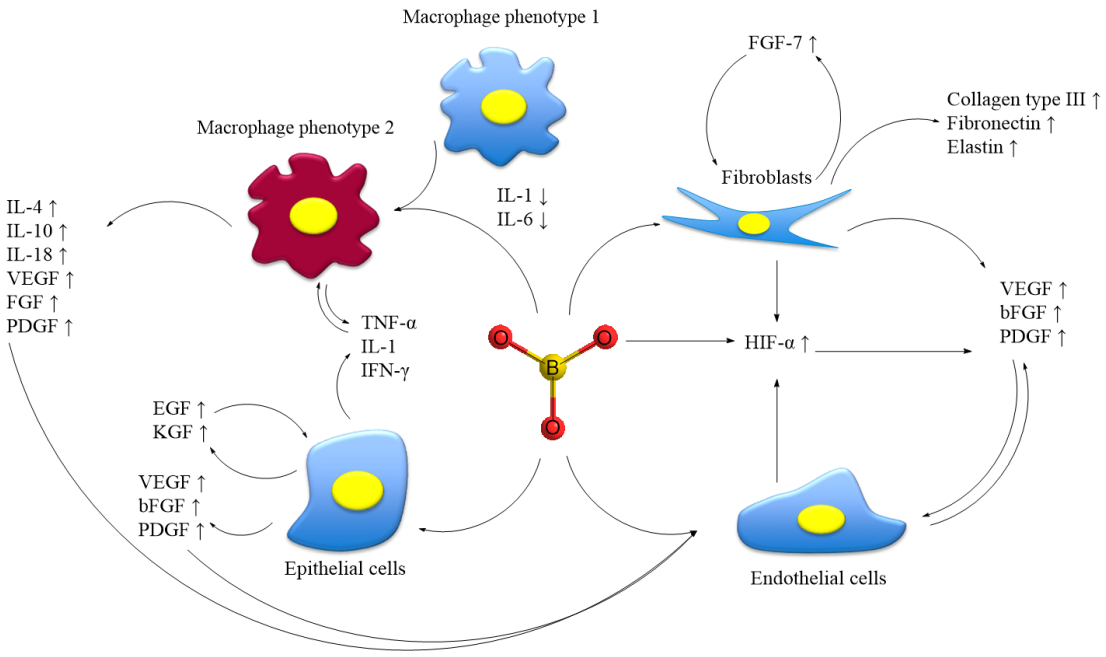


Figure 5. 1. Schematic of the role of boron released from BG to the cells in the diabetic ulcer regeneration cascade

In vitro assessments of the BG fibres mats were also conducted on fibroblasts, the most abundant cells in the wound area [12, 80, 81, 110]. The dissolution products of the fibre mats were cultured with HDFs and their influence on HDF viability was measured. The role of BG fibre mats to ECM deposition was characterized through the ELISA assessment

of PDGF and TGF-β expressed from HDFs, while the role of BG fibres to angiogenesis was characterized through the ELISA assessment of VEGF, bFGF, and HIF-α expressed from HDFs. We also characterized the viability and migration of HUVECs in media conditioned with HDF cells cultured with the dissolution products of BG fibres and correlated them to the protein expression profiles from fibroblasts. Protein expression from HUVEC was also characterized to validate whether BG dissolution products were directly involved in HUVEC activities without being primarily involved with HDFs.

5.2 Methods

5.2.1 Synthesis of the borosilicate BG fibre mats

All reagents were obtained from Sigma Aldrich unless otherwise stated. The preparation of the sol-gel precursor initially followed the conventional sol-gel approach, reported in Chapter 4. In general, the ethanol and nitric acid were mixed for 20 minutes and then the sol-gel precursor (tetraethyl orthosilicate (TEOS), triethyl borate (TEB), and calcium nitrate tetrahydrate ($Ca(NO3)_2$)) was added correspondingly, and homogeneously mixed [97, 286].

This approach worked well when synthesizing 65S30C5B fibres. During the synthesis of 55S30C15B fibres, a little precipitation occurred during the sol-gel process but would disappear at a longer aging time. The precipitation effect was due to the low solubility of borate ions (usually in the form of boric acid) in ethanol. While the dissolved borate ions are expected to be re-incorporated into the BG network, the level of precipitation was expected to decrease with the increase of aging time. The aging time is better to be slightly beyond 48 h rather than 24-48 h, as described in Chapter 4. In addition, even though there was sometimes still a little precipitation after the aging phase, they disappeared when mixed with the polymer binder. Therefore, when synthesizing 55S30C15B fibres, the parameters were not changed.

The further increase of borate content caused mass precipitation, so the level of ethanol needs to be increased for a full dissolution. Otherwise, undissolved boric acid will form its own crystallinity, or incorporate floating Ca ions to form calcium borate. The influence of the increased level of ethanol was first tested on sol-gel BG particles. During the synthesis of the sol-gel BG particles, the precursor was added as previously described, but instead of aging for 48 h under room temperature, the mixture was aged for 3 d under 60 °C to enable the formation of a gel. The gel was dried at 80 °C for 1 d and then at 130 °C for 40

h before the sintering process. But at first, crystal peaks for calcium borate occurred for BG with >35% borate incorporation.

This is because the stabilization temperature of the BGs (600 °C) exceeds the crystallization temperature of calcium borate (450 °C) [289, 295, 296], so the crystallization may also be formed even the boric acid is being dissolved. A modified sol-gel approach was proposed to solve the above-mentioned problem. TEOS and TEB were added to the mixture of ethanol and nitric and mixed for 1 d before the addition of ($Ca(NO_3)_2$)). This aimed to ensure the incorporation of boron to the BG network (the binding of borate to silicate groups) before binding of borate and Ca during the hydrolyzation and condensation phase. The crystallization temperature of calcium silicate is 1100 °C so Ca does not crystalize with a mixed network of silicate and borate at 600 °C [889]. Though this differs from the conventional approach, according to Lin *et al.*, Ca is only incorporated into the BG matrix after the formation of secondary particles [284] and heating to 400°C, so theoretically, Ca be added by the end of the gelling phase, as long as diffusion can occur and diffusion paths are not too long. This method enables the formation of BG particles with up to 55% borate incorporation. Beyond this point, the ethanol needed for the complete dissolution of the boric acid is so high that after 3 days of aging, the mixture is still a liquid. Therefore, after the drying phase, borate still binds with Ca which results in the formation of calcium borate after sintering. Another possible reason there are higher concentration of borate than silicates so that it is difficult to ensure that each borate group is locked within adjacent silicate groups.

The increase of ethanol in the sol-gel precursor also makes it unable to be electrospun because the viscosity, surface tension, and electroconductivity of the solution were greatly affected. The PVB binder solution also consists of ethanol, which can also dissolve borate groups, so that ethanol used in the preparation of the sol-gel precursor can be reduced. The new weight of PVB in the PVB binder solution is calculated as:

$$w = 1 + \frac{V_E - V_0}{11.4} \tag{5.1}$$

where w is the weight of PVB, V_E is the volume of ethanol used during the sol-gel process, V_0 is the volume of ethanol in the conventional sol-gel process, and 1 g/11.4ml is the original ratio used for the PVB binder. Since both the surface tension and viscosity of the mixture (precursor+binder) are primarily contributed to by the PVB binder, this change should theoretically result in similar solution parameters as those described in Chapter 4. Table 5. 1 illustrated the detailed quantities of the ingredients.

Table 5. 1. Nominal sol-gel compositions and the quantities of TEOS, nitric acid, ethanol, calcium nitrate, and triethyl borate used.

Compositions and initials (mol%)	TEOS (mL)	Nitric acid (mL)	Ethanol (mL)	$Ca(NO_3)_2$• $4H_2O$ (g)	TEB (ml)	PVB (g/11.4ml)
70Si-30Ca-0B (70S30C)	7.2	1.7	3.7	3.2	0	1
65Si-30Ca-5B (65S30C5B)	6.7	1.7	3.7	3.2	0.8	1
55Si-30Ca-15B (55S30C15B)	5.7	1.7	3.7	3.2	2.4	1
35Si-30Ca-35B (35S30C35B)	3.6	1.7	5.6	3.2	5.5	1.5
15Si-30Ca-55B (15S30C55B)	1.5	1.7	7.4	3.2	8.7	2.1
50Si-30Ca-65B (5S30C65B)	0.5	1.7	8.5	3.2	10.3	2.8
0Si-30Ca-70B (70B30C)	0	1.7	9	3.2	11.1	3

The electrospinning was similar to that described in Chapter 4. In general, 7 ml of the as-prepared mixture was sucked into a 10 ml syringe with a gauge 22 stainless steel needle. The electrospinning process was operated under the following parameters: electric field strength: 10 kV; flow rate: 0.4 mLh^{-1}; air gap distance: 12 cm; relative humidity: 25%-35%; inner diameter of spinneret: 0.7 mm; room temperature. The heating parameters were changed to ensure the complete removal of the polymer components. The resultant scaffolds were heated to 300 °C at a rate of 1 °C/min and dwelled for 6 h, and then heated to 600 °C at a rate of 1 °C/min and dwelled for 3 h before cooling naturally.

5.2.2 Characterization

The diffraction patterns were recorded with an XRD analyzer (Bruker D2 PHASER) using Cu-Kα radiation (λ = 1.542 Å) at 30 kV and 10 mA. The samples were scanned in the interval of $10°<2\theta<70°$ with a step size of 0.035° and a count rate of 12s per step. The chemical functional groups of the BG scaffolds were analyzed by ATR-FTIR Nicolet iS10. The scaffolds were crushed and analyzed in a range of 500–4000 cm^{-1}. A thin layer of the fibrous scaffold was sputter-coated with 20 nm chromium and characterized under the Inlens mode of an LEO-1525 SEM, with 5 kV accelerating voltage and 8 mm working distance. ImageJ was applied to derive the average diameters of the fibre from the SEM images.

5.2.3 Dissolution profiles

The dissolution profiles of the resultant BG scaffold in Dulbecco's Modified Eagle Medium (DMEM) were acquired according to that described by Norris *et al.* [97]. 25 mg of the resultant BG scaffolds were immersed in 37.5 mL of 5 mM TRIS or DMEM and cultured in an incubator shaker at 37 °C and 120 rpm, according to the standard suggested by Maçon *et al.* [802]. 0.5 mL of the dissolution products from each sample were collected at each time point (4, 24,,48, 72, 96, and 168 h), filtered with a 0.2 μm surfactant-free cellulose acetate filter (Corning, USA), and diluted with 4.5 mL of 2 M nitric acid. The resultant mixtures were characterized using ICP-AES at the wavelengths of 317.9 nm (Ca), 251.6 nm (Si), and 249.7 nm (B). The pH of the dissolution was measured at each time point by a pH meter with a thermal probe (Oakton pH 11 m with Oakton general-purpose glass pH probe, Ag/AgCl electrode, and Oakton ATC probe) attached to it. The values were taken as the average from three readings.

5.2.4 Biocompatibility test and protein expression on fibroblasts

In order to evaluate the viability of HDFs in media containing dissolution products of BG scaffolds, HDFs were seeded into 96-well plates at a density of 1×10^3 cells per cm^2 and cultured with DMEM (Gibco) containing 10% (v/v) fetal bovine serum and 1% penicillin/streptomycin (FBS, Thermo Trace Ltd., Melbourne, Australia). After incubation for 24 h, the DMEM was replaced by 100 μL of the dissolution products of BG scaffolds (6 $\mathrm{mg\,mL^{-1}}$ in DMEM), and their respective diluted products (1/2 and 1/4 with DMEM). HDFs cultured with pure DMEM were used as the blank control group. On days 1, 3, and 7, the metabolic activities (MA) of the HDFs were assessed through a Cell Counting Kit (CCK)-8 assay (Beyotime) according to the manufacturer's instruction. The results of metabolic activity were shown as units of optical density (OD) absorbance from an enzyme-linked immunoabsorbent assay microplate reader (Synergy 2, Bio-TEK) at a wavelength of 450 nm. On day 3, the supernatants of HDFs were extracted for the characterization of VEGF, bFGF, PDGF, TGF-β, and HIF-α through an Elisa assay (Abcam) according to the manufacturer's instructions. Finally, the cell proliferation rates were calculated using the following formula:

Cell viability rate = OD value of the experimental groups/OD value of the blank group * 100%

5.2.5 Proliferation, migration, and protein expression on endothelial cells

HUVECs were seeded in 96-well plates at a density of 3×10^3 cells per cm^2 and cultured with the endothelial cell culture medium (Sciencell, USA) with 5% (v/v) fetal bovine serum (FBS, Thermo Trace Ltd., Melbourne, Australia) and 1% (v/v) endothelial cell growth supplement/heparin kit (ECGS/H, Promocell). The BG-HDF conditioned media were acquired by extracting the supernatant of HDFs that has been cultured in BG dissolution products for 2 days. The conditioned media were mixed with endothelial cell culture medium (by 1:1 and 1:3) and 100 µL of the resultant mixture was applied to HUVECs. CCK-8 assay was applied in determining the MA of HUVECs on days 1, 3, and 7. Supernatant extracted by day 3 was assessed for VEGF, bFGF, HIF-α, and eNOS through the ELISA assay.

In addition, HUVECs were cultured in a 24-well Transwell plate with the endothelial cell culture medium until confluent. To investigate the role of BG-HDF conditioned medium on HUVEC migration, 250 µL of the above-mentioned mixture was added to the top layer of the well, while 300 µL of the mixture was added to the bottom layer. After being cultured for 16 hours under 37 °C and a 5% CO_2 atmosphere, the cells were stained with crystal violet (CV) for 1 min, and optical images were obtained using an optical microscope (Leica). The migrated cell numbers were analyzed by the Image J software.

5.2.6 Statistical analysis

The statistical significance of the results using a one-way ANOVA test followed by Dunn's Multiple Comparison. The significances between individual groups of the in vitro and in vivo assessment were marked as (*P <0.05, **P<0.01, ***P <0.001,****P <0.0001).

5.3 Results and Discussion

5.3.1 3D ECM-mimic borate-based bioactive glass fibre mats

Seven formulations of BG fibres, with borate concentrations ranging from 0 to 70 mol%, were prepared through the sol-gel electrospinning approach (Figure 5. 2 (a-g)). All fibres mats had fibre thickness within 0.5-2 mm [96], which is described as a 3D structure. The structure was formed due to the branching effect during electrospinning, which was caused by the repulsion force of Ca^{2+} ions and PVB molecules.

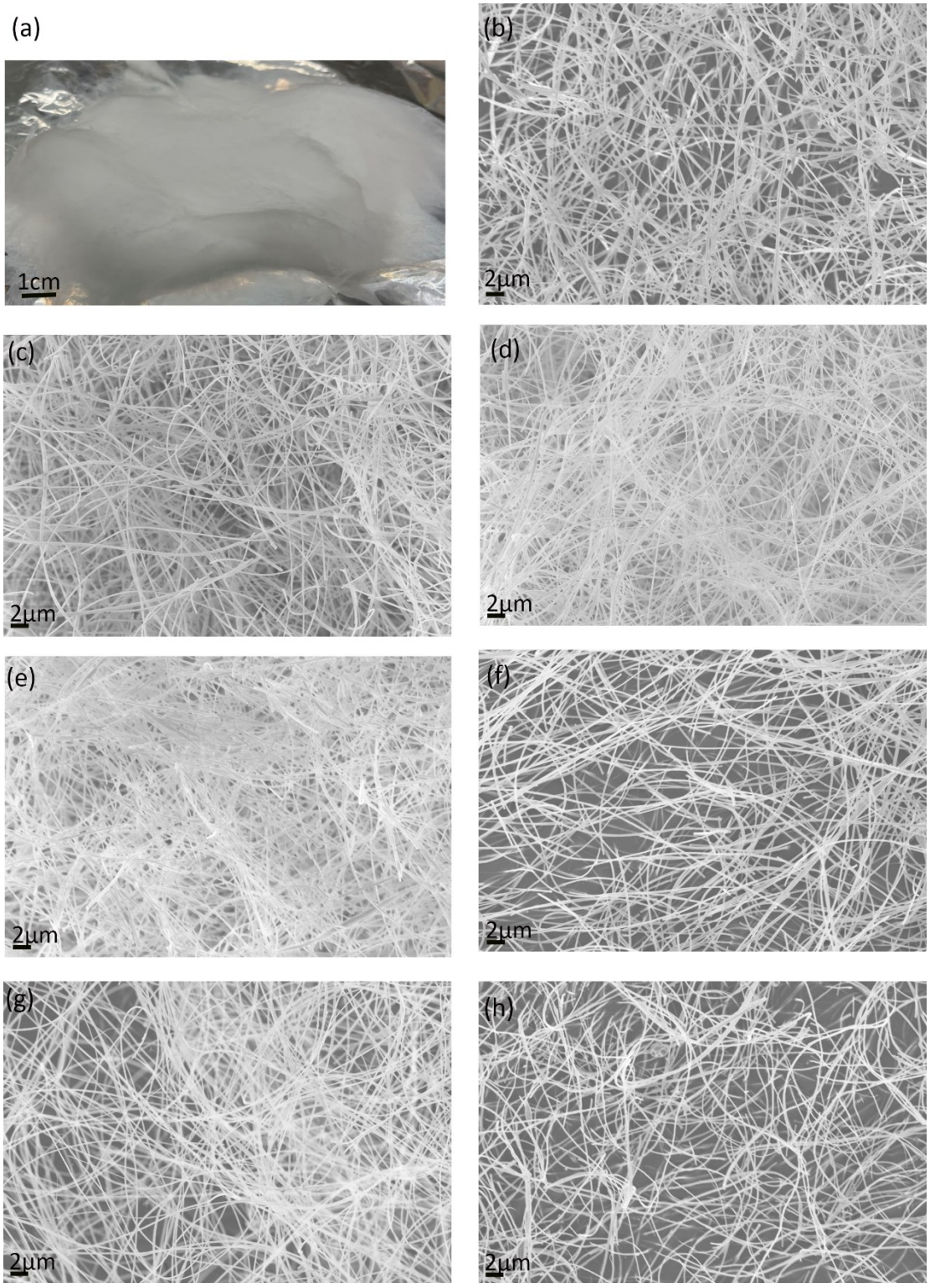


Figure 5. 2. (a) Schematics of 3D borosilicate BG fibre mats (b-h) SEM images of the electrospun bioactive glass fibre mats with composition (70-x) SiO_2-30 CaO-x B_2O_3, in mol% where x = (b) 0; (c) 5; (d) 15; (e) 35; (f) 55; (g) 65; (h) 70;

The diameters of the fibres were within 96-320 nm (Table 5. 2), which mimicked the collagen and fibronectin fibrils in the ECM. 70S30C fibres had the thickest diameters. The

incorporation of boron might have changed the parameters of the precursor (most likely electroconductivity as the PVB precursor was not changed until the borate content exceed 35 mol%). The fibre thickness then increased with the increase of borate composition up to 35 mol%. But the further increase of borate required the increase of PVB concentration so that after the PVB was being sublimed, the remaining BG fibres were much thinner. BG fibres with > 55 mol% borate had a darker appearance, probably due to the combined effect of calcium borate crystallization and carbon deposition from PVB, but their morphology was unchanged.

Table 5. 2. Fibre diameters of the electrospun bioactive glass scaffolds.

Sample	Fibre diameter (μm)
70S30C	0.32±0.07
65S30C5B	0.141±0.038
55S30C15B	0.198±0.032
35S30C35B	0.204±0.049
15S30C55B	0.176±0.036
5S30C65B	0.126±0.046
70B30C	0.096±0.033

5.3.2 Chemical structure of 3D ECM-mimic fibre mats

This study proposes a modified sol-gel approach to synthesizing borosilicate BGs, in which TEB was thoroughly mixed with TEOS to ensure that individual borate groups integrate with silicate groups. This microstructure highly increased thermostability gel, so that no crystallization occurred until the borate content in BG exceeded 55 mol%, due to the combined effect of ethanol evaporation during aging and drying, and that borates are more than silicates. XRD patterns (Figure 5. 3) of BG fibres with < 55 mol% borates have an amorphous halo around 20°-34° (2θ), similar to that of BG particles. The only peak may result from the deposition of carbon from PVB sublimation because the calcium borate crystallization should have a much higher intensity at 29.75°. However, for BG particles with >55 mol% borate incorporation, strong crystallization peaks are shown in the XRD pattern. The excessive amount of ethanol during the sol-gel process which prevents hydrolysis and condensation and the ethanol evaporation during aging and drying are major reasons for the crystallinity. For fibres with 55 mol% borate incorporation, the solvent evaporates during the jet propagation but there is little time for secondary particles to re-aligned themselves from amorphous states into the crystallized states. There are still a few peaks around 26.4°, 29.75°, and 46.8° which corresponded to the XRD patterns of calcium borate [890]. This is because there are still some secondary particles that are formed completely by borate groups so that when Ca ions are attached to borate secondary ions, they crystalize during BG stabilization. For BG with >65 mol% borate

content, the PVB concentration was so high that it cannot be fully removed through sublimation. Carbon from PVB reacted with borate groups and form boron carbide, which corresponded to peaks of 31° and 33° in the XRD patterns (Figure 5. 3 (a)) [891]. Besides, the peak around 29° may represent the formation of calcium carbonate [892].

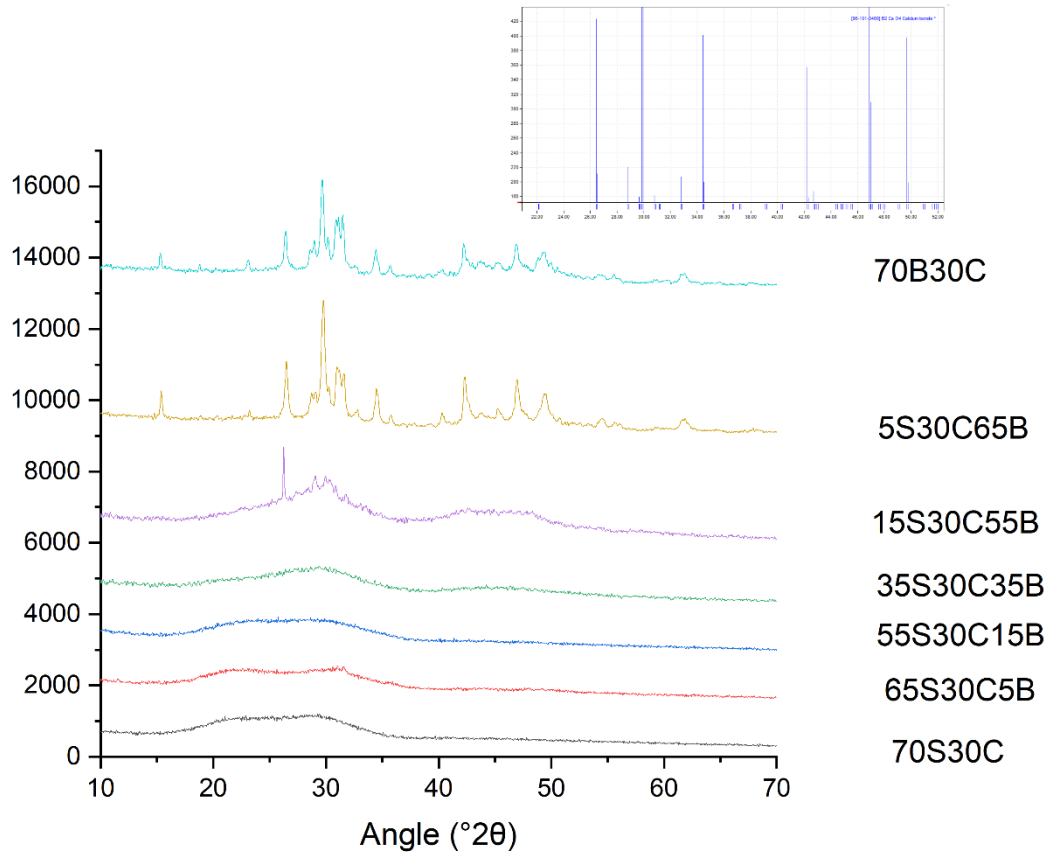


Figure 5. 3. XRD patterns of as-produced 70S30C, 65S30C5B, 55S30C15B, 35S30C35B, 15S30C55B, 5S30C65B, 70B30C bioactive glass fibre mats (along with an indication of the crystallization peaks for calcium borate).

FTIR (Figure 5. 4) analyzes the bonding in BG fibre mats. The presence of Si-O bonding is represented by the bands at 1040 cm^{-1} (vibration of Si-O bond), 790 cm^{-1} (vibration of Si-OH bond), and 470 cm^{-1} (Si-O-Si rocking) [252, 284, 808]. FTIR spectra also indicate the successful incorporation of boron into the BG microstructure, which corresponds to previous literature [886-888, 893, 894]. All BG fibres have bands at 925 cm^{-1} (Si-O-B vibration) and 1095 cm^{-1} (B-O vibration), but only 35S30C35B has a small band around 1400 cm^{-1}(B-O-B stretching) [895, 896]. This indicates that most borate groups are locked within silicate groups. There are also no bands presented at 1500 cm^{-1} (CO_3^{2-} bonding), 1420 cm^{-1} (NO_3^- bonding), 1638 cm^{-1} (OH^- bonding in water), and 1300–1500 cm^{-1} (OH bonding in ethanol).

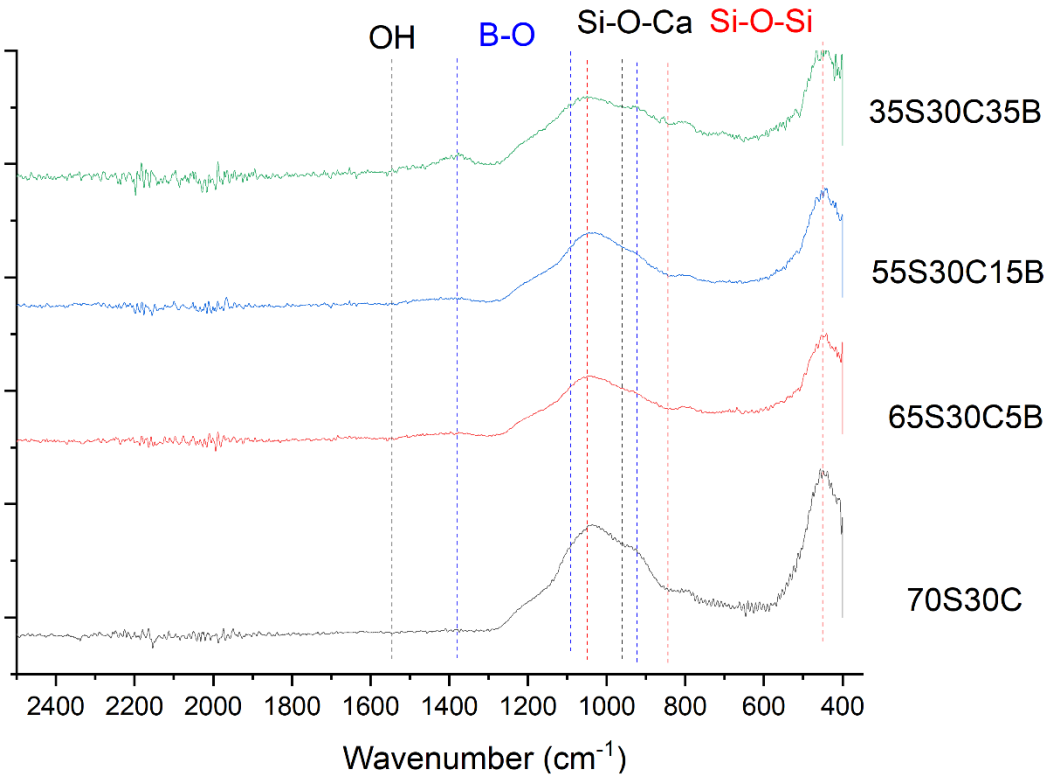


Figure 5. 4. FTIR spectra patterns of as-produced 70S30C, 65S30C5B, 55S30C15B, and 35S30C35B bioactive glass fibre mats.

5.3.3 Dissolution studies

The degradation of BGs into therapeutic ions is their major mechanism in wound healing. The dissolution profiles of BO_3^{3-}, Ca^{2+}, and Si (expected to be in the form of SiO_4^{4-}) from BG fibre mats were assessed in DMEM to understand the level of therapeutic level in real-life once the BG fibre mats are being implanted. In general, borosilicate BGs degrade much faster than silicate BGs as the B-O-B bonding does not require an excessive alkaline environment to break. The Ca^{2+} release from 70S30C was less than all BG fibres due to the faster dissolution of borosilicate BGs within the first 24-48 hours, but on day 7, the Ca^{2+} release from 70S30C was similar to that from 65S30C5B and 35S30C35B (Figure 5. 5 (a)). This is because of that deposition occurred to balance the excessively released Ca^{2+} on the first 2 days. The Ca^{2+} release from 55S30C15B was less than others. This can be due to the formation of BO_4 groups in the BG network [897]. BO_4 groups are usually formed due to the unsaturated oxygen atoms and cannot bond with another BO_4 group. Also, one BO_3 group can only bond with one BO_4 group so that the charges of unsaturated

oxygen atoms do not locally aggregate. The only approach to prevent the formation of the BO_4 group is to add strong alkali ions that neutralize the unsaturated charges. For instance, in industrial uses, Na and/or K are added to neutralize oxygen atoms in which Na/K: B ratio should be larger than 1:5 [898]. In comparison, Ca has a much weaker electronegativity and therefore not enough to neutralize the charges. It was hypothesized that BO_4 starts forming when borate composition increases from 5 to 15% so that the degradation kinetics of 55S30C15B was slower than that of 65S30C5B. With the further increase of borate composition in BGs, the degradation kinetics increased despite the increased formation of BO_4 groups as there were more borates in BG.

A similar trend was found in the release of silicate ions. Though borate was incorporated in the BG system, replacing silicates, the SiO_4^{4-} release in borosilicate BG fibres was higher than that in silicate BGs at all time points. 35S30C35B fibres had the highest SiO_4^{4-} release on day 7 even though its silicate composition was the minimum. The BO_3^{3-} release profile corresponded to both the borate content in BGs and the degradation kinetics so that the BO_3^{3-} release from 55S30C15B was not significantly different from that from 65S30C5B. 35S30C35B fibres had the highest BO_3^{3-} release at all time points.

The release profiles of BO_3^{3-}, Ca^{2+}, and Si agree with previous studies on the dissolution profiles of borosilicate BGs [899-901]. Ca^{2+} was reported to involve in various cellular activities during the wound healing cascade. For example, Ca^{2+} increases fibroblast proliferation [817-819] and keratinocyte proliferation [811, 817, 820, 821], but the exact concentration remains unknown, as some found that the therapeutic level was <20 $\mu g\ mL^{-1}$ while others said that >56 $\mu g\ mL^{-1}$ was ideal. The cytotoxic level of Ca^{2+} remains unknown and is highly dependent on the surrounding environment. Silicates can stimulate the proliferation of endothelial cells and fibroblasts in ionic or nanoparticle form [814, 815]. In general, BG dissolution products that contain 70 to 100 $\mu g\ mL^{-1}$ SiO_4^{4-} were non-toxic to cells, but the therapeutic ion concentration was not mentioned [399, 902, 903]. There has been a contradiction in the ideal BO_3^{3-} concentrations for cells. Some reports proposed that cell viability started to reduce when exceeding 10 $\mu g\ mL^{-1}$, although the cell types are not those in skin regeneration [904, 905]. But, Durand *et al.* proposed that the threshold toxicity level of BO_3^{3-} ions to endothelial cells are between 50-250 $\mu g\ mL^{-1}$ [57]. Recent studies on borate/borosilicate BGs also found that dissolution products containing 250-400 $\mu g\ mL^{-1}$ BO_3^{3-} was non-toxic to bone cells [902, 906]. The therapeutic level of boron may also be interrupted by surrounding elements so that the therapeutic level remains unknown. Besides, while the test is based on a static environment, its prediction of ion release is not as good as the dynamic one, which was described in the previous sections.

It would be better to create a system that enables a continuous flow of DMEM in order to have a more precise measurement of ion release.

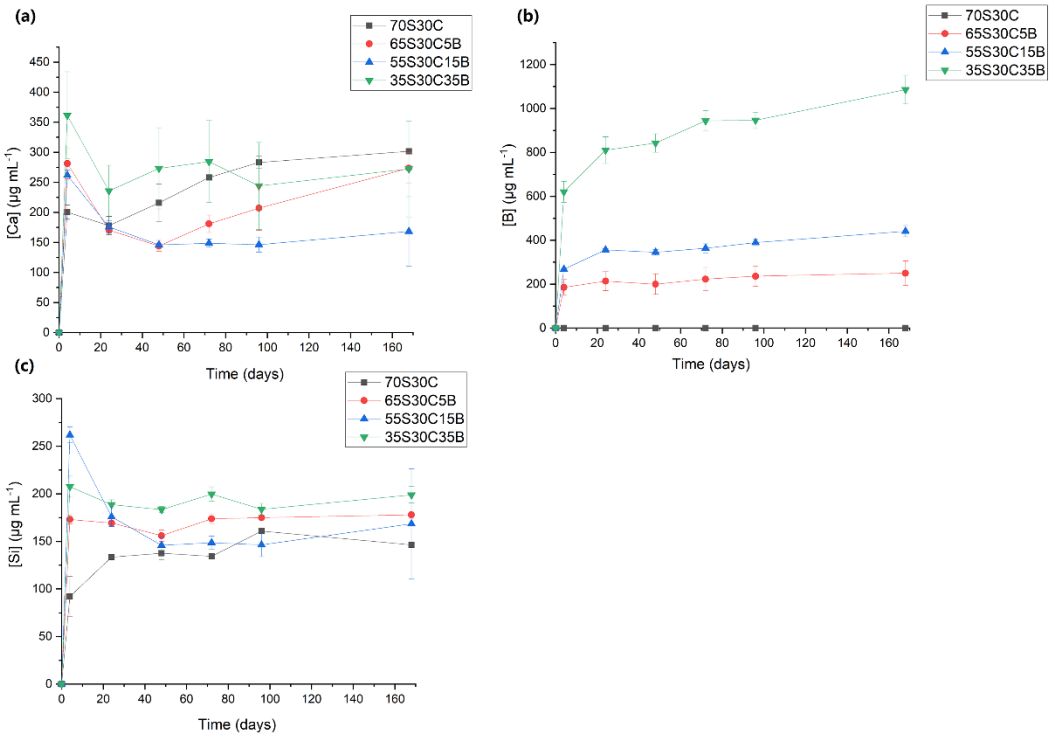


Figure 5. 5. Elemental concentration profiles (ICP) of DMEM following immersion of bioactive glass fibre mats 70S30C, 65S30C5B, 55S30C15B, and 35S30C35B over 7 d (a) Ca, (b) B, and (c) Si.

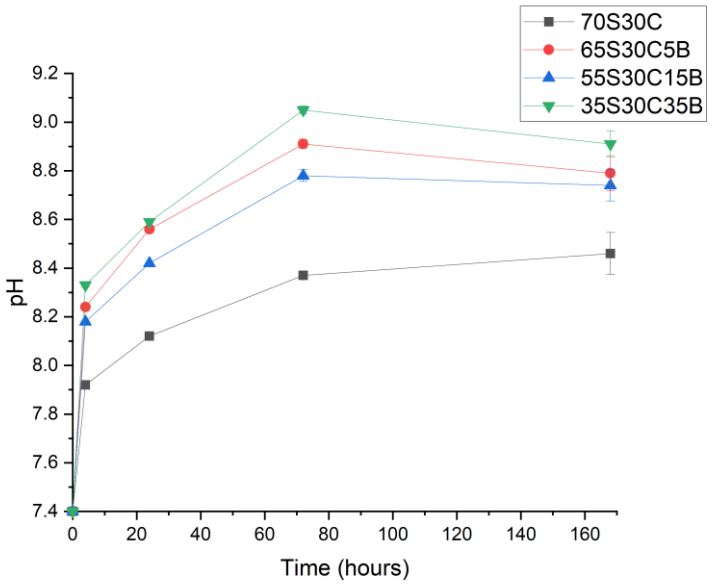


Figure 5. 6. pH change of DMEM following immersion of bioactive glass fibre mats 70S30C, 65S30C5B, 55S30C15B, and 35S30C35B over 7 d.

Figure 5. 6 indicates the pH change during the static dissolution studies. It can be seen that the dissolution products of borosilicate BGs induced a pH of around 9 after 3 days in DMEM. It is expected that the value increase on day 7. However, the values on day 7 may be subjected to bacteria in growth, as cotton-like moths are seen in a few pots. The bacteria leads to an acidic environment and those products containing moths have a pH below 7 so they were excluded from statics. Fortunately, the generation of bacteria did not seem to affect much of the ion dissolution profiles. As described in the previous section, the recovery of chronic wounds experienced a decrease in pH from 10 to 7 [830]. Therefore, further studies are still needed to understand the effect of pH on the release of ions as well as on the biological properties of dissolution products.

5.3.4 In vitro cytocompatibility assessment on HDF

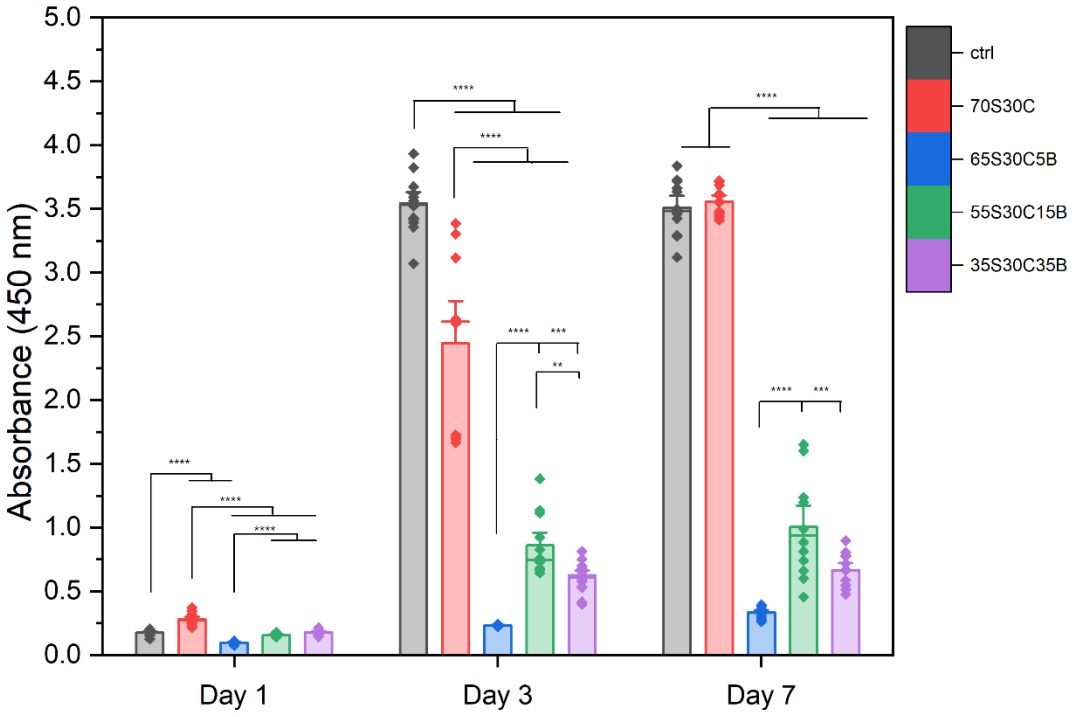


Figure 5. 7. The effect of the dissolution products of the 70S30C, 65S30C5B, 55S30C15B, and 35S30C35B fibre mats on the MA of HDFs at days 1, 3, and 7, represented by the intensity of absorbance at 450 nm. (*P <0.05, **P<0.01, ***P <0.001,****P <0.0001, n=12)

In vitro cytocompatibility assessments were conducted on fibroblasts (HDF cell lines). On day 1, both undiluted and diluted 70S30C dissolution products induced higher metabolic activity of HDFs (Figure 5. 7). This was due to the synergistic effect of both silicate ions [814, 815, 907] and calcium ions in the proliferation of fibroblasts [817-819]. The

incorporation of 5 mol% of borate induced toxicity to fibroblasts but the further incorporation of borate reduced the cytotoxicity. This was because of the high Ca content in the dissolution products, which induced a high alkaline environment and resulted in cytotoxicity. The highest pH of dissolution products of borosilicate fibres can reach 8.9-9 (Figure 5. 6). 55S30C15B had similar pH as 65S30C5B on day 7, but it may also have a higher boron level. This may indicate that 45 μg mL^{-1} of BO_3^{3-} was not only non-cytotoxic but also stimulate the metabolic activities of fibroblasts. Besides, diluted samples also had a lower pH and lower Ca release so they induced similar levels of metabolic activities as the control (Figure 5. 8 (a)).

On day 3, all undiluted dissolution products of BG fibres down-regulated the fibroblast viability. The cytotoxic effects of both 70S30C and 65S30C5B can be due to the excessive release of Ca^{2+} [261, 831], which was in correspondence to the previously reported inhibition effect of calcium-silicate BGs on fibroblasts [53, 54]. 65S30C5B had a much higher release of Ca^{2+} (120 μg mL^{-1} than 80 μg mL^{-1}) so that induced the highest reduction to the MA.

The MA of the diluted 70S30C and 65S30C5B dissolution products followed a similar trend. Similar to the trend on day 1, the dissolution products of 55S30C15B fibres had similar pH and Ca release as that of 65S30C5B fibres, but different BO_3^{3-}. Therefore, 55S30C15B fibres induced higher HDF viability than 65S30C5B fibres, but lower HDF viability than 70S30C fibres, but its 1/2 diluted product was completely non-toxic while that of 70S30C fibres remained cytotoxic (Figure 5. 8 (b)). This was because once the pH was relieved from dilutions, the released BO_3^{3-}, though halved, could still stimulate the viability of fibroblasts. BO_3^{3-} released from 35S30C35B may have exceeded the cytotoxic level so 35S30C35B fibres had higher cytotoxic levels than 55S30C15B fibres, but the reason for the cytotoxic effect of 1/4 diluted dissolution products of 35S30C35B was unknown.

Undiluted dissolution products from 70S30C fibres were completely non-toxic at day 7, while undiluted dissolution products from borosilicate fibres still down-regulated the metabolic activities of fibroblasts. Similar to the trend on day 3, 55S30C15B fibres stimulated the highest metabolic activities while 65S30C5B fibres stimulated the lowest. 1/2 diluted dissolution products of 70S30C and 55S30C15B fibres were non-toxic, but that for 65S30C5B and 35S30C35B were still toxic (Figure 5. 8 (c)). All 1/4 diluted BG dissolution products did not reduce the metabolic activities of HDFs.

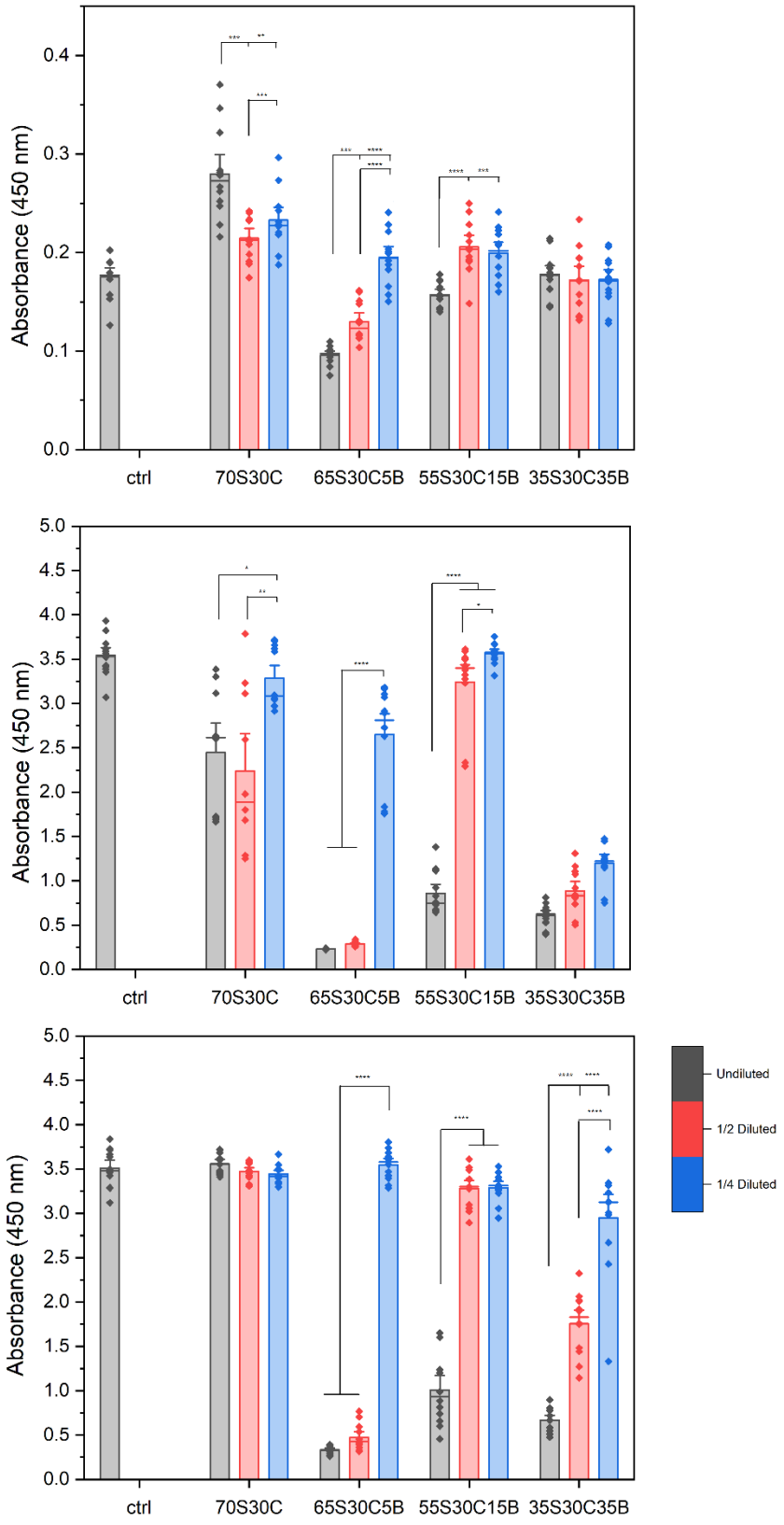


Figure 5. 8. The effect of undiluted, 1/2 diluted, and 1/4 diluted dissolution products on MA of HDFs at day (a) 1, (b) 3, and (c) 7, represented by the intensity of absorbance at 450 nm. (*P <0.05, **P<0.01, ***P <0.001,****P <0.0001, n=12)

The study of metabolic activity cannot fully represent the state or the number of cells in the in vitro studies. It was likely that the therapeutic ions interact with cells to create a hypoxia-mimic environment, which temporarily suppressed the cells (which means reducing metabolic activities) to express more proteins but does not cause cell death [908]. For instance, hypoxia reduces fibroblast activities and their capability in differentiating into myofibroblasts [909]. Furthermore, the decreased viability may also be due to the localized culture environment, as Brown *et al.* employed dynamic culture (which better mimicked the in vivo environment) and found no toxic effect under boron concentrations that were cytotoxic in static in vitro culture [448].

5.3.5 PDGF expression from fibroblasts

Platelet derived growth factors (PDGF) are important proteins that function throughout the chronic wound healing cascade. It was the first growth factor approved by the Food and Drug Administration for neuropathic wound healing [910]. It is delivered from the blood vessels through chemotaxis for the activation of fibroblasts and monocyte-to-macrophage differentiation [118, 119]. PDGF (both PDGF-AA and PDGF-BB)greatly enhances the rate of tissue granulation [911] and the level of collagen in wounds [912]. It is also a major regulator in various cellular responses, such as the ECM protein expressions from fibroblasts, angiogenesis, and epithelialization [110, 117, 841-843].

All undiluted dissolution products of BG fibres stimulated the expression of PDGF compared to the control (Figure 5. 9). Undiluted 70S30C products stimulated the highest PDGF expressions while all borosilicate BG fibres induced similar expressions. This is due to the Ca^{2+} release from BG fibres, as calcium influx is essential for PDGF stimulation [844, 845]. B incorporation was reported to stimulate PDGF expressions, as $50.6B_2O_3 - 23.7CaO - 6.43Na_2O - 8.24MgO - 8.46K_2O - 2.57SrO$ (mol%) BGs promoted higher expressions of PDGF in fibroblasts [66], but in this study, PDGF expressions decreased with the increase of borate content in BGs probably because of the reduced metabolic activities. All 1/2 and 1/4 diluted BG dissolution products hardly affected the PDGF expressions from HDFs. There has not been solid proof why the undiluted dissolution products simulate higher PDGF expressions than the diluted ones, and that the PDGF expressions seem inversely correlated to the viability. Usually, the gene expression to generate proteins is positively correlated to the metabolism of cells, which is the opposite of what our data shows. It has been reported that fibroblasts may shift to a quiescent phenotype from a proliferative phenotype after completing their role in ECM protein expressions and angiogenic factor expressions, but this behaviour has only been reported in primary HDFs [913]. One possible explanation can be that the high ion concentration

and pH force fibroblasts to generate more proteins that support their own survival (which can be hypoxia).

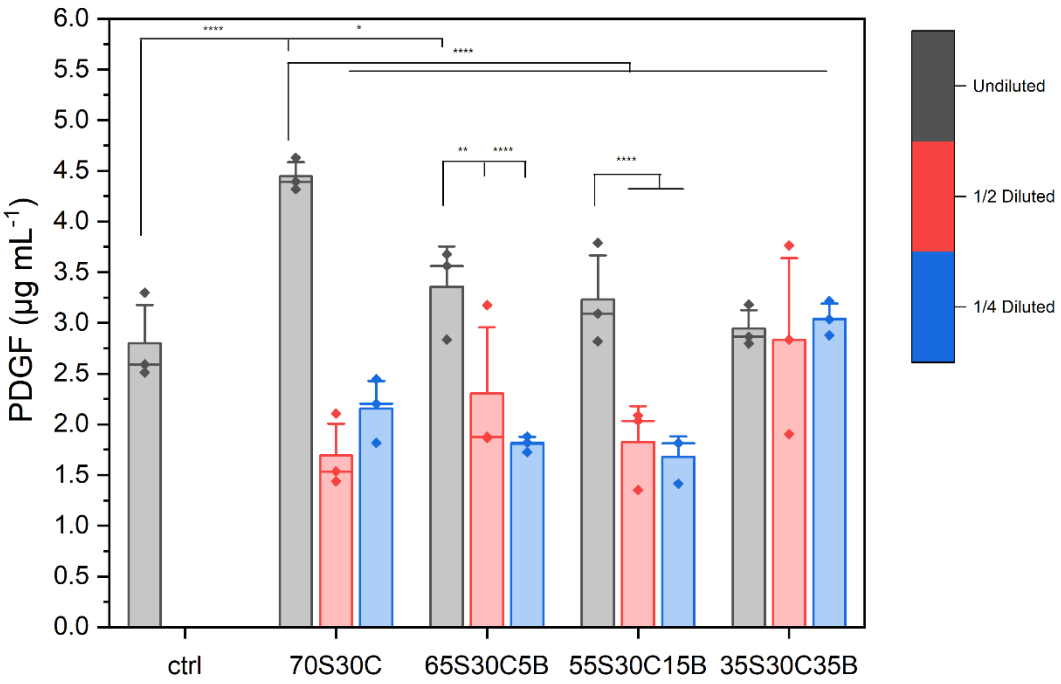


Figure 5. 9. PDGF expressed from the HDFs (ELISA assay) cultured with the undiluted and 1/2 diluted dissolution products of the 70S30C, 65S30C5B, 55S30C15B, and 35S30C35B fibre mats, for 3 days. (*P <0.05, **P<0.01, ***P <0.001,****P <0.0001, n=3).

5.3.6 TGF-β expression from fibroblasts

Diabetic ulcers are often accompanied by substantial TGF-β reduction [914]. The first reason is that TGF-β is a signal derived from platelets and neutrophils to induce leukocyte chemotaxis to promote leukocyte activities, including their activation, their aggregation, and release of protease/protease inhibitors [18, 114-116]. TGF-β also supports fibroblast activities from their chemotactic and pro-mitotic activities to their differentiation into myofibroblasts [846], regulation for ECM protein deposition [847, 915], and angiogenesis [114].

The undiluted dissolution products of 70S30C and 65S30C5B significantly reduced TGF-β expressions from fibroblasts (Figure 5. 10). This agrees with the reduced fibroblast proliferation by Day 3, as TGF-β is an important signal for fibroblast activities. Diluted 70S30C and 65S30C5B up-regulated TGF-β expressions from fibroblasts. This is because Ca^{2+} released stimulate Factor IV in the integrin activation of TGF-β [848, 849]. Undiluted 55S30C15B and 35S30C35B products also had high Ca^{2+} released to up-regulated TGF-

β expression from HDFs. This may indicate that boron stimulates TGF-β expressions from fibroblasts, but the ideal concentration has not been found. All 1/4 diluted dissolution products induced similar levels of TGF-β expressions to the blank media.

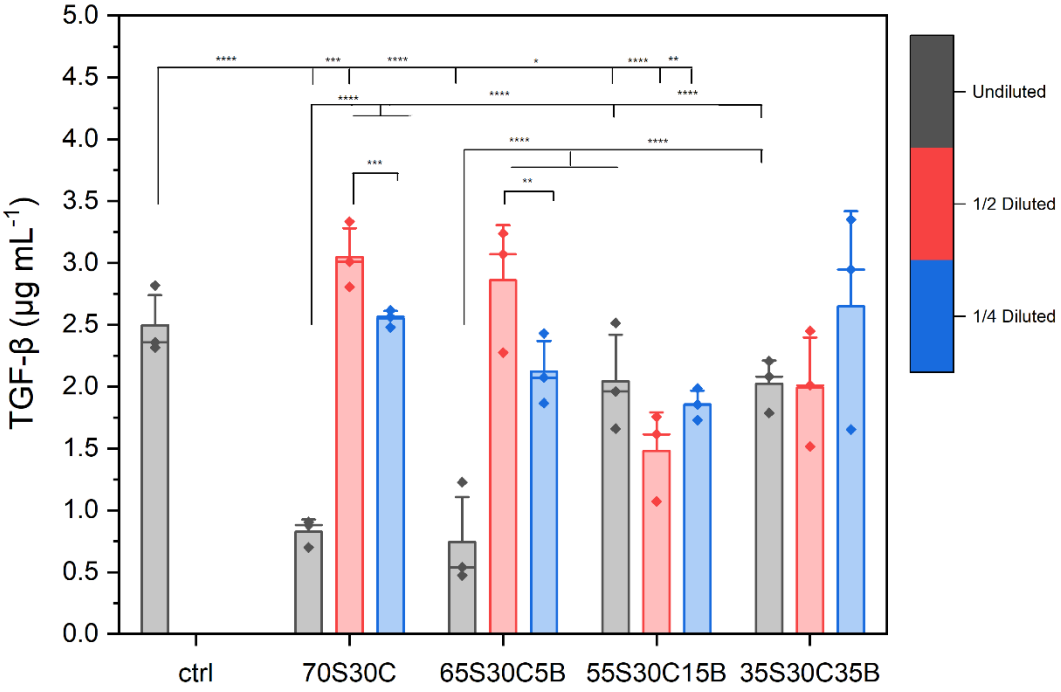


Figure 5. 10. TGF-β expressed from the HDFs (ELISA assay) cultured with the undiluted and 1/2 diluted dissolution products of the 70S30C, 65S30C5B, 55S30C15B, and 35S30C35B fibre mats, for 3 days. (*P <0.05, **P<0.01, ***P <0.001,****P <0.0001, n=3).

5.3.7 HIF-1α expression from fibroblasts

Hypoxia-inducible factor 1-alpha (HIF-1α) is a protein that induces the transcription of more than 60 growth factor expressions, including VEGF and bFGF, through the generation of a hypoxia-mimic environment [852, 853]. Diabetes commonly comes with HIF-1α dysfunction as a high glucose environment impairs HIF-1α-to-p300 interaction [916] and much in vivo evidence stated the importance of the stabilization of HIF-1α to chronic wound regeneration [917-919].

All undiluted BG dissolution products increased HIF-1α expression from HDFs (Figure 5. 11). This agrees with the Ca^{2+} release profile, as Ca^{2+} activates HIF-1α through the upstream expression of ERK in the hypoxia signal transduction pathway [854, 855] and stimulates the translation of HIF-1α to α subunits through the activation of classical protein kinase and mammalian targets of rapamycin [856, 857]. 1/2 and 1/4 diluted 70S30C dissolution products stimulated higher HIF-1α expression than undiluted media, as a more

neutral pH favours the increase of HIF-1α expressions [920, 921]. The HIF-1α expressions from undiluted dissolution products of borosilicate BG were similar to that of 70S30C, but those from diluted dissolution products of borosilicate BG were much lower. This may be because regardless of the culture environment, the HIF-1α expressions from HDFs tended to be at a constant level and the excessive HIF-1α balanced with the increased HIF-1α binding to HDFs (which stimulates angiogenic factor expression). BO_3^{3-} at all concentrations may be able to interact with HIF-1α and HDFs to accelerate their binding rate.

In previous sections, we predicted that the decrease in cellular metabolic activities was due to the induced hypoxia in cells. If the hypothesis is true, we will expect a significant difference in HIF-1α expression from BG samples compared to the control per cell. Although we have not tested the total DNA analysis so we would not know the exact cell number, the metabolic activity may have an indication of the actual cell number (as the increase in metabolic activity can only be due to the increase of activity per cell or the increase in cell number). Since the control HDFs have 5-10 times to HDFs cultured with BG samples and the HIF-1α expressions between groups are similar, it can be deduced that the protein expression from cells increases significantly, which may add proof to our previous hypothesis.

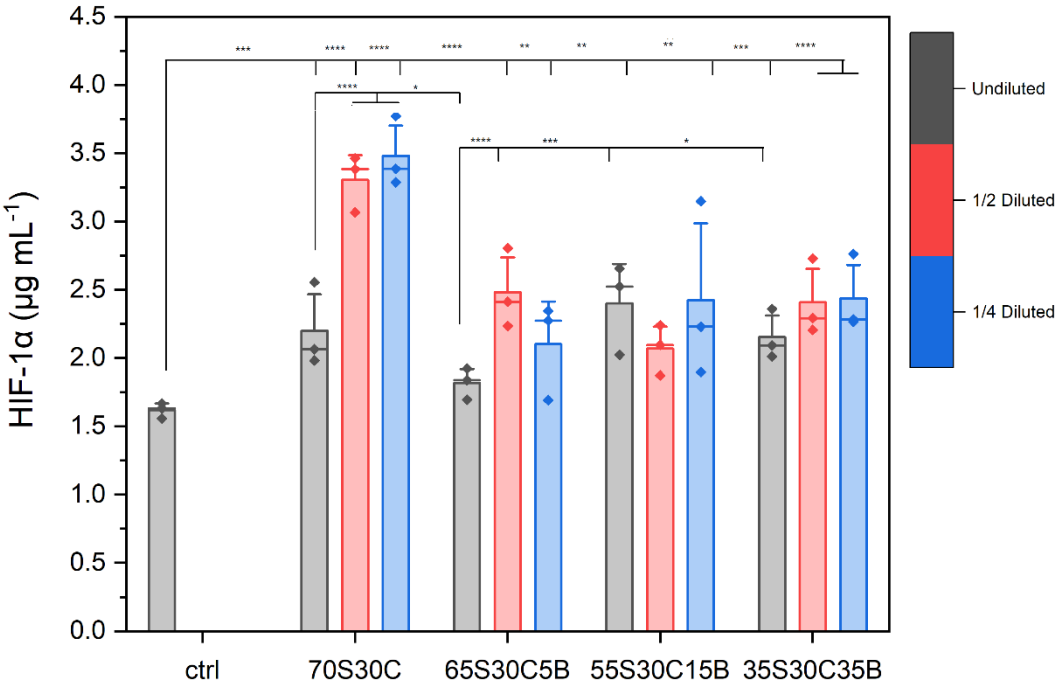


Figure 5. 11. HIF-1α expressed from the HDFs (ELISA assay) cultured with the undiluted and 1/2 diluted dissolution products of the 70S30C, 65S30C5B, 55S30C15B, and 35S30C35B fibre mats, for 3 days. (*P <0.05, **P<0.01, ***P <0.001,****P <0.0001, n=3).

5.3.8 VEGF expression from fibroblasts

Angiogenesis is one of the most important steps in the chronic wound healing cascade as it enables better delivery of nutrients, oxygen, and proteins to the wound site [25]. The interplay of HIF-1α and fibroblasts up-regulates the expressions of VEGF [868, 922, 923]. The binding of VEGF with their receptors on the endothelial cell membrane stimulates the proliferation and migration of endothelial cells to form tubules. Many papers reported the efficacy of SiO_2-CaO based BGs on the up-regulation of VEGF from fibroblasts [53, 54, 588, 592].

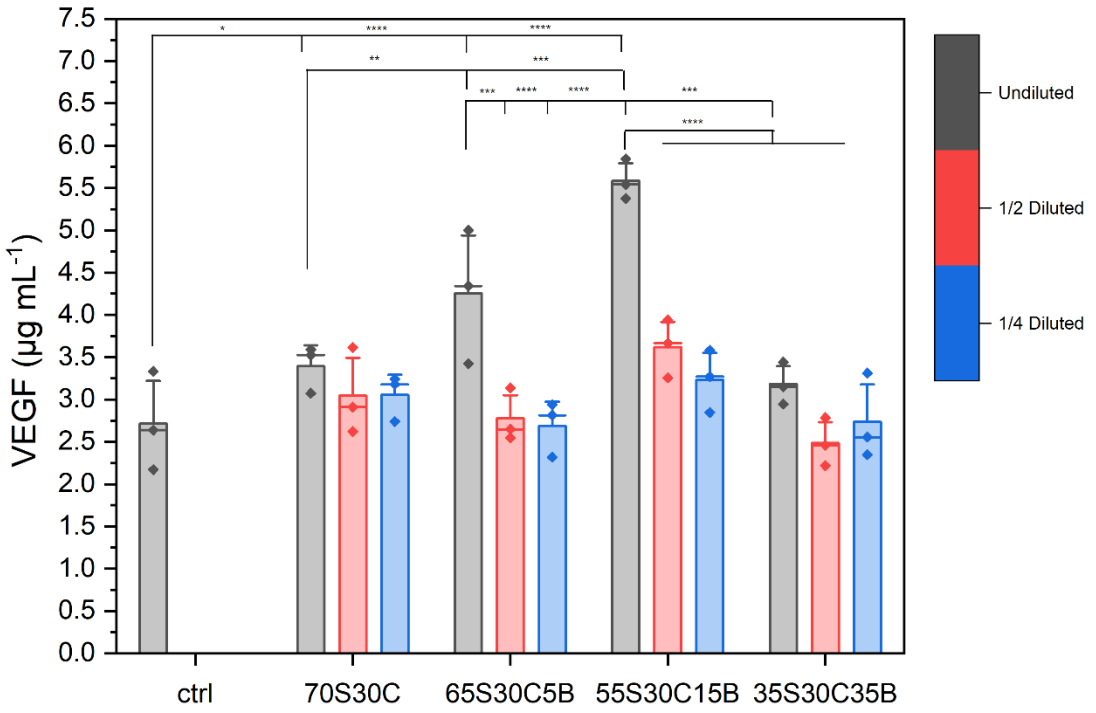


Figure 5. 12. VEGF expressed from the HDFs (ELISA assay) cultured with the undiluted and 1/2 diluted dissolution products of the 70S30C, 65S30C5B, 55S30C15B, and 35S30C35B fibre mats, for 3 days. (*P <0.05, **P<0.01, ***P <0.001,****P <0.0001, n=3).

The undiluted dissolution products of the 70S30C upregulated the expressions of VEGF from fibroblasts compared to the control (Figure 5. 12), which agrees with Norris *et al.*, who found that SiO_2-CaO based BG fibres up-regulated VEGF expressions from fibroblasts [97]. This is due to the synergistic effect of SiO_4^{4-} [598, 600, 601] and Ca^{2+} ions [605, 610]. The incorporation of borate up to 15 mol% further stimulated the expressions of VEGF from fibroblasts. This agrees with Haro Durand *et al.*, who found similar up-regulation of VEGF when culturing fibroblasts with 45S5 BG containing 2 wt% borates [57,

618]. Further incorporation of borate up to 35% decreased the expressions of VEGF and bFGF due to reduced metabolic activities. Both 1/2 and 1/4 diluted dissolution products all induced similar VEGF expressions from HDFs as the control.

5.3.9 bFGF (FGF-2) expression from fibroblasts

bFGF (FGF-2) is another important factor during the angiogenic cascade. Like VEGF, it was also stimulated due to the interplay of HIF-1α and fibroblasts [868, 922, 923]. The function of bFGF in angiogenesis was slightly weaker than that of VEGF, as it has been proposed that the formation of blood vessels can occur with no presence of bFGF, but not with VEGF [924, 925]. But, as a factor from the FGF family, bFGF promoted fibroblast proliferation and migration, the deposition, and arrangement of the ECM, wound closure and re-epithelialization, etc. [868-870].

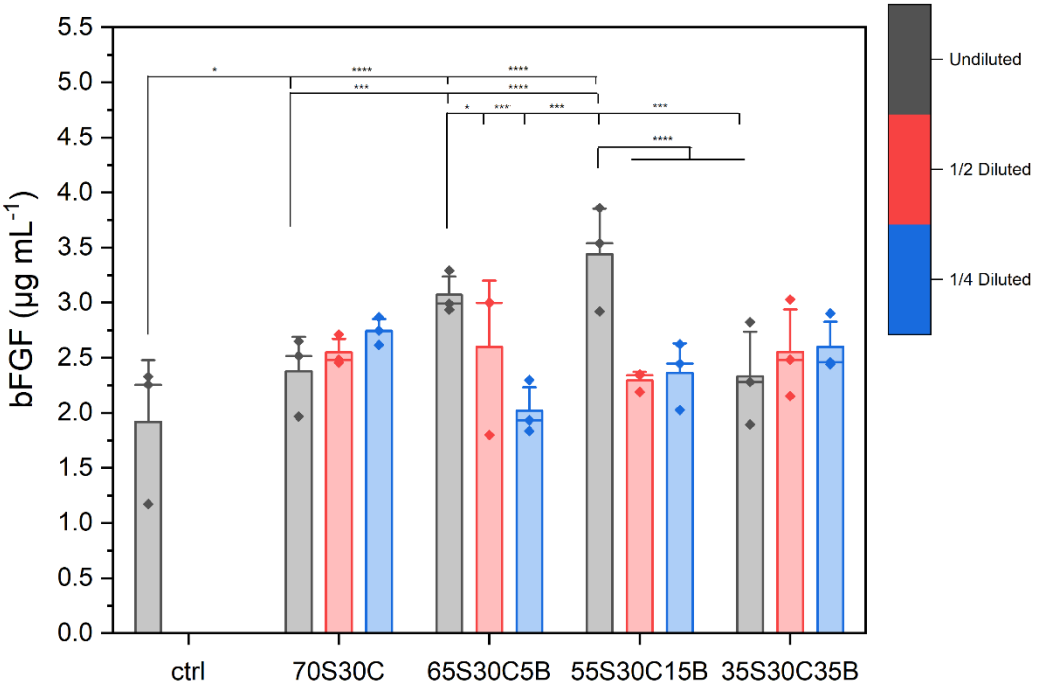


Figure 5. 13. bFGF(FGF-2) expressed from the HDFs (ELISA assay) cultured with the undiluted and 1/2 diluted dissolution products of the 70S30C, 65S30C5B, 55S30C15B, and 35S30C35B fibre mats, for 3 days. (*P <0.05, **P<0.01, ***P <0.001,****P <0.0001, n=3).

The undiluted dissolution products of the 70S30C upregulated the expressions of bFGF from HDFs (Figure 5. 13) and the 1/2 and 1/4 diluted 70S30C products had slightly higher bFGF expressions. SiO_4^{4-} [598, 600, 601] and Ca^{2+} ions [605, 610] both contribute to the

bFGF expressions, but the further increase of ion concentration beyond that from 1/2 diluted 70S30C product did not have a significant effect. Undiluted 65S30C5B stimulated higher bFGF expressions than undiluted 70S30C product, while undiluted 55S30C15B stimulated higher bFGF expressions than undiluted 65S30C5B product. 35S30C35B induced much lower bFGF expression than 55S30C15B due to the lower cell viability. This was most likely due to the effect of borate ions, but the mechanism remains uncertain [57, 618]. The difference in therapeutic ion levels of each protein, the influence of one ion on another ion's activity, the effect of pH, the accurate correlation between ion concentration and biological responses, and the effect of other factors remain undiscovered.

5.3.10 In vitro endothelial cell viability and protein expressions

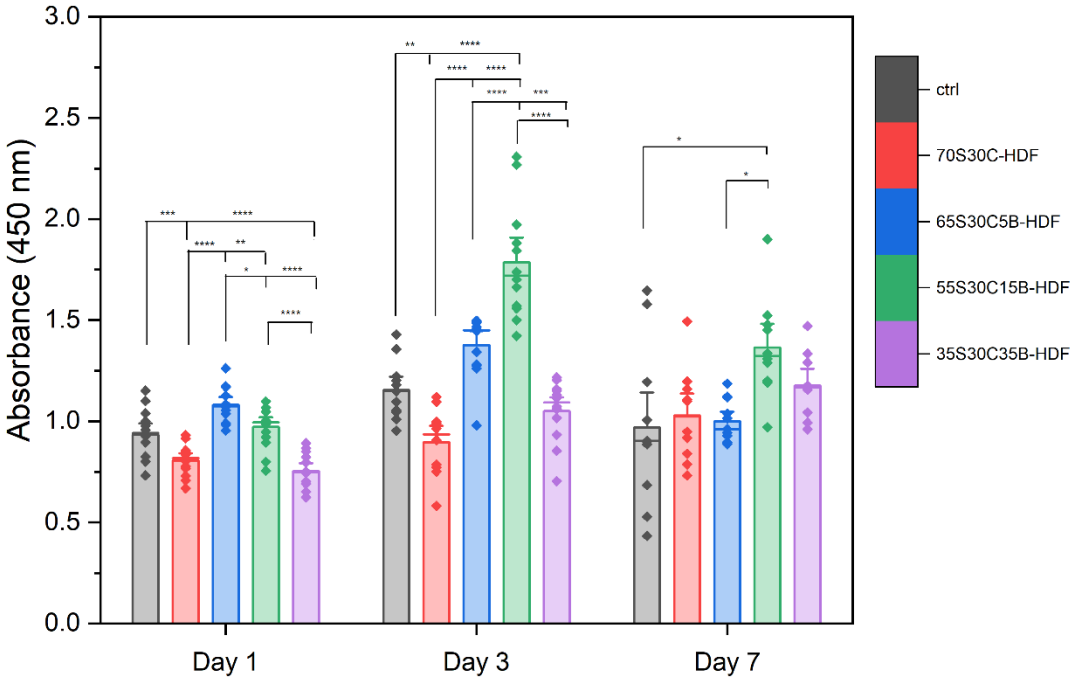


Figure 5. 14. Metabolic activity of HUVECs at day 1, 3, and 7 from HUVECs at day 3 after being cultured in the BG-HDF conditioned media, conditioned with 70S30C, 65S30C5B, 55S30C15B, and 35S30C35B fibre mats and the DMEM-HDF conditioned media. (*P <0.05, **P<0.01, ***P <0.001,****P <0.0001, n=12).

BG fibres seemed to stimulate angiogenesis through a combined effect of (1) the angiogenic factors released from fibroblasts and (2) the role of released ions directly on the proliferation and migration of endothelial cells and their protein expressions. To investigate this combined effect, BG-HDF conditioned media, pre-cultured with BG for 2 days, were applied to endothelial cells to mimic the angiogenic environment. On day 1, the 70S30C-HDF and 35S30C35B-HDF media reduced the metabolic activities of

HUVECs (Figure 5. 14 (a)). This agrees with the previous results that the dissolution products of 70S30C and 35S30C35B reduced the metabolic activity of HDFs (Figure 5. 8), as high Ca^{2+} or BO_3^{3-} release was cytotoxic. 65S30C5B-HDF media did not reduce the metabolic activity of HUVECs because 65S30C5B stimulated higher VEGF and bFGF expressions from HDFs.

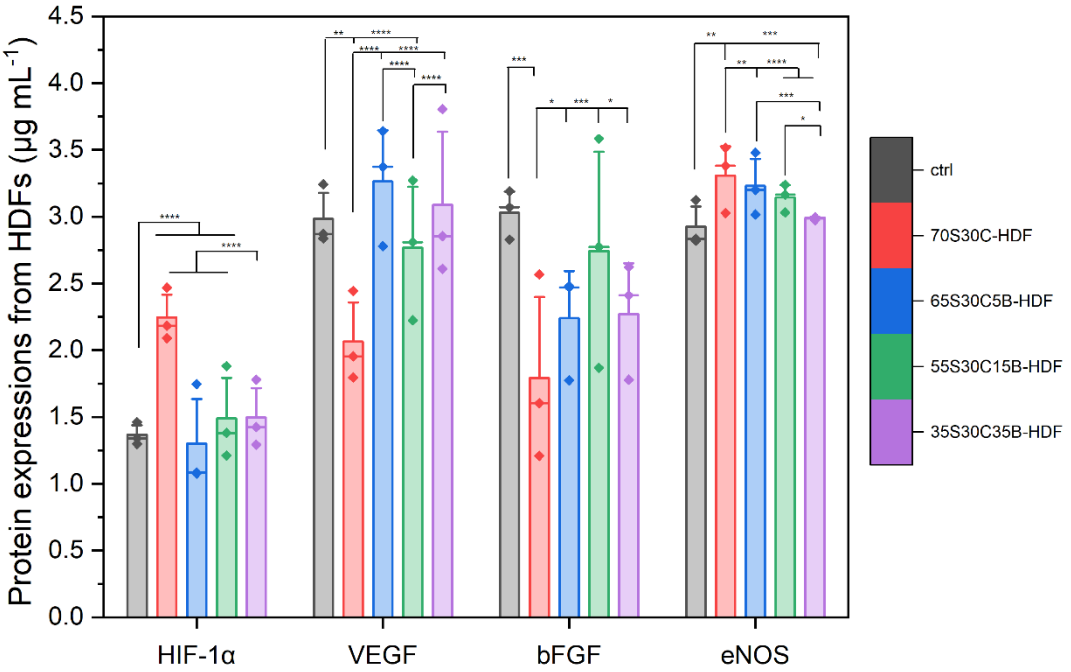


Figure 5. 15. Elisa results of HIF-1α, VEGF, bFGF (FGF-2), and eNOS expressions from HUVECs at day 3 after being cultured in the BG-HDF conditioned media, conditioned with 70S30C, 65S30C5B, 55S30C15B, and 35S30C35B fibre mats and the DMEM-HDF conditioned media. (*P <0.05, **P<0.01, ***P <0.001,****P <0.0001, n=3).

The metabolic activities of HUVECs on day 3 were relevant to not only the proteins from HDFs media but also the proteins expressed by HUVECs themselves. The protein expression profiles of HUVECs (Figure 5. 14 (b)) revealed: 70S30C-HDF media up-regulated HIF-α but down-regulated VEGF and bFGF; 65S30C5B-HDF media up-regulated HIF-α but did not influence VEGF and bFGF; 55S30C15B-HDF media up-regulated HIF-α and highly up-regulated VEGF; 35S30C35B-HDF had no influence to all proteins compared to the DMEM-HDF media. As a result, 70S30C-HDF media decreased the metabolic effect, 65S30C5B-HDF media slightly increased the metabolic effect, 55S30C15B-HDF media strongly increased the metabolic effect, and 35S30C35B-HDF media did not affect the metabolic effect compared to the DMEM-HDF media, which agrees with the profile at day 3. On day 7, the cells were confluent, so the metabolic for all

media were similar except for the reduction in 70S30C-HDF media, which disagrees with Midha *et al.*, who found that 70S30C-HDF media up-regulated the metabolic activities of HUVECs [873]. The discrepancy may be due to the difference in BG dose and ion level, as only small doses of BG stimulated HUVEC proliferation while large doses were cytotoxic, or the different operational parameters of the study (cell seeding density, etc.) [53, 54, 588].

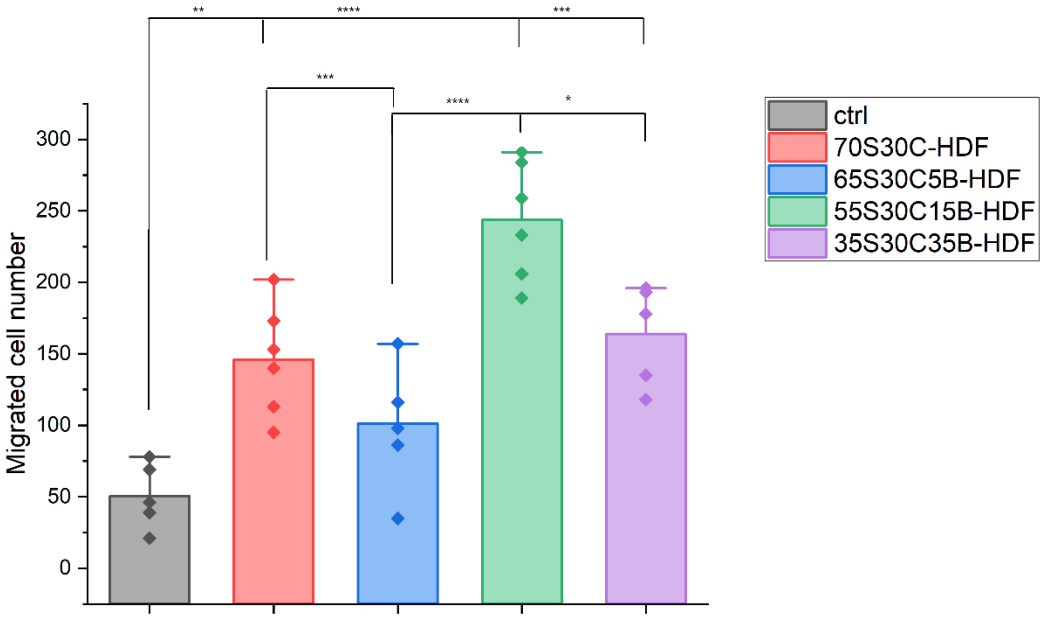


Figure 5. 16. Cell number of migrated HUVECs after being cultured for 16 hours in a Transwell assay with the DMEM-HDF medium, and 70S30C-HDF, 65S30C5B-HDF, 55S30C15B-HDF medium, and 35S30C35B-HDF medium. (*P <0.05, **P<0.01, ***P <0.001,****P <0.0001, n=6).

Ca^{2+} has been reported to stimulate various endothelial cell activities, including fueling ligand-receptor interactions [877], mediating protein kinase C, a protease that regulates endothelial permeability [878, 879], and promoting the expressions of messenger RNAs [880], etc. One of its main functions is to induce the expression of eNOS, the nitric oxide in vascular endothelium [881], through its interaction with VEGF [885]. Our result revealed (Figure 5. 15 (b)) increased eNOS expressions from HUVECs when treated with 70S30C-HDF media, which agrees with previous findings [235, 885, 926]. The eNOS expressions further decreased with the incorporation of B_2O_3, as boron reduces oxidative stress [927]. The incorporation of B_2O_3 further improved the metabolic activities until reaching cytotoxic level, which agrees with Durand *et al.*, who reported that 2 wt% of B_2O_3 incorporated in 45S5 BG stimulated the proliferation of endothelial cells and their expressions of VEGF

and bFGF [57]. The critical BO_3^{3-} concentration was estimated to be 60 μg mL^{-1} [57], but more evidence is needed. Besides, the concentration-to-effect mechanism remains unknown.

5.3.11 In vitro endothelial cell migration

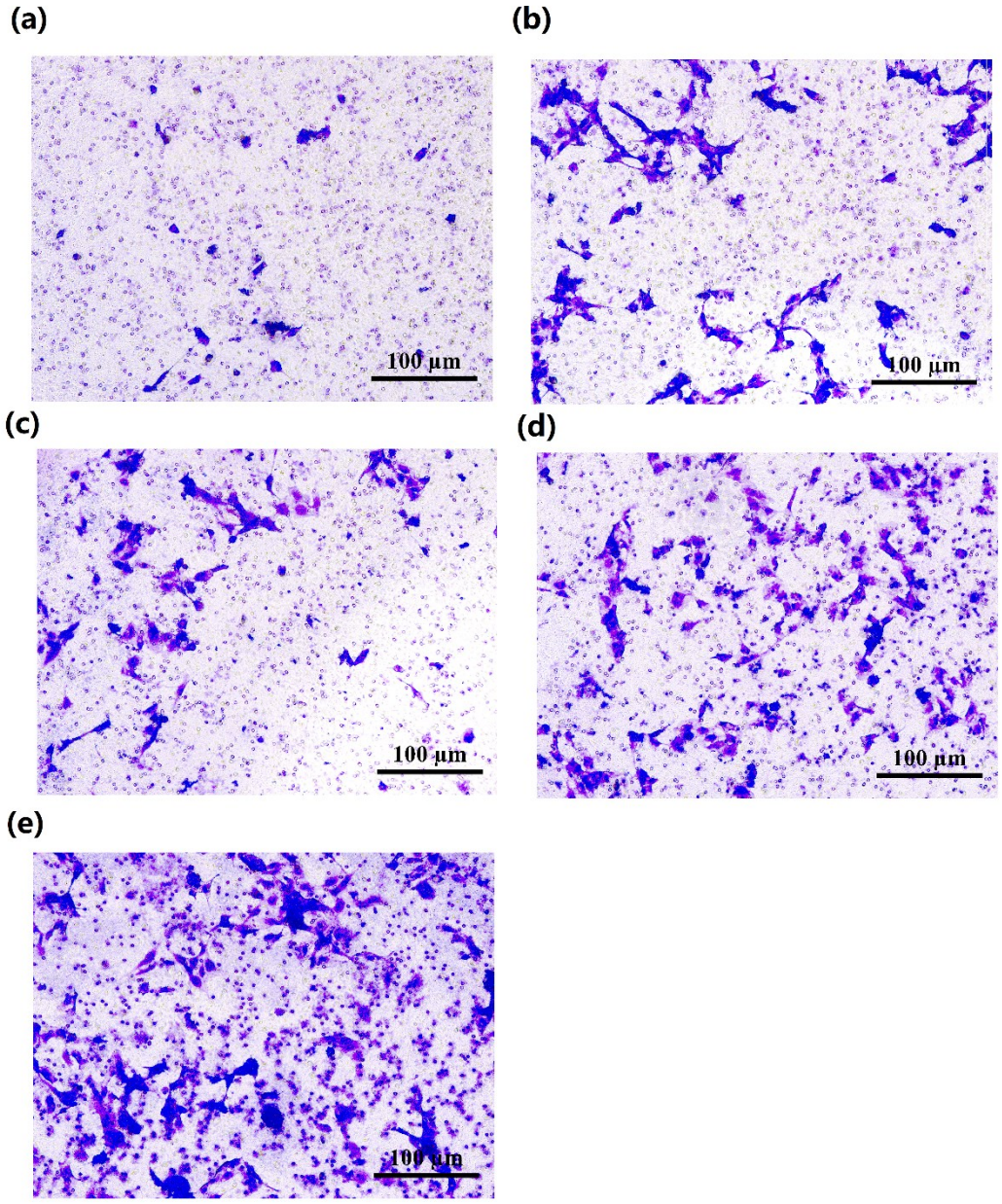


Figure 5. 17. (a-e) images of migrated HUVECs after being cultured for 16 hours in a Transwell assay with (a) the DMEM-HDF medium, (b) 70S30C-HDF conditioned medium, (c) 65S30C5B-HDF conditioned medium, (d) 55S30C15B-HDF conditioned medium, and (e) 35S30C35B-HDF conditioned medium.

Migration allows endothelial cells to form tubular structures. At its activation stage, endothelial cells sense the VEGF gradient and migrate toward the more concentric sites [874]. They then protrude, attach their protrusions to the ECM fibres, form stress fibres to contract themselves, and finally relieve the stress to complete one cycle of migration [928]. VEGF and bFGF are two major chemotaxes throughout the process, as they deplete at their binding site to activate the protrusion, integrin-binding of endothelial cells to the ECM, stress fibres generation, etc. [875, 876, 929]. Within 16 hours, all BG-HDF media stimulated the migration of endothelial cells than the DMEM-HDF media (Figure 5. 16, Figure 5. 17), which agrees with the ELISA pattern from fibroblasts (Figure 5. 12, Figure 5. 13). While the test only runs for 16 hours, it was unlikely that the proliferation have much influence to cellular activity particular considering that cells at the upper chamber are confluent. Similar stimulation effects were found in the form of nanoparticles or nanofibres of SiO_2-CaO based BGs [543, 698, 724], which is the key reason for their success in in vivo angiogenesis [91, 552]. BO_3^{3-} incorporation further stimulates the migration of endothelial cells [57, 91, 617]. The main mechanism was their stimulation of VEGF and bFGF from fibroblasts [69, 257, 611]. Boron also stimulates the activities of ion-channel NaBC1 and VEGF receptors on endothelial cells [613]. These mechanisms explain the overwhelming angiogenic efficacies of borate-based BGs in vivo compared with silicate-based BGs [72, 84, 620, 930].

5.4 Concluding remarks

Diabetic ulcers have been a great threat to our healthcare system. In this chapter, a modified sol-gel electrospinning approach was proposed to electrospin BGs with a composition of (70-x) mol% SiO_2-30 mol% CaO- x mol% B_2O_3 (x=0, 5, 15, and 35, while higher compositions induced crystallization or carbon deposition) as wound matrices for the regeneration of diabetic ulcers. The scaffold had a 3D structure consisting of entwined fibrils, which mimicked the ECM environment to stimulate cell attachment and migration and facilitate a controlled release of BO_3^{3-}, Ca^{2+}, and SiO_4^{4-} which were therapeutic to stimulate ECM deposition and angiogenesis. Though the undiluted dissolution products inhibited cell viability, the 1/2 diluted product of 55S30C15B fibres was non-cytotoxic. 55S30C15B fibres stimulated more PDGF, TGF-β, and HIF-1α expressions than the control and much higher expressions of VEGF and bFGF than other BG samples. This chapter also accessed the function of BG dissolution products to endothelial cell activities, in terms of their viability and migration. The protein expression from endothelial cells was also studied to understand the mechanism of BGs in angiogenesis. In summary, the borosilicate BG fibres can be promising strategies for wound healing applications.

55S30C15B fibre mat has the best efficacy in angiogenesis and ECM deposition. Further in vitro assessment of the role of BG in anti-inflammatory effects, epithelialization or neuron regeneration may provide further insight into the understanding of the mechanism of BG fibre mats in the regeneration of diabetic ulcers. In vivo studies were also conducted to understand the function of the fibres in real life, as detailed in Chapter 6.

6 In vivo analysis of borate-based bioactive glass fibre mat on diabetic rodent model

6.1 Introduction

Diabetic ulcers are a complex disease caused by combined effects of various factors, such as high inflammation, neuropathy, local ischemia, dysfunctional keratinocytes, etc. [186, 187]. While these factors have synergistic effects on each other, it is difficult to cover all the above-mentioned factors through in vitro studies. In vivo assessment is one of the most important steps in proving the efficacy of materials as it better mimicked the real-life situation once the sample is being implanted. Combining in vitro and in vivo results provides evidence to understand the mechanism of BGs to individual steps of wound healing. In this chapter, the role of BG samples was analyzed in vivo in diabetic C57BJ/6 mice. The type of mice, age, and weight were selected based on previous literature [785-787] and these mice were intraperitoneally injected with streptozocin to induce a diabetic type II model. After all, mice were diabetic, their skin was removed by a licensed surgeon to mimic the condition of diabetic ulcers. 48 diabetic mice were randomized into four groups (*n*=12): control, 70S30C powder, 55S30C15B powder, and 55S30C15B fibre.

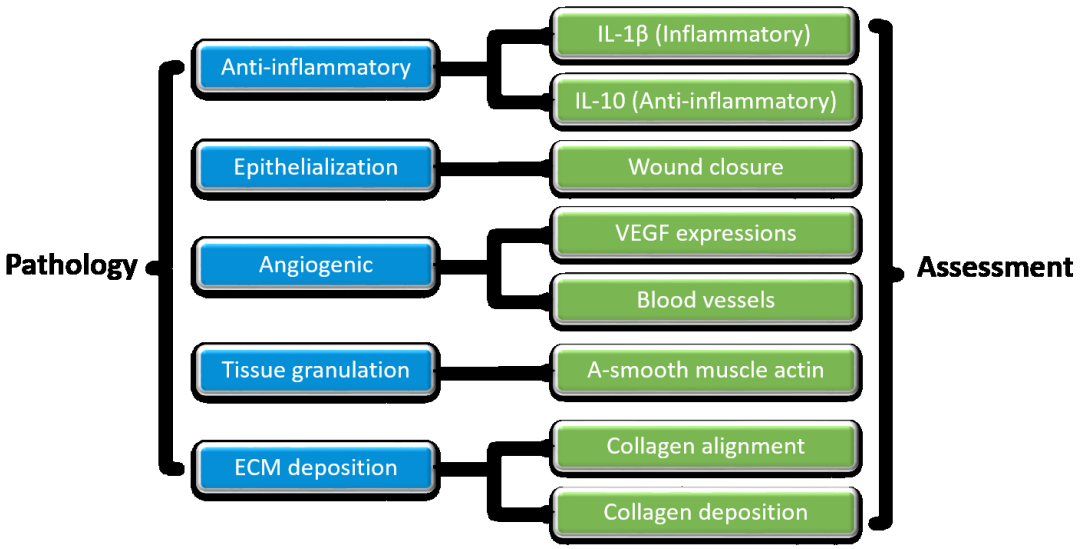


Figure 6. 1. Schematic of the effect of BG samples on different steps in diabetic ulcer pathology and their corresponding assessment approach

Figure 6. 1 summarizes the effect of BG samples on different steps in diabetic ulcer pathology to be investigated, and their corresponding characterization techniques. The in

vivo wound closure and epithelialization rate was determined from optical images of the wound area and histology analysis of the wound tissue; IL-1β (one of the most representative inflammatory cytokines) and IL-10 (one of the most representative anti-inflammatory cytokines) were assessed through IHC as representatives for the anti-inflammatory effect; angiogenesis was determined by investigating the VEGF expressions and number of blood vessels (represented by circles of CD31 protein) in wound site through IHC; alpha-smooth muscle actin (α-SMA) was characterized to understand both the number of large blood vessel infiltration and the number of myofibroblasts; ECM deposition and alignment were determined through histology (Masson Trichrome Staining).

6.2 Methods

6.2.1 Design of the animal model

The animal studies were conducted at Northeastern University, Shenyang, China, and all animal protocols were approved by the Ethical Committee ofNortheastern University. As described in Section 5, the pre-fabricated BG fibres have a 3D structure that mimics the ECM environment and stimulates protein expressions to promote angiogenesis and ECM regeneration, which makes them a potential candidate for diabetic ulcer regeneration. A diabetic wound model is designed to characterize the in vivo efficacies of the BGs in a real-life diabetic environment.

The animal model was designed from scratch despite there having been various literature reporting the protocols for the diabetic model. Diabetic model can be generated on various animals, such as male Wistar rats [931], SD rats [791], OF-1 female mice [932], female Balb/c mice [933, 934], C57BL/6 mice [786, 787], SKH1 mice [644] (Mo-Sci), Nude mice [55], ICR mice [594, 735]. For rats, it usually takes a longer time for them to become diabetic through the injection of streptozocin because they are larger and heavier, which means less likely to be affected by drugs. From different types of mice, C57BL/6 and ICR are the most commonly used, but ICR is more sensitive to the injection of STZ [935] so the distributions between groups may be higher than that of C57BL/6. C57BL/6J mice (5-6 weeks old, male) were purchased from the Huafukang Animal Center (Beijing, China) and fed for another 2 weeks. During the period, they were fed a high-fat diet, so that mimicked the diabetic environment, and were separated into 3 mice per cage. The nurturing of the animal follows the regulation of animal welfare.

The diabetic type II model was created by intraperitoneally injecting streptozocin (Sigma-Aldrich) into the mice. STZ solution was prepared by dissolving STZ in 1% in citrate buffer solution [936]. The mice can be injected with a strong dose (> 130 mg kg^{-1}) once or twice or be injected with a lower dose (45-75 mg kg^{-1}, the dose in this study was 50 mg kg^{-1}) for a week. The former approach was easier, but usually had a higher risk for mouse death or the generation of type I diabetes. Before each injection, the mice need to be fasted overnight. The mice can be given food 2 hours after the injection and if needed, slightly injected with Novoline or Neutral Protamine Zinc Insulin to prevent the death of mice due to excessively high blood glucose. In the initial 6-10 hours, the mice underwent the second phase, where excessive insulin was released due to the defected islet cells. Food and water were necessities during this period and the mice were also fed with glucose water. Prevention of infection caused by urination and preventing the fighting of mice by reducing the population per cage were also important to ensure mice survival. After the final injection, the mice started behaving normally and became permanently affected by high blood glucose levels after 24-48 hours. After 4-7 days, the skins of the mice became chronically affected. The blood glucose level was taken on days 3 and 7 after the final injection. If the level for both time points were similar and both exceeded the normal value (12-15 mmol/L for C57BL/6J mice), the mice were determined as diabetic.

The mice were separated into four groups (control, 70S30C powder, 55S30C15B powder, and 55S30C15B fibre) and two time points (days 7 and 13) so that there are 6 mice per group per time point. This enables us to understand the role of bioactive glass, borate incorporation, and fibre morphology individually in different steps in the wound healing cascade, through the comparison between each group. On the day of the surgery, the mice were anesthetized using a mixed solvent of pentobarbital sodium and chloral hydrate. After the mice were fully immobile, their skin was shaved and a 10 mm puncher was pressed onto their skin to cast a circular full-thickness skin wound. Prof. Huiling Gao held the animal license and took charge of the surgery and animal sacrifice. The wound sites were then implanted with 100 mg of wound matrices accordingly and covered with a transparent dressing (Tegaderm, 3M) (the control group was only covered with Tegaderm). This dressing prevents BG samples from falling out.

We did our best to minimize the number of mice per cage, but the movement and fighting of the animals make it difficult for the Tegaderm attachment to the skin. From day 2 onwards, we spotted that a few Tegaderm of the mice were lifted (half detached, half attached to the skin). In this case, we attach a new Tegaderm on top of the old one to ensure no lease of exudates of samples. There was one mouse in the 55S fibre group whose Tegaderm was completely removed, in which I put a new Tegaderm with a few new

fibre mats on that make it consistent with the other groups. Then, we had a better watch to make sure any Tegardem ‘Lifting’ is resolved immediately at seen. On day 7, the ‘Lifting’ effect happens so often that we decided to remove the Tegaderm from all groups.

6.2.2 Wound closure assay

For wound closure assessment, the wounds of different groups were photographed on days 0, 3, 7, 10, and 13 with a ruler as a size reference. Then, the relative wound area was analyzed by ImageJ and calculated as the percentage of the wound area at individual time points relative to the original burn wound area. On days 7 and 13, 6 mice were sacrificed from each group and their skin was removed for further histological and IHC analysis. The mice were anesthetized through a similar approach and sacrificed through neck-breaking, which follows the animal welfare regulations. Before soaking them in paraformaldehyde, the bottom of the dermis layer was photographed to visually understand the structure of the newly formed dermis layer and the extent of blood vessel infiltration and/or formation in the dermis layer.

6.2.3 Histology analysis

The removed skin tissues were fixed in 4% paraformaldehyde for 48 h, embedded in paraffin, and cut into 7 μm sections. After drying, the sections were dewaxed, washed, and stained using Hematoxylin and eosin (H&E) for histology analysis according to the manufacturer’s instructions. Images of H&E staining were acquired from optical cameras. The cell numbers were quantified by counting three randomly selected areas and the wound gap was measured through the ImageJ.

The sections were also fixed with Bouin’s solution overnight and went through Masson Trichrome staining to analyze the collagen deposition and alignment of the regenerated tissues. The collagen deposition was quantified using a digital camera and ImageJ based on previously reported research [937]. The blue color was segregated through the ‘Color deconvolution’ command and was changed into ‘black and white’ figures using a threshold of 170. Then, the relative area of the ‘black’ color was quantified through ‘Measure>Analyse particles’. The analysis of cell number, and collagen deposition are described in Figure 6. 2.

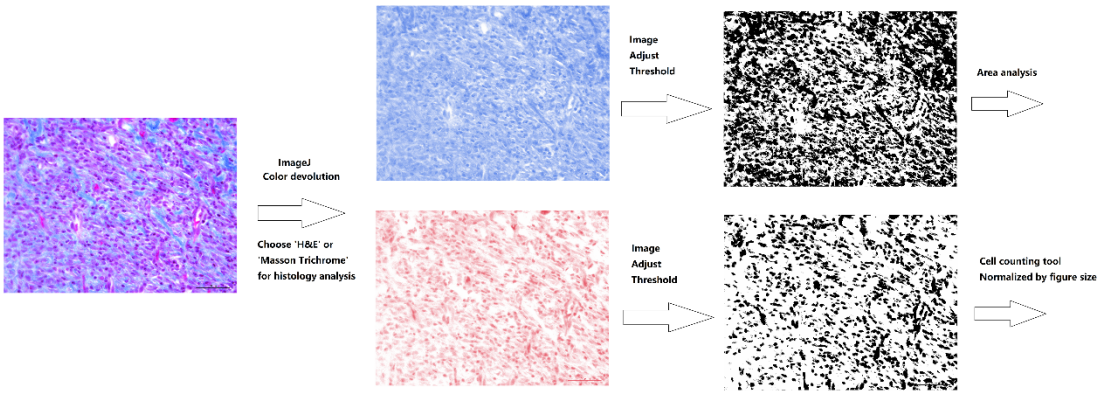


Figure 6. 2. Schematics of Histology analysis: Analysis of collagen area and number of cells from Masson Trichrome Staining using Color devolution from ImageJ

6.2.4 Immunohistochemistry analysis

Immunohistochemical analysis was performed on CD31 (Abcam), VEGF (Abcam), α-SMA (Abcam) in order to analyze the angiogenesis, and ECM deposition effect of the wound matrix on diabetic ulcers. The sections were dewaxed, washed, fixed using citrate buffer solution (pH = 6), and then cultured using 3% H_2O_2 for protein retrieval. Blocking the samples with 10% BSA in PBS quenches endogenous biotins or enzymes. The above-mentioned primary antibodies were diluted according to the manufacturer's instruction and applied to incubate the sections overnight at 4 °C. Then, the sections were further incubated with goat anti-rabbit antibodies and Horseradish Peroxidase for labeling. The sections were further visualized using DAB staining and counterstained using hematoxylin. IHC studies of IL-1β and IL-10 were conducted by WanleiBio company following a similar protocol. The primary antibodies used for these two proteins were from the same company.

Images were taken through a microscope equipped with a digital camera (DMI 4000, Leica). The number of blood vessels was determined by counting three randomly selected areas according to the CD31 staining. The remaining proteins were quantified using a similar approach to that of the Masson Trichrome staining. ImageJ was applied to measure the relative stained area to the overall area of the wound, taken from three randomly selected areas. The steps of the analysis are summarized in Figure 6. 3.

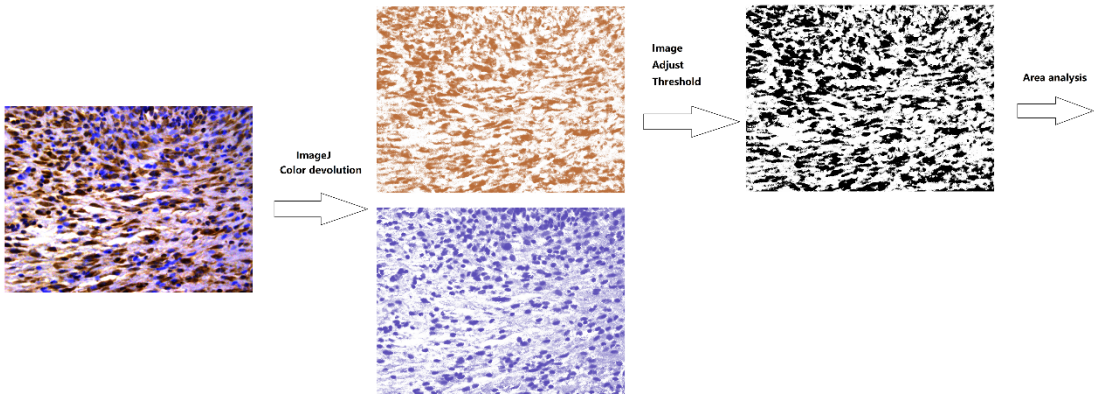


Figure 6. 3. Schematics of Immunohistochemistry analysis： Analysis of VEGF area in wounds using Color devolution from ImageJ.

6.3 Results and Discussion

6.3.1 In vivo wound closure assay

In vivo wound healing assessments were conducted on the STZ-induced diabetic C57BL/6 mouse model to confirm the healing efficacy of the designed fibre mats and understand its mechanisms regarding individual healing steps. As shown in Figure 6. 4, wound healing in groups treated with BG samples significantly improved in comparison to the control group (wound treated with the transparent dressing only) in 13 days. Massive exudates were expressed in the control group on day 3, which indicated a chronic reaction that significantly inhibited the wound closure. Therefore, there was no sign of wound closure but might have enlarged the wounds (Figure 6. 5). Wounds treated with 70S30C powder healed slightly and wounds treated with 55S30C15B powder healed even further, but they also experienced high expression of exudates. Wounds treated with 55S30C15B fibres had much fewer exudates and better closure.

This trend in wound area was maintained on days 7, 10, and 13. By day 7, the control and 70S30C powder treated group still suffered from exudates, while wounds treated with 55S30C15B powder or fibre had much fewer exudates, which may indicate that the borosilicate BGs had better anti-inflammatory effects. This agrees with previous literature that reported the anti-inflammatory effect of borate ions or when incorporating borate into BG systems [65, 67]. All BG-treated groups reached the final wound contraction stage on day 10, while high levels of keratinocytes resided at the edge of the wound, lacking cues to migrate and completely cover the wound, which agrees with the pathology of diabetic

ulcer healing [24, 938, 939]. The wounds in the control group healed much slower and merely reached the final stage on day 13, while wounds treate with 55S30C15B fibre almost have full closure.

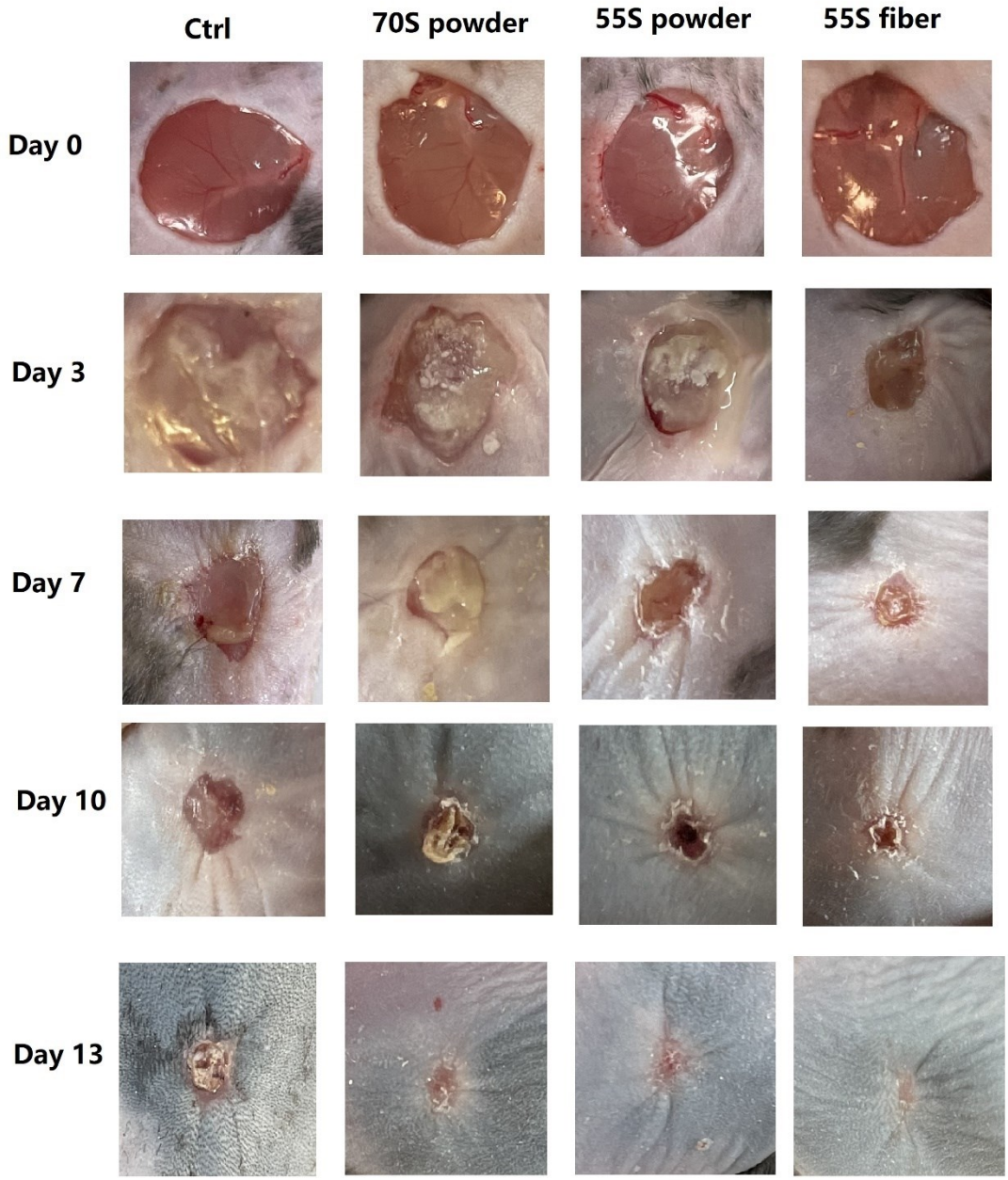


Figure 6. 4. Images of regenerated wound area taken on days 0, 3, 7, 10, and 13 post-surgery on diabetic C57BJ/6 mice treated with 70S30C (70S) powder, 55S30C15B (55S) powder, and 55S30C15B (55S) fibre.

In this study, the wound area is determined as the 'pink' areas instead of epithelialized areas, because the BG-treated wounds are fully epithelialized at day 13 and even the control group is having little skin that is not epithelialized. Some of the limitations of the test are being avoided with some measures. For example, the Tegaderm 'lifting' issues are

being resolved by attaching a new Tegaderm on top of the old ones, but this can make a great difference between animals because some contraction of the skin may occur during the time without Tegaderm. Iodine was used to prevent infection during surgery or during the replacement of the Tegaderm. Some of the samples may be removed during the removal of Tegaderm on day 3 (to take pictures), which can be one reason for the different biological behaviours in the same group.

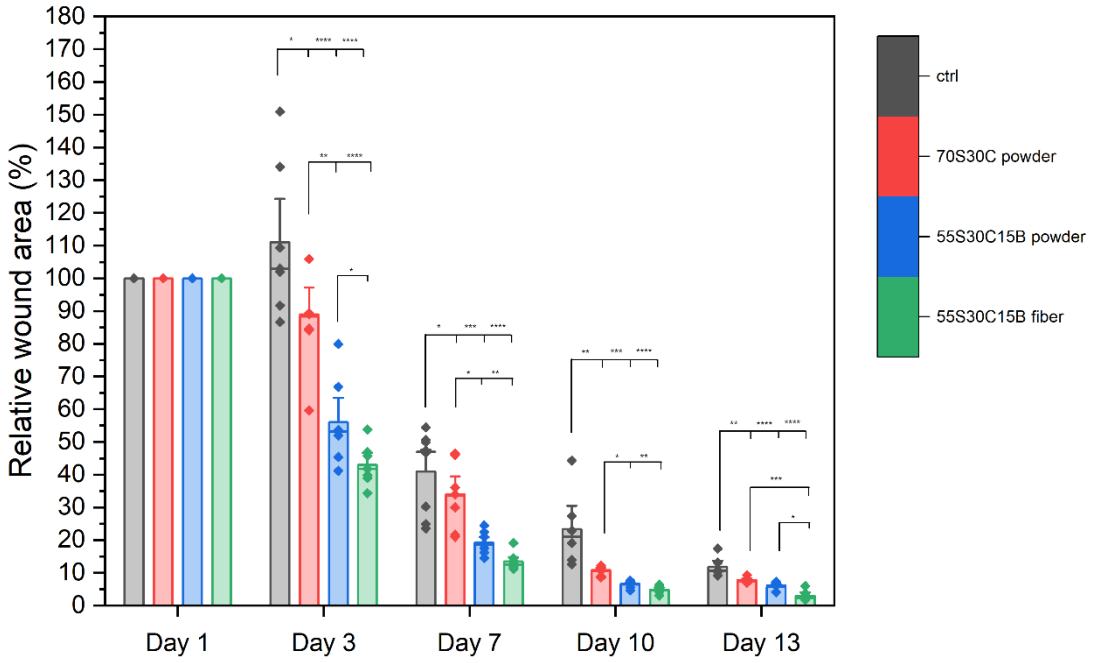


Figure 6. 5. Relative wound area of different treatment groups after 0, 3, 7, 10, and 13 days post-surgery on diabetic C57BJ/6 mice treated with 70S30C powder, 55S30C15B powder, and 55S30C15B fibre. (*P <0.05, **P<0.01, ***P <0.001,****P <0.0001, n=6).

6.3.2 Angiogenesis assessment through optical images

The animals were sacrificed on days 7 and 13, respectively, and the dermis layers of the removed tissue were characterized under an optical microscope to assess the blood vessel formation (Figure 6. 6). By day 7, the wound dermis of the control group was much larger and thicker than other groups. There was also hardly any sign of blood vessel infiltration for wounds in the control groups. The wound dermis for BG treated groups was thinner so that the exudates were visible from the back of the skin and have more blood vessels, which agrees with the results from CD31 immunohistochemical staining (Figure 6. 20, Figure 6. 21). When the wound healing cascade surpasses the ‘inflammation’ phase and comes to the ‘proliferation’ phase, capillary networks are grown on the wound area to replace infiltrated arteriole (larger blood vessels with a thin smooth muscle layer) in the delivery of oxygen and nutrients. On day 13, BG-treated wounds showed obvious capillary

network formation and the thickness of the wound is similar to that of the intact tissues. The wound dermis of the control group was still thicker and poorly vascularized. This agrees with the in vitro angiogenic tests and CD31 immunohistochemistry analysis, and also with previous research that proved the efficacy of BGs in the closure of diabetic wounds [516, 710, 721, 785].

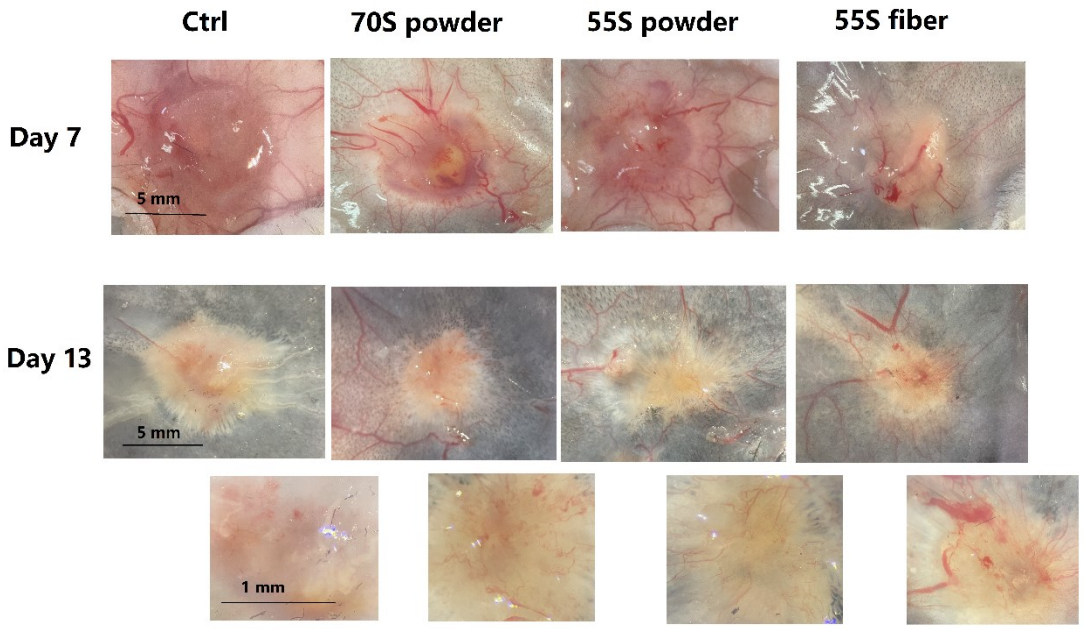


Figure 6. 6. Blood vessel formation of the sacrificed skin tissue of different treatment groups after 7 and 13 days post-surgery on diabetic C57BJ/6 mice treated with 70S30C (70S) powder, 55S30C15B (55S) powder, and 55S30C15B (55S) fibre.

6.3.3 H&E Staining

The histology of the wound areas was analyzed through the H&E and Masson Trichrome staining. H&E staining was conducted to study the levels of epithelialization, wound gaps, and cell number. On day 7, neo-epidermis formed in wounds treated with 55S30C15B powder or fibres, but not in the control or those treated with 70S30C powder (Figure 6. 7). This can be due to the lack of keratinocyte migration cues in diabetic ulcer healing [24, 938, 939]. Treatment with borate ions significantly accelerates the epithelialization rate of diabetic ulcers, with agrees with previous literature on the role of boric acid to wound healing and epithelialization [940, 941]. On day 13, the epidermis layer from the control group remained detached from the dermis layer, separated by a clot of keratin and fibrin (Figure 6. 8). All BG treated wounds had a fully regenerated epidermis, which agrees with the wound closure assay as well as previous literature on the effect of BGs in vivo [644, 942-944]. The wound gaps on both day 7 and day 13 corresponded to the relative wound

area (Figure 6. 9). In general, wounds treated with 55S30C15B fibres healed the fastest, and wounds in the control group healed the slowest in both time points. 55S30C15B powder stimulated faster healing than 70S30C powder on day 7, but the difference was not significant on day 13.

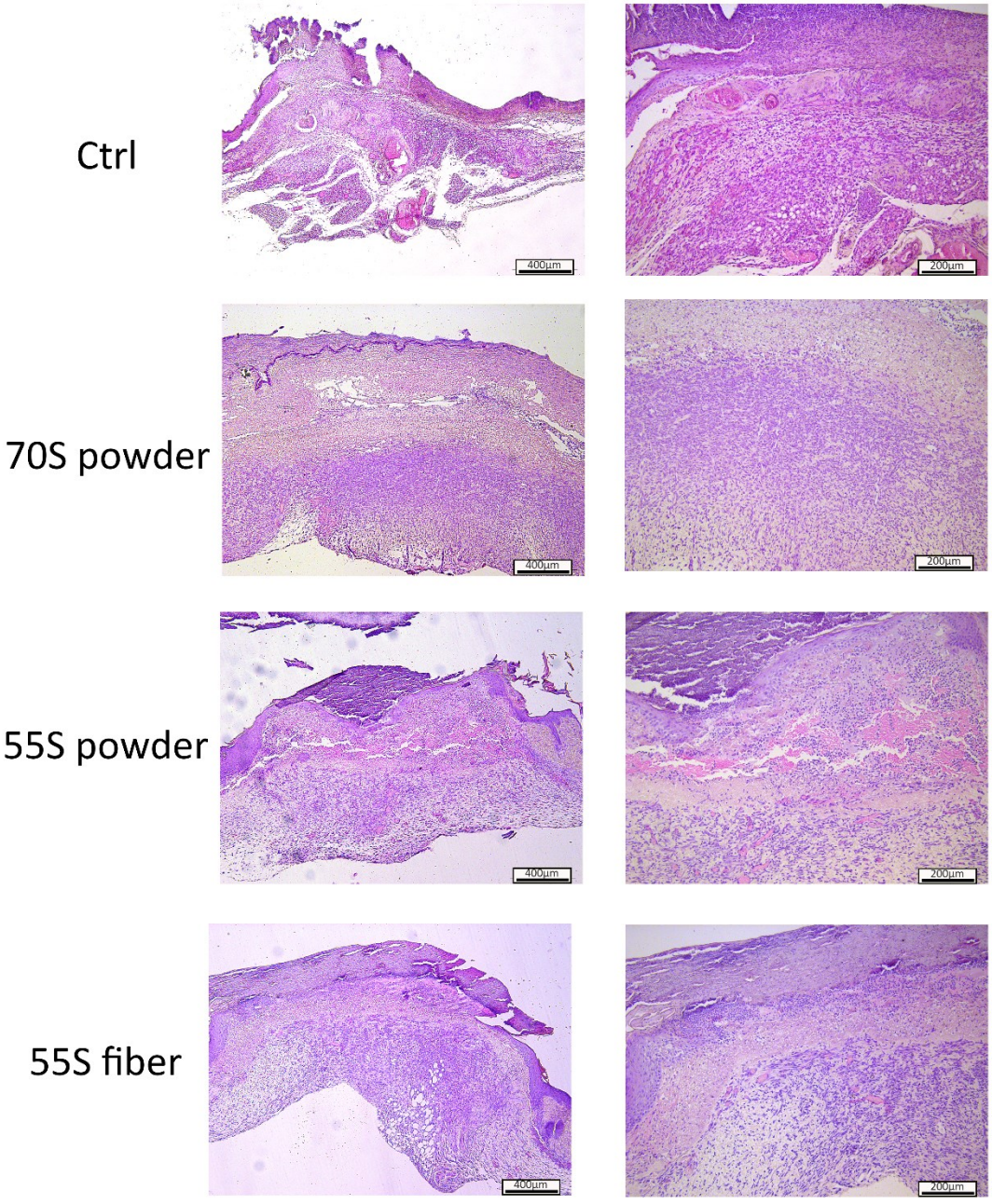


Figure 6. 7. Images of H&E staining of diabetic C57BJ/6 mice wound sections treated with 70S30C (70S) powder, 55S30C15B (55S) powder, and 55S30C15B (55S) fibre on 7 days post-surgery.

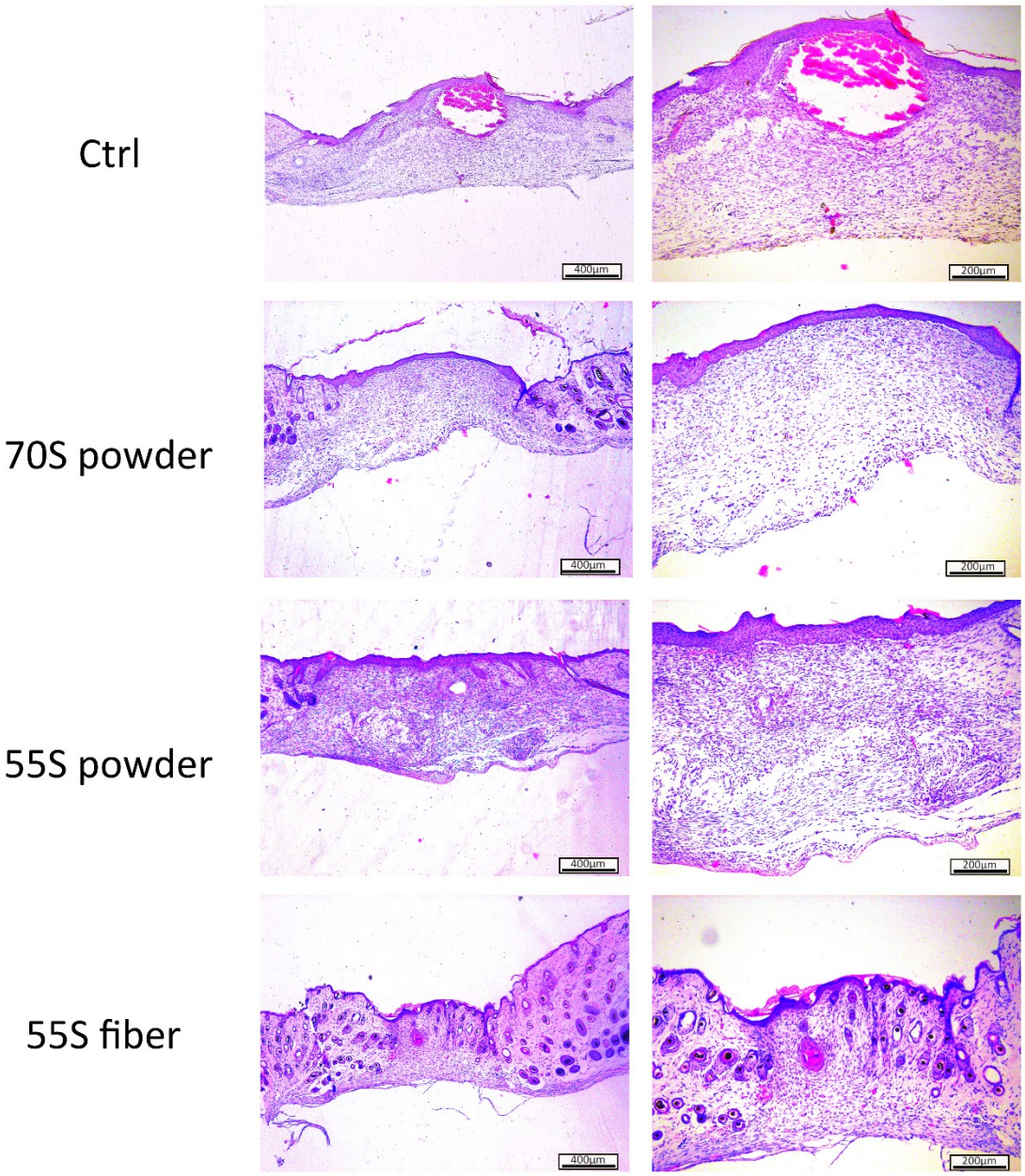


Figure 6. 8. Images of H&E staining of diabetic C57BJ/6 mice wound sections treated with 70S30C (70S) powder, 55S30C15B (55S) powder, and 55S30C15B (55S) fibre 13 days post-surgery.

Massive infiltration of macrophages was observed in wounds from the control group on day 7 (round blue dots). In the control group, however, cells were only observed at the edge of the wounds while the center of the wounds was a very thin layer of tissues. This was likely that the thin tissues were fibrin, which was aggregating together to form a fibrin clot, which then served as a platform for cell infiltration (Figure 6. 7). Massive macrophage infiltration was observed in wounds treated with 70S30C powder. High densities of

macrophages existed both on the edge and in the center of the wounds. This indicates the healing cascade of BG-treated wounds is much faster than untreated wounds. Wounds treated with 55S30C15B powder or fibres had much fewer macrophages and they can only be seen at the center of the wounds. Fibroblasts (elongated blue dots) replaced macrophages at the edge of the wounds, indicating a transfer from the 'inflammation' phase to the 'proliferation' phase. 55S30C15B fibres treated wounds have more fibroblasts than 55S30C15B powder treated wounds. On day 13, the cell number between groups were indistinguishable (Figure 6. 8), as all wounds completed the 'inflammation phase' and the density of fibroblasts in wounds was similar.

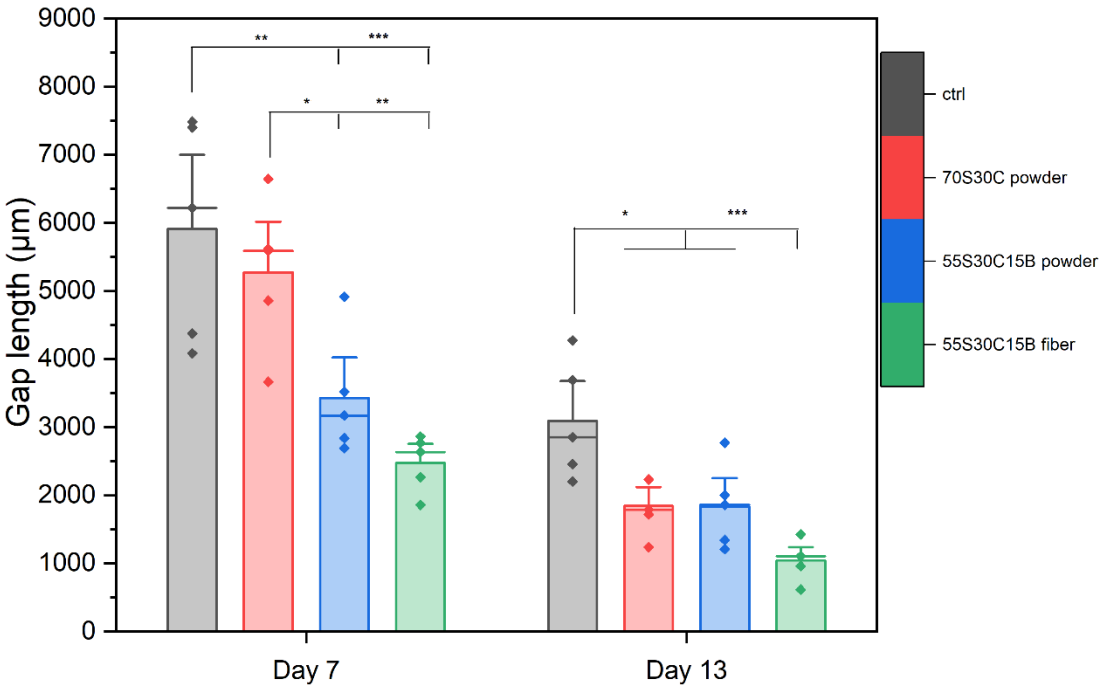


Figure 6. 9. The length of wound gap derived from H&E staining of diabetic C57BJ/6 mice wound sections treated with 70S30C powder, 55S30C15B powder, and 55S30C15B fibre 7 and 13 days post surgery. (*P <0.05, **P<0.01, ***P <0.001,****P <0.0001, n=5).

6.3.4 Masson Trichrome Staining

The Masson Trichrome staining aims to analyze the collagen deposition (light blue) and alignment in the dermis layer. Figure 6. 10 revealed that the control group on day 7 had the least amount of collagen, as the wound area was highly occupied with macrophages (purple) and infiltrated adipose tissue (large white space within frames of collagen fibrils) from the hypodermis.

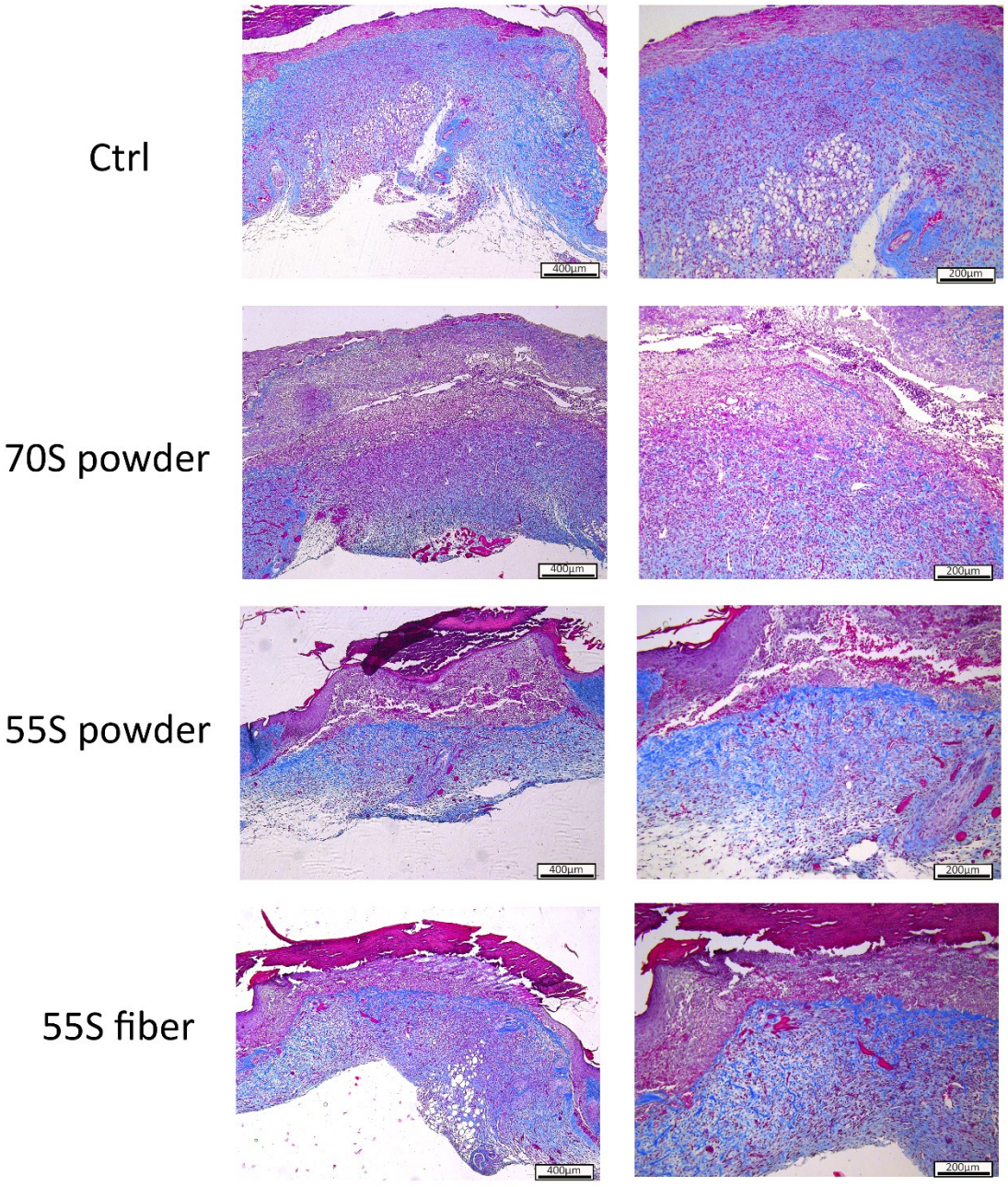


Figure 6. 10. Images of Masson Trichrome staining of diabetic C57BJ/6 mice wound sections treated with 70S30C (70S) powder, 55S30C15B (55S) powder, and 55S30C15B (55S) fibre 7 days post-surgery.

BG-treated wounds had more collagen deposition than the control, which agrees with previous results on electrospun composite scaffolds containing SiO_2-CaO BGs that provoked a significant increase in collagen deposition (measurements summarized in Figure 6. 12) in diabetic ulcers compared to BG-free polymer fibres [594, 725]. The release of therapeutic BO_3^{3-} ions provided further cues to ECM deposition [65], and borate-based

BGs stimulated more collagen deposition in wounds in vitro [66] and in vivo [84, 308]. 55S30C15B fibres treated wounds had the highest deposition. This can be because the ECM mimic fibre mat exhibited better physical cues for ECM protein attachment than the powders.

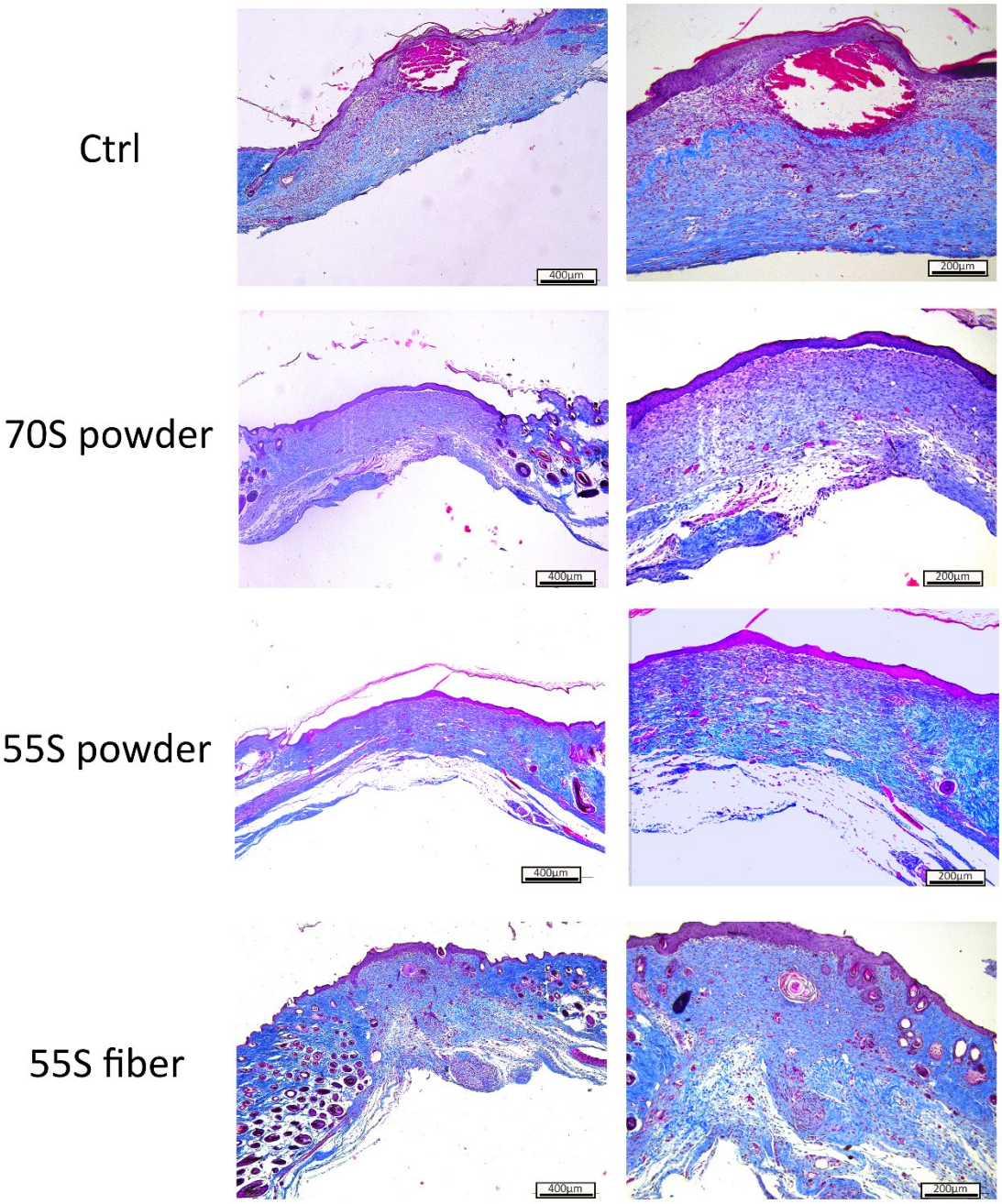


Figure 6. 11. Images of Masson Trichrome staining of diabetic C57BJ/6 mice wound sections treated with 70S30C powder, 55S30C15B powder, and 55S30C15B fibre on 13 days post-surgery.

On day 13, all wounds had collagen that was horizontally aligned across the dermis layer but at the center of the wound area (Figure 6. 11). There were still signs of macrophage aggregation in wounds of the control group. 55S30C15B fibres treated wounds had the best stimulation to collagen deposition in diabetic ulcers as it has the highest collagen density in the dermis layer. Besides, blood vessels (red circles) can also be observed in all BG-treated wounds, but little can be observed from wounds in the control group.

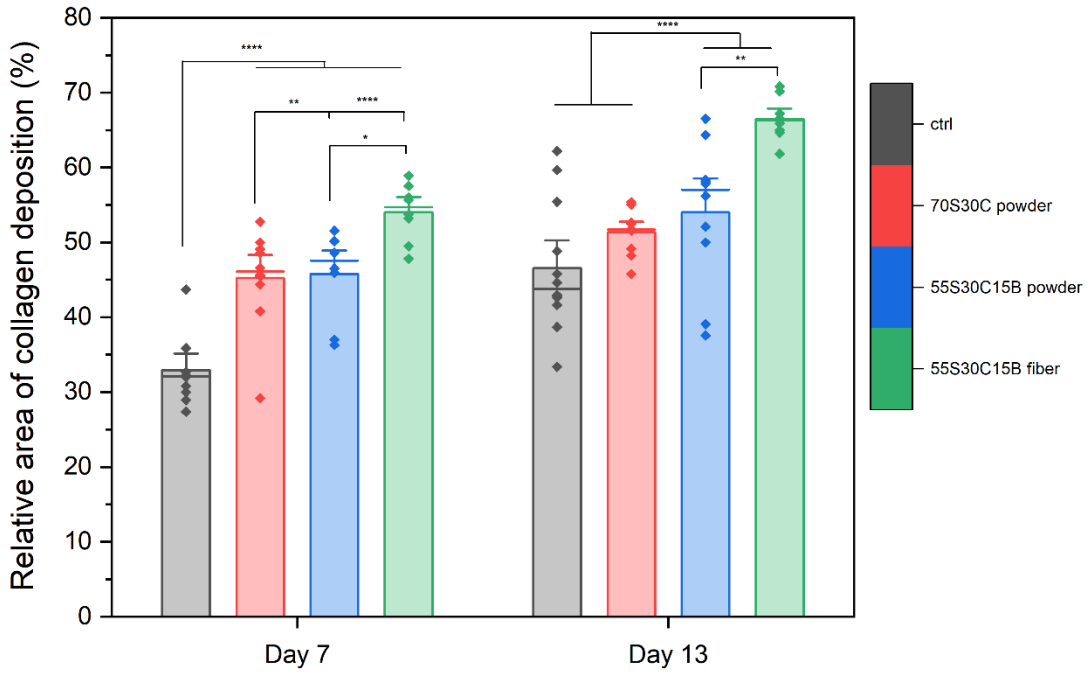


Figure 6. 12. The relative area of collagen deposition derived from Masson Trichrome staining of diabetic C57BJ/6 mice wound sections treated with 70S30C powder, 55S30C15B powder, and 55S30C15B fibre 13 days post surgery. (*P <0.05, **P<0.01, ***P <0.001,****P <0.0001, n = 5 groups *2 image/group).

6.3.5 Anti-inflammation immunohistochemistry assessment

'Inflammation' is the second phase in the wound healing cascade. In chronic wound regeneration, massive macrophages infiltrated the wound site and secrete massive cytokines and protease which leads to chronic inflammation, healthy cells apoptosis, and ECM degradation [16, 20-22]. SiO_2-CaO based BGs such as 45S5 [51] 58S [527], and $75SiO_2$-$20CaO$-$5P_2O_5$ [528], have all been reported to stimulate the switch of macrophages from their inflammatory phenotype (M1) to its anti-inflammatory phenotype (M2), and down-regulate inflammatory cytokines and up-regulate anti-inflammatory cytokines. The anti-inflammatory effects of the BG samples were characterized through

the immunochemical staining of IL-1β (inflammatory cytokines) and IL-10 (anti-inflammatory cytokines).

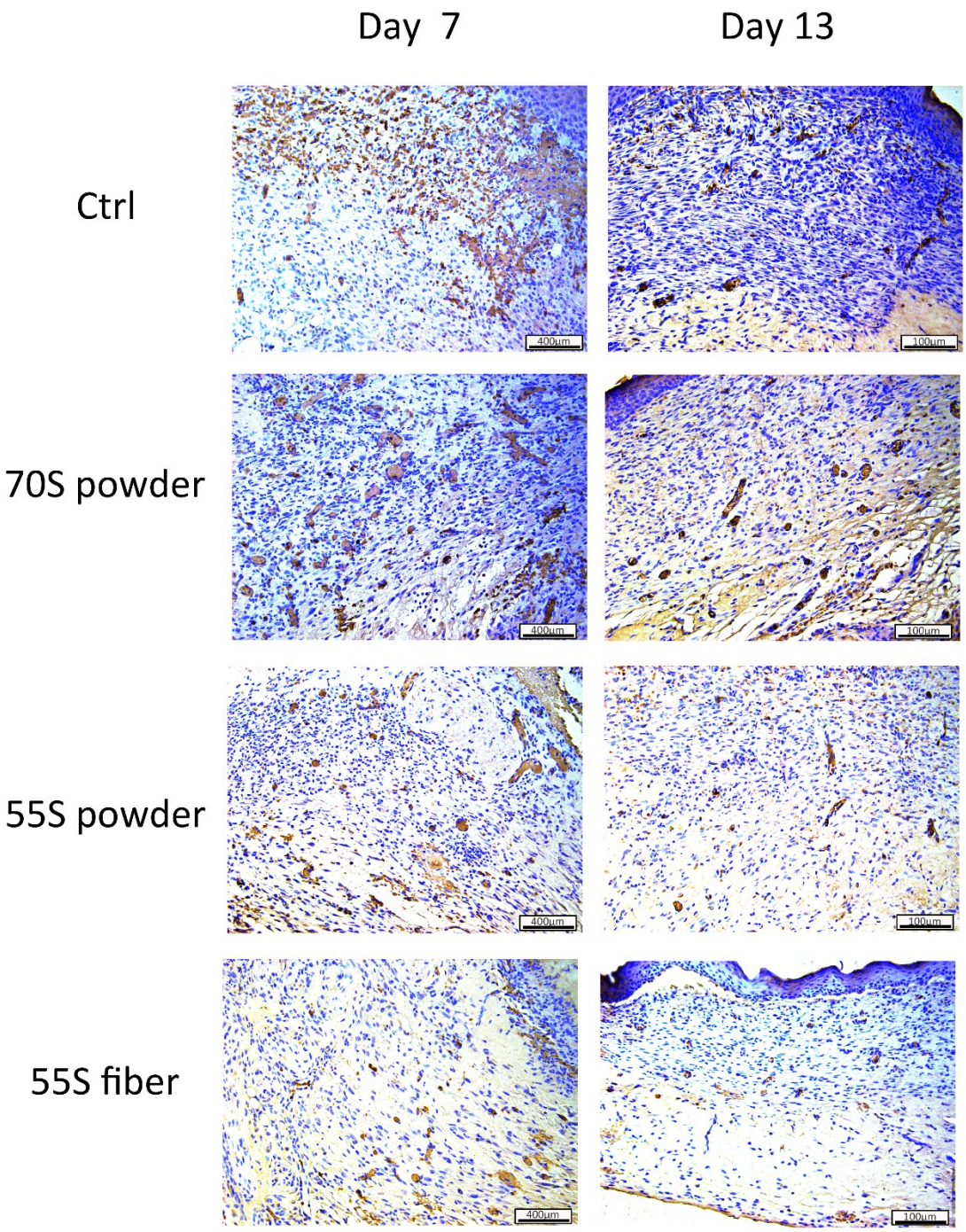


Figure 6. 13. Images of IL-1β immunohistochemistry staining of diabetic C57BJ/6 mice wound sections treated with 70S30C (70S) powder, 55S30C15B (55S) powder, and 55S30C15B (55S) fibre on 7 and 13 days post-surgery.

On day 7, wounds in the control group had the highest IL-1β (Figure 6. 13, Figure 6. 14) and lowest IL-10 (Figure 6. 15, Figure 6. 16) expressions compared to the wounds treated with BGs. This agrees with Figure 6. 4, which revealed the highest chronic inflammation in the control group. There was not much significance in IL-1β expressions between wounds treated with 70S30C and 55S30C15B powder. BG fibres induced a little lower IL-1β expressions than BG powders. But both 55S30C15B powder and fibres induced higher IL-10 expressions in the wound area than 70S30C powder. This could be due to the release of BO_3^{3-} ions, as BO_3^{3-} was reported to inhibit iNOS and COX-2 [65], two important inflammatory mediators, and its function as an anti-oxidant [554]. But while the exact mechanism of the BO_3^{3-} ions remain unknown, this study could preliminarily explain the mechanism of BO_3^{3-} ions to cytokine expressions in vivo.

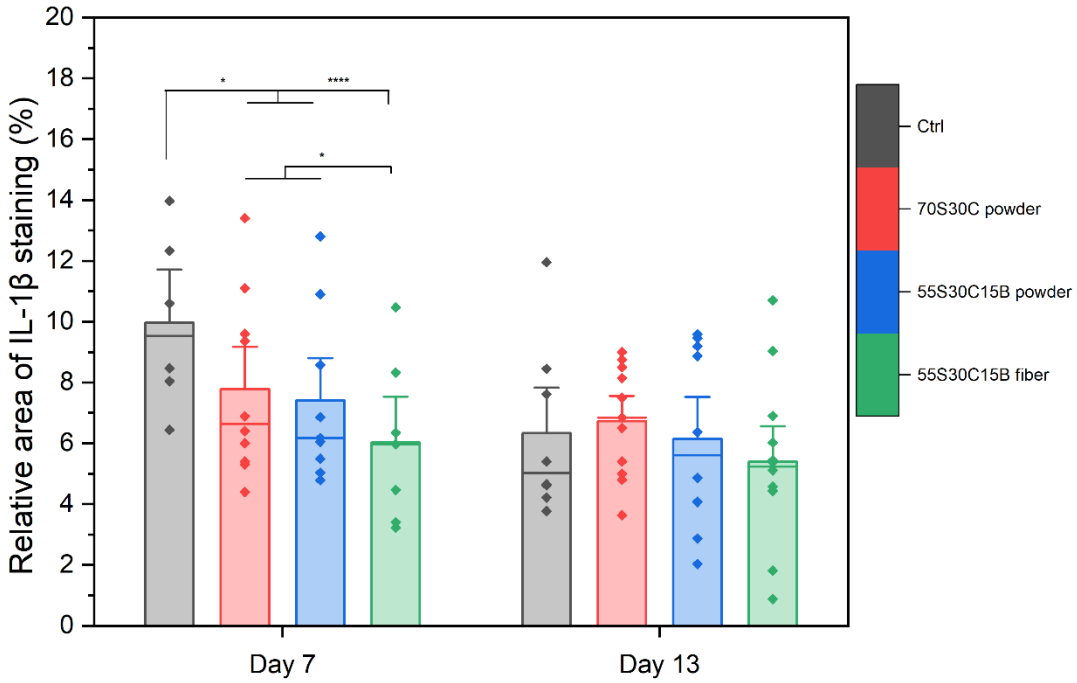


Figure 6. 14. Quantification of IL-1β relative area in percentage derived from IL-1β immunohistochemistry staining of diabetic C57BJ/6 mice wound sections treated with 70S30C powder, 55S30C15B powder, and 55S30C15B fibre on 7 and 13 days post surgery. (*P <0.05, **P<0.01, ***P <0.001,****P <0.0001, n = 5 groups *2 image/group).

On day 13, both IL-1β nearly disappeared in all BG-treated wounds as the 'inflammation' phase terminated (Figure 6. 13), but wounds from the control group still had signs of positive staining at the top of the dermis layer. For BG-treated wounds, positive stainings were located inside the blood vessels, as the vascular network may transport protein from distant tissues. Besides, the platelets may have specific binding sites to cytokine

antibodies. This resulted in the 'IL-1β' expressions being similar among all groups. IL-10 expressions followed a similar pattern (Figure 6. 15) as IL-1β and there was also little significance among all groups.

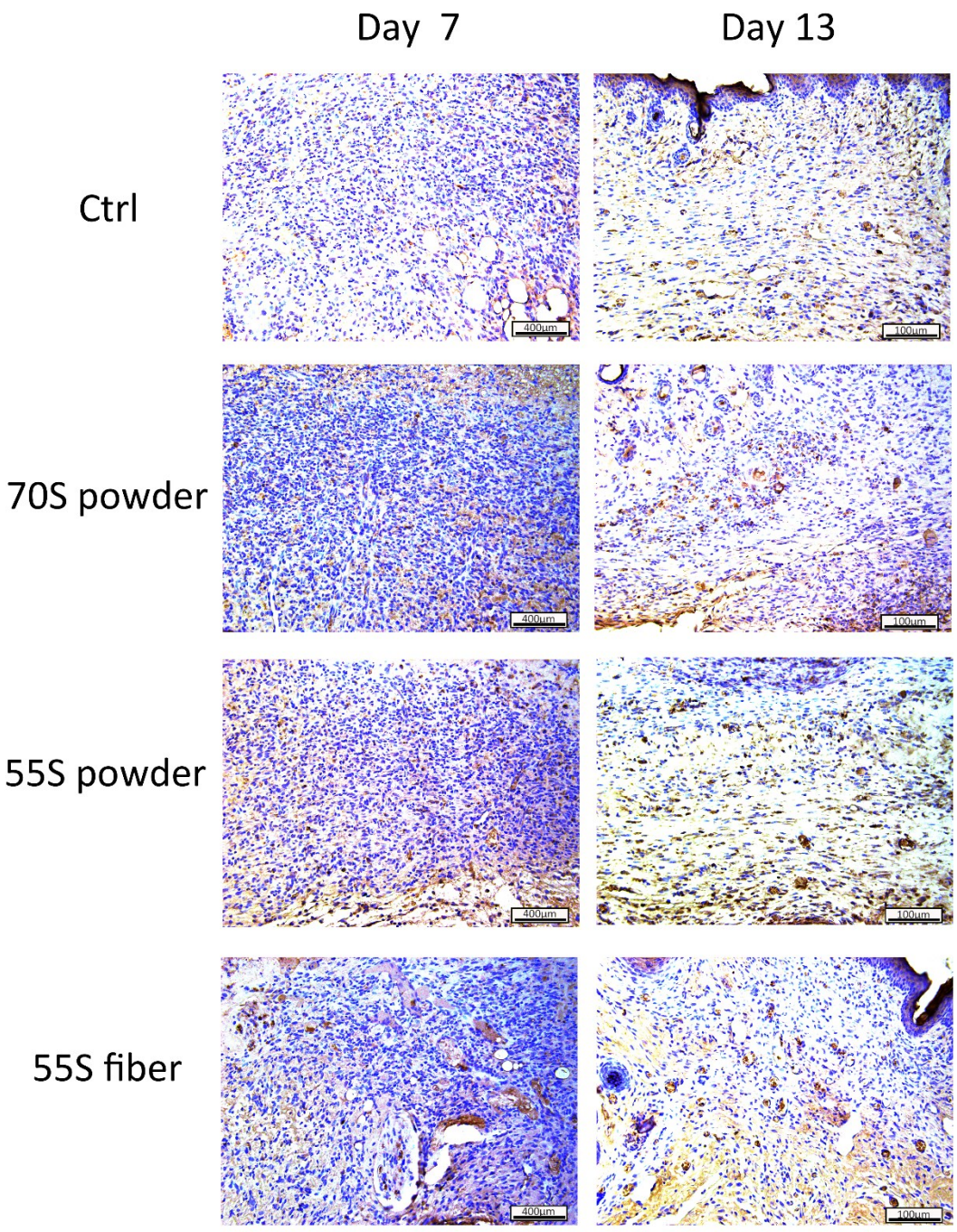


Figure 6. 15. Images of IL-10 immunohistochemistry staining of diabetic C57BJ/6 mice wound sections treated with 70S30C (70S) powder, 55S30C15B (55S) powder, and 55S30C15B (55S) fibre on 7 and 13 days post-surgery.

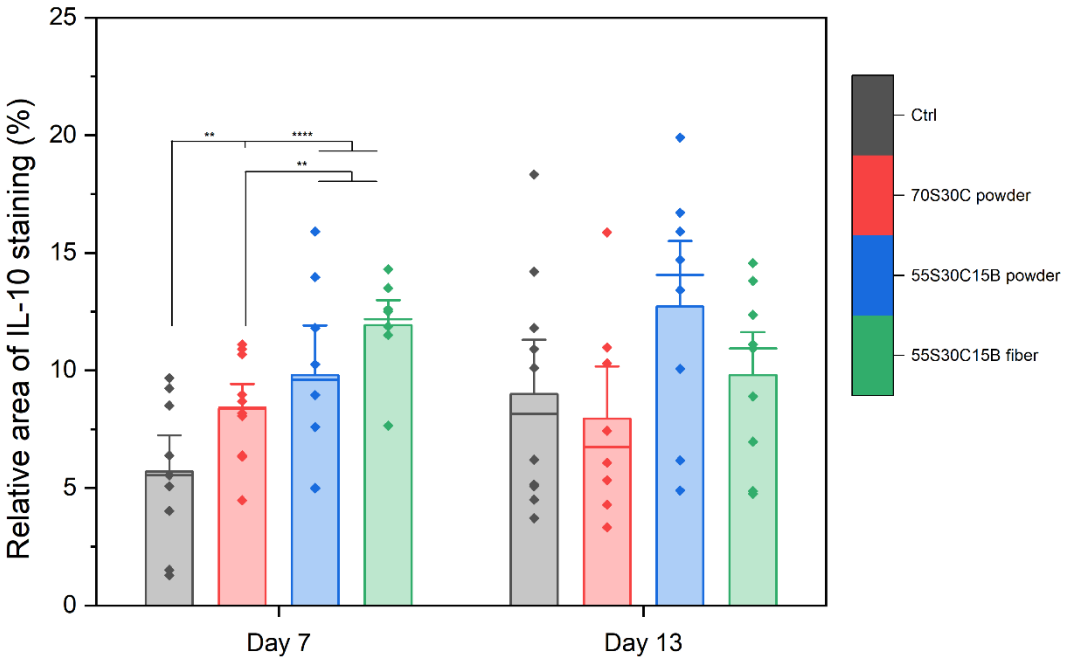


Figure 6. 16. Quantification of IL-10 relative area in percentage derived from IL-1β immunohistochemistry staining of diabetic C57BJ/6 mice wound sections treated with 70S30C powder, 55S30C15B powder, and 55S30C15B fibre on 7 and 13 days post surgery. (*P <0.05, **P<0.01, ***P <0.001,****P <0.0001, n = 5 groups *2 image/group).

6.3.6 Angiogenesis immunohistochemistry assessment

The angiogenic effects of the BG samples were analyzed through in vivo VEGF expression and the number of blood vessels per unit area (highlighted through CD31 immunohistochemistry). The main sources of VEGF in the wound area are macrophages, fibroblast, and endothelial cells [81]. Wounds from the control group on day 7 merely started the 'inflammation' phase so it was apparent that these wounds will not have VEGF expressions. Figure 6. 17 revealed that wounds from the control group merely have VEGF surrounding the infiltrated adipose tissue (adipose stem cells can also express VEGF, but not highly). High levels of VEGF were expressed in the 70S30C treated wounds, but the source may be predominantly macrophages, as few fibroblasts were generated in 70S30C treated wounds on day 7 (Figure 6. 7). The incorporation of boron further stimulates the VEGF expressions (Figure 6. 19). While the VEGF source can be both macrophages and fibroblasts, this agrees with the in vitro protein expression patterns from HDFs. 55S30C15B fibre promoted fewer VEGF expressions than 55S30C15B powder. As explained in the previous chapter, the main role of VEGF is to stimulate the migration of endothelial cells and the migration requires surrounding fibrils for the attachment of cells. BG fibres could induce this ECM-mimic environment so that less VEGF is needed for the

activation of angiogenesis. Another possible explanation can be that the angiogenesis activation of 55S30C15B fibre was completed and less VEGF was required for the ongoing activities.

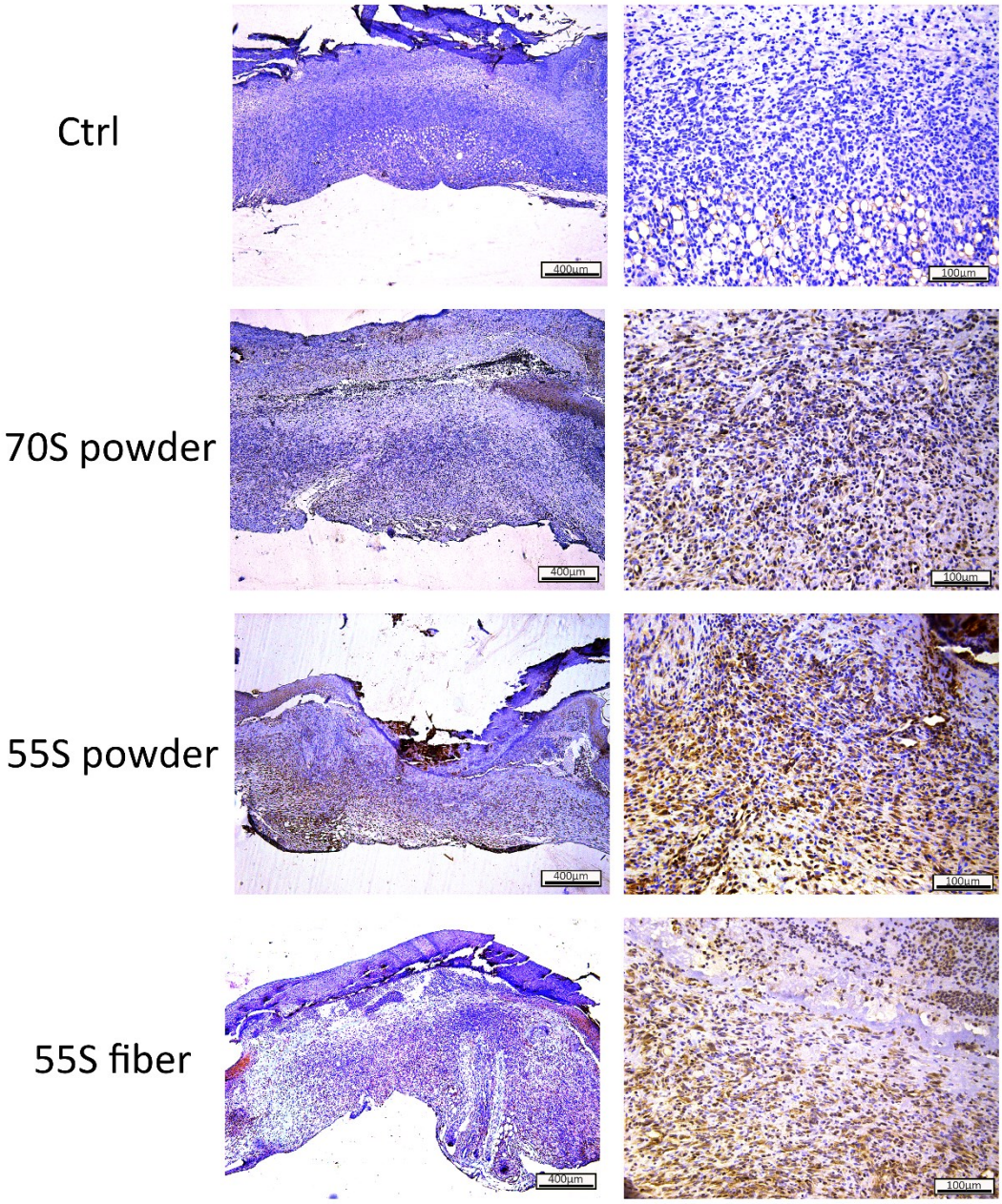


Figure 6. 17. Images of VEGF immunohistochemistry staining of diabetic C57BJ/6 mice wound sections treated with 70S30C (70S) powder, 55S30C15B (55S) powder, and 55S30C15B (55S) fibre on 7 days post-surgery.

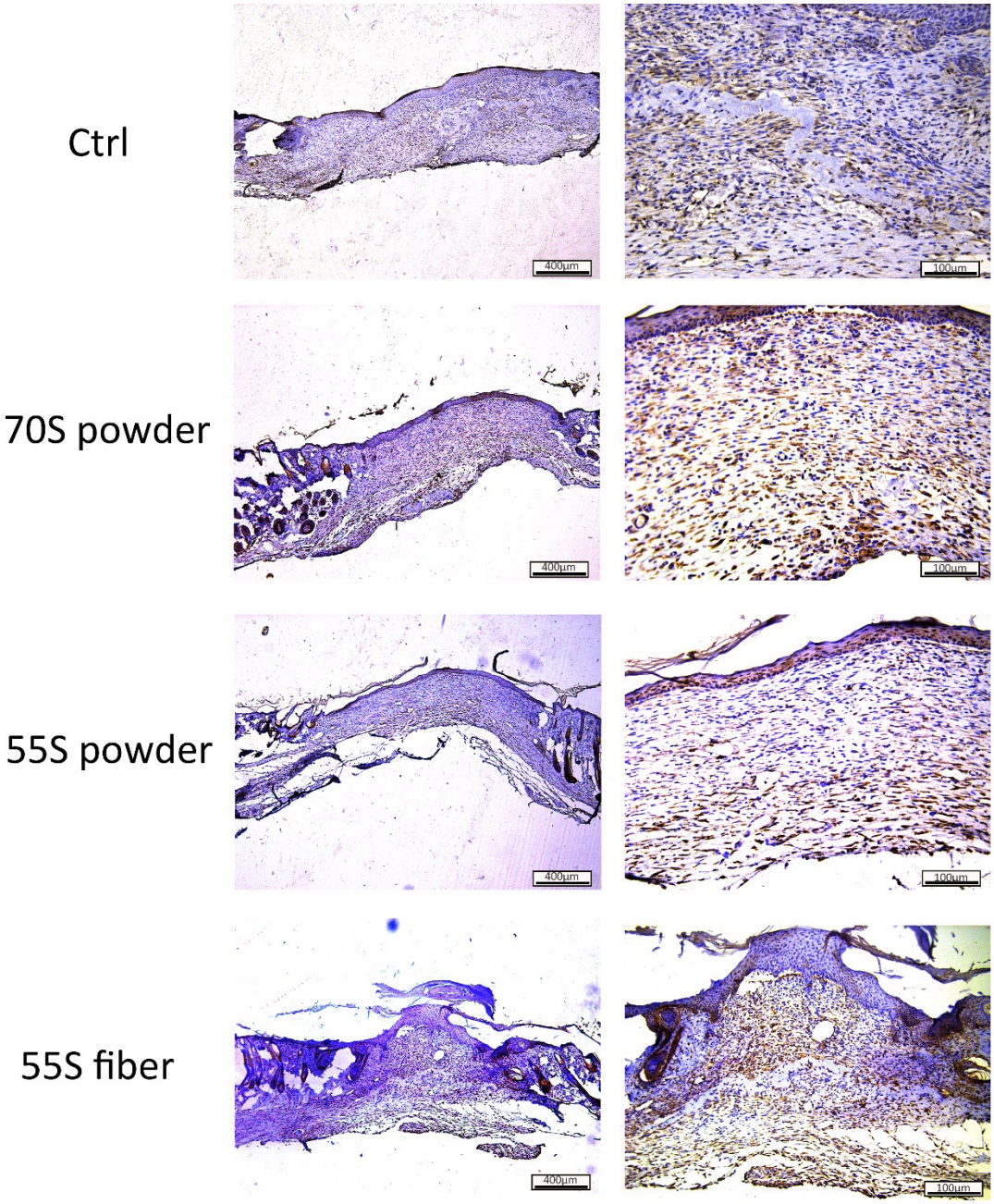


Figure 6. 18. Images of VEGF immunohistochemistry staining of diabetic C57BJ/6 mice wound sections treated with 70S30C (70S) powder, 55S30C15B (55S) powder, and 55S30C15B (55S) fibre on 7 days post-surgery.

On day 13, the VEGF expression of the control group, 70S30C powder group, and 55S30C15B powder group was similar (Figure 6. 18). But according to the blood vessel formation profile (Figure 6. 21), the angiogenic step for wounds in the control group may have just started. For BG powder treated groups, the activation of angiogenesis was completed so that the highest VEGF concentration (like that in the 55S30C15B powder group on day 7) was no longer needed while only a sustained dose of VEGF is required

for ongoing angiogenic activities. VEGF expression of wounds treated with 55S30C15B fibre was half of that of wounds treated with 55S30C15B powder, which may indicate that the vessel formation for the 55S30C15B fibre is fully complete.

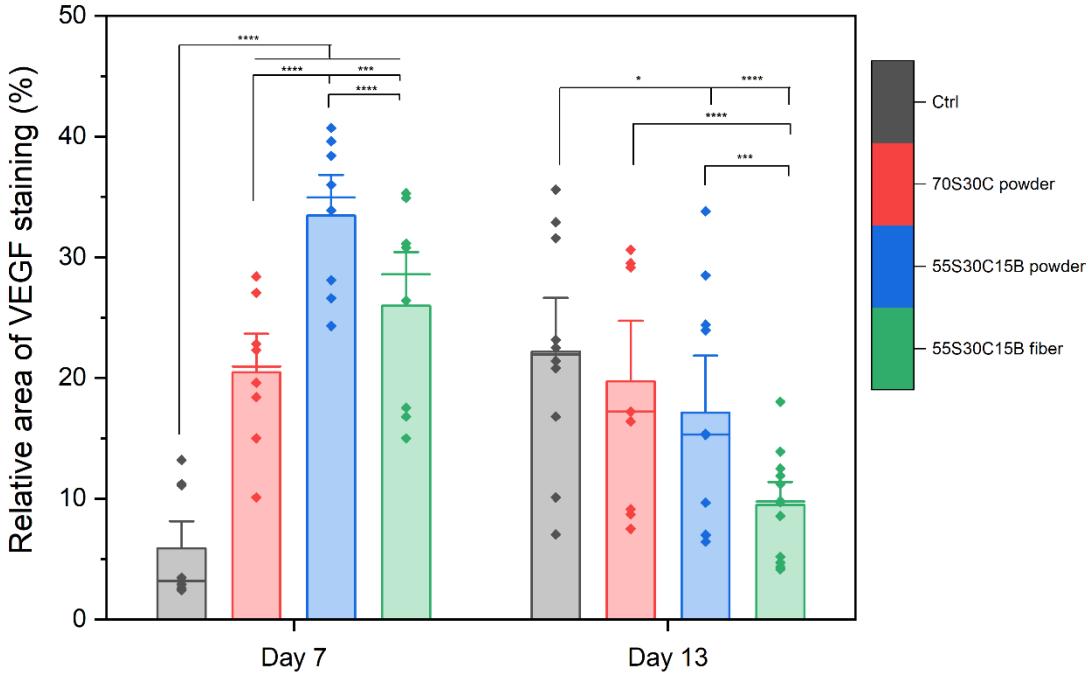


Figure 6. 19. Quantification of relative area of VEGF derived from VEGF immunohistochemistry staining of diabetic C57BJ/6 mice wound sections treated with 70S30C powder, 55S30C15B powder, and 55S30C15B fibre on 7 and 13 days post surgery. (*P <0.05, **P<0.01, ***P <0.001,****P <0.0001, n = 5 groups *2 image/group).

The number of blood vessel formation also agrees with the in vitro studies on HUVEC proliferation and migration (Figure 5. 14). There were few blood vessels in the wounds of the control group, except for those infiltrated from the hypodermis (Figure 6. 20, Figure 6. 22). 70S30C powder highly stimulated vascularization in wounds, which agrees with that SiO_2-CaO based BGs stimulated better angiogenesis when incorporated in chitosan-silk fibroin composites [593], alginate hydrogels [235], PDLLA electrospun fibre mats [594], or collagen-PCL nanofibres [725]. 55S30C15B powder and fibres stimulated higher blood vessel formation than 70S30C powder, which also agrees with that borate-based BGs, such as 1393-B3, induced higher blood vessel formation in wounds in vivo, but did not explain the mechanisms [66, 84]. The distinction between the 55S30C15B powder and 55S30C15B fibre groups is because the attachment of cells to fibrils is the important step for their migration so that the fibrous structure favours the migration of endothelial cells (as explained in the HUVEC migration section) [874, 928]. This also explains the in vivo VEGF expression pattern (Figure 6. 17), as having more migration pathways means fewer

migration signals (VEGF) to be expressed. A similar pattern was found on day 13, in which 55S30C15B powder and fibre stimulated the highest blood vessel formation, which was slightly higher than 70S30C powder and 2 times than the control (Figure 6. 21). The BG treated wounds may have reached the maximum level of angiogenesis, which is why the VEGF level went down sharply at day 13 in 55S30C15B fibre treated wounds. The angiogenesis step for the control group may have just started.

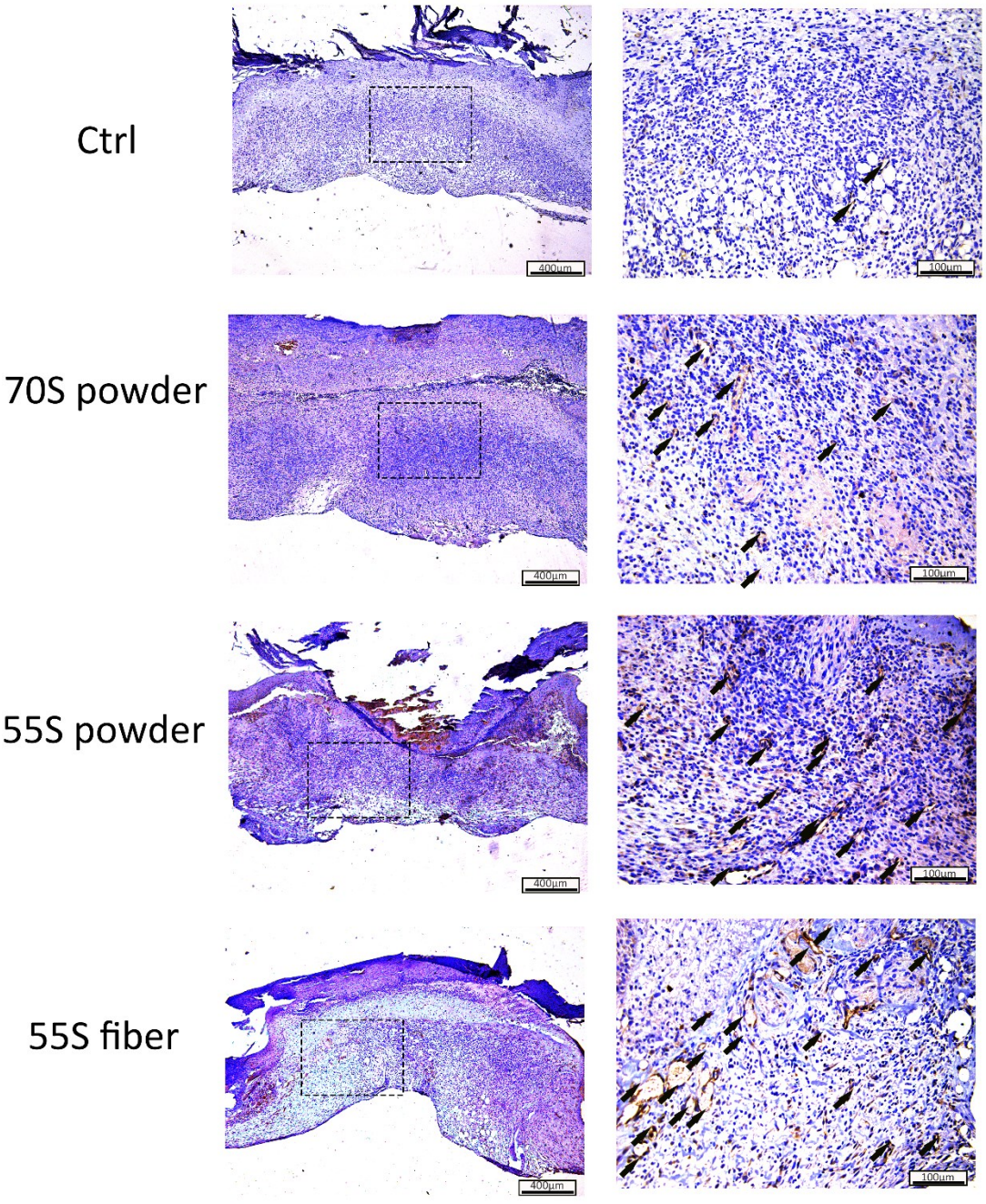


Figure 6. 20. Images of CD31 immunohistochemistry staining of diabetic C57BJ/6 mice wound sections treated with 70S30C (70S) powder, 55S30C15B (55S) powder, and 55S30C15B (55S) fibre on 7 days post-surgery.

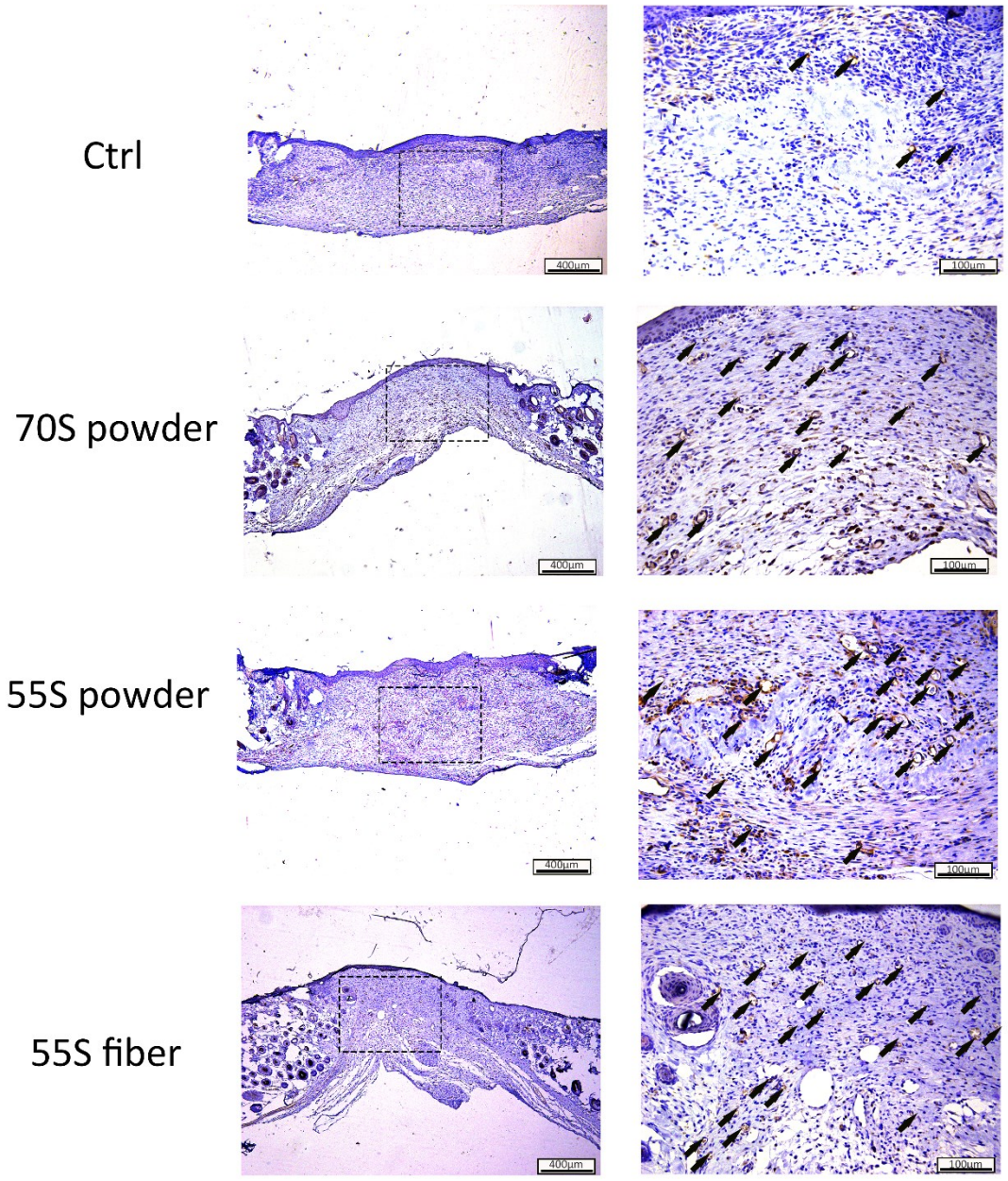


Figure 6. 21. Images of CD31 immunohistochemistry staining of diabetic C57BJ/6 mice wound sections treated with 70S30C (70S) powder, 55S30C15B (55S) powder, and 55S30C15B (55S) fibre 13 days post-surgery.

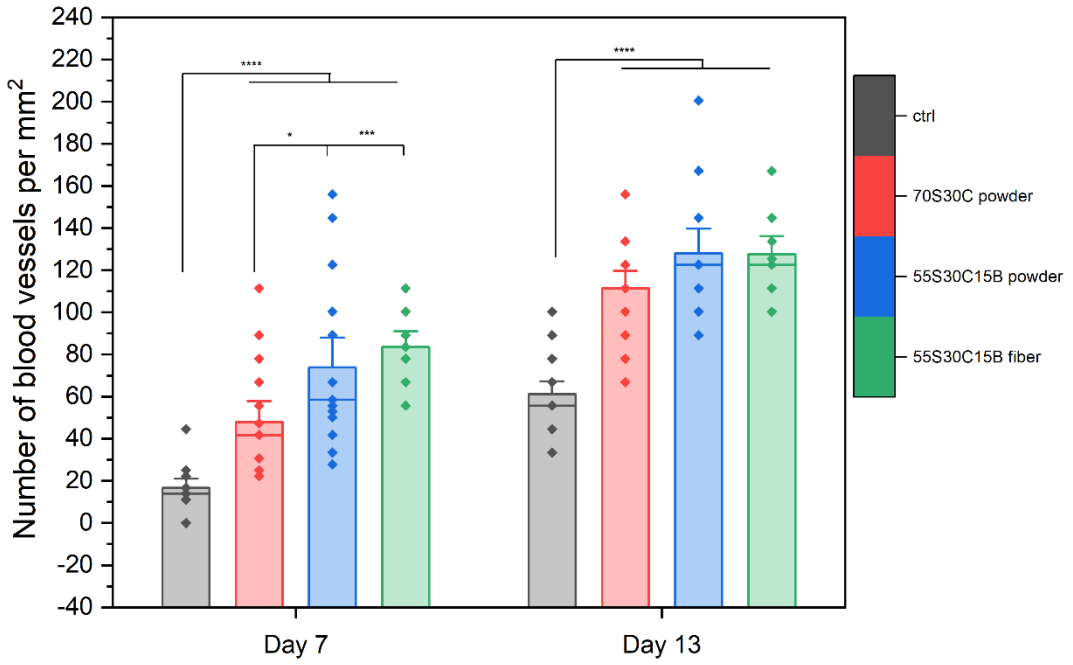


Figure 6. 22. Number of blood vessels per mm^2 derived from CD31 immunohistochemistry staining of diabetic C57BJ/6 mice wound sections treated with 70S30C powder, 55S30C15B powder, and 55S30C15B fibre on 7 and 13 days post surgery. (*P <0.05, **P<0.01, ***P <0.001,****P <0.0001, n = 5 groups *3 image/group).

6.3.7 Alpha-smooth muscle actin immunohistochemistry assessment

Alpha-smooth muscle actin (α-SMA) is an important marker of fibroblast differentiation into myofibroblasts, a matured phenotype of fibroblasts in the wound [945, 946]. At the early stage of wound healing, higher levels of α-SMA indicate faster tissue granulation and wound closure kinetics, as α-SMA are microfilaments in myofibroblasts and they exist in bundles to produce tension to the surrounding ECM in order to promote wound contraction [947, 948]. On day 7, hardly any α-SMA expressions were observed in the control group, which agrees with the histology results that little tissue granulation occurred (Figure 6. 23). Wounds with 70S30C powder had myofibroblasts formation at the bottom half of the dermis layer while wounds treated with 55S30C15B powder or fibres had myofibroblasts formation across the dermis layer. The release of BO_3^{3-} can be the most likely reason, but few articles provided the evidence. 55S30C15B fibres stimulated more α-SMA expressions than 55S30C15B powder. This is because fibroblasts only differentiate in an ECM-mimic microenvironment and the fibres can enable fibroblast attachment without the formation of preliminary ECM matrix [949, 950]. The previous report merely suggested that

45S5 BG stimulate urine stem cells in releasing growth factors that promoted α-SMA expressions from fibroblasts in vitro [951], but the role of BGs directly to cells was unknown.

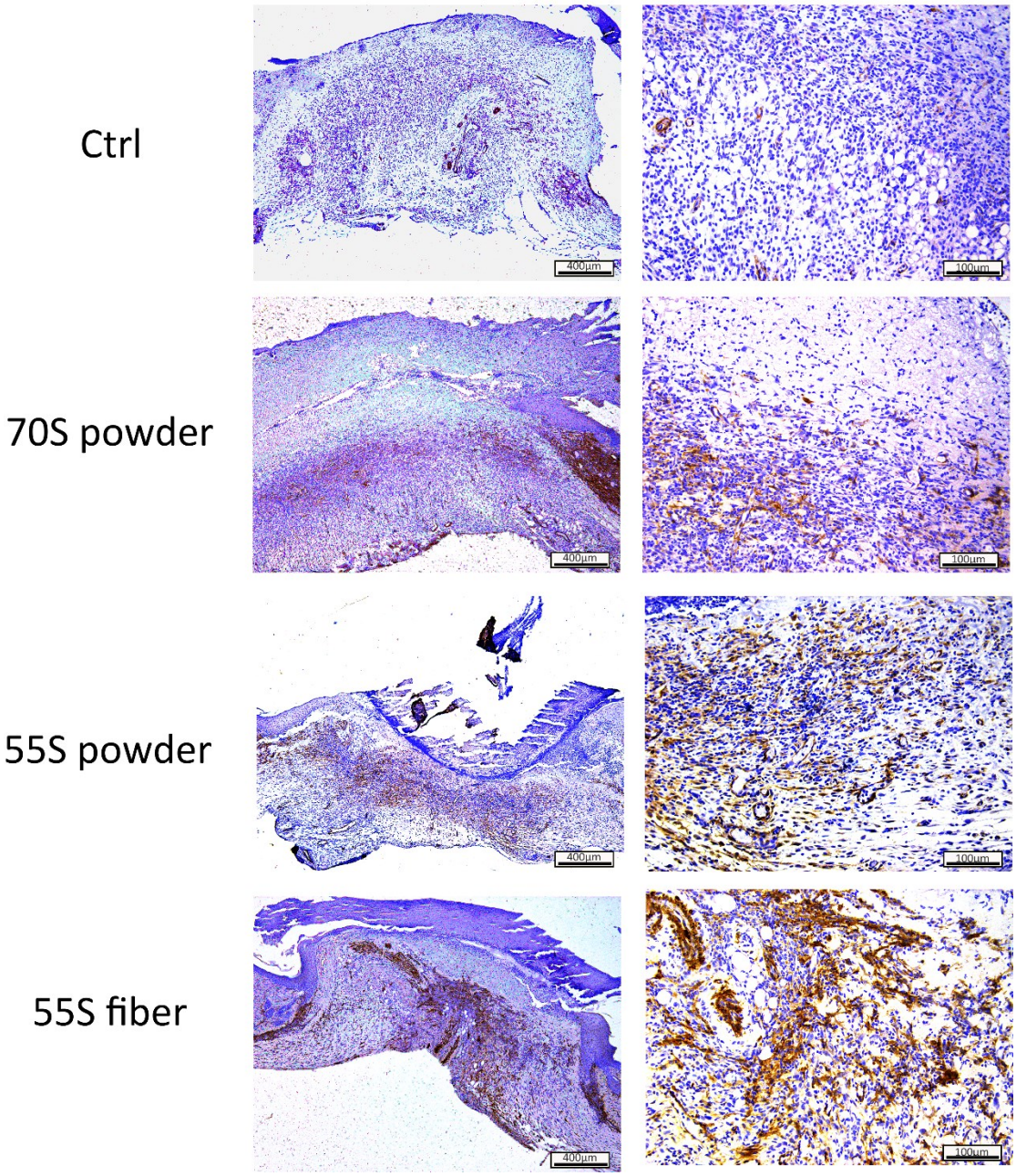


Figure 6. 23. Images of α-SMA immunohistochemistry staining of diabetic C57BJ/6 mice wound sections treated with 70S30C (70S) powder, 55S30C15B (55S) powder, and 55S30C15B (55S) fibre on 7 days post-surgery.

On day 13, wounds treated with 55S30C15B fibres were fully closed and myofibroblast apoptosis was activated to prevent further wound contraction and scar formation (Figure 6. 24). The healing cascade reaches the end of the ‘proliferation’ phase and the start of

the ‘remodeling’ phase and once all myofibroblasts are removed, the healing cascade terminates. Wounds treated with 70S30C and 55S30C15B powder were nearly closed so that their α-SMA levels were both the maximum while wounds in the control group were contracting much slower so that they had the least level of α-SMA (Figure 6. 26). Further studies are required to understand the mechanism of BGs and therapeutic ions to α-SMA expressions and myofibroblast activities.

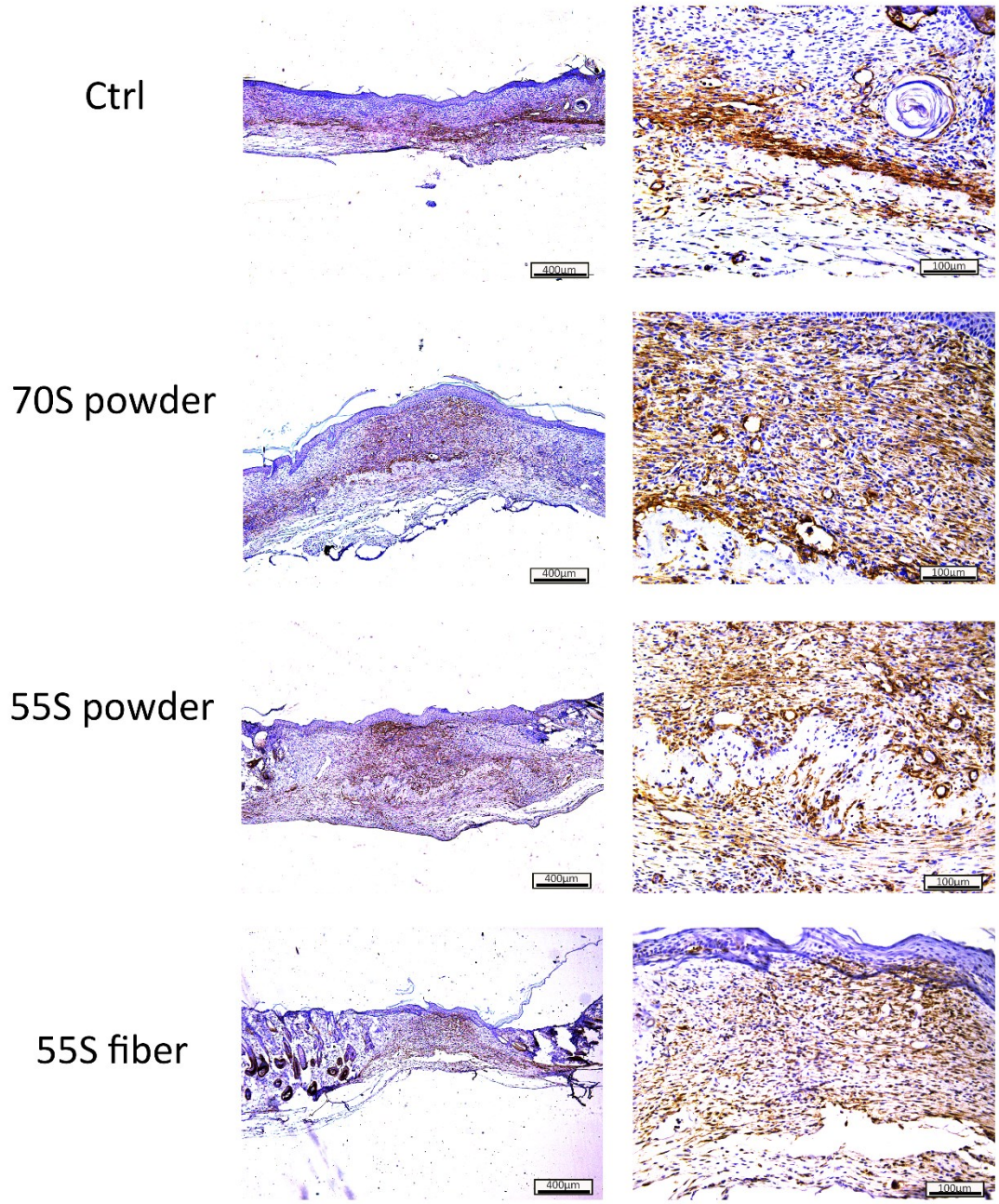


Figure 6. 24. Images of α-SMA immunohistochemistry staining of diabetic C57BJ/6 mice wound sections treated with 70S30C (70S) powder, 55S30C15B (55S) powder, and 55S30C15B (55S) fibre 13 days post-surgery.

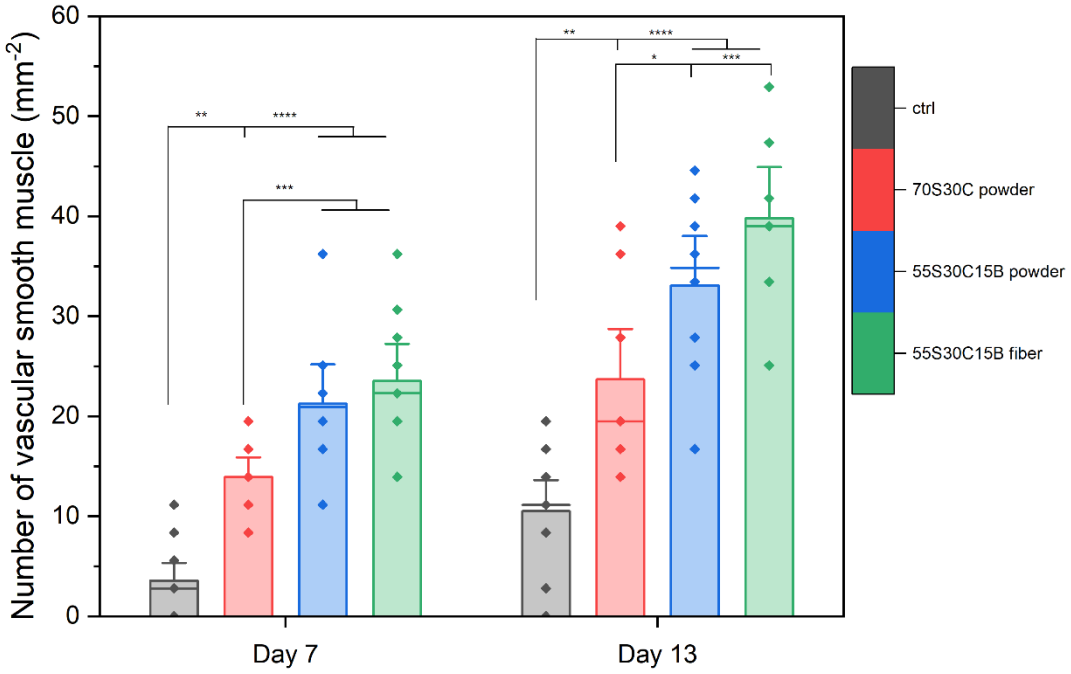


Figure 6. 25. The number of vascular smooth muscles per mm^2 derived from α-SMA immunohistochemistry staining of diabetic C57BJ/6 mice wounds sections treated with 70S30C powder, 55S30C15B powder, and 55S30C15B fibre on 7 and 13 days post-surgery. (*P <0.05, **P<0.01, ***P <0.001,****P <0.0001, n = 5 groups *2 image/group).

α-SMA is also commonly expressed in the vascular smooth muscle of arterioles or larger blood vessels [791, 932]. α-SMA at the vascular smooth muscle exists as a sealed loop, while those symbolling myofibroblasts are scattered at the pericellular matrix of the cells. The immunohistochemistry analysis also indicated the numbers of large blood vessels in different animal groups (Figure 6. 25). In agreement with the optical microscope analysis (Figure 6. 6) and the blood vessel formation profiles (Figure 6. 20, Figure 6. 21), there were very few large blood vessel formations on day 7, which means that the control group had the lease vascular infiltration. Wounds treated with 70S30C powder had many vessels infiltrated but all failed to infiltrate into the top layer of the dermis. Both 55S30C15B powder and 55S30C15B fibres induced a thorough blood vessel infiltration, but wounds treated with 55S30C15B fibres had arterioles parallel to the wound surface, which may indicate that these arterioles were formed inside the wounds rather than infiltrated from the hypodermis. The same trend followed on day 13. 55S30C15B fibres simulated the highest number of arteriole formation and the formed arterioles were smaller than those from wounds treated with 70S30C and 55S30C15B powder. The control group still had the least number of arterioles formed, which agrees with the blood vessel formation profiles (Figure 6. 21). Zhu *et al.* reported that BG-containing hydrogels stimulated higher arteriole

formation (marked by α-SMA), but the function of BGs on their own remains unknown. This study may potentially reveal the mechanism of BGs in the arteriole formation [235].

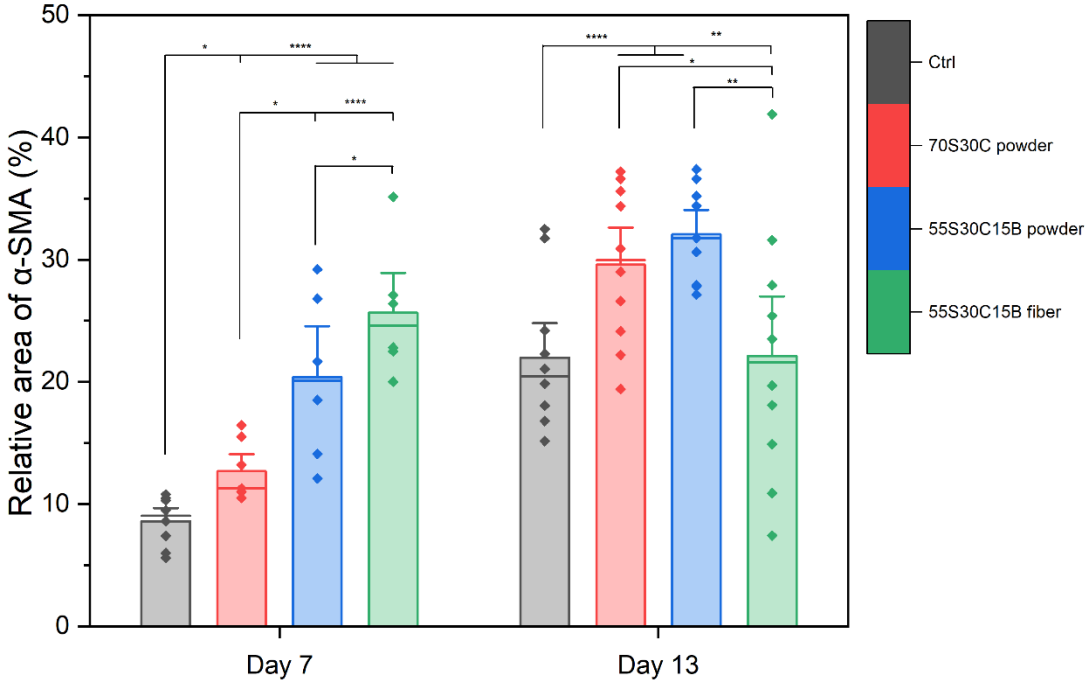


Figure 6. 26. The relative area of α-SMA derived from α-SMA immunohistochemistry staining of diabetic C57BJ/6 mice wound sections treated with 70S30C powder, 55S30C15B powder, and 55S30C15B fibre on 7 and 13 days post-surgery. (*P <0.05, **P<0.01, ***P <0.001,****P <0.0001, n = 5 groups *2 image/group)

6.4 Concluding remarks

This chapter reported the animal studies conducted on 70S30C powder, 55S30C15B powder, and 55S30C15B fibre in order to understand the efficacy of the BG samples on in vivo diabetic ulcer regeneration. Optical images of the wound area were taken to understand the wound closure rate and blood vessel formation in wounds; histology assessments were conducted to understand epithelialization, cell infiltration, and collagen deposition; IL-1β and IL-10 immunohistochemistry characterized the anti-inflammatory effect; angiogenesis was determined by investigating through VEGF and CD31 immunohistochemistry; alpha-smooth muscle actin (α-SMA) was characterized to understand both the number of large blood vessel infiltration and the number of myofibroblasts. In general, all BG treated samples had better efficacies in all the above-mentioned steps. Through comparison between groups, we understand that the incorporation of boron to BG provides better biological cues to stimulate wound healing,

while processing BGs to fibres also accelerates all the above-mentioned steps. The effect of BG, boron incorporation and fibre VS power is summarized in Table 6. 1. The in vivo study proved the efficacy of the 55S30C15B fibres as promising strategies for real-life diabetic ulcer regeneration.

Table 6. 1. The effect of BG implantation, the effect of boron incorporation, and the effect of fibre VS powder in wound healing steps are derived from the pairwise comparison among wounds treated with nothing (control), 70S30C powder, 55S30C15B powder, and 55S30C15B fibre mats respectively. (Little means no significance, Medium means *0.01 < P < 0.05 of significance, High means **0.0001 < P < 0.01 significance, and very high means ****P < 0.0001 significance)

	Effect of BG implantation	**Effect of B incorporation**	**Fibre VS powder**
Wound closure	High	High	High
Macrophage number	Very High	Very High	Little
Collagen deposition	High	High	High
Collagen alignment	Medium	Little	Little
IL-1β	High	Little	Medium
IL-10	High	High	Little
VEGF	Very High	High	Medium
Blood vessels	Very High	High	Medium
α-smooth muscle actin	Very High	High	High

7 Conclusion and future work

7.1 Conclusion

The aim of this thesis was to design wound matrices for the healing of different types of wounds. 3D ECM-mimic bioactive glass fibre mats were being fabricated to promote a sustained release of Zn or borate ions for burn regeneration and diabetic ulcer healing respectively. Both fibre mats were found to release a therapeutic range of ions and their efficacies were proved in vivo. The efficacies of borosilicate fibre mats were further confirmed in vivo and their mechanisms for individual wound healing steps were investigated.

7.1.1 Sol-gel electrospinning parameters for BG fibre mats

The sol-gel electrospinning parameters were optimized based on the protocol proposed by Poologasundarampillai *et al.*, and Norris *et al.* [96, 97]. First, the influence of ventilation was solved by adjusting the collector according to the track of the wind. Then, the effect of humidity has been re-characterized. While previous studies reported that > 35% humidity was ideal for 3D fibre formation, it was found that > 35% humidity only resulted in high beading and more branched fibres. The lower the humidity, the thinner the fibres. Humidity >45% resulted in mutual attraction between fibres so that they would not reach the collector. Other parameters such as voltage and working distance were also re-evaluated with the presence of ventilation. The ideal parameters are: voltage 10 kV; flow rate: 0.4 mL h^{-1}; air gap distance: 12 cm; relative humidity: 25%-35%; inner diameter of spinneret: 0.7 mm; room temperature.

For the synthesis of Zn-containing BGs, the viscosity, surface tension, and electroconductivity was hardly interrupted due to the low composition of Zn, so the parameters for the preparation of the sol-gel precursor, preparation of the binder, and the stabilization process were similar to that proposed by Norris *et al.* [97]. The sol-gel precursors of the Zn-BG fibre mats were prepared through the step-wise addition of TEOS, $Ca(NO_3)_2 \cdot 4H_2O$ (g), $Zn(NO_3)_2 \cdot 6H_2O$ (g) to a mixture of ethanol, water, and 2 M nitric acid. After 24-48 hours of aging, they were mixed with a PVB binder (1g/11.4 ml) by a ratio of 1:1 before being loaded into the electrospinner. Electrospun BG fibres were sintered through healing to 600 °C at a rate of 1 °C min^{-1} with a dwell at 600 °C for 3 h before oven cooling.

For the synthesis of borosilicate BG fibre mats, the parameters were similar to that of Zn-containing BGs until the borate composition exceeds 55%. Beyond this point, a modified sol-gel approach was applied to ensure the binding of silicates and borates into BG networks before the addition of calcium ions. This aims to prevent the crystallization of calcium borate. Besides, more ethanol was required to dissolve borate groups and a longer aging time (>48 h) was needed correspondingly for complete gelation time. The weight of PVB in the PVB binder also increased with the increase of ethanol in the sol-gel precursor in order to maintain constant viscosity and surface tension. The operational parameters were similar to that of Zn-containing BGs, but during stabilization, borosilicate fibres were kept at 300 °C for 6 h to completely remove the polymer components and prevent carbon deposition. Even though, high crystallization occurred when borate content exceeded 55%.

7.1.2 BG fibre mats releasing zinc ions for the regeneration of burn injuries

We synthesized BG fibres mats with a composition of 70 mol% SiO_2-(30-x) mol% CaO- x mol% ZnO as scaffolds for burn regeneration. Zn incorporation hardly influenced the chemical and physical structure of the fibre mats, which mimicked the ECM environment to stimulate cell attachment and migration. The fibre mats facilitated a controlled release of Zn^{2+}, Ca^{2+}, and SiO_4^{4-} which were therapeutic for antibacterial activities, anti-inflammation, angiogenesis, and follicle regeneration. In vitro studies found that Zn incorporation prevented the cytotoxic effect of SiO_2-CaO BGs on fibroblasts and stimulated their expression of growth factors (PDGF, VEGF, bFGF, TGF-β, and HIF-1α) for ECM deposition and angiogenesis. BG fibres were also found to stimulate higher migration and proliferation when applying the HDFs media that had been precultured with BG dissolution products to HUVECs. Their stimulation of protein expressions was also characterized to understand their mechanism in angiogenesis. In summary, this chapter provides evidence that proves the efficacy of Zn-containing BG fibre mats as healing devices for burn injury.

7.1.3 Borosilicate BG fibre mats for diabetic ulcer regeneration

In this chapter, we successfully prepared the ECM-mimic BG fibre mats with a composition of (70-x) mol% SiO_2-30 mol% CaO- x mol% B_2O_3 (x=0, 5, 15, and 35, while higher compositions induced crystallization or carbon deposition) through the modified sol-gel electrospinning approach. Boron incorporation hardly affected both the chemical and physical structure of the fibre mats, but greatly influence their dissolution profiles. The

release of BO_3^{3-}, Ca^{2+}, and SiO_4^{4-} were therapeutic to the ECM deposition and angiogenesis, which was further confirmed through in vitro study on HDF viability and protein expressions (PDGF, VEGF, bFGF, TGF-β, and HIF-1α). The BG-HDF conditioned media were further accessed on HUVEC cells and were found to stimulate their viability, migration, and protein expressions. The results proved the potential of borosilicate BG fibre mats as strategies for the regeneration of diabetic ulcers.

7.1.4 In vivo assessment of BGs in diabetic ulcer regeneration

In this chapter, animal studies were conducted on 70S30C powder, 55S30C15B powder, and 55S30C15B fibre to characterize their in vivo efficacy of the BG samples in the regeneration of diabetic ulcers. The diabetic model was created on C57BJ/6 mice based on previous literature. Images of the wound area and the backside of the dermis layer on days 3, 7, 10, and 13 revealed that wounds treated with 55S30C15B healed the fastest, followed by wounds treated with 55S30C15B powder, 70S30C powder, and nothing (control). A similar tendency was found in the epithelialization, cell infiltration, collagen deposition, anti-inflammation, angiogenesis, and myofibroblast maturation (α-SMA). Comparing individual groups, it was found that wounds treated with 70S30C had either high or very high significance to wounds from the control group, which indicates the effect of BGs in stimulating wound healing. Wounds treated with 55S30C15B powder had faster (high significance) wound closure, collagen deposition, angiogenesis, and myofibroblast maturation due to the release of therapeutic BO_3^{3-} ions. They also had a much faster anti-inflammation (less macrophage on day 7) because boron incorporation highly up-regulated IL-10 expression in wounds, but no effects were found on IL-1β expressions. Processing BGs into fibre mats induced structural cues that favoured cell attachment and migration. Thereby, wounds treated with 55S30C15B fibres had a much faster wound closure and epithelialization rate compared to those treated with 55S30C15B powder, as well as collagen deposition and tissue granulation. Endothelial cells also migrated faster on the ECM-mimic structure so that less VEGF was needed in wounds from the 55S30C15B fibre group to activate angiogenesis. The in vivo study proves the efficacy of the 55S30C15B fibres as promising strategies for real-life diabetic ulcer regeneration and also explains the effect of BG, boron incorporation, and structure on individual steps in the regeneration of diabetic ulcers.

7.2 Future work

The work proposed in this thesis indicates the success of applying BGs as 3D ECM-mimic matrices for soft tissue engineering. The effects of different therapeutic ions have also

been studied in vitro and in vivo. But, this is merely a starting point of the investigation. For example, it would have an impact to investigate the antibacterial or anti-inflammatory properties of BG fibre mats in vitro and study the paracrine effect from macrophages. It could also be interesting to study the cell attachment on the fibre mats. For Zn-containing BG fibres, studies on in vivo burn model can add further credence to its efficacies. In a macroscopic view, it would be meaningful to study the two fields mentioned below for the development of BG-based fibre mats for soft tissue engineering.

7.2.1 Synergistic effects of multiple therapeutic ions in the BG system

Few articles reported BGs with more than 3 therapeutic ions so little was known about how these ions influence the physical and chemical structure, how they affect the BG degradation and ion release, and how they interplay with each other during the wound healing cascade. In some of my collaboration projects, we found that Zr can prevent the release of Ca and Zn as well as the physical structure of the BGs, but more studies are needed to fully understand the correlation between ion concentration and their functions. For example, it could be interesting to investigate the synergistic effect of Cu and Zn in silicate BG systems. Or, it can be worthwhile to study the release profile of Cu and/or Zn in borate/borosilicate BGs. Recently, phosphate BGs are finding use in soft tissue engineering due to their fast degradation. This may also provide insights into the investigation of BG fibre mats and their translation of them into real-life products.

7.2.2 inorganic-organic hybrid fibre mats for the regeneration of load-bearing tissues

On the other hand, BG fibres are limited by their mechanical properties. BGs are very brittle so their fibres can be easily broken through external shear. One of the studies that I am currently carrying out is to synthesize covalently-networked inorganic-organic hybrids as load-bearing materials. We are managing to apply them for either deep wound regeneration, in which the hybrid fibres mimic the hypodermis ECM matrix, or muscle regeneration, in which the hybrid fibres mimic the myocyte bundles (muscle fibre). Chitosan was selected as the organic component as it is biodegradable and promotes blood clotting [952, 953], anti-microbial and antioxidant activities [954, 955], activities of fibroblasts, and ECM deposition [956-959] in the wound healing cascade. They also have ideal mechanical properties, biological cues that attract tissue bonding and cell attachment, and diol groups for covalent networking.

In my Ph.D., I successfully synthesized covalently linked borate-chitosan hybrids that were covalently linked through (3-Glycidyloxypropyl)trimethoxysilane (GPTMS). Chemical characterization through FTIR proved the formation of the borate-chitosan hybrid as the epoxy ring of GPTMS opened, which indicates the successful bond formation. Mechanical testing also found that the elastic modulus of the material can reach up to 8 MPa, which was stronger than the modulus of most soft tissues. Because the old electrospinner cannot supply a voltage beyond 20 kV, it was not likely to fabricate electrospun fibres with these materials. Instead, electrosprayed hybrid particles were formed, which were formed only when the solution parameters were ideal for jet activation, but the voltage is not enough. With the purchase of the new machine, it is likely to process hybrids into fibre mats and the electrospinning parameter for chitosan hybrids is being optimized. Once the fibre mats are fabricated, future work in dissolution studies and in vitro studies can be used to find their biological effects and corresponding mechanism.

References

[1] X. Zhang, X. Wei, L. Liu, G.P. Marti, M.S. Ghanamah, M.J. Arshad, L. Strom, R. Spence, J. Jeng, S. Milner, Association of increasing burn severity in mice with delayed mobilization of circulating angiogenic cells, Archives of Surgery 145(3) (2010) 259-266.
[2] M.G. Jeschke, M.E. van Baar, M.A. Choudhry, K.K. Chung, N.S. Gibran, S. Logsetty, Burn injury, Nature Reviews Disease Primers 6(1) (2020) 1-25.
[3] L.H. Evers, D. Bhavsar, P. Mailänder, The biology of burn injury, Experimental dermatology 19(9) (2010) 777-783.
[4] G.J. Summer, K.A. Puntillo, C. Miaskowski, P.G. Green, J.D. Levine, Burn injury pain: the continuing challenge, The journal of pain 8(7) (2007) 533-548.
[5] A.M. Lachiewicz, C.G. Hauck, D.J. Weber, B.A. Cairns, D. van Duin, Bacterial infections after burn injuries: impact of multidrug resistance, Clinical Infectious Diseases 65(12) (2017) 2130-2136.
[6] O. Kallinen, K. Maisniemi, T. Böhling, E. Tukiainen, V. Koljonen, Multiple organ failure as a cause of death in patients with severe burns, Journal of burn care & research 33(2) (2012) 206-211.
[7] C. Smolle, J. Cambiaso-Daniel, A.A. Forbes, P. Wurzer, G. Hundeshagen, L.K. Branski, F. Huss, L.-P. Kamolz, Recent trends in burn epidemiology worldwide: a systematic review, Burns 43(2) (2017) 249-257.
[8] D.G. Greenhalgh, Management of burns, New England Journal of Medicine 380(24) (2019) 2349-2359.
[9] C. Porter, R.G. Tompkins, C.C. Finnerty, L.S. Sidossis, O.E. Suman, D.N. Herndon, The metabolic stress response to burn trauma: current understanding and therapies, The Lancet 388(10052) (2016) 1417-1426.
[10] K. Lay, T. Kume, E. Fuchs, FOXC1 maintains the hair follicle stem cell niche and governs stem cell quiescence to preserve long-term tissue-regenerating potential, Proceedings of the National Academy of Sciences 113(11) (2016) E1506-E1515.
[11] J. Li, Y.P. Zhang, R.S. Kirsner, Angiogenesis in wound repair: angiogenic growth factors and the extracellular matrix, Microscopy research and technique 60(1) (2003) 107-114.
[12] A. Young, C.-E. McNaught, The physiology of wound healing, Surgery (Oxford) 29(10) (2011) 475-479.
[13] S. Guo, L.A. Dipietro, Factors affecting wound healing, J Dent Res 89(3) (2010) 219-29.
[14] P.K. Moulik, R. Mtonga, G.V. Gill, Amputation and mortality in new-onset diabetic foot ulcers stratified by etiology, Diabetes care 26(2) (2003) 491-494.
[15] M.E. Levin, Preventing amputation in the patient with diabetes, Diabetes care 18(10) (1995) 1383-1394.
[16] M. Schafer, S. Werner, Oxidative stress in normal and impaired wound repair, Pharmacol Res 58(2) (2008) 165-71.
[17] D.G. Armstrong, J. Wrobel, J.M. Robbins, Guest editorial: are diabetes-related wounds and amputations worse than cancer, Int Wound J 4(4) (2007) 286-287.
[18] R.G. Frykberg, J. Banks, Challenges in the Treatment of Chronic Wounds, Adv Wound Care (New Rochelle) 4(9) (2015) 560-582.
[19] J. Hodde, R. Allam, Extracellular wound matrices: small intestinal submucosa wound matrix for chronic wound healing, Wounds 19(2) (2007) 157-162.

[20] N.J. Trengove, H. Bielefeldt-Ohmann, M.C. Stacey, Mitogenic activity and cytokine levels in non-healing and healing chronic leg ulcers, Wound Repair Regen 8(1) (2000) 13-25.
[21] B.A. Mast, G.S. Schultz, Interactions of cytokines, growth factors, and proteases in acute and chronic wounds, Wound Repair Regen 4(4) (1996) 411-20.
[22] M.C. Robson, The role of growth factors in the healing of chronic wounds, Wound Repair Regen 5(1) (1997) 12-7.
[23] S.A. Eming, P. Martin, M. Tomic-Canic, Wound repair and regeneration: mechanisms, signaling, and translation, Sci Transl Med 6(265) (2014) 265sr6.
[24] W.H. Eaglstein, V. Falanga, Chronic wounds, Surgical Clinics 77(3) (1997) 689-700.
[25] S.M. Bauer, R.J. Bauer, O.C. Velazquez, Angiogenesis, vasculogenesis, and induction of healing in chronic wounds, Vascular and endovascular surgery 39(4) (2005) 293-306.
[26] R.J. Bodnar, Chemokine regulation of angiogenesis during wound healing, Advances in wound care 4(11) (2015) 641-650.
[27] M.G. Tonnesen, X. Feng, R.A. Clark, Angiogenesis in wound healing, Journal of Investigative Dermatology Symposium Proceedings, Elsevier, 2000, pp. 40-46.
[28] A. Veves, V. Falanga, D.G. Armstrong, M.L. Sabolinski, Graftskin, a human skin equivalent, is effective in the management of noninfected neuropathic diabetic foot ulcers: a prospective randomized multicenter clinical trial, Diabetes care 24(2) (2001) 290-295.
[29] M. Kubota, S. Shimmura, S. Kubota, H. Miyashita, N. Kato, K. Noda, Y. Ozawa, T. Usui, S. Ishida, K. Umezawa, Hydrogen and N-acetyl-L-cysteine rescue oxidative stress-induced angiogenesis in a mouse cornealalkali-burn model, Investigative ophthalmology & visual science 52(1) (2011) 427-433.
[30] M. Galeano, D. Altavilla, A. Bitto, L. Minutoli, M. Calò, P.L. Cascio, F. Polito, G. Giugliano, G. Squadrito, C. Mioni, Recombinant human erythropoietin improves angiogenesis and wound healing in experimental burn wounds, Critical care medicine 34(4) (2006) 1139-1146.
[31] S. Hacker, R. Mittermayr, S. Nickl, T. Haider, D. Lebherz-Eichinger, L. Beer, A. Mitterbauer, H. Leiss, M. Zimmermann, T. Schweiger, Paracrine factors from irradiated peripheral blood mononuclear cells improve skin regeneration and angiogenesis in a porcine burn model, Scientific reports 6(1) (2016) 1-13.
[32] L.L. Hench, The future of bioactive ceramics, J Mater Sci Mater Med 26(2) (2015) 86.
[33] P. Basu, U.N. Kumar, I. Manjubala, Wound healing materials - a perspective for skin tissue engineering, Current Science 112(12) (2017) 2392-2404.
[34] I. Negut, G. Dorcioman, V. Grumezescu, Scaffolds for Wound Healing Applications, Polymers (Basel) 12(9) (2020) 2010.
[35] A.D. Juncos Bombin, N.J. Dunne, H.O. McCarthy, Electrospinning of natural polymers for the production of nanofibres for wound healing applications, Mater Sci Eng C Mater Biol Appl 114 (2020) 110994.
[36] Z. Zhang, W. Li, Y. Liu, Z. Yang, L. Ma, H. Zhuang, E. Wang, C. Wu, Z. Huan, F. Guo, Design of a biofluid-absorbing bioactive sandwich-structured Zn–Si bioceramic composite wound dressing for hair follicle regeneration and skin burn wound healing, Bioactive materials 6(7) (2021) 1910-1920.

[37] L. Ma, Y. Zhou, Z. Zhang, Y. Liu, D. Zhai, H. Zhuang, Q. Li, J. Yuye, C. Wu, J. Chang, Multifunctional bioactive Nd-Ca-Si glasses for fluorescence thermometry, photothermal therapy, and burn tissue repair, Science advances 6(32) (2020) eabb1311.
[38] Z. Zhang, Q. Dai, Y. Zhang, H. Zhuang, E. Wang, Q. Xu, L. Ma, C. Wu, Z. Huan, F. Guo, Design of a multifunctional biomaterial inspired by ancient Chinese medicine for hair regeneration in burned skin, ACS applied materials & interfaces 12(11) (2020) 12489-12499.
[39] L.L. Hench, J.M. Polak, Third-generation biomedical materials, Science 295(5557) (2002) 1014-7.
[40] C.Y. Ning, L. Zhou, G.X. Tan, Fourth-generation biomedical materials, Materials Today 19(1) (2016) 2-3.
[41] L.L. Hench, I. Thompson, Twenty-first century challenges for biomaterials, J R Soc Interface 7 Suppl 4(suppl_4) (2010) S379-91.
[42] X. Wang, J. Xue, B. Ma, J. Wu, J. Chang, M. Gelinsky, C. Wu, Black Bioceramics: Combining Regeneration with Therapy, Adv Mater 32(48) (2020) e2005140.
[43] B. Dalisson, J. Barralet, Bioinorganics and Wound Healing, Adv Healthc Mater 8(18) (2019) e1900764.
[44] P. Habibovic, J.E. Barralet, Bioinorganics and biomaterials: bone repair, Acta Biomater 7(8) (2011) 3013-26.
[45] M.N. Rahaman, D.E. Day, B.S. Bal, Q. Fu, S.B. Jung, L.F. Bonewald, A.P. Tomsia, Bioactive glass in tissue engineering, Acta Biomater 7(6) (2011) 2355-73.
[46] J.R. Jones, Review of bioactive glass: from Hench to hybrids, Acta Biomater 9(1) (2013) 4457-86.
[47] T.A. Ostomel, Q. Shi, G.D. Stucky, Oxide hemostatic activity, J Am Chem Soc 128(26) (2006) 8384-5.
[48] S. Pourshahrestani, E. Zeimaran, N. Adib Kadri, N. Gargiulo, S. Samuel, S.V. Naveen, T. Kamarul, M.R. Towler, Gallium-containing mesoporous bioactive glass with potent hemostatic activity and antibacterial efficacy, J Mater Chem B 4(1) (2016) 71-86.
[49] E. Munukka, O. Lepparanta, M. Korkeamaki, M. Vaahtio, T. Peltola, D. Zhang, L. Hupa, H. Ylanen, J.I. Salonen, M.K. Viljanen, E. Eerola, Bactericidal effects of bioactive glasses on clinically important aerobic bacteria, J Mater Sci Mater Med 19(1) (2008) 27-32.
[50] I. Allan, H. Newman, M. Wilson, Antibacterial activity of particulate bioglass against supra- and subgingival bacteria, Biomaterials 22(12) (2001) 1683-7.
[51] X. Dong, J. Chang, H. Li, Bioglass promotes wound healing through modulating the paracrine effects between macrophages and repairing cells, J Mater Chem B 5(26) (2017) 5240-5250.
[52] F. Zhao, W. Xie, W. Zhang, X. Fu, W. Gao, B. Lei, X. Chen, 3D Printing Nanoscale Bioactive Glass Scaffolds Enhance Osteoblast Migration and Extramembranous Osteogenesis through Stimulating Immunomodulation, Adv Healthc Mater 7(16) (2018) e1800361.
[53] R.M. Day, A.R. Boccaccini, S. Shurey, J.A. Roether, A. Forbes, L.L. Hench, S.M. Gabe, Assessment of polyglycolic acid mesh and bioactive glass for soft-tissue engineering scaffolds, Biomaterials 25(27) (2004) 5857-66.
[54] R.M. Day, Bioactive glass stimulates the secretion of angiogenic growth factors and angiogenesis in vitro, Tissue Eng 11(5-6) (2005) 768-77.

[55] H. Yu, J. Peng, Y. Xu, J. Chang, H. Li, Bioglass Activated Skin Tissue Engineering Constructs for Wound Healing, ACS Appl Mater Interfaces 8(1) (2016) 703-15.
[56] H. Li, J. He, H. Yu, C.R. Green, J. Chang, Bioglass promotes wound healing by affecting gap junction connexin 43 mediated endothelial cell behavior, Biomaterials 84 (2016) 64-75.
[57] L.A. Haro Durand, A. Gongora, J.M. Porto Lopez, A.R. Boccaccini, M.P. Zago, A. Baldi, A. Gorustovich, In vitro endothelial cell response to ionic dissolution products from boron-doped bioactive glass in the SiO2-CaO-P2O5-Na2O system, J Mater Chem B 2(43) (2014) 7620-7630.
[58] T.H. Qazi, J.C. Berkmann, J. Schoon, S. Geissler, G.N. Duda, A.R. Boccaccini, E. Lippens, Dosage and composition of bioactive glasses differentially regulate angiogenic and osteogenic response of human MSCs, J Biomed Mater Res A 106(11) (2018) 2827-2837.
[59] J. Pasquet, Y. Chevalier, E. Couval, D. Bouvier, G. Noizet, C. Morliere, M.A. Bolzinger, Antimicrobial activity of zinc oxide particles on five micro-organisms of the Challenge Tests related to their physicochemical properties, Int J Pharm 460(1-2) (2014) 92-100.
[60] J. Pasquet, Y. Chevalier, J. Pelletier, E. Couval, D. Bouvier, M.A. Bolzinger, The contribution of zinc ions to the antimicrobial activity of zinc oxide, Colloids and Surfaces a-Physicochemical and Engineering Aspects 457 (2014) 263-274.
[61] A.S. Prasad, O. Kucuk, Zinc in cancer prevention, Cancer Metastasis Rev 21(3-4) (2002) 291-5.
[62] A.S. Prasad, F.W. Beck, D.C. Snell, O. Kucuk, Zinc in cancer prevention, Nutr Cancer 61(6) (2009) 879-87.
[63] R. Augustine, E.A. Dominic, I. Reju, B. Kaimal, N. Kalarikkal, S. Thomas, Investigation of angiogenesis and its mechanism using zinc oxide nanoparticle-loaded electrospun tissue engineering scaffolds, Rsc Advances 4(93) (2014) 51528-51536.
[64] M. Sheffer, A.J. Simon, J. Jacob-Hirsch, G. Rechavi, E. Domany, D. Givol, G. D'Orazi, Genome-wide analysis discloses reversal of the hypoxia-induced changes of gene expression in colon cancer cells by zinc supplementation, Oncotarget 2(12) (2011) 1191-202.
[65] S. Demirci, A. Dogan, S. Aydin, E.C. Dulger, F. Sahin, Boron promotes streptozotocin-induced diabetic wound healing: roles in cell proliferation and migration, growth factor expression, and inflammation, Mol Cell Biochem 417(1-2) (2016) 119-33.
[66] R. Chen, Q. Li, S. Xu, J. Han, P. Huang, Z. Yu, D. Jia, J. Liu, H. Jia, M. Shen, Nanosized HCA-coated borate bioactive glass with improved wound healing effects on rodent model, Chemical Engineering Journal (2021) 130299.
[67] C. Yin, Q. Zhao, W. Li, Z. Zhao, J. Wang, T. Deng, P. Zhang, K. Shen, Z. Li, Y. Zhang, Biomimetic anti-inflammatory nano-capsule serves as a cytokine blocker and M2 polarization inducer for bone tissue repair, Acta Biomater 102 (2020) 416-426.
[68] W. Jia, H. Hu, A. Li, H. Deng, C.L. Hogue, J.C. Mauro, C. Zhang, Q. Fu, Glass-activated regeneration of volumetric muscle loss, Acta Biomater 103 (2020) 306-317.
[69] B. Dousset, M. Benderdour, K. Hess, R. Mayap-Nzietchueng, F. Belleville, A. Duprez, Effects of boron in wound healing, Trace Elements in Man and Animals 10, Springer2002, pp. 1061-1065.
[70] S. Ahtzaz, T.S. Waris, L. Shahzadi, A.A. Chaudhry, I.U. Rehman, M. Yar, Boron for tissue regeneration-it's loading into chitosan/collagen hydrogels and testing on chorioallantoic membrane to study the effect on angiogenesis, International Journal of Polymeric Materials and Polymeric Biomaterials 69(8) (2020) 525-534.

[71] P. Balasubramanian, T. Buttner, V.M. Pacheco, A.R. Boccaccini, Boron-containing bioactive glasses in bone and soft tissue engineering, Journal of the European Ceramic Society 38(3) (2018) 855-869.
[72] S. Chen, Q. Yang, R.K. Brow, K. Liu, K.A. Brow, Y. Ma, H. Shi, In vitro stimulation of vascular endothelial growth factor by borate-based glass fibers under dynamic flow conditions, Mater Sci Eng C Mater Biol Appl 73 (2017) 447-455.
[73] A. Dogan, S. Demirci, A.B. Caglayan, E. Kilic, M.Y. Gunal, U. Uslu, A. Cumbul, F. Sahin, Sodium pentaborate pentahydrate and pluronic containing hydrogel increases cutaneous wound healing in vitro and in vivo, Biol Trace Elem Res 162(1-3) (2014) 72-9.
[74] F.M. Watt, H. Fujiwara, Cell-extracellular matrix interactions in normal and diseased skin, Cold Spring Harbor Perspectives in Biology 3(4) (2011) a005124.
[75] M. Yanagishita, Function of proteoglycans in the extracellular matrix, Pathology International 43(6) (1993) 283-293.
[76] J. Ishihara, A. Ishihara, K. Fukunaga, K. Sasaki, M.J. White, P.S. Briquez, J.A. Hubbell, Laminin heparin-binding peptides bind to several growth factors and enhance diabetic wound healing, Nature communications 9(1) (2018) 1-14.
[77] L. Parisi, A. Toffoli, B. Ghezzi, B. Mozzoni, S. Lumetti, G.M. Macaluso, A glance on the role of fibronectin in controlling cell response at biomaterial interface, Japanese dental science review 56(1) (2020) 50-55.
[78] J.W. Madden, E.E. Peacock Jr, Studies on the biology of collagen during wound healing. 3. Dynamic metabolism of scar collagen and remodeling of dermal wounds, Annals of surgery 174(3) (1971) 511.
[79] P.D. Verhaegen, P.P. Van Zuijlen, N.M. Pennings, J. Van Marle, F.B. Niessen, C.M. Van Der Horst, E. Middelkoop, Differences in collagen architecture between keloid, hypertrophic scar, normotrophic scar, and normal skin: an objective histopathological analysis, Wound Repair and Regeneration 17(5) (2009) 649-656.
[80] G.S. Schultz, R.G. Sibbald, V. Falanga, E.A. Ayello, C. Dowsett, K. Harding, M. Romanelli, M.C. Stacey, L. Teot, W. Vanscheidt, Wound bed preparation: a systematic approach to wound management, Wound Repair Regen 11 Suppl 1 (2003) S1-28.
[81] B.K. Sun, Z. Siprashvili, P.A. Khavari, Advances in skin grafting and treatment of cutaneous wounds, Science 346(6212) (2014) 941-5.
[82] M.B. Witte, A. Barbul, General principles of wound healing, Surg Clin North Am 77(3) (1997) 509-28.
[83] S.B. Jung, D.E. Day, Wound care, Google Patents, 2011.
[84] J. Zhou, H. Wang, S. Zhao, N. Zhou, L. Li, W. Huang, D. Wang, C. Zhang, In vivo and in vitro studies of borate based glass micro-fibers for dermal repairing, Mater Sci Eng C Mater Biol Appl 60 (2016) 437-445.
[85] S. Zhao, L. Li, H. Wang, Y. Zhang, X. Cheng, N. Zhou, M.N. Rahaman, Z. Liu, W. Huang, C. Zhang, Wound dressings composed of copper-doped borate bioactive glass microfibers stimulate angiogenesis and heal full-thickness skin defects in a rodent model, Biomaterials 53 (2015) 379-91.
[86] S. Lonnqvist, P. Emanuelsson, G. Kratz, Influence of acidic pH on keratinocyte function and re-epithelialisation of human in vitro wounds, J Plast Surg Hand Surg 49(6) (2015) 346-52.

[87] C.R. Kruse, M. Singh, S. Targosinski, I. Sinha, J.A. Sorensen, E. Eriksson, K. Nuutila, The effect of pH on cell viability, cell migration, cell proliferation, wound closure, and wound reepithelialization: In vitro and in vivo study, Wound Repair Regen 25(2) (2017) 260-269.
[88] A. Lengheden, L. Jansson, pH effects on experimental wound healing of human fibroblasts in vitro, Eur J Oral Sci 103(3) (1995) 148-55.
[89] M. Hernandez, S. Choi, A.M. DiLorenzo, Study of pH and Cellular Response in Pulmonary Fibroblasts After Exposure to Market Street World Trade Center Particulate Matter, OnLine Journal of Biological Sciences 12(4) (2012) 142-148.
[90] S.D. Dib-Hajj, S.G. Waxman, Sodium Channels in Human Pain Disorders: Genetics and Pharmacogenomics, Annu Rev Neurosci 42 (2019) 87-106.
[91] Q. Yang, S. Chen, H. Shi, H. Xiao, Y. Ma, In vitro study of improved wound-healing effect of bioactive borate-based glass nano-/micro-fibers, Mater Sci Eng C Mater Biol Appl 55 (2015) 105-17.
[92] S.-S. Choi, S.G. Lee, S.S. Im, S.H. Kim, Y.L. Joo, Silica nanofibers from electrospinning/sol-gel process, Journal of Materials Science Letters 22(12) (2003) 891-893.
[93] H.Q. Dai, J. Gong, H. Kim, D. Lee, A novel method for preparing ultra-fine alumina-borate oxide fibres via an electrospinning technique, Nanotechnology 13(5) (2002) 674-677.
[94] H.W. Kim, H.E. Kim, J.C. Knowles, Production and potential of bioactive glass nanofibers as a next-generation biomaterial, Advanced Functional Materials 16(12) (2006) 1529-1535.
[95] H. Lu, T. Zhang, X.P. Wang, Q.F. Fang, Electrospun submicron bioactive glass fibers for bone tissue scaffold, J Mater Sci Mater Med 20(3) (2009) 793-8.
[96] G. Poologasundarampillai, D. Wang, S. Li, J. Nakamura, R. Bradley, P.D. Lee, M.M. Stevens, D.S. McPhail, T. Kasuga, J.R. Jones, Cotton-wool-like bioactive glasses for bone regeneration, Acta Biomater 10(8) (2014) 3733-46.
[97] E. Norris, C. Ramos-Rivera, G. Poologasundarampillai, J.P. Clark, Q. Ju, A. Obata, J.V. Hanna, T. Kasuga, C.A. Mitchell, G. Jell, J.R. Jones, Electrospinning 3D bioactive glasses for wound healing, Biomed Mater 15(1) (2020) 015014.
[98] S. Shruti, A.J. Salinas, G. Lusvardi, G. Malavasi, L. Menabue, M. Vallet-Regi, Mesoporous bioactive scaffolds prepared with cerium-, gallium- and zinc-containing glasses, Acta Biomaterialia 9(1) (2013) 4836-4844.
[99] V. Aina, G. Malavasi, A. Fiorio Pla, L. Munaron, C. Morterra, Zinc-containing bioactive glasses: surface reactivity and behaviour towards endothelial cells, Acta Biomater 5(4) (2009) 1211-22.
[100] A.J. Salinas, S. Shruti, G. Malavasi, L. Menabue, M. Vallet-Regi, Substitutions of cerium, gallium and zinc in ordered mesoporous bioactive glasses, Acta Biomater 7(9) (2011) 3452-8.
[101] S. Haimi, G. Gorianc, L. Moimas, B. Lindroos, H. Huhtala, S. Raty, H. Kuokkanen, G.K. Sandor, C. Schmid, S. Miettinen, R. Suuronen, Characterization of zinc-releasing three-dimensional bioactive glass scaffolds and their effect on human adipose stem cell proliferation and osteogenic differentiation, Acta Biomaterialia 5(8) (2009) 3122-3131.
[102] A.J. Gale, Continuing education course #2: current understanding of hemostasis, Toxicol Pathol 39(1) (2011) 273-80.
[103] G. Broughton, 2nd, J.E. Janis, C.E. Attinger, The basic science of wound healing, Plast Reconstr Surg 117(7 Suppl) (2006) 12S-34S.

[104] G. Han, R. Ceilley, Chronic Wound Healing: A Review of Current Management and Treatments, Adv Ther 34(3) (2017) 599-610.
[105] C. Dunnill, T. Patton, J. Brennan, J. Barrett, M. Dryden, J. Cooke, D. Leaper, N.T. Georgopoulos, Reactive oxygen species (ROS) and wound healing: the functional role of ROS and emerging ROS-modulating technologies for augmentation of the healing process, Int Wound J 14(1) (2017) 89-96.
[106] J. Bylund, H. Björnsdottir, M. Sundqvist, A. Karlsson, C. Dahlgren, Measurement of respiratory burst products, released or retained, during activation of professional phagocytes, Neutrophil methods and protocols, Springer2014, pp. 321-338.
[107] H.-M. Shen, S. Pervaiz, Reactive oxygen species in cell fate decisions, Essentials of apoptosis, Springer2009, pp. 199-221.
[108] D. Trachootham, W. Lu, M.A. Ogasawara, R.D. Nilsa, P. Huang, Redox regulation of cell survival, Antioxid Redox Signal 10(8) (2008) 1343-74.
[109] Raja, K. Sivamani, M.S. Garcia, R.R. Isseroff, Wound re-epithelialization: modulating keratinocyte migration in wound healing, Front Biosci 12(3) (2007) 2849-68.
[110] S. Barrientos, O. Stojadinovic, M.S. Golinko, H. Brem, M. Tomic-Canic, Growth factors and cytokines in wound healing, Wound Repair Regen 16(5) (2008) 585-601.
[111] T.J. Koh, L.A. DiPietro, Inflammation and wound healing: the role of the macrophage, Expert Rev Mol Med 13 (2011) e23.
[112] J. Kudlow, J. Bjorge, TGF alpha in normal physiology, Seminars in Cancer Biology, 1990, pp. 293-302.
[113] G. Schultz, W. Clark, D.S. Rotatori, EGF and TGF-α in wound healing and repair, Journal of cellular biochemistry 45(4) (1991) 346-352.
[114] D.H. Adams, N. Ruzehaji, X.L. Strudwick, J. Greenwood, H. Campbell, R. Arkell, A. Cowin, Attenuation of Flightless I, an actin - remodelling protein, improves burn injury repair via modulation of transforming growth factor (TGF)-β1 and TGF-β3, British Journal of Dermatology 161(2) (2009) 326-336.
[115] I. Khan, S.U. Rahman, E. Tang, K. Engel, B. Hall, A.B. Kulkarni, P.R. Arany, Accelerated burn wound healing with photobiomodulation therapy involves activation of endogenous latent TGF-β1, Scientific reports 11(1) (2021) 1-15.
[116] E. Alemzadeh, A. Oryan, A.A. Mohammadi, Hyaluronic acid hydrogel loaded by adipose stem cells enhances wound healing by modulating IL-1β, TGF-β1, and bFGF in burn wound model in rat, Journal of Biomedical Materials Research Part B: Applied Biomaterials 108(2) (2020) 555-567.
[117] G.F. Pierce, T.A. Mustoe, B.W. Altrock, T.F. Deuel, A. Thomason, Role of platelet-derived growth factor in wound healing, Journal of cellular biochemistry 45(4) (1991) 319-326.
[118] J. Xu, R.A. Clark, Extracellular matrix alters PDGF regulation of fibroblast integrins, J Cell Biol 132(1-2) (1996) 239-49.
[119] M.S. Agren, H.H. Steenfos, S. Dabelsteen, J.B. Hansen, E. Dabelsteen, Proliferation and mitogenic response to PDGF-BB of fibroblasts isolated from chronic venous leg ulcers is ulcer-age dependent, Journal of Investigative Dermatology 112(4) (1999) 463-469.
[120] G. Neufeld, T. Cohen, S. Gengrinovitch, Z. Poltorak, Vascular endothelial growth factor (VEGF) and its receptors, The FASEB journal 13(1) (1999) 9-22.

[121] N. Ferrara, H.-P. Gerber, J. LeCouter, The biology of VEGF and its receptors, Nature medicine 9(6) (2003) 669-676.
[122] D. Gospodarowicz, G. Neufeld, L. Schweigerer, Fibroblast growth factor, Molecular and cellular endocrinology 46(3) (1986) 187-204.
[123] A. Baird, P.A. Walicke, Fibroblast growth factors, British Medical Bulletin 45(2) (1989) 438-452.
[124] S. Werner, K.G. Peters, M.T. Longaker, F. Fuller-Pace, M.J. Banda, L.T. Williams, Large induction of keratinocyte growth factor expression in the dermis during wound healing, Proceedings of the National Academy of Sciences 89(15) (1992) 6896-6900.
[125] J.S. Rubin, D.P. Bottaro, M. Chedid, T. Miki, D. Ron, H.-G. Cheon, W.G. Taylor, E. Fortney, H. Sakata, P.W. Finch, Keratinocyte growth factor, Cell biology international 19(5) (1995) 399-412.
[126] M.A. Nugent, R.V. Iozzo, Fibroblast growth factor-2, The international journal of biochemistry & cell biology 32(2) (2000) 115-120.
[127] M.H. Gartner, J.D. Benson, M.D. Caldwell, Insulin-like growth factors I and II expression in the healing wound, Journal of Surgical Research 52(4) (1992) 389-394.
[128] V. Todorović, P. Peško, M. Micev, M. Bjelović, M. Budeč, M. Mićić, D. Bašanac, O. Ilić-Stojanović, Insulin-like growth factor-I in wound healing of rat skin, Regulatory peptides 150(1-3) (2008) 7-13.
[129] A. Igarashi, H. Okochi, D. Bradham, G.R. Grotendorst, Regulation of connective tissue growth factor gene expression in human skin fibroblasts and during wound repair, Molecular biology of the cell 4(6) (1993) 637-645.
[130] M.P. Alfaro, D.L. Deskins, M. Wallus, J. DasGupta, J.M. Davidson, L.B. Nanney, M. A Guney, M. Gannon, P.P. Young, A physiological role for connective tissue growth factor in early wound healing, Laboratory Investigation 93(1) (2013) 81-95.
[131] R. Pakala, J.T. Willerson, C.R. Benedict, Effect of serotonin, thromboxane A2, and specific receptor antagonists on vascular smooth muscle cell proliferation, Circulation 96(7) (1997) 2280-2286.
[132] K.E. Gilman, K.H. Limesand, The complex role of prostaglandin E2-EP receptor signaling in wound healing, American Journal of Physiology-Regulatory, Integrative and Comparative Physiology 320(3) (2021) R287-R296.
[133] S. Zhang, Y. Liu, X. Zhang, D. Zhu, X. Qi, X. Cao, Y. Fang, Y. Che, Z.-C. Han, Z.-X. He, Prostaglandin E2 hydrogel improves cutaneous wound healing via M2 macrophages polarization, Theranostics 8(19) (2018) 5348.
[134] G.S. Ashcroft, M.J. Jeong, J.J. Ashworth, M. Hardman, W. Jin, N. Moutsopoulos, T. Wild, N. McCartney-Francis, D. Sim, G. McGrady, Tumor necrosis factor-alpha (TNF-α) is a therapeutic target for impaired cutaneous wound healing, Wound Repair and Regeneration 20(1) (2012) 38-49.
[135] H. Zelová, J. Hošek, TNF-α signalling and inflammation: interactions between old acquaintances, Inflammation Research 62(7) (2013) 641-651.
[136] D. Sauder, P. Kilian, J. McLane, T. Quick, H. Jakubovic, S. Davis, W. Eaglstein, P. Mertz, Interleukin-1 enhances epidermal wound healing, Lymphokine research 9(4) (1990) 465-473.
[137] K.M. Doersch, D.J. DelloStritto, M.K. Newell-Rogers, The contribution of interleukin-2 to effective wound healing, Experimental biology and medicine 242(4) (2017) 384-396.

[138] R.B. Mateo, J.S. Reichner, J.E. Albina, Interleukin-6 activity in wounds, American Journal of Physiology-Regulatory, Integrative and Comparative Physiology 266(6) (1994) R1840-R1844.
[139] R.M. Gallucci, D.K. Sloan, J.M. Heck, A.R. Murray, S.J. O'Dell, Interleukin 6 indirectly induces keratinocyte migration, Journal of Investigative Dermatology 122(3) (2004) 764-772.
[140] H.-O. Rennekampff, J.F. Hansbrough, V. Kiessig, C. Doré, M. Sticherling, J.-M. Schröder, Bioactive interleukin-8 is expressed in wounds and enhances wound healing, Journal of Surgical Research 93(1) (2000) 41-54.
[141] Y. Ishida, T. Kondo, T. Takayasu, Y. Iwakura, N. Mukaida, The essential involvement of cross-talk between IFN-γ and TGF-β in the skin wound-healing process, The Journal of Immunology 172(3) (2004) 1848-1855.
[142] H. Mühl, J. Pfeilschifter, Anti-inflammatory properties of pro-inflammatory interferon-γ, International immunopharmacology 3(9) (2003) 1247-1255.
[143] V. Salmon-Ehr, L. Ramont, G. Godeau, P. Birembaut, M. Guenounou, P. Bernard, F.-X. Maquart, Implication of interleukin-4 in wound healing, Laboratory investigation 80(8) (2000) 1337-1343.
[144] A. King, S. Balaji, L.D. Le, T.M. Crombleholme, S.G. Keswani, Regenerative wound healing: The role of interleukin-10, Advances in wound care 3(4) (2014) 315-323.
[145] S.A. Eming, S. Werner, P. Bugnon, C. Wickenhauser, L. Siewe, O. Utermöhlen, J.M. Davidson, T. Krieg, A. Roers, Accelerated wound closure in mice deficient for interleukin-10, The American journal of pathology 170(1) (2007) 188-202.
[146] K. Gronert, Lipoxins in the eye and their role in wound healing, Prostaglandins, Leukotrienes and Essential Fatty Acids 73(3-4) (2005) 221-229.
[147] A. Vasconcelos, A.P. Pêgo, L. Henriques, M. Lamghari, A. Cavaco-Paulo, Protein matrices for improved wound healing: elastase inhibition by a synthetic peptide model, Biomacromolecules 11(9) (2010) 2213-2220.
[148] M.P. Caley, V.L. Martins, E.A. O'Toole, Metalloproteinases and wound healing, Advances in wound care 4(4) (2015) 225-234.
[149] L.J. Stevens, A. Page-McCaw, A secreted MMP is required for reepithelialization during wound healing, Molecular biology of the cell 23(6) (2012) 1068-1079.
[150] T. Salonurmi, M. Parikka, S. Kontusaari, E. Pirilä, C. Munaut, T. Salo, K. Tryggvason, Overexpression of TIMP-1 under the MMP-9 promoter interferes with wound healing in transgenic mice, Cell and tissue research 315(1) (2004) 27-37.
[151] A.C. Gonzalez, T.F. Costa, Z.A. Andrade, A.R. Medrado, Wound healing - A literature review, An Bras Dermatol 91(5) (2016) 614-620.
[152] K. Suzuma, H. Takagi, A. Otani, Y. Honda, Hypoxia and vascular endothelial growth factor stimulate angiogenic integrin expression in bovine retinal microvascular endothelial cells, Invest Ophthalmol Vis Sci 39(6) (1998) 1028-35.
[153] K. Riedel, F. Riedel, U.R. Goessler, G. Germann, M. Sauerbier, TGF-β antisense therapy increases angiogenic potential in human keratinocytes in vitro*, Archives of medical research 38(1) (2007) 45-51.
[154] D. Kiritsi, A. Nystrom, The role of TGFbeta in wound healing pathologies, Mech Ageing Dev 172 (2018) 51-58.

[155] E.J. Battegay, J. Rupp, L. Iruela-Arispe, E.H. Sage, M. Pech, PDGF-BB modulates endothelial proliferation and angiogenesis in vitro via PDGF beta-receptors, The Journal of cell biology 125(4) (1994) 917-928.
[156] A.T. Grazul-Bilska, M.L. Johnson, J.J. Bilski, D.A. Redmer, L.P. Reynolds, A. Abdullah, K.M. Abdullah, Wound healing: the role of growth factors, Drugs Today (Barc) 39(10) (2003) 787-800.
[157] P.W. Finch, J.S. Rubin, Keratinocyte growth factor/fibroblast growth factor 7, a homeostatic factor with therapeutic potential for epithelial protection and repair, Adv Cancer Res 91 (2004) 69-136.
[158] Y. Li, J. Fan, M. Chen, W. Li, D.T. Woodley, Transforming growth factor-alpha: a major human serum factor that promotes human keratinocyte migration, J Invest Dermatol 126(9) (2006) 2096-105.
[159] C. Amendt, P. Schirmacher, H. Weber, M. Blessing, Expression of a dominant negative type II TGF-beta receptor in mouse skin results in an increase in carcinoma incidence and an acceleration of carcinoma development, Oncogene 17(1) (1998) 25-34.
[160] Y. Ando, P.J. Jensen, Epidermal growth factor and insulin-like growth factor I enhance keratinocyte migration, J Invest Dermatol 100(5) (1993) 633-9.
[161] T.T. Meckmongkol, R. Harmon, P. McKeown-Longo, L. Van De Water, The fibronectin synergy site modulates TGF-beta-dependent fibroblast contraction, Biochem Biophys Res Commun 360(4) (2007) 709-14.
[162] B. Hinz, Masters and servants of the force: the role of matrix adhesions in myofibroblast force perception and transmission, Eur J Cell Biol 85(3-4) (2006) 175-81.
[163] L. Yang, T. Chan, J. Demare, T. Iwashina, A. Ghahary, P.G. Scott, E.E. Tredget, Healing of burn wounds in transgenic mice overexpressing transforming growth factor-β1 in the epidermis, The American journal of pathology 159(6) (2001) 2147-2157.
[164] M.H. Branton, J.B. Kopp, TGF-beta and fibrosis, Microbes Infect 1(15) (1999) 1349-65.
[165] S.L. Friedman, D. Sheppard, J.S. Duffield, S. Violette, Therapy for fibrotic diseases: nearing the starting line, Science translational medicine 5(167) (2013) 167sr1-167sr1.
[166] J. Canady, S. Karrer, M. Fleck, A.K. Bosserhoff, Fibrosing connective tissue disorders of the skin: molecular similarities and distinctions, J Dermatol Sci 70(3) (2013) 151-8.
[167] G. Sun, X. Zhang, Y.-I. Shen, R. Sebastian, L.E. Dickinson, K. Fox-Talbot, M. Reinblatt, C. Steenbergen, J.W. Harmon, S. Gerecht, Dextran hydrogel scaffolds enhance angiogenic responses and promote complete skin regeneration during burn wound healing, Proceedings of the National Academy of Sciences 108(52) (2011) 20976-20981.
[168] A. Shpichka, D. Butnaru, E.A. Bezrukov, R.B. Sukhanov, A. Atala, V. Burdukovskii, Y. Zhang, P. Timashev, Skin tissue regeneration for burn injury, Stem cell research & therapy 10(1) (2019) 1-16.
[169] R.W. Tarnuzzer, J. Colon, S. Patil, S. Seal, Vacancy engineered ceria nanostructures for protection from radiation-induced cellular damage, Nano Lett 5(12) (2005) 2573-7.
[170] S.M. Leininger, The role of nutrition in wound healing, Critical Care Nursing Quarterly 25(1) (2002) 13-21.
[171] D.J. MacKay, A.L. Miller, Nutritional support for wound healing, Alternative medicine review 8(4) (2003).

[172] M. Arnold, A. Barbul, Nutrition and wound healing, Plastic and reconstructive surgery 117(7S) (2006) 42S-58S.
[173] P. Martin, Wound healing--aiming for perfect skin regeneration, Science 276(5309) (1997) 75-81.
[174] C.H. Lyder, Pressure ulcer prevention and management, Jama 289(2) (2003) 223-226.
[175] J.E. Grey, S. Enoch, ABC of wound healing: pressure ulcers, Bmj 332(Suppl S6) (2006).
[176] M. Reddy, S.S. Gill, P.A. Rochon, Preventing pressure ulcers: a systematic review, Jama 296(8) (2006) 974-984.
[177] J. Whitney, L. Phillips, R. Aslam, A. Barbul, F. Gottrup, L. Gould, M.C. Robson, G. Rodeheaver, D. Thomas, N. Stotts, Guidelines for the treatment of pressure ulcers, Wound Repair and Regeneration 14(6) (2006) 663-679.
[178] Y. Qui, R. Quijano, S. Wang, N.H. Hwang, Fluid dynamics of venous valve closure, Annals of biomedical engineering 23(6) (1995) 750-759.
[179] J.J. Bergan, G.W. Schmid-Schönbein, P.D.C. Smith, A.N. Nicolaides, M.R. Boisseau, B. Eklof, Chronic venous disease, New England Journal of Medicine 355(5) (2006) 488-498.
[180] O. Stojadinovic, I. Pastar, S. Vukelic, M.G. Mahoney, D. Brennan, A. Krzyzanowska, M. Golinko, H. Brem, M. Tomic-Canic, Deregulation of keratinocyte differentiation and activation: a hallmark of venous ulcers, Journal of cellular and molecular medicine 12(6b) (2008) 2675-2690.
[181] C.A. Charles, M. Tomic-Canic, V. Vincek, M. Nassiri, O. Stojadinovic, W.H. Eaglstein, R.S. Kirsner, A gene signature of nonhealing venous ulcers: potential diagnostic markers, Journal of the American Academy of Dermatology 59(5) (2008) 758-771.
[182] I. Pastar, A.A. Khan, O. Stojadinovic, E.A. Lebrun, M.C. Medina, H. Brem, R.S. Kirsner, J.J. Jimenez, C. Leslie, M. Tomic-Canic, Induction of specific microRNAs inhibits cutaneous wound healing, Journal of Biological Chemistry 287(35) (2012) 29324-29335.
[183] C.J. Nolan, P. Damm, M. Prentki, Type 2 diabetes across generations: from pathophysiology to prevention and management, The Lancet 378(9786) (2011) 169-181.
[184] G. Reiber, B. Lipsky, G. Gibbons, The burden of diabetic foot ulcers, The American journal of surgery 176(2) (1998) 5S-10S.
[185] W.J. Jeffcoate, K.G. Harding, Diabetic foot ulcers, The lancet 361(9368) (2003) 1545-1551.
[186] A. Alavi, R.G. Sibbald, D. Mayer, L. Goodman, M. Botros, D.G. Armstrong, K. Woo, T. Boeni, E.A. Ayello, R.S. Kirsner, Diabetic foot ulcers: Part I. Pathophysiology and prevention, Journal of the American Academy of Dermatology 70(1) (2014) 1. e1-1. e18.
[187] A.G. Mowat, J. Baum, Chemotaxis of polymorphonuclear leukocytes from patients with diabetes mellitus, New England journal of medicine 284(12) (1971) 621-627.
[188] V. Madan, J.T. Lear, R.-M. Szeimies, Non-melanoma skin cancer, The lancet 375(9715) (2010) 673-685.
[189] T.L. Diepgen, V. Mahler, The epidemiology of skin cancer, British Journal of Dermatology 146 (2002) 1-6.
[190] J.R. Fishman, M.G. Parker, Malignancy and chronic wounds: Marjolin's ulcer, The Journal of burn care & rehabilitation 12(3) (1991) 218-223.
[191] K.Y. Woo, R.G. Sibbald, Local wound care for malignant and palliative wounds, Advances in skin & wound care 23(9) (2010) 417-428.

[192] J.T. Trent, R.S. Kirsner, Wounds and malignancy, Advances in skin & wound care 16(1) (2003) 31-34.
[193] P. Rous, J.G. Kidd, Conditional neoplasms and subthreshold neoplastic states A study of the tar tumors of rabbits, Journal of experimental medicine 73(3) (1941) 365-390.
[194] L.M. Coussens, Z. Werb, Inflammation and cancer, Nature 420(6917) (2002) 860-867.
[195] J. Perez-Losada, A. Balmain, Stem-cell hierarchy in skin cancer, Nature Reviews Cancer 3(6) (2003) 434-443.
[196] E.A. Gantwerker, D.B. Hom, Skin: histology and physiology of wound healing, Clinics in plastic surgery 39(1) (2012) 85-97.
[197] R. Schleip, H. Jäger, W. Klingler, What is 'fascia'? A review of different nomenclatures, Journal of bodywork and movement therapies 16(4) (2012) 496-502.
[198] D. Correa-Gallegos, D. Jiang, S. Christ, P. Ramesh, H. Ye, J. Wannemacher, S. Kalgudde Gopal, Q. Yu, M. Aichler, A. Walch, U. Mirastschijski, T. Volz, Y. Rinkevich, Patch repair of deep wounds by mobilized fascia, Nature 576(7786) (2019) 287-292.
[199] D.L. Steed, Debridement, The American journal of surgery 187(5) (2004) S71-S74.
[200] D. Rao, P. Sane, E. Georgiev, Collagenase in the treatment of dermal and decubitus ulcers, Journal of the American Geriatrics Society 23(1) (1975) 22-30.
[201] L. Shi, R. Ermis, B. Kiedaisch, D. Carson, The effect of various wound dressings on the activity of debriding enzymes, Advances in skin & wound care 23(10) (2010) 456-462.
[202] S.E. Ziffren, H.E. Heist, S.C. May, N.A. Womack, The secretion of collagenase by maggots and its implication, Annals of surgery 138(6) (1953) 932.
[203] S. Thomas, A. Andrews, M. Jones, J. Church, Maggots are useful in treating infected or necrotic wounds, Bmj 318(7186) (1999) 807.
[204] N. Trengove, M. Stacey, D. McGechie, N. Stingemore, S. Mata, Qualitative bacteriology and leg ulcer healing, Journal of wound care 5(6) (1996) 277-280.
[205] X. Gu, Z. Xu, L. Gu, H. Xu, F. Han, B. Chen, X. Pan, Preparation and antibacterial properties of gold nanoparticles: A review, Environmental Chemistry Letters 19(1) (2021) 167-187.
[206] X. Zhao, Y. Jia, R. Dong, J. Deng, H. Tang, F. Hu, S. Liu, X. Jiang, Bimetallic nanoparticles against multi-drug resistant bacteria, Chemical Communications 56(74) (2020) 10918-10921.
[207] M. Singh, K. Nuutila, C. Kruse, M.C. Robson, E. Caterson, E. Eriksson, Challenging the conventional therapy: emerging skin graft techniques for wound healing, Plastic and reconstructive surgery 136(4) (2015) 524e-530e.
[208] M.B. Dreifke, A.A. Jayasuriya, A.C. Jayasuriya, Current wound healing procedures and potential care, Mater Sci Eng C Mater Biol Appl 48 (2015) 651-62.
[209] D.J. Wainwright, Use of an Acellular Allograft Dermal Matrix (Alloderm) in the Management of Full-Thickness Burns, Burns 21(4) (1995) 243-248.
[210] H. Green, O. Kehinde, J. Thomas, Growth of Cultured Human Epidermal-Cells into Multiple Epithelia Suitable for Grafting, Proceedings of the National Academy of Sciences of the United States of America 76(11) (1979) 5665-5668.
[211] T.J. Phillips, Keratinocyte grafts for wound healing, Clin Dermatol 12(1) (1994) 171-81.
[212] D.N. Sauder, B.M. Stanulis-Praeger, B.A. Gilchrest, Autocrine growth stimulation of human keratinocytes by epidermal cell-derived thymocyte-activating factor: implications for skin aging, Arch Dermatol Res 280(2) (1988) 71-6.

[213] B.M. Stanulis-Praeger, B.A. Gilchrest, Growth factor responsiveness declines during adulthood for human skin-derived cells, Mech Ageing Dev 35(2) (1986) 185-98.
[214] S. Dhivya, V.V. Padma, E. Santhini, Wound dressings - a review, Biomedicine (Taipei) 5(4) (2015) 22.
[215] M. Ramos-e-Silva, M.C. Ribeiro de Castro, New dressings, including tissue-engineered living skin, Clin Dermatol 20(6) (2002) 715-23.
[216] S. Thomas, Hydrocolloids, J Wound Care 1(2) (1992) 27-30.
[217] J.A. Ramshaw, J.A. Werkmeister, V. Glattauer, Collagen-based biomaterials, Biotechnol Genet Eng Rev 13(1) (1996) 335-82.
[218] W.J. Chen, Functions of hyaluronan in wound repair, Hyaluronan (2002) 147-156.
[219] M. Moczar, L. Robert, Stimulation of cell proliferation by hyaluronidase during in vitro aging of human skin fibroblasts, Experimental gerontology 28(1) (1993) 59-68.
[220] P.H. Weigel, G.M. Fuller, R.D. LeBoeuf, A model for the role of hyaluronic acid and fibrin in the early events during the inflammatory response and wound healing, J Theor Biol 119(2) (1986) 219-34.
[221] T. Chandy, C.P. Sharma, Chitosan - as a Biomaterial, Biomaterials Artificial Cells and Artificial Organs 18(1) (1990) 1-24.
[222] M. Ishihara, K. Nakanishi, K. Ono, M. Sato, M. Kikuchi, Y. Saito, H. Yura, T. Matsui, H. Hattori, M. Uenoyama, A. Kurita, Photocrosslinkable chitosan as a dressing for wound occlusion and accelerator in healing process, Biomaterials 23(3) (2002) 833-840.
[223] A. Thomas, K. Harding, K. Moore, Alginates from wound dressings activate human macrophages to secrete tumour necrosis factor-α, Biomaterials 21(17) (2000) 1797-1802.
[224] I. Liakos, L. Rizzello, D.J. Scurr, P.P. Pompa, I.S. Bayer, A. Athanassiou, All-natural composite wound dressing films of essential oils encapsulated in sodium alginate with antimicrobial properties, International journal of pharmaceutics 463(2) (2014) 137-145.
[225] J.E. Babensee, L.V. McIntire, A.G. Mikos, Growth factor delivery for tissue engineering, Pharmaceutical research 17(5) (2000) 497-504.
[226] A.K.A. Silva, C. Richard, M. Bessodes, D. Scherman, O.-W. Merten, Growth factor delivery approaches in hydrogels, Biomacromolecules 10(1) (2009) 9-18.
[227] T.P. Richardson, M.C. Peters, A.B. Ennett, D.J. Mooney, Polymeric system for dual growth factor delivery, Nature biotechnology 19(11) (2001) 1029-1034.
[228] R. Langer, New methods of drug delivery, Science 249(4976) (1990) 1527-1533.
[229] H. Chu, J. Gao, C.-W. Chen, J. Huard, Y. Wang, Injectable fibroblast growth factor-2 coacervate for persistent angiogenesis, Proceedings of the National Academy of Sciences 108(33) (2011) 13444-13449.
[230] A. Buckley, J.M. Davidson, C.D. Kamerath, T.B. Wolt, S.C. Woodward, Sustained release of epidermal growth factor accelerates wound repair, Proceedings of the National Academy of Sciences 82(21) (1985) 7340-7344.
[231] K. Khosrotehrani, Mesenchymal stem cell therapy in skin: why and what for?, Experimental dermatology 22(5) (2013) 307-310.
[232] C. Shi, Y. Zhu, Y. Su, T. Cheng, Stem cells and their applications in skin-cell therapy, Trends in biotechnology 24(1) (2006) 48-52.

[233] S. Kargozar, F. Baino, S. Hamzehlou, R.G. Hill, M. Mozafari, Bioactive Glasses: Sprouting Angiogenesis in Tissue Engineering, Trends Biotechnol 36(4) (2018) 430-444.
[234] S. Kargozar, R.K. Singh, H.W. Kim, F. Baino, "Hard" ceramics for "Soft" tissue engineering: Paradox or opportunity?, Acta Biomater 115 (2020) 1-28.
[235] Y. Zhu, Z. Ma, L. Kong, Y. He, H.F. Chan, H. Li, Modulation of macrophages by bioactive glass/sodium alginate hydrogel is crucial in skin regeneration enhancement, Biomaterials 256 (2020) 120216.
[236] S. Kargozar, M. Mozafari, S. Hamzehlou, F. Baino, Using bioactive glasses in the management of burns, Frontiers in bioengineering and biotechnology 7 (2019) 62.
[237] F. Baino, S. Hamzehlou, S. Kargozar, Bioactive Glasses: Where Are We and Where Are We Going?, J Funct Biomater 9(1) (2018).
[238] T. Mehrabi, A.S. Mesgar, Z. Mohammadi, Bioactive Glasses: A Promising Therapeutic Ion Release Strategy for Enhancing Wound Healing, ACS Biomater Sci Eng 6(10) (2020) 5399-5430.
[239] E.D. Zanotto, J.C. Mauro, The glassy state of matter: Its definition and ultimate fate, Journal of Non-Crystalline Solids 471 (2017) 490-495.
[240] H. Scholze, Glass: nature, structure, and properties, Springer Science & Business Media2012.
[241] E.U. Condon, Physics of the glassy state. I. constitution and structure, American Journal of Physics 22(2) (1954) 43-53.
[242] J.E. Shelby, Introduction to glass science and technology, Royal Society of Chemistry2005.
[243] J. Zarzycki, Glasses and the vitreous state, Cambridge university press1991.
[244] J. Wu, J.F. Stebbins, Effects of cation field strength on the structure of aluminoborosilicate glasses: high-resolution 11B, 27Al and 23Na MAS NMR, Journal of Non-Crystalline Solids 355(9) (2009) 556-562.
[245] J. Wu, J.F. Stebbins, Cation field strength effects on boron coordination in binary borate glasses, Journal of the American Ceramic Society 97(9) (2014) 2794-2801.
[246] L. Barbieri, S. Bruni, F. Cariati, C. Leonelli, G.C. Pellacani, C. Siligardi, U. Russo, Influence of some transition metal cations on the properties of BaO-containing glasses and glass-ceramics, Materials research bulletin 34(12-13) (1999) 1825-1836.
[247] M.O. Hunault, L. Galoisy, G. Lelong, M. Newville, G. Calas, Effect of cation field strength on Co2+ speciation in alkali-borate glasses, Journal of Non-Crystalline Solids 451 (2016) 101-110.
[248] L.L. Hench, R.J. Splinter, W. Allen, T. Greenlee, Bonding mechanisms at the interface of ceramic prosthetic materials, Journal of biomedical materials research 5(6) (1971) 117-141.
[249] J. Wilson, S.B. Low, Bioactive ceramics for periodontal treatment: comparative studies in the Patus monkey, J Appl Biomater 3(2) (1992) 123-9.
[250] J. Jones, A. Clare, Bio-glasses: an introduction, John Wiley & Sons2012.
[251] M. Alcaide, P. Portoles, A. Lopez-Noriega, D. Arcos, M. Vallet-Regi, M.T. Portoles, Interaction of an ordered mesoporous bioactive glass with osteoblasts, fibroblasts and lymphocytes, demonstrating its biocompatibility as a potential bone graft material, Acta Biomater 6(3) (2010) 892-9.
[252] J.R. Jones, L.M. Ehrenfried, P. Saravanapavan, L.L. Hench, Controlling ion release from bioactive glass foam scaffolds with antibacterial properties, J Mater Sci Mater Med 17(11) (2006) 989-96.

[253] A. Hoppe, N.S. Guldal, A.R. Boccaccini, A review of the biological response to ionic dissolution products from bioactive glasses and glass-ceramics, Biomaterials 32(11) (2011) 2757-74.
[254] H. Li, K. Xue, N. Kong, K. Liu, J. Chang, Silicate bioceramics enhanced vascularization and osteogenesis through stimulating interactions between endothelia cells and bone marrow stromal cells, Biomaterials 35(12) (2014) 3803-18.
[255] K. Dashnyam, A. El-Fiqi, J.O. Buitrago, R.A. Perez, J.C. Knowles, H.W. Kim, A mini review focused on the proangiogenic role of silicate ions released from silicon-containing biomaterials, J Tissue Eng 8 (2017) 2041731417707339.
[256] M. Benderdour, T. Van Bui, K. Hess, A. Dicko, F. Belleville, B. Dousset, Effects of boron derivatives on extracellular matrix formation, J Trace Elem Med Biol 14(3) (2000) 168-73.
[257] R.M. Nzietchueng, B. Dousset, P. Franck, M. Benderdour, P. Nabet, K. Hess, Mechanisms implicated in the effects of boron on wound healing, J Trace Elem Med Biol 16(4) (2002) 239-44.
[258] M. Benderdour, K. Hess, M. Dzondo-Gadet, P. Nabet, F. Belleville, B. Dousset, Boron modulates extracellular matrix and TNFα synthesis in human fibroblasts, Biochemical and biophysical research communications 246(3) (1998) 746-751.
[259] C.E. Camalier, M. Yi, L.R. Yu, B.L. Hood, K.A. Conrads, Y.J. Lee, Y. Lin, L.M. Garneys, G.F. Bouloux, M.R. Young, T.D. Veenstra, R.M. Stephens, N.H. Colburn, T.P. Conrads, G.R. Beck, Jr., An integrated understanding of the physiological response to elevated extracellular phosphate, J Cell Physiol 228(7) (2013) 1536-50.
[260] Y. Lin, K.E. McKinnon, S.W. Ha, G.R. Beck, Jr., Inorganic phosphate induces cancer cell mediated angiogenesis dependent on forkhead box protein C2 (FOXC2) regulated osteopontin expression, Mol Carcinog 54(9) (2015) 926-34.
[261] J.W. Doyle, T.P. Roth, R.M. Smith, Y.Q. Li, R.M. Dunn, Effect of calcium alginate on cellular wound healing processes modeled in vitro, Journal of Biomedical Materials Research 32(4) (1996) 561-568.
[262] A.B. Lansdown, Calcium: a potential central regulator in wound healing in the skin, Wound Repair Regen 10(5) (2002) 271-85.
[263] H. Hattori, Y. Amano, Y. Nogami, B. Takase, M. Ishihara, Hemostasis for severe hemorrhage with photocrosslinkable chitosan hydrogel and calcium alginate, Ann Biomed Eng 38(12) (2010) 3724-32.
[264] H. Li, J. Chang, Stimulation of proangiogenesis by calcium silicate bioactive ceramic, Acta Biomater 9(2) (2013) 5379-89.
[265] L. Munaron, Intracellular calcium, endothelial cells and angiogenesis, Recent Pat Anticancer Drug Discov 1(1) (2006) 105-19.
[266] M. Raffi, S. Mehrwan, T.M. Bhatti, J.I. Akhter, A. Hameed, W. Yawar, M.M. ul Hasan, Investigations into the antibacterial behavior of copper nanoparticles against Escherichia coli, Annals of Microbiology 60(1) (2010) 75-80.
[267] A.K. Chatterjee, R. Chakraborty, T. Basu, Mechanism of antibacterial activity of copper nanoparticles, Nanotechnology 25(13) (2014) 135101.
[268] W. Feng, F. Ye, W. Xue, Z. Zhou, Y.J. Kang, Copper regulation of hypoxia-inducible factor-1 activity, Mol Pharmacol 75(1) (2009) 174-82.

[269] D.C. Rigiracciolo, A. Scarpelli, R. Lappano, A. Pisano, M.F. Santolla, P. De Marco, F. Cirillo, A.R. Cappello, V. Dolce, A. Belfiore, M. Maggiolini, E.M. De Francesco, Copper activates HIF-1alpha/GPER/VEGF signalling in cancer cells, Oncotarget 6(33) (2015) 34158-77.
[270] C. Giacomelli, M.L. Trincavelli, C. Satriano, O. Hansson, D. La Mendola, E. Rizzarelli, C. Martini, lozenge Copper (II) ions modulate Angiogenin activity in human endothelial cells, International Journal of Biochemistry & Cell Biology 60 (2015) 185-196.
[271] N. Mroczek-Sosnowska, E. Sawosz, K.P. Vadalasetty, M. Lukasiewicz, J. Niemiec, M. Wierzbicki, M. Kutwin, S. Jaworski, A. Chwalibog, Nanoparticles of Copper Stimulate Angiogenesis at Systemic and Molecular Level, International Journal of Molecular Sciences 16(3) (2015) 4838-4849.
[272] I.H. Lee, H.S. Yu, N.J. Lakhkar, H.W. Kim, M.S. Gong, J.C. Knowles, I.B. Wall, Development, characterisation and biocompatibility testing of a cobalt-containing titanium phosphate-based glass for engineering of vascularized hard tissues, Mater Sci Eng C Mater Biol Appl 33(4) (2013) 2104-12.
[273] T. Tanaka, I. Kojima, T. Ohse, J.R. Ingelfinger, S. Adler, T. Fujita, M. Nangaku, Cobalt promotes angiogenesis via hypoxia-inducible factor and protects tubulointerstitium in the remnant kidney model, Lab Invest 85(10) (2005) 1292-307.
[274] A.B. Lansdown, U. Mirastschijski, N. Stubbs, E. Scanlon, M.S. Agren, Zinc in wound healing: theoretical, experimental, and clinical aspects, Wound Repair Regen 15(1) (2007) 2-16.
[275] M.S. Agren, M. Chvapil, L. Franzen, Enhancement of re-epithelialization with topical zinc oxide in porcine partial-thickness wounds, J Surg Res 50(2) (1991) 101-5.
[276] Y. Yin, Q. Cui, Y. Li, N. Irwin, D. Fischer, A.R. Harvey, L.I. Benowitz, Macrophage-derived factors stimulate optic nerve regeneration, J Neurosci 23(6) (2003) 2284-93.
[277] A. Sirelkhatim, S. Mahmud, A. Seeni, N.H.M. Kaus, L.C. Ann, S.K.M. Bakhori, H. Hasan, D. Mohamad, Review on Zinc Oxide Nanoparticles: Antibacterial Activity and Toxicity Mechanism, Nanomicro Lett 7(3) (2015) 219-242.
[278] H.N. Wilkinson, B.-A. Guinn, M.J. Hardman, Combined Metallomics/Transcriptomics Profiling Reveals a Major Role for Metals in Wound Repair, Frontiers in Cell and Developmental Biology 9 (2021) 788596-788596.
[279] X. Yan, C. Yu, X. Zhou, J. Tang, D. Zhao, Highly ordered mesoporous bioactive glasses with superior in vitro bone-forming bioactivities, Angew Chem Int Ed Engl 43(44) (2004) 5980-4.
[280] C. Wu, J. Chang, Y. Xiao, Mesoporous bioactive glasses as drug delivery and bone tissue regeneration platforms, Therapeutic Delivery 2(9) (2011) 1189-1198.
[281] C.D. Moreira, S.M. Carvalho, H.S. Mansur, M.M. Pereira, Thermogelling chitosan-collagen-bioactive glass nanoparticle hybrids as potential injectable systems for tissue engineering, Mater Sci Eng C Mater Biol Appl 58 (2016) 1207-16.
[282] S.B. Jung, D.E. Day, T. Day, W. Stoecker, P. Taylor, Treatment of Non-Healing Diabetic Venous Stasis Ulcers with Bioactive Glass Nanofibers, Wound Repair and Regeneration 19(2) (2011) A30-A30.
[283] L.L. Hench, J.K. West, The sol-gel process, Chemical Reviews 90(1) (2002) 33-72.
[284] S. Lin, C. Ionescu, K.J. Pike, M.E. Smith, J.R. Jones, Nanostructure evolution and calcium distribution in sol-gel derived bioactive glass, Journal of Materials Chemistry 19(9) (2009) 1276-1282.

[285] X. Yan, X. Huang, C. Yu, H. Deng, Y. Wang, Z. Zhang, S. Qiao, G. Lu, D. Zhao, The in-vitro bioactivity of mesoporous bioactive glasses, Biomaterials 27(18) (2006) 3396-403.
[286] P. Saravanapavan, L.L. Hench, Mesoporous calcium silicate glasses. I. Synthesis, Journal of Non-Crystalline Solids 318(1-2) (2003) 1-13.
[287] P. Sepulveda, J.R. Jones, L.L. Hench, Characterization of melt-derived 45S5 and sol-gel-derived 58S bioactive glasses, J Biomed Mater Res 58(6) (2001) 734-40.
[288] C.J. Brinker, G.W. Scherer, Sol-gel science: the physics and chemistry of sol-gel processing, Academic press2013.
[289] L.L. Hench, S.H. Wang, The Sol-Gel Glass Transformation of Silica, Phase Transitions 24-6(2) (1990) 785-834.
[290] R. Iler, L. Hench, D. Ulrich, Science of ceramic chemical processing, John Wiley & Sons, New York (1986) 3-20.
[291] J.R. Jones, Bioactive glass 3D scaffolds for tissue engineering, (2002).
[292] M.D. Sacks, R.S. Sheu, Rheological Properties of Silica Sol-Gel Materials, Journal of Non-Crystalline Solids 92(2-3) (1987) 383-396.
[293] S. Sakka, K. Kamiya, The Sol-Gel Transition in the Hydrolysis of Metal Alkoxides in Relation to the Formation of Glass-Fibers and Films, Journal of Non-Crystalline Solids 48(1) (1982) 31-46.
[294] K. Ishizaki, S. Komarneni, M. Nanko, Sol-gel processing, designing porosity, pore size and polarity, and shaping processes, Porous Materials, Springer1998, pp. 67-180.
[295] M.M. Pereira, A.E. Clark, L.L. Hench, Calcium phosphate formation on sol-gel-derived bioactive glasses in vitro, J Biomed Mater Res 28(6) (1994) 693-8.
[296] D. Arcos, D.C. Greenspan, M. Vallet-Regí, Influence of the Stabilization Temperature on Textural and Structural Features and Ion Release in SiO2−CaO−P2O5Sol−Gel Glasses, Chemistry of Materials 14(4) (2002) 1515-1522.
[297] A.K. Nayak, Hydroxyapatite synthesis methodologies: an overview, International Journal of ChemTech Research 2(2) (2010) 903-907.
[298] W. Xia, J. Chang, Well-ordered mesoporous bioactive glasses (MBG): a promising bioactive drug delivery system, J Control Release 110(3) (2006) 522-30.
[299] X. Li, X.P. Wang, H.R. Chen, P. Jiang, X.P. Dong, J.L. Shi, Hierarchically porous bioactive glass scaffolds synthesized with a PUF and P123 cotemplated approach, Chemistry of Materials 19(17) (2007) 4322-4326.
[300] P.H. Yan, J.Q. Wang, S. Liu, J.F. Ou, Z.Q. Lei, S.R. Yang, "Green" synthesis of highly ordered mesoporous bioactive glass using acetic anhydride as the catalyst, Journal of Non-Crystalline Solids 356(28-30) (2010) 1514-1518.
[301] H.S. Yun, S.E. Kim, Y.T. Hyun, Preparation of 3D cubic ordered mesoporous bioactive glasses, Solid State Sciences 10(8) (2008) 1083-1092.
[302] H.S. Yun, S.H. Kim, S. Lee, I.H. Song, Synthesis of high surface area mesoporous bioactive glass nanospheres, Materials Letters 64(16) (2010) 1850-1853.
[303] S. Zhao, Y.B. Li, D.X. Li, Synthesis and in vitro bioactivity of CaO-SiO2-P2O5 mesoporous microspheres, Microporous and Mesoporous Materials 135(1-3) (2010) 67-73.

[304] A. Bari, N. Bloise, S. Fiorilli, G. Novajra, M. Vallet-Regi, G. Bruni, A. Torres-Pardo, J.M. Gonzalez-Calbet, L. Visai, C. Vitale-Brovarone, Copper-containing mesoporous bioactive glass nanoparticles as multifunctional agent for bone regeneration, Acta Biomater 55 (2017) 493-504.
[305] C. Wu, J. Chang, Multifunctional mesoporous bioactive glasses for effective delivery of therapeutic ions and drug/growth factors, J Control Release 193 (2014) 282-95.
[306] M. Nagrath, A. Alhalawani, A. Rahimnejad Yazdi, M.R. Towler, Bioactive glass fiber fabrication via a combination of sol-gel process with electro-spinning technique, Mater Sci Eng C Mater Biol Appl 101 (2019) 521-538.
[307] S. Parham, A.Z. Kharazi, H.R. Bakhsheshi-Rad, H. Ghayour, A.F. Ismail, H. Nur, F. Berto, Electrospun Nano-Fibers for Biomedical and Tissue Engineering Applications: A Comprehensive Review, Materials (Basel) 13(9) (2020).
[308] S.B. Jung, D.E. Day, Scaffolds with trace element for tissue regeneration in mammals, Google Patents, 2012.
[309] F. Quintero, J. Pou, R. Comesana, F. Lusquinos, A. Riveiro, A.B. Mann, R.G. Hill, Z.Y. Wu, J.R. Jones, Laser Spinning of Bioactive Glass Nanofibers, Advanced Functional Materials 19(19) (2009) 3084-3090.
[310] M.M. Echezarreta-Lopez, T. de Miguel, F. Quintero, J. Pou, M. Landin, Fabrication of Zn-Sr-doped laser-spinning glass nanofibers with antibacterial properties, J Biomater Appl 31(6) (2017) 819-831.
[311] M.M. Echezarreta-Lopez, T. De Miguel, F. Quintero, J. Pou, M. Landin, Antibacterial properties of laser spinning glass nanofibers, Int J Pharm 477(1-2) (2014) 113-21.
[312] S. Homaeigohar, A.R. Boccaccini, Antibacterial biohybrid nanofibers for wound dressings, Acta Biomater 107 (2020) 25-49.
[313] J. Xue, T. Wu, Y. Dai, Y. Xia, Electrospinning and Electrospun Nanofibers: Methods, Materials, and Applications, Chem Rev 119(8) (2019) 5298-5415.
[314] D.H. Reneker, A.L. Yarin, H. Fong, S. Koombhongse, Bending instability of electrically charged liquid jets of polymer solutions in electrospinning, Journal of Applied Physics 87(9) (2000) 4531-4547.
[315] S.H. Tan, R. Inai, M. Kotaki, S. Ramakrishna, Systematic parameter study for ultra-fine fiber fabrication via electrospinning process, Polymer 46(16) (2005) 6128-6134.
[316] N. Bhardwaj, S.C. Kundu, Electrospinning: a fascinating fiber fabrication technique, Biotechnol Adv 28(3) (2010) 325-47.
[317] A.D.J. Bombin, N.J. Dunne, H.O. McCarthy, Electrospinning of natural polymers for the production of nanofibres for wound healing applications, Materials Science and Engineering: C 114 (2020) 110994.
[318] J.D. Schiffman, C.L. Schauer, A review: Electrospinning of biopolymer nanofibers and their applications, Polymer Reviews 48(2) (2008) 317-352.
[319] J. Xue, J. Xie, W. Liu, Y. Xia, Electrospun Nanofibers: New Concepts, Materials, and Applications, Acc Chem Res 50(8) (2017) 1976-1987.
[320] Y.S. Huang, C.C. Kuo, C.C. Huang, S.C. Jang, W.C. Tsen, F.S. Chuang, B.Y. Chen, J.J. Chen, J.D. Chow, Y.C. Shu, Novel highly aligned, double-layered, hollow fibrous polycarbonate membranes with a perfectly tightly packed pentagonal pore structure fabricated using the electrospinning process, Rsc Advances 5(108) (2015) 88857-88865.

[321] J.-H. He, Y. Wu, W.-W. Zuo, Critical length of straight jet in electrospinning, Polymer 46(26) (2005) 12637-12640.
[322] A.M. Gañán-Calvo, Cone-jet analytical extension of Taylor's electrostatic solution and the asymptotic universal scaling laws in electrospraying, Physical review letters 79(2) (1997) 217.
[323] G. Collins, J. Federici, Y. Imura, L.H. Catalani, Charge generation, charge transport, and residual charge in the electrospinning of polymers: A review of issues and complications, Journal of Applied Physics 111(4) (2012) 044701.
[324] L.H. Catalani, G. Collins, M. Jaffe, Evidence for molecular orientation and residual charge in the electrospinning of poly (butylene terephthalate) nanofibers, Macromolecules 40(5) (2007) 1693-1697.
[325] C.L. Shao, H. Kim, J. Gong, D. Lee, A novel method for making silica nanofibres by using electrospun fibres of polyvinylalcohol/silica composite as precursor, Nanotechnology 13(5) (2002) 635-637.
[326] S. Tanriverdi, B. Mavis, G. Gunduz, U. Colak, Electrospinning and characterization of alumina borosilicate ceramic nanofibres, Materials Science-Poland 25(4) (2007) 957-968.
[327] D. Terada, H. Kobayashi, K. Zhang, A. Tiwari, C. Yoshikawa, N. Hanagata, Transient charge-masking effect of applied voltage on electrospinning of pure chitosan nanofibers from aqueous solutions, Science and technology of advanced materials (2012).
[328] H.-W. TONG, M. WANG, Negative voltage electrospinning and positive voltage electrospinning of tissue engineering scaffolds: a comparative study and charge retention on scaffolds, Nano Life 2(01) (2012) 1250004.
[329] J. Hu, X. Wang, B. Ding, J. Lin, J. Yu, G. Sun, One-step Electro-spinning/netting Technique for Controllably Preparing Polyurethane Nano-fiber/net, Macromolecular rapid communications 32(21) (2011) 1729-1734.
[330] S. Sarkar, S. Deevi, G. Tepper, Biased AC electrospinning of aligned polymer nanofibers, Macromolecular rapid communications 28(9) (2007) 1034-1039.
[331] S.K. Tiwari, S.S. Venkatraman, Importance of viscosity parameters in electrospinning: Of monolithic and core-shell fibers, Materials Science & Engineering C-Materials for Biological Applications 32(5) (2012) 1037-1042.
[332] A. Anisiei, F. Oancea, L. Marin, Electrospinning of chitosan-based nanofibers: from design to prospective applications, Reviews in Chemical Engineering (2021).
[333] K.R. Koko, B.M. McCauley, J.P. Gaughan, R.S. Nolan, M.W. Fromer, A.L.R. Hagaman, R.L. Choron, S.A. Brown, J.P. Hazelton, Kaolin-based hemostatic dressing improves hemorrhage control from a penetrating inferior vena cava injury in coagulopathic swine, J Trauma Acute Care Surg 83(1) (2017) 71-76.
[334] R. Dhanalakshmi, A. Pandikumar, K. Sujatha, P. Gunasekaran, Photocatalytic and antimicrobial activities of functionalized silicate sol–gel embedded ZnO–TiO₂ nanocomposite materials, Materials Express 3(4) (2013) 291-300.
[335] C. Liu, W. Yao, M. Tian, J. Wei, Q. Song, W. Qiao, Mussel-inspired degradable antibacterial polydopamine/silica nanoparticle for rapid hemostasis, Biomaterials 179 (2018) 83-95.
[336] G. Patil, A. Torris, P.R. Suresha, S. Jadhav, M.V. Badiger, V. Ghormade, Design and synthesis of a new topical agent for halting blood loss rapidly: A multimodal chitosan-gelatin xerogel

composite loaded with silica nanoparticles and calcium, Colloids Surf B Biointerfaces 198 (2021) 111454.
[337] J. Chen, L. Qiu, Q. Li, J. Ai, H. Liu, Q. Chen, Rapid hemostasis accompanied by antibacterial action of calcium crosslinking tannic acid-coated mesoporous silica/silver Janus nanoparticles, Mater Sci Eng C Mater Biol Appl 123 (2021) 111958.
[338] C. Wang, H. Zhou, H. Niu, X. Ma, Y. Yuan, H. Hong, C. Liu, Tannic acid-loaded mesoporous silica for rapid hemostasis and antibacterial activity, Biomater Sci 6(12) (2018) 3318-3331.
[339] Y. Hou, Y. Xia, Y. Pan, S. Tang, X. Sun, Y. Xie, H. Guo, J. Wei, Influences of mesoporous zinc-calcium silicate on water absorption, degradability, antibacterial efficacy, hemostatic performances and cell viability to microporous starch based hemostat, Mater Sci Eng C Mater Biol Appl 76 (2017) 340-349.
[340] D.J. Li, W. Nie, L. Chen, Y.K. Miao, X. Zhang, F.C. Chen, B. Yu, R.G. Ao, B.Q. Yu, C.L. He, Fabrication of curcumin-loaded mesoporous silica incorporated polyvinyl pyrrolidone nanofibers for rapid hemostasis and antibacterial treatment, Rsc Advances 7(13) (2017) 7973-7982.
[341] S. Pourshahrestani, N.A. Kadri, E. Zeimaran, M.R. Towler, Well-ordered mesoporous silica and bioactive glasses: promise for improved hemostasis, Biomater Sci 7(1) (2018) 31-50.
[342] D. Chimene, D.L. Alge, A.K. Gaharwar, Two-Dimensional Nanomaterials for Biomedical Applications: Emerging Trends and Future Prospects, Adv Mater 27(45) (2015) 7261-84.
[343] A.K. Gaharwar, R.K. Avery, A. Assmann, A. Paul, G.H. McKinley, A. Khademhosseini, B.D. Olsen, Shear-thinning nanocomposite hydrogels for the treatment of hemorrhage, ACS Nano 8(10) (2014) 9833-42.
[344] A. Nemmar, P. Yuvaraju, S. Beegam, J. Yasin, R.A. Dhaheri, M.A. Fahim, B.H. Ali, In vitro platelet aggregation and oxidative stress caused by amorphous silica nanoparticles, Int J Physiol Pathophysiol Pharmacol 7(1) (2015) 27-33.
[345] J.J. Corbalan, C. Medina, A. Jacoby, T. Malinski, M.W. Radomski, Amorphous silica nanoparticles aggregate human platelets: potential implications for vascular homeostasis, Int J Nanomedicine 7 (2012) 631-9.
[346] E. Manias, A. Touny, L. Wu, K. Strawhecker, B. Lu, T.C. Chung, Polypropylene/Montmorillonite nanocomposites. Review of the synthetic routes and materials properties, Chemistry of Materials 13(10) (2001) 3516-3523.
[347] B.S. Kheirabadi, M.R. Scherer, J.S. Estep, M.A. Dubick, J.B. Holcomb, Determination of efficacy of new hemostatic dressings in a model of extremity arterial hemorrhage in swine, J Trauma 67(3) (2009) 450-9; discussion 459-60.
[348] G. Li, K. Quan, Y. Liang, T. Li, Q. Yuan, L. Tao, Q. Xie, X. Wang, Graphene-Montmorillonite Composite Sponge for Safe and Effective Hemostasis, ACS Appl Mater Interfaces 8(51) (2016) 35071-35080.
[349] C. Dai, Y. Yuan, C. Liu, J. Wei, H. Hong, X. Li, X. Pan, Degradable, antibacterial silver exchanged mesoporous silica spheres for hemorrhage control, Biomaterials 30(29) (2009) 5364-75.
[350] P. Rhee, C. Brown, M. Martin, A. Salim, D. Plurad, D. Green, L. Chambers, D. Demetriades, G. Velmahos, H. Alam, QuikClot use in trauma for hemorrhage control: Case series of 103 documented uses, Journal of Trauma-Injury Infection and Critical Care 64(4) (2008) 1093-1099.

[351] D.S. Kauvar, R. Lefering, C.E. Wade, Impact of hemorrhage on trauma outcome: an overview of epidemiology, clinical presentations, and therapeutic considerations, J Trauma 60(6 Suppl) (2006) S3-11.
[352] N. Howe, B. Cherpelis, Obtaining rapid and effective hemostasis: Part I. Update and review of topical hemostatic agents, J Am Acad Dermatol 69(5) (2013) 659 e1-659 e17.
[353] M. Mikaelsson, The role of calcium in coagulation and anticoagulation, Coagulation and blood transfusion, Springer1991, pp. 29-37.
[354] S.R. Coughlin, Thrombin signalling and protease-activated receptors, Nature 407(6801) (2000) 258-64.
[355] M. Hoffman, Remodeling the blood coagulation cascade, J Thromb Thrombolysis 16(1-2) (2003) 17-20.
[356] C. Dai, C. Liu, J. Wei, H. Hong, Q. Zhao, Molecular imprinted macroporous chitosan coated mesoporous silica xerogels for hemorrhage control, Biomaterials 31(30) (2010) 7620-30.
[357] X. Wu, J. Wei, X. Lu, Y. Lv, F. Chen, Y. Zhang, C. Liu, Chemical characteristics and hemostatic performances of ordered mesoporous calcium-doped silica xerogels, Biomed Mater 5(3) (2010) 35006.
[358] T.A. Ostomel, Q. Shi, C.K. Tsung, H. Liang, G.D. Stucky, Spherical bioactive glass with enhanced rates of hydroxyapatite deposition and hemostatic activity, Small 2(11) (2006) 1261-5.
[359] M.T. Matter, F. Starsich, M. Galli, M. Hilber, A.A. Schlegel, S. Bertazzo, S.E. Pratsinis, I.K. Herrmann, Developing a tissue glue by engineering the adhesive and hemostatic properties of metal oxide nanoparticles, Nanoscale 9(24) (2017) 8418-8426.
[360] G. Hu, L. Xiao, P. Tong, D. Bi, H. Wang, H. Ma, G. Zhu, H. Liu, Antibacterial hemostatic dressings with nanoporous bioglass containing silver, Int J Nanomedicine 7 (2012) 2613-20.
[361] S. Huang, X. Kang, Z. Cheng, P. Ma, Y. Jia, J. Lin, Electrospinning preparation and drug delivery properties of Eu3+/Tb3+ doped mesoporous bioactive glass nanofibers, J Colloid Interface Sci 387(1) (2012) 285-91.
[362] S. Saha, A. Bhattacharjee, S.H. Rahaman, S. Ray, M.K. Marei, H. Jain, J. Chakraborty, Prospects of antibacterial bioactive glass nanofibers for wound healing: An in vitro study, International Journal of Applied Glass Science 11(2) (2020) 320-328.
[363] M. Rogosnitzky, Method of wound hemostasis using liquid gallium nitrate, Google Patents, 2014.
[364] P.H. Goodley, M. Rogosnitzky, The effect of gallium nitrate on arresting blood flow from a wound, Case Rep Med 2011 (2011) 819710.
[365] J. Goncalves, N. Wasif, D. Esposito, J.M. Coico, B. Schwartz, P.J. Higgins, R.S. Bockman, L. Staiano-Coico, Gallium nitrate accelerates partial thickness wound repair and alters keratinocyte integrin expression to favor a motile phenotype, J Surg Res 103(2) (2002) 134-40.
[366] S. Shruti, A.J. Salinas, E. Ferrari, G. Malavasi, G. Lusvardi, A.L. Doadrio, L. Menabue, M. Vallet-Regi, Curcumin release from cerium, gallium and zinc containing mesoporous bioactive glasses, Microporous and Mesoporous Materials 180 (2013) 92-101.
[367] S. Pourshahrestani, N.A. Kadri, E. Zeimaran, N. Gargiulo, S. Samuel, S.V. Naveen, K. Hasikin, T. Kamarul, M.R. Towler, Comparative efficacy of hemorrhage control of a novel mesoporous bioactive glass versus two commercial hemostats, Biomed Mater 13(2) (2018) 025020.
[368] C.T. Olson, R.W. Hoffmann, Tantalum oxide composition, Google Patents, 1949.

[369] M. Nagrath, R. Gallant, A.R. Yazdi, A. Mendonca, S. Rahman, L. Chiu, S.D. Waldman, H. Ni, M.R. Towler, Tantalum-containing mesoporous bioactive glass powder for hemostasis, J Biomater Appl 35(8) (2021) 924-932.
[370] A. Mendonca, M.S. Rahman, A. Alhalawani, O. Rodriguez, R.C. Gallant, H. Ni, O.M. Clarkin, M.R. Towler, The effect of tantalum incorporation on the physical and chemical properties of ternary silicon-calcium-phosphorous mesoporous bioactive glasses, J Biomed Mater Res B Appl Biomater 107(7) (2019) 2229-2237.
[371] N.J. Mutch, E.K. Waters, J.H. Morrissey, Immobilized transition metal ions stimulate contact activation and drive factor XII-mediated coagulation, J Thromb Haemost 10(10) (2012) 2108-15.
[372] M. Pan, Z. Tang, J. Tu, Z. Wang, Q. Chen, R. Xiao, H. Liu, Porous chitosan microspheres containing zinc ion for enhanced thrombosis and hemostasis, Mater Sci Eng C Mater Biol Appl 85 (2018) 27-36.
[373] H. Tapiero, K.D. Tew, Trace elements in human physiology and pathology: zinc and metallothioneins, Biomed Pharmacother 57(9) (2003) 399-411.
[374] P.E. Bock, K.R. Srinivasan, J.D. Shore, Activation of intrinsic blood coagulation by ellagic acid: insoluble ellagic acid-metal ion complexes are the activating species, Biochemistry 20(25) (1981) 7258-66.
[375] E.M. Liotta, S. Prabhakaran, R.S. Sangha, R.A. Bush, A.E. Long, S.A. Trevick, M.B. Potts, B.S. Jahromi, M. Kim, E.M. Manno, F.A. Sorond, A.M. Naidech, M.B. Maas, Magnesium, hemostasis, and outcomes in patients with intracerebral hemorrhage, Neurology 89(8) (2017) 813-819.
[376] L. Mussoni, L. Sironi, L. Tedeschi, A.M. Calvio, S. Colli, E. Tremoli, Magnesium inhibits arterial thrombi after vascular injury in rat: in vivo impairment of coagulation, Thromb Haemost 86(5) (2001) 1292-5.
[377] T. Waltimo, T.J. Brunner, M. Vollenweider, W.J. Stark, M. Zehnder, Antimicrobial effect of nanometric bioactive glass 45S5, J Dent Res 86(8) (2007) 754-7.
[378] M. Zehnder, T. Waltimo, B. Sener, E. Soderling, Dentin enhances the effectiveness of bioactive glass S53P4 against a strain of Enterococcus faecalis, Oral Surg Oral Med Oral Pathol Oral Radiol Endod 101(4) (2006) 530-5.
[379] X. Jiang, B. Lv, Q. Shen, X. Wang, Preparation of silicon-modified antimicrobial polyethylene endotracheal tubes, J Biomed Mater Res B Appl Biomater 105(1) (2017) 91-98.
[380] D. Zhang, O. Lepparanta, E. Munukka, H. Ylanen, M.K. Viljanen, E. Eerola, M. Hupa, L. Hupa, Antibacterial effects and dissolution behavior of six bioactive glasses, J Biomed Mater Res A 93(2) (2010) 475-83.
[381] M. Zehnder, E. Soderling, J. Salonen, T. Waltimo, Preliminary evaluation of bioactive glass S53P4 as an endodontic medication in vitro, J Endod 30(4) (2004) 220-4.
[382] S. Kaya, M. Cresswell, A.R. Boccaccini, Mesoporous silica-based bioactive glasses for antibiotic-free antibacterial applications, Mater Sci Eng C Mater Biol Appl 83 (2018) 99-107.
[383] M.S.K. Mubina, S. Shailajha, R. Sankaranarayanan, L. Saranya, In vitro bioactivity, mechanical behavior and antibacterial properties of mesoporous SiO2-CaO-Na2O-P2O5 nano bioactive glass ceramics, J Mech Behav Biomed Mater 100 (2019) 103379.
[384] V. Mortazavi, M.M. Nahrkhalaji, M.H. Fathi, S.B. Mousavi, B.N. Esfahani, Antibacterial effects of sol-gel-derived bioactive glass nanoparticle on aerobic bacteria, J Biomed Mater Res A 94(1) (2010) 160-8.

[385] N. Pajares-Chamorro, J. Shook, N.D. Hammer, X. Chatzistavrou, Resurrection of antibiotics that methicillin-resistant Staphylococcus aureus resists by silver-doped bioactive glass-ceramic microparticles, Acta Biomater 96 (2019) 537-546.
[386] A.B. Lansdown, Silver in health care: antimicrobial effects and safety in use, Biofunctional textiles and the skin, Karger Publishers2006, pp. 17-34.
[387] W.K. Jung, H.C. Koo, K.W. Kim, S. Shin, S.H. Kim, Y.H. Park, Antibacterial activity and mechanism of action of the silver ion in Staphylococcus aureus and Escherichia coli, Appl Environ Microbiol 74(7) (2008) 2171-8.
[388] K. Mijnendonckx, N. Leys, J. Mahillon, S. Silver, R. Van Houdt, Antimicrobial silver: uses, toxicity and potential for resistance, Biometals 26(4) (2013) 609-21.
[389] P. Dibrov, J. Dzioba, K.K. Gosink, C.C. Hase, Chemiosmotic mechanism of antimicrobial activity of Ag(+) in Vibrio cholerae, Antimicrob Agents Chemother 46(8) (2002) 2668-70.
[390] S. Eckhardt, P.S. Brunetto, J. Gagnon, M. Priebe, B. Giese, K.M. Fromm, Nanobio silver: its interactions with peptides and bacteria, and its uses in medicine, Chem Rev 113(7) (2013) 4708-54.
[391] Y. Ono, S. Nakaji, K. Sugawara, T. Kumae, [Effects of metals (silver, nickel, cobalt and chromium) on the reactive oxygen species generating capacity of human neutrophils and on the serum opsonic activity], Nihon Eiseigaku Zasshi 49(3) (1994) 645-53.
[392] A.M. Jones, S. Garg, D. He, A.N. Pham, T.D. Waite, Superoxide-mediated formation and charging of silver nanoparticles, Environ Sci Technol 45(4) (2011) 1428-34.
[393] M. Bellantone, N.J. Coleman, L.L. Hench, Bacteriostatic action of a novel four-component bioactive glass, J Biomed Mater Res 51(3) (2000) 484-90.
[394] M. Bellantone, H.D. Williams, L.L. Hench, Broad-spectrum bactericidal activity of Ag2O-doped bioactive glass, Antimicrobial Agents and Chemotherapy 46(6) (2002) 1940-1945.
[395] A. Balamurugan, G. Balossier, D. Laurent-Maquin, S. Pina, A.H. Rebelo, J. Faure, J.M. Ferreira, An in vitro biological and anti-bacterial study on a sol-gel derived silver-incorporated bioglass system, Dent Mater 24(10) (2008) 1343-51.
[396] H. Palza, B. Escobar, J. Bejarano, D. Bravo, M. Diaz-Dosque, J. Perez, Designing antimicrobial bioactive glass materials with embedded metal ions synthesized by the sol-gel method, Mater Sci Eng C Mater Biol Appl 33(7) (2013) 3795-801.
[397] A.C. Marsh, N.P. Mellott, N. Pajares-Chamorro, M. Crimp, A. Wren, N.D. Hammer, X. Chatzistavrou, Fabrication and multiscale characterization of 3D silver containing bioactive glass-ceramic scaffolds, Bioact Mater 4 (2019) 215-223.
[398] M. Miola, E. Verne, C. Vitale-Brovarone, F. Baino, Antibacterial Bioglass-Derived Scaffolds: Innovative Synthesis Approach and Characterization, International Journal of Applied Glass Science 7(2) (2016) 238-247.
[399] H. Wang, S.C. Zhao, X. Cui, Y.Y. Pan, W.H. Huang, S. Ye, S.H. Luo, M.N. Rahaman, C.Q. Zhang, D.P. Wang, Evaluation of three-dimensional silver-doped borate bioactive glass scaffolds for bone repair: Biodegradability, biocompatibility, and antibacterial activity, Journal of Materials Research 30(18) (2015) 2722-2735.
[400] X. Qin, R. Cao, J.J. Zheng, G.J. Shi, L.J. Ji, A.P. Zhu, H. Yao, A new strategy for synthesizing silver doped mesoporous bioactive glass fibers and their bioactivity, antibacterial activity and drug loading performance, Rsc Advances 10(73) (2020) 44835-44840.

[401] R. Ciceo Lucacel, T. Radu, A.S. Tătar, I. Lupan, O. Ponta, V. Simon, The influence of local structure and surface morphology on the antibacterial activity of silver-containing calcium borosilicate glasses, Journal of Non-Crystalline Solids 404 (2014) 98-103.
[402] A.A. Ahmed, A.A. Ali, D.A.R. Mahmoud, A.M. El-Fiqi, Study on the preparation and properties of silver-doped phosphate antibacterial glasses (Part I), Solid State Sciences 13(5) (2011) 981-992.
[403] A.M. Mulligan, M. Wilson, J.C. Knowles, Effect of increasing silver content in phosphate-based glasses on biofilms of Streptococcus sanguis, J Biomed Mater Res A 67(2) (2003) 401-12.
[404] L.C.A. da Silva, F.G. Neto, S.S.C. Pimentel, R. da Silva Palácios, F. Sato, K.M. Retamiro, N.S. Fernandes, C.V. Nakamura, F. Pedrochi, A. Steimacher, The role of Ag2O on antibacterial and bioactive properties of borate glasses, Journal of Non-Crystalline Solids 554 (2021) 120611.
[405] K. Magyari, R. Stefan, D.C. Vodnar, A. Vulpoi, L. Baia, The silver influence on the structure and antibacterial properties of the bioactive 10B2O3− 30Na2O− 60P2O2 glass, Journal of non-crystalline solids 402 (2014) 182-186.
[406] D. Carta, J.R. Jones, S. Lin, G. Poologasundarampillai, R.J. Newport, D.M. Pickup, Neutron diffraction study of antibacterial bioactive calcium silicate sol-gel glasses containing silver, Int J Appl Glass Sci 8(4) (2017) 364-371.
[407] M. Diba, A. Boccaccini, Silver-containing bioactive glasses for tissue engineering applications, Precious Metals for Biomedical Applications, Elsevier2014, pp. 177-211.
[408] N. Azizabadi, P.A. Azar, M.S. Tehrani, P. Derakhshi, Synthesis and characteristics of gel-derived SiO2-CaO-P2O5 -SrO-Ag2O-ZnO bioactive glass: Bioactivity, biocompatibility, and antibacterial properties, Journal of Non-Crystalline Solids 556 (2021) 120568.
[409] M.S.N. Shahrbabak, F. Sharifianjazi, D. Rahban, A. Salimi, A Comparative Investigation on Bioactivity and Antibacterial Properties of Sol-Gel Derived 58S Bioactive Glass Substituted by Ag and Zn, Silicon 11(6) (2019) 2741-2751.
[410] R.A. Festa, D.J. Thiele, Copper: an essential metal in biology, Curr Biol 21(21) (2011) R877-83.
[411] G. Grass, C. Rensing, M. Solioz, Metallic copper as an antimicrobial surface, Appl Environ Microbiol 77(5) (2011) 1541-7.
[412] S. Kargozar, M. Montazerian, S. Hamzehlou, H.W. Kim, F. Baino, Mesoporous bioactive glasses: Promising platforms for antibacterial strategies, Acta Biomater 81 (2018) 1-19.
[413] L. Macomber, J.A. Imlay, The iron-sulfur clusters of dehydratases are primary intracellular targets of copper toxicity, Proc Natl Acad Sci U S A 106(20) (2009) 8344-9.
[414] G. Borkow, J. Gabbay, Copper as a biocidal tool, Curr Med Chem 12(18) (2005) 2163-75.
[415] Y. Yoshida, S. Furuta, E. Niki, Effects of metal chelating agents on the oxidation of lipids induced by copper and iron, Biochim Biophys Acta 1210(1) (1993) 81-8.
[416] C.F. DRAKE, W.M. ALLEN, The use of controlled-release glass for the controlled delivery of bioactive materials, Biochemical Society Transactions 13(2) (1985) 516-520.
[417] A.M. Mulligan, M. Wilson, J.C. Knowles, The effect of increasing copper content in phosphate-based glasses on biofilms of Streptococcus sanguis, Biomaterials 24(10) (2003) 1797-807.

[418] F. Foroutan, J. McGuire, P. Gupta, A. Nikolaou, B.A. Kyffin, N.L. Kelly, J.V. Hanna, J. Gutierrez-Merino, J.C. Knowles, S.Y. Baek, E. Velliou, D. Carta, Antibacterial Copper-Doped Calcium Phosphate Glasses for Bone Tissue Regeneration, ACS Biomater Sci Eng 5(11) (2019) 6054-6062.
[419] L. Mojtabavi, A. Razavi, The Effects of Copper Addition on The Structure and Antibacterial Properties of Biomedical Glasses, European Chemical Bulletin 9(1) (2019).
[420] T.M. Gross, J. Lahiri, A. Golas, J. Luo, F. Verrier, J.L. Kurzejewski, D.E. Baker, J. Wang, P.F. Novak, M.J. Snyder, Copper-containing glass ceramic with high antimicrobial efficacy, Nat Commun 10(1) (2019) 1979.
[421] M. Miola, E. Bertone, E. Verne, In situ chemical and physical reduction of copper on bioactive glass surface, Applied Surface Science 495 (2019) 143559.
[422] M. Miola, E. Verne, Bioactive and Antibacterial Glass Powders Doped with Copper by Ion-Exchange in Aqueous Solutions, Materials (Basel) 9(6) (2016).
[423] A. Moghanian, A. Ghorbanoghli, M. Kazem-Rostami, A. Pazhouheshgar, E. Salari, M.S. Yazdi, T. Alimardani, H. Jahani, F.S. Jazi, M. Tahriri, Novel antibacterial Cu/Mg-substituted 58S-bioglass: Synthesis, characterization and investigation of in vitro bioactivity, International Journal of Applied Glass Science 11(4) (2020) 685-698.
[424] K.R. Raghupathi, R.T. Koodali, A.C. Manna, Size-dependent bacterial growth inhibition and mechanism of antibacterial activity of zinc oxide nanoparticles, Langmuir 27(7) (2011) 4020-8.
[425] N. Jones, B. Ray, K.T. Ranjit, A.C. Manna, Antibacterial activity of ZnO nanoparticle suspensions on a broad spectrum of microorganisms, FEMS Microbiol Lett 279(1) (2008) 71-6.
[426] M. Premanathan, K. Karthikeyan, K. Jeyasubramanian, G. Manivannan, Selective toxicity of ZnO nanoparticles toward Gram-positive bacteria and cancer cells by apoptosis through lipid peroxidation, Nanomed.-Nanotechnol. Biol. Med. 7(2) (2011) 184-192.
[427] L. Zhang, Y. Ding, M. Povey, D. York, ZnO nanofluids–A potential antibacterial agent, Progress in Natural Science 18(8) (2008) 939-944.
[428] W. Jiang, H. Mashayekhi, B. Xing, Bacterial toxicity comparison between nano-and micro-scaled oxide particles, Environmental pollution 157(5) (2009) 1619-1625.
[429] R.K. Dutta, P.K. Sharma, R. Bhargava, N. Kumar, A.C. Pandey, Differential susceptibility of Escherichia coli cells toward transition metal-doped and matrix-embedded ZnO nanoparticles, J Phys Chem B 114(16) (2010) 5594-9.
[430] L. Courtheoux, J. Lao, J.M. Nedelec, E. Jallot, Controlled bioactivity in zinc-doped sol-gel-derived binary bioactive glasses, Journal of Physical Chemistry C 112(35) (2008) 13663-13667.
[431] R.K. Singh, A. Srinivasan, Bioactivity of SiO2-CaO-P2O5-Na2O glasses containing zinc-iron oxide, Applied Surface Science 256(6) (2010) 1725-1730.
[432] M. Kamitakahara, C. Ohtsuki, H. Inada, M. Tanihara, T. Miyazaki, Effect of ZnO addition on bioactive CaO-SiO2-P2O5-CaF2 glass-ceramics containing apatite and wollastonite, Acta Biomater 2(4) (2006) 467-71.
[433] A. Oki, B. Parveen, S. Hossain, S. Adeniji, H. Donahue, Preparation and in vitro bioactivity of zinc containing sol-gel-derived bioglass materials, J Biomed Mater Res A 69(2) (2004) 216-21.
[434] L. Liu, S. Pushalkar, D. Saxena, R.Z. LeGeros, Y. Zhang, Antibacterial property expressed by a novel calcium phosphate glass, J Biomed Mater Res B Appl Biomater 102(3) (2014) 423-9.

[435] R. Sergi, D. Bellucci, R. Salvatori, G. Maisetta, G. Batoni, V. Cannillo, Zinc containing bioactive glasses with ultra-high crystallization temperature, good biological performance and antibacterial effects, Mater Sci Eng C Mater Biol Appl 104 (2019) 109910.
[436] K. Schuhladen, L. Stich, J. Schmidt, A. Steinkasserer, A.R. Boccaccini, E. Zinser, Cu, Zn doped borate bioactive glasses: antibacterial efficacy and dose-dependent in vitro modulation of murine dendritic cells, Biomater Sci 8(8) (2020) 2143-2155.
[437] M. Riaz, R. Zia, F. Saleemi, H. Ikram, F. Bashir, In vitro antimicrobial activity of ZnO based glass-ceramics against pathogenic bacteria, J Mater Sci Mater Med 26(12) (2015) 268.
[438] A. Wajda, W.H. Goldmann, R. Detsch, A.R. Boccaccini, M. Sitarz, Influence of zinc ions on structure, bioactivity, biocompatibility and antibacterial potential of melt-derived and gel-derived glasses from CaO-SiO2 system, Journal of Non-Crystalline Solids 511 (2019) 86-99.
[439] M.M. Babu, P.S. Prasad, P.V. Rao, N.P. Govindan, R.K. Singh, H.-W. Kim, N. Veeraiah, Titanium incorporated Zinc-Phosphate bioactive glasses for bone tissue repair and regeneration: Impact of Ti4+ on physico-mechanical and in vitro bioactivity, Ceramics International 45(17) (2019) 23715-23727.
[440] V. Uskokovic, G. Abuna, P. Ferreira, V.M. Wu, L. Gower, F.C.P. Pires-de-Souza, R.M. Murata, M.A.C. Sinhoreti, S. Geraldeli, Synthesis and characterization of nanoparticulate niobium- and zinc-doped bioglass-ceramic/chitosan hybrids for dental applications, Journal of Sol-Gel Science and Technology 97(2) (2021) 245-258.
[441] A. Moghanian, M. Zohourfazeli, M.H.M. Tajer, A.K. Miri, Comprehensive in vitro studies of novel sol gel-derived Zr4+/Zn2+co-substituted bioactive glass with enhanced biological properties for bone healing, Journal of Non-Crystalline Solids 566 (2021) 120887.
[442] M.J. Lee, Y.B. Seo, J.Y. Seo, J.H. Ryu, H.J. Ahn, K.M. Kim, J.S. Kwon, S.H. Choi, Development of a Bioactive Flowable Resin Composite Containing a Zinc-Doped Phosphate-Based Glass, Nanomaterials (Basel) 10(11) (2020) 2311.
[443] Z. Sayin, U.S. Ucan, A. Sakmanoglu, Antibacterial and Antibiofilm Effects of Boron on Different Bacteria, Biol Trace Elem Res 173(1) (2016) 241-6.
[444] O. Borokhov, D. Schubert, Antimicrobial properties of boron derivatives, ACS Publications2007.
[445] R. De Gray, W. Fitzgibbons, Mechanism of microbicidal action of organoborates in fuel-water systems, Development of Industrial Microbiology 7 (1966) 384-391.
[446] A. Brittingham, W.A. Wilson, The antimicrobial effect of boric acid on Trichomonas vaginalis, Sex Transm Dis 41(12) (2014) 718-22.
[447] F. De Seta, M. Schmidt, B. Vu, M. Essmann, B. Larsen, Antifungal mechanisms supporting boric acid therapy of Candida vaginitis, J Antimicrob Chemother 63(2) (2009) 325-36.
[448] R.F. Brown, M.N. Rahaman, A.B. Dwilewicz, W. Huang, D.E. Day, Y. Li, B.S. Bal, Effect of borate glass composition on its conversion to hydroxyapatite and on the proliferation of MC3T3-E1 cells, J Biomed Mater Res A 88(2) (2009) 392-400.
[449] S. Jung, T. Day, T. Boone, B. Buziak, A. Omar, Anti-biofilm activity of two novel, borate based, bioactive glass wound dressings, Biomedical Glasses 5(1) (2019) 67-75.
[450] A. Fatih Isik, N.O. San Keskin, Y. Ulcay, Synthesis and in vitro antimicrobial characterization of Boron-PVA Electrospun nanofibers, The Journal of The Textile Institute 110(4) (2019) 575-580.

[451] E.A. Bursali, S. Coskun, M. Kizil, M. Yurdakoc, Synthesis, characterization and in vitro antimicrobial activities of boron/starch/polyvinyl alcohol hydrogels, Carbohydrate Polymers 83(3) (2011) 1377-1383.
[452] A. Mukheem, S. Shahabuddin, N. Akbar, A. Miskon, N. Muhamad Sarih, K. Sudesh, N. Ahmed Khan, R. Saidur, N. Sridewi, Boron Nitride Doped Polyhydroxyalkanoate/Chitosan Nanocomposite for Antibacterial and Biological Applications, Nanomaterials (Basel) 9(4) (2019) 645.
[453] O.N. Chupakhin, T.G. Khonina, N.V. Kungurov, N.V. Zilberberg, N.P. Evstigneeva, M.M. Kokhan, A.I. Polishchuk, E.V. Shadrina, E.Y. Larchenko, L.P. Larionov, M.S. Karabanalov, Silicon-boron-containing glycerohydrogel having wound healing, regenerative, and antimicrobial activity, Russian Chemical Bulletin 66(3) (2017) 558-563.
[454] S. Prasad, A. Gaddam, A. Jana, S. Kant, P.K. Sinha, S. Tripathy, K. Annapurna, J.M.F. Ferreira, A.R. Allu, K. Biswas, Structure and Stability of High CaO- and P2O5-Containing Silicate and Borosilicate Bioactive Glasses, J Phys Chem B 123(35) (2019) 7558-7569.
[455] R. Warrell Jr, M. Isaacs, C. Coonley, N. Alcock, R. Bockman, Metabolic effects of gallium nitrate administered by prolonged infusion, Cancer treatment reports 69(6) (1985) 653.
[456] R. Warrell Jr, M. Isaacs, N. Alcock, R. Bockman, Gallium nitrate for treatment of refractory hypercalcemia from parathyroid carcinoma, Annals of internal medicine 107(5) (1987) 683-686.
[457] L.R. Bernstein, Mechanisms of therapeutic activity for gallium, Pharmacol Rev 50(4) (1998) 665-82.
[458] D.M. Pickup, S.P. Valappil, R.M. Moss, H.L. Twyman, P. Guerry, M.E. Smith, M. Wilson, J.C. Knowles, R.J. Newport, Preparation, structural characterisation and antibacterial properties of Ga-doped sol-gel phosphate-based glass, Journal of Materials Science 44(7) (2009) 1858-1867.
[459] R. Sahdev, T.I. Ansari, S.M. Higham, S.P. Valappil, Potential use of gallium-doped phosphate-based glass material for periodontitis treatment, J Biomater Appl 30(1) (2015) 85-92.
[460] S.P. Valappil, D. Ready, E.A. Abou Neel, D.M. Pickup, W. Chrzanowski, L.A. O'Dell, R.J. Newport, M.E. Smith, M. Wilson, J.C. Knowles, Antimicrobial gallium-doped phosphate-based glasses, Advanced Functional Materials 18(5) (2008) 732-741.
[461] A. Rahimnejad Yazdi, L. Torkan, W. Stone, M.R. Towler, The impact of gallium content on degradation, bioactivity, and antibacterial potency of zinc borate bioactive glass, J Biomed Mater Res B Appl Biomater 106(1) (2018) 367-376.
[462] S.P. Valappil, D. Ready, E.A. Abou Neel, D.M. Pickup, L.A. O'Dell, W. Chrzanowski, J. Pratten, R.J. Newport, M.E. Smith, M. Wilson, J.C. Knowles, Controlled delivery of antimicrobial gallium ions from phosphate-based glasses, Acta Biomater 5(4) (2009) 1198-210.
[463] A. Wajda, W.H. Goldmann, R. Detsch, A. Grunewald, A.R. Boccaccini, M. Sitarz, Structural characterization and evaluation of antibacterial and angiogenic potential of gallium-containing melt-derived and gel-derived glasses from CaO-SiO2 system, Ceramics International 44(18) (2018) 22698-22709.
[464] M.Q. Wang, Y.Q. Yang, G.H. Chi, K. Yuan, F. Zhou, L. Dong, H.B. Liu, Q.H. Zhou, W.H. Gong, S.B. Yang, T.T. Tang, A 3D printed Ga containing scaffold with both anti-infection and bone homeostasis-regulating properties for the treatment of infected bone defects, Journal of Materials Chemistry B 9(23) (2021) 4735-4745.
[465] A.J. Salinas, M. Vallet-Regi, Glasses in bone regeneration: A multiscale issue, Journal of Non-Crystalline Solids 432 (2016) 9-14.

[466] S. Mittal, A.K. Pandey, Cerium oxide nanoparticles induced toxicity in human lung cells: role of ROS mediated DNA damage and apoptosis, Biomed Res Int 2014 (2014) 891934.
[467] E. Alpaslan, B.M. Geilich, H. Yazici, T.J. Webster, pH-Controlled Cerium Oxide Nanoparticle Inhibition of Both Gram-Positive and Gram-Negative Bacteria Growth, Sci Rep 7(1) (2017) 45859.
[468] J.P. Garner, P.S. Heppell, Cerium nitrate in the management of burns, Burns 31(5) (2005) 539-47.
[469] C. Leonelli, G. Lusvardi, G. Malavasi, L. Menabue, M. Tonelli, Synthesis and characterization of cerium-doped glasses and in vitro evaluation of bioactivity, Journal of Non-Crystalline Solids 316(2-3) (2003) 198-216.
[470] Y.F. Goh, A.Z. Alshemary, M. Akram, M.R.A. Kadir, R. Hussain, In-vitro characterization of antibacterial bioactive glass containing ceria, Ceramics International 40(1) (2014) 729-737.
[471] S.M. Glasdam, S. Glasdam, G.H. Peters, The Importance of Magnesium in the Human Body: A Systematic Literature Review, Adv Clin Chem 73 (2016) 169-93.
[472] J.H. de Baaij, J.G. Hoenderop, R.J. Bindels, Magnesium in man: implications for health and disease, Physiol Rev 95(1) (2015) 1-46.
[473] S. Kumari, A.K. Badana, M.M. G, S. G, R. Malla, Reactive Oxygen Species: A Key Constituent in Cancer Survival, Biomark Insights 13 (2018) 1177271918755391.
[474] P. Bhattacharya, A. Dey, S. Neogi, An insight into the mechanism of antibacterial activity by magnesium oxide nanoparticles, Journal of Materials Chemistry B 9(26) (2021) 5329-5339.
[475] A. Som, L. Yang, G.C. Wong, G.N. Tew, Divalent metal ion triggered activity of a synthetic antimicrobial in cardiolipin membranes, J Am Chem Soc 131(42) (2009) 15102-3.
[476] Y. Xie, L. Yang, Calcium and Magnesium Ions Are Membrane-Active against Stationary-Phase Staphylococcus aureus with High Specificity, Sci Rep 6(1) (2016) 20628.
[477] S. Hayat, S. Muzammil, M.H. Rasool, Z. Nisar, S.Z. Hussain, A.N. Sabri, S. Jamil, In vitro antibiofilm and anti-adhesion effects of magnesium oxide nanoparticles against antibiotic resistant bacteria, Microbiol Immunol 62(4) (2018) 211-220.
[478] S. Zaatreh, D. Haffner, M. Strauss, T. Dauben, C. Zamponi, W. Mittelmeier, E. Quandt, B. Kreikemeyer, R. Bader, Thin magnesium layer confirmed as an antibacterial and biocompatible implant coating in a co-culture model, Molecular Medicine Reports 15(4) (2017) 1624-1630.
[479] X. Gao, S. Mukherjee, P.M. Matthews, L.A. Hammad, D.B. Kearns, C.E. Dann, 3rd, Functional characterization of core components of the Bacillus subtilis cyclic-di-GMP signaling pathway, J Bacteriol 195(21) (2013) 4782-92.
[480] Y. Chen, Y. Chai, J.H. Guo, R. Losick, Evidence for cyclic Di-GMP-mediated signaling in Bacillus subtilis, J Bacteriol 194(18) (2012) 5080-90.
[481] A. Moghanian, A. Sedghi, A. Ghorbanoghli, E. Salari, The effect of magnesium content on in vitro bioactivity, biological behavior and antibacterial activity of sol-gel derived 58S bioactive glass, Ceramics International 44(8) (2018) 9422-9432.
[482] J. Lao, J.M. Nedelec, E. Jallot, New insight into the physicochemistry at the interface between sol-gel-derived bioactive glasses and biological medium: A PIXE-RBS study, Journal of Physical Chemistry C 112(25) (2008) 9418-9427.
[483] P. Jha, S.S. Danewalia, G. Sharma, K. Singh, Antimicrobial and bioactive phosphate-free glass-ceramics for bone tissue engineering applications, Mater Sci Eng C Mater Biol Appl 86 (2018) 9-17.

[484] M. Blochberger, L. Hupa, D.S. Brauer, Influence of zinc and magnesium substitution on ion release from Bioglass 45S5 at physiological and acidic pH, Biomedical glasses 1(1) (2015).
[485] R.R. Breaker, New insight on the response of bacteria to fluoride, Caries Res 46(1) (2012) 78-81.
[486] Y.T. Xu, Q. Wu, Y.M. Chen, R.J. Smales, S.Y. Shi, M.T. Wang, Antimicrobial effects of a bioactive glass combined with fluoride or triclosan on Streptococcus mutans biofilm, Arch Oral Biol 60(7) (2015) 1059-65.
[487] J. Liu, S.C.F. Rawlinson, R.G. Hill, F. Fortune, Fluoride incorporation in high phosphate containing bioactive glasses and in vitro osteogenic, angiogenic and antibacterial effects, Dent Mater 32(10) (2016) e221-e237.
[488] S. Prasad, S. Ganisetti, A. Jana, S. Kant, P.K. Sinha, S. Tripathy, K. Illath, T.G. Ajithkumar, K. Annapurna, A.R. Allu, K. Biswas, Elucidating the effect of CaF2 on structure, biocompatibility and antibacterial properties of S53P4 glass, Journal of Alloys and Compounds 831 (2020).
[489] R. Baron, Y. Tsouderos, In vitro effects of S12911-2 on osteoclast function and bone marrow macrophage differentiation, Eur J Pharmacol 450(1) (2002) 11-7.
[490] E. Canalis, M. Hott, P. Deloffre, Y. Tsouderos, P.J. Marie, The divalent strontium salt S12911 enhances bone cell replication and bone formation in vitro, Bone 18(6) (1996) 517-23.
[491] G.J. Atkins, K.J. Welldon, P. Halbout, D.M. Findlay, Strontium ranelate treatment of human primary osteoblasts promotes an osteocyte-like phenotype while eliciting an osteoprotegerin response, Osteoporos Int 20(4) (2009) 653-64.
[492] J. Liu, S.C. Rawlinson, R.G. Hill, F. Fortune, Strontium-substituted bioactive glasses in vitro osteogenic and antibacterial effects, Dent Mater 32(3) (2016) 412-22.
[493] N. Baheiraei, H. Eyni, B. Bakhshi, R. Najafloo, N. Rabiee, Effects of strontium ions with potential antibacterial activity on in vivo bone regeneration, Scientific Reports 11(1) (2021) 1-9.
[494] D.S. Brauer, N. Karpukhina, G. Kedia, A. Bhat, R.V. Law, I. Radecka, R.G. Hill, Bactericidal strontium-releasing injectable bone cements based on bioactive glasses, J R Soc Interface 10(78) (2013) 20120647.
[495] N. Gupta, D. Santhiya, S. Murugavel, A. Kumar, A. Aditya, M. Ganguli, S. Gupta, Effects of transition metal ion dopants (Ag, Cu and Fe) on the structural, mechanical and antibacterial properties of bioactive glass, Colloids and Surfaces a-Physicochemical and Engineering Aspects 538 (2018) 393-403.
[496] H. Zhu, C. Hu, F. Zhang, X. Feng, J. Li, T. Liu, J. Chen, J. Zhang, Preparation and antibacterial property of silver-containing mesoporous 58S bioactive glass, Mater Sci Eng C Mater Biol Appl 42 (2014) 22-30.
[497] A.M. El-Kady, A.F. Ali, R.A. Rizk, M.M. Ahmed, Synthesis, characterization and microbiological response of silver doped bioactive glass nanoparticles, Ceramics International 38(1) (2012) 177-188.
[498] C.R. Mariappan, N. Ranga, Influence of silver on the structure, dielectric and antibacterial effect of silver doped bioglass-ceramic nanoparticles, Ceramics International 43(2) (2017) 2196-2201.
[499] A.A. El-Rashidy, G. Waly, A. Gad, A.A. Hashem, P. Balasubramanian, S. Kaya, A.R. Boccaccini, I. Sami, Preparation and in vitro characterization of silver-doped bioactive glass nanoparticles

fabricated using a sol-gel process and modified Stober method, Journal of Non-Crystalline Solids 483 (2018) 26-36.
[500] A.C. Vale, A.L. Carvalho, A.M. Barbosa, E. Torrado, J.F. Mano, N.M. Alves, Novel Antibacterial and Bioactive Silicate Glass Nanoparticles for Biomedical Applications, Advanced Engineering Materials 20(5) (2018).
[501] N. Gargiulo, A.M. Cusano, F. Causa, D. Caputo, P.A. Netti, Silver-containing mesoporous bioactive glass with improved antibacterial properties, J Mater Sci Mater Med 24(9) (2013) 2129-35.
[502] K. Zheng, P. Balasubramanian, T.E. Paterson, R. Stein, S. MacNeil, S. Fiorilli, C. Vitale-Brovarone, J. Shepherd, A.R. Boccaccini, Ag modified mesoporous bioactive glass nanoparticles for enhanced antibacterial activity in 3D infected skin model, Mater Sci Eng C Mater Biol Appl 103 (2019) 109764.
[503] W. Fan, D. Wu, T. Ma, B. Fan, Ag-loaded mesoporous bioactive glasses against Enterococcus faecalis biofilm in root canal of human teeth, Dent Mater J 34(1) (2015) 54-60.
[504] C. Wu, Y. Zhou, M. Xu, P. Han, L. Chen, J. Chang, Y. Xiao, Copper-containing mesoporous bioactive glass scaffolds with multifunctional properties of angiogenesis capacity, osteostimulation and antibacterial activity, Biomaterials 34(2) (2013) 422-33.
[505] S. Chitra, P. Bargavi, M. Balasubramaniam, R.R. Chandran, S. Balakumar, Impact of copper on in-vitro biomineralization, drug release efficacy and antimicrobial properties of bioactive glasses, Mater Sci Eng C Mater Biol Appl 109 (2020) 110598.
[506] R. Koohkan, T. Hooshmand, M. Tahriri, D. Mohebbi-Kalhori, Synthesis, characterization and in vitro bioactivity of mesoporous copper silicate bioactive glasses, Ceramics International 44(2) (2018) 2390-2399.
[507] S. Sanchez-Salcedo, S. Shruti, A.J. Salinas, G. Malavasi, L. Menabue, M. Vallet-Regi, In vitro antibacterial capacity and cytocompatibility of SiO2-CaO-P2O5 meso-macroporous glass scaffolds enriched with ZnO, J Mater Chem B 2(30) (2014) 4836-4847.
[508] F. Baghbani, F. Moztarzadeh, L. Hajibaki, M. Mozafari, Synthesis, characterization and evaluation of bioactivity and antibacterial activity of quinary glass system (SiO 2–CaO–P 2 O 5–MgO–ZnO): in vitro study, Bulletin of Materials Science 36(7) (2013) 1339-1346.
[509] I. Atkinson, E.M. Anghel, L. Predoana, O.C. Mocioiu, L. Jecu, I. Raut, C. Munteanu, D. Culita, M. Zaharescu, Influence of ZnO addition on the structural, in vitro behavior and antimicrobial activity of sol–gel derived CaO–P 2 O 5 –SiO 2 bioactive glasses, Ceramics International 42(2) (2016) 3033-3045.
[510] N. Esfahanizadeh, M.R. Nourani, A. Bahador, N. Akhondi, M. Montazeri, The Anti-biofilm Activity of Nanometric Zinc doped Bioactive Glass against Putative Periodontal Pathogens: An in vitro Study, Biomedical Glasses 4(1) (2018) 95-107.
[511] A.M. Deliormanlı, H. Seda Vatansever, H. Yesil, F. Özdal-Kurt, In vivo evaluation of cerium, gallium and vanadium-doped borate-based bioactive glass scaffolds using rat subcutaneous implantation model, Ceramics International 42(10) (2016) 11574-11583.
[512] S.P. Valappil, M. Coombes, L. Wright, G.J. Owens, R.J. Lynch, C.K. Hope, S.M. Higham, Role of gallium and silver from phosphate-based glasses on in vitro dual species oral biofilm models of Porphyromonas gingivalis and Streptococcus gordonii, Acta Biomater 8(5) (2012) 1957-65.

[513] S. Sanchez-Salcedo, G. Malavasi, A.J. Salinas, G. Lusvardi, L. Rigamonti, L. Menabue, M. Vallet-Regi, Highly-Bioreactive Silica-Based Mesoporous Bioactive Glasses Enriched with Gallium(III), Materials (Basel) 11(3) (2018).
[514] M.M. Farag, Z.M. Al-Rashidy, M.M. Ahmed, In vitro drug release behavior of Ce-doped nano-bioactive glass carriers under oxidative stress, J Mater Sci Mater Med 30(2) (2019) 18.
[515] Q. Nawaz, M.A.U. Rehman, A. Burkovski, J. Schmidt, A.M. Beltran, A. Shahid, N.K. Alber, W. Peukert, A.R. Boccaccini, Synthesis and characterization of manganese containing mesoporous bioactive glass nanoparticles for biomedical applications, J Mater Sci Mater Med 29(5) (2018) 64.
[516] X. He, Y. Liu, Y. Tan, L.M. Grover, J. Song, S. Duan, D. Zhao, X. Tan, Rubidium-containing mesoporous bioactive glass scaffolds support angiogenesis, osteogenesis and antibacterial activity, Mater Sci Eng C Mater Biol Appl 105 (2019) 110155.
[517] S. Prasad S, I. Ratha, T. Adarsh, A. Anand, P.K. Sinha, P. Diwan, K. Annapurna, K. Biswas, In vitro bioactivity and antibacterial properties of bismuth oxide modified bioactive glasses, Journal of Materials Research 33(2) (2017) 178-190.
[518] A. Moghanian, M. Zohourfazeli, M.H.M. Tajer, The effect of zirconium content on in vitro bioactivity, biological behavior and antibacterial activity of sol-gel derived 58S bioactive glass, Journal of Non-Crystalline Solids 546 (2020) 120262.
[519] Z. Tabia, S. Akhtach, K. El Mabrouk, M. Bricha, K. Nouneh, A. Ballamurugan, Tantalum doped SiO2-CaO-P2O5 based bioactive glasses: Investigation of in vitro bioactivity and antibacterial activities, Biomedical Glasses 6(1) (2020) 10-22.
[520] M. Łaczka, K. Cholewa, A. Łaczka-Osyczka, Gel-derived powders of CaO P2O5 SiO2 system as a starting material to production of bioactive ceramics, Journal of alloys and compounds 248(1-2) (1997) 42-51.
[521] B. Turyna, J. Milc, A. Laczka, K. Cholewa, M. Laczka, Biocompatibility of glass-crystalline materials obtained by the sol-gel method: Effect on macrophage function, Biomaterials 17(14) (1996) 1379-1386.
[522] M. Bosetti, L. Hench, M. Cannas, Interaction of bioactive glasses with peritoneal macrophages and monocytes in vitro, J Biomed Mater Res 60(1) (2002) 79-85.
[523] A. Grandjean-Laquerriere, P. Laquerriere, D. Laurent-Maquin, M. Guenounou, T.M. Phillips, The effect of the physical characteristics of hydroxyapatite particles on human monocytes IL-18 production in vitro, Biomaterials 25(28) (2004) 5921-7.
[524] P. Laquerriere, A. Grandjean-Laquerriere, E. Jallot, G. Balossier, P. Frayssinet, M. Guenounou, Importance of hydroxyapatite particles characteristics on cytokines production by human monocytes in vitro, Biomaterials 24(16) (2003) 2739-47.
[525] C.W. Denko, M. Petricevic, Hydroxyapatite crystal-induced inflammation and prostaglandin E1, The Journal of rheumatology 6(2) (1979) 117-123.
[526] R.M. Day, A.R. Boccaccini, Effect of particulate bioactive glasses on human macrophages and monocytes in vitro, J Biomed Mater Res A 73(1) (2005) 73-9.
[527] W. Xie, X. Fu, F. Tang, Y. Mo, J. Cheng, H. Wang, X. Chen, Dose-dependent modulation effects of bioactive glass particles on macrophages and diabetic wound healing, J Mater Chem B 7(6) (2019) 940-952.

[528] N. Gomez-Cerezo, L. Casarrubios, I. Morales, M.J. Feito, M. Vallet-Regi, D. Arcos, M.T. Portoles, Effects of a mesoporous bioactive glass on osteoblasts, osteoclasts and macrophages, J Colloid Interface Sci 528 (2018) 309-320.
[529] F. Maehira, N. Ishimine, I. Miyagi, Y. Eguchi, K. Shimada, D. Kawaguchi, Y. Oshiro, Anti-diabetic effects including diabetic nephropathy of anti-osteoporotic trace minerals on diabetic mice, Nutrition 27(4) (2011) 488-95.
[530] B.-N. Lee, J.-U. Hong, S.-M. Kim, J.-H. Jang, H.-S. Chang, Y.-C. Hwang, I.-N. Hwang, W.-M. Oh, Anti-inflammatory and Osteogenic Effects of Calcium Silicate–based Root Canal Sealers, Journal of endodontics 45(1) (2019) 73-78.
[531] M.J. Gonzalez-Munoz, I. Meseguer, M.I. Sanchez-Reus, A. Schultz, R. Olivero, J. Benedi, F.J. Sanchez-Muniz, Beer consumption reduces cerebral oxidation caused by aluminum toxicity by normalizing gene expression of tumor necrotic factor alpha and several antioxidant enzymes, Food Chem Toxicol 46(3) (2008) 1111-8.
[532] E.J. Kim, S.Y. Bu, M.K. Sung, M.H. Kang, M.K. Choi, Analysis of antioxidant and anti-inflammatory activity of silicon in murine macrophages, Biol Trace Elem Res 156(1-3) (2013) 329-37.
[533] M.A. Gronski, J.M. Kinchen, I.J. Juncadella, N.C. Franc, K.S. Ravichandran, An essential role for calcium flux in phagocytes for apoptotic cell engulfment and the anti-inflammatory response, Cell Death & Differentiation 16(10) (2009) 1323-1331.
[534] J.E. Weder, C.T. Dillon, T.W. Hambley, B.J. Kennedy, P.A. Lay, J.R. Biffin, H.L. Regtop, N.M. Davies, Copper complexes of non-steroidal anti-inflammatory drugs: an opportunity yet to be realized, Coordination Chemistry Reviews 232(1-2) (2002) 95-126.
[535] A. Hussain, M.F. Alajmi, M.T. Rehman, S. Amir, F.M. Husain, A. Alsalme, M.A. Siddiqui, A.A. Alkhedhairy, R.A. Khan, Copper(II) complexes as potential anticancer and Nonsteroidal anti-inflammatory agents: In vitro and in vivo studies, Scientific Reports 9(1) (2019) 1-17.
[536] G. Psomas, Copper(II) and zinc(II) coordination compounds of non-steroidal anti-inflammatory drugs: Structural features and antioxidant activity, Coordination Chemistry Reviews 412 (2020) 213259.
[537] G. Wilkinson, R.D. Gillard, J.A. McCleverty, Comprehensive coordination chemistry. The synthesis, reactions, properties and applications of coordination compounds. V. 3. Main group and early transition elements, (1987).
[538] G. Berthon, Is copper pro-or anti-inflammatory? A reconciling view and a novel approach for the use of copper in the control of inflammation, Agents and actions 39(3) (1993) 210-217.
[539] R. Milanino, A. Conforti, L. Franco, M. Marrella, G. Velo, Copper and inflammation--a possible rationale for the pharmacological manipulation of inflammatory disorders, Agents Actions 16(6) (1985) 504-13.
[540] M.C. Linder, M. Hazegh-Azam, Copper biochemistry and molecular biology, Am J Clin Nutr 63(5) (1996) 797S-811S.
[541] M.C. Linder, L. Wooten, P. Cerveza, S. Cotton, R. Shulze, N. Lomeli, Copper transport, Am J Clin Nutr 67(5 Suppl) (1998) 965S-971S.
[542] G. Berthon, Handbook of metal-ligand interactions in biological fluids, Marcel Dekker1995.

[543] Y. Zhou, S. Han, L. Xiao, P. Han, S. Wang, J. He, J. Chang, C. Wu, Y. Xiao, Accelerated host angiogenesis and immune responses by ion release from mesoporous bioactive glass, J Mater Chem B 6(20) (2018) 3274-3284.
[544] R. Lin, C. Deng, X. Li, Y. Liu, M. Zhang, C. Qin, Q. Yao, L. Wang, C. Wu, Copper-incorporated bioactive glass-ceramics inducing anti-inflammatory phenotype and regeneration of cartilage/bone interface, Theranostics 9(21) (2019) 6300-6313.
[545] C. Lang, C. Murgia, M. Leong, L.W. Tan, G. Perozzi, D. Knight, R. Ruffin, P. Zalewski, Anti-inflammatory effects of zinc and alterations in zinc transporter mRNA in mouse models of allergic inflammation, Am J Physiol Lung Cell Mol Physiol 292(2) (2007) L577-84.
[546] S. Krizkova, M. Ryvolova, J. Hrabeta, V. Adam, M. Stiborova, T. Eckschlager, R. Kizek, Metallothioneins and zinc in cancer diagnosis and therapy, Drug Metab Rev 44(4) (2012) 287-301.
[547] R. Hasan, L. Rink, H. Haase, Zinc signals in neutrophil granulocytes are required for the formation of neutrophil extracellular traps, Innate Immun 19(3) (2013) 253-64.
[548] R. Hasan, L. Rink, H. Haase, Chelation of Free Zn(2)(+) Impairs Chemotaxis, Phagocytosis, Oxidative Burst, Degranulation, and Cytokine Production by Neutrophil Granulocytes, Biol Trace Elem Res 171(1) (2016) 79-88.
[549] I. Wessels, M. Maywald, L. Rink, Zinc as a Gatekeeper of Immune Function, Nutrients 9(12) (2017).
[550] J.M. Nedelec, L. Courtheoux, E. Jallot, C. Kinowski, J. Lao, P. Laquerriere, C. Mansuy, G. Renaudin, S. Turrell, Materials doping through sol–gel chemistry: a little something can make a big difference, Journal of Sol-Gel Science and Technology 46(3) (2007) 259-271.
[551] X. Bai, W. Liu, L. Xu, Q. Ye, H. Zhou, C. Berg, H. Yuan, J. Li, W. Xia, Sequential macrophage transition facilitates endogenous bone regeneration induced by Zn-doped porous microcrystalline bioactive glass, J Mater Chem B 9(12) (2021) 2885-2898.
[552] J.Y. Zhu, G.H. Jiang, G. Song, T.Q. Liu, C. Cao, Y.H. Yang, Y.J. Zhang, W.J. Hong, Incorporation of ZnO/Bioactive Glass Nanoparticles into Alginate/Chitosan Composite Hydrogels for Wound Closure, Acs Applied Bio Materials 2(11) (2019) 5042-5052.
[553] E.A. Varmette, J.R. Nowalk, L.M. Flick, M.M. Hall, Abrogation of the inflammatory response in LPS-stimulated RAW 264.7 murine macrophages by Zn- and Cu-doped bioactive sol-gel glasses, J Biomed Mater Res A 90(2) (2009) 317-25.
[554] F.H. Nielsen, Evidence for the nutritional essentiality of boron, Journal of Trace Elements in Experimental Medicine 9(4) (1996) 215-229.
[555] T. Pirmohamed, J.M. Dowding, S. Singh, B. Wasserman, E. Heckert, A.S. Karakoti, J.E. King, S. Seal, W.T. Self, Nanoceria exhibit redox state-dependent catalase mimetic activity, Chem Commun (Camb) 46(16) (2010) 2736-8.
[556] S.M. Hirst, A.S. Karakoti, R.D. Tyler, N. Sriranganathan, S. Seal, C.M. Reilly, Anti-inflammatory properties of cerium oxide nanoparticles, Small 5(24) (2009) 2848-56.
[557] C. Korsvik, S. Patil, S. Seal, W.T. Self, Superoxide dismutase mimetic properties exhibited by vacancy engineered ceria nanoparticles, Chem Commun (Camb) (10) (2007) 1056-8.
[558] I. Celardo, M. De Nicola, C. Mandoli, J.Z. Pedersen, E. Traversa, L. Ghibelli, Ce(3)+ ions determine redox-dependent anti-apoptotic effect of cerium oxide nanoparticles, ACS Nano 5(6) (2011) 4537-49.

[559] S. Das, J.M. Dowding, K.E. Klump, J.F. McGinnis, W. Self, S. Seal, Cerium oxide nanoparticles: applications and prospects in nanomedicine, Nanomedicine (Lond) 8(9) (2013) 1483-508.
[560] G.A. Silva, Neuroscience nanotechnology: progress, opportunities and challenges, Nat Rev Neurosci 7(1) (2006) 65-74.
[561] R.W. Tarnuzzer, J. Colon, S. Patil, S. Seal, Vacancy engineered ceria nanostructures for protection from radiation-induced cellular damage, Nano letters 5(12) (2005) 2573-2577.
[562] S.V. Kyosseva, L. Chen, S. Seal, J.F. McGinnis, Nanoceria inhibit expression of genes associated with inflammation and angiogenesis in the retina of Vldlr null mice, Exp Eye Res 116 (2013) 63-74.
[563] D. Gonzalez-Flores, M. De Nicola, E. Bruni, F. Caputo, A.B. Rodriguez, J.A. Pariente, L. Ghibelli, Nanoceria protects from alterations in oxidative metabolism and calcium overloads induced by TNFalpha and cycloheximide in U937 cells: pharmacological potential of nanoparticles, Mol Cell Biochem 397(1-2) (2014) 245-53.
[564] Z. Serebrovska, R.J. Swanson, V. Portnichenko, A. Shysh, S. Pavlovich, L. Tumanovska, A. Dorovskych, V. Lysenko, V. Tertykh, Y. Bolbukh, V. Dosenko, Anti-inflammatory and antioxidant effect of cerium dioxide nanoparticles immobilized on the surface of silica nanoparticles in rat experimental pneumonia, Biomed Pharmacother 92 (2017) 69-77.
[565] N. Kobyliak, O. Virchenko, T. Falalyeyeva, M. Kondro, T. Beregova, P. Bodnar, O. Shcherbakov, R. Bubnov, M. Caprnda, D. Delev, J. Sabo, P. Kruzliak, L. Rodrigo, R. Opatrilova, M. Spivak, Cerium dioxide nanoparticles possess anti-inflammatory properties in the conditions of the obesity-associated NAFLD in rats, Biomed Pharmacother 90 (2017) 608-614.
[566] K. Zheng, E. Torre, A. Bari, N. Taccardi, C. Cassinelli, M. Morra, S. Fiorilli, C. Vitale-Brovarone, G. Iviglia, A.R. Boccaccini, Antioxidant mesoporous Ce-doped bioactive glass nanoparticles with anti-inflammatory and pro-osteogenic activities, Mater Today Bio 5 (2020) 100041.
[567] P.L. Nadworny, J. Wang, E.E. Tredget, R.E. Burrell, Anti-inflammatory activity of nanocrystalline silver in a porcine contact dermatitis model, Nanomedicine 4(3) (2008) 241-51.
[568] P.L. Nadworny, J. Wang, E.E. Tredget, R.E. Burrell, Anti-inflammatory activity of nanocrystalline silver-derived solutions in porcine contact dermatitis, J Inflamm (Lond) 7(1) (2010) 13.
[569] K.C. Bhol, J. Alroy, P.J. Schechter, Anti-inflammatory effect of topical nanocrystalline silver cream on allergic contact dermatitis in a guinea pig model, Clin Exp Dermatol 29(3) (2004) 282-7.
[570] J. Tian, K.K. Wong, C.M. Ho, C.N. Lok, W.Y. Yu, C.M. Che, J.F. Chiu, P.K. Tam, Topical delivery of silver nanoparticles promotes wound healing, ChemMedChem 2(1) (2007) 129-36.
[571] K.K. Wong, S.O. Cheung, L. Huang, J. Niu, C. Tao, C.M. Ho, C.M. Che, P.K. Tam, Further evidence of the anti-inflammatory effects of silver nanoparticles, ChemMedChem 4(7) (2009) 1129-35.
[572] A. Hebeish, M.H. El-Rafie, M.A. El-Sheikh, A.A. Seleem, M.E. El-Naggar, Antimicrobial wound dressing and anti-inflammatory efficacy of silver nanoparticles, Int J Biol Macromol 65 (2014) 509-15.
[573] J.M. de Lima, E. Pinheiro Ferreira, R.F. Bonan, D.N. Silva-Teixeira, L.R. Goulart, J.R. de Souza, E.S. de Medeiros, P.R.F. Bonan, L.R.C. Castellano, Cytokine Regulation from Human Peripheral

Blood Leukocytes Cultured In Vitro with Silver Doped Bioactive Glasses Microparticles, Biomed Res Int 2019 (2019) 3210530.
[574] S. Sergeant, L.C. McPhail, Opsonized zymosan stimulates the redistribution of protein kinase C isoforms in human neutrophils, J Immunol 159(6) (1997) 2877-85.
[575] L. Bunetel, E.W. Ers, A. Novella, A. Bodin, P. Pellen-Mussi, H. Oudadesse, In vitro chemical and biological effects of Ag, Cu and Cu plus Zn adjunction in 46S6 bioactive glasses, Materials Research Express 2(9) (2015).
[576] F. Romero-Gavilan, N. Araujo-Gomes, I. Garcia-Arnaez, C. Martinez-Ramos, F. Elortza, M. Azkargorta, I. Iloro, M. Gurruchaga, J. Suay, I. Goni, The effect of strontium incorporation into sol-gel biomaterials on their protein adsorption and cell interactions, Colloids Surf B Biointerfaces 174 (2019) 9-16.
[577] G. Renaudin, P. Laquerriere, Y. Filinchuk, E. Jallot, J.M. Nedelec, Structural characterization of sol-gel derived Sr-substituted calcium phosphates with anti-osteoporotic and anti-inflammatory properties, Journal of Materials Chemistry 18(30) (2008) 3593-3600.
[578] R. de Melo Nunes, M.R. Martins, F.S. da Silva Junior, A.C.R. de Melo Leite, V.C.C. Girão, F. de Queiroz Cunha, A.L.L.F. Marinho, A.C.M.D. Pinto, F.A.C. Rocha, Strontium ranelate analgesia in arthritis models is associated to decreased cytokine release and opioid-dependent mechanisms, Inflammation Research 64(10) (2015) 781-787.
[579] D.-W. Zhao, C. Liu, K.-Q. Zuo, P. Su, L.-B. Li, G.-Y. Xiao, L. Cheng, Strontium-zinc phosphate chemical conversion coating improves the osseointegration of titanium implants by regulating macrophage polarization, Chemical Engineering Journal (2020) 127362.
[580] F. Zhao, B. Lei, X. Li, Y. Mo, R. Wang, D. Chen, X. Chen, Promoting in vivo early angiogenesis with sub-micrometer strontium-contained bioactive microspheres through modulating macrophage phenotypes, Biomaterials 178 (2018) 36-47.
[581] W. Zhang, F. Zhao, D. Huang, X. Fu, X. Li, X. Chen, Strontium-Substituted Submicrometer Bioactive Glasses Modulate Macrophage Responses for Improved Bone Regeneration, ACS Appl Mater Interfaces 8(45) (2016) 30747-30758.
[582] J. Mahmood, H. Takita, Y. Ojima, M. Kobayashi, T. Kohgo, Y. Kuboki, Geometric effect of matrix upon cell differentiation: BMP-induced osteogenesis using a new bioglass with a feasible structure, J Biochem 129(1) (2001) 163-71.
[583] M. Kazemi, M. Azami, B. Johari, M. Ahmadzadehzarajabad, B. Nazari, S. Kargozar, S. Hajighasemlou, M. Mozafari, M. Soleimani, A. Samadikuchaksaraei, Bone Regeneration in rat using a gelatin/bioactive glass nanocomposite scaffold along with endothelial cells (HUVEC s), International Journal of Applied Ceramic Technology 15(6) (2018) 1427-1438.
[584] Y.N. Lin, W. Xiao, X. Liu, B.S. Bal, L.F. Bonewald, M.N. Rahaman, Long-term bone regeneration, mineralization and angiogenesis in rat calvarial defects implanted with strong porous bioactive glass (13-93) scaffolds, Journal of Non-Crystalline Solids 432 (2016) 120-129.
[585] A. Leu, J.K. Leach, Proangiogenic potential of a collagen/bioactive glass substrate, Pharm Res 25(5) (2008) 1222-9.
[586] A. Leu, S.M. Stieger, P. Dayton, K.W. Ferrara, J.K. Leach, Angiogenic response to bioactive glass promotes bone healing in an irradiated calvarial defect, Tissue Eng Part A 15(4) (2009) 877-85.

[587] G.E. Vargas, L.A. Haro Durand, V. Cadena, M. Romero, R.V. Mesones, M. Mackovic, S. Spallek, E. Spiecker, A.R. Boccaccini, A.A. Gorustovich, Effect of nano-sized bioactive glass particles on the angiogenic properties of collagen based composites, J Mater Sci Mater Med 24(5) (2013) 1261-9.
[588] H. Keshaw, A. Forbes, R.M. Day, Release of angiogenic growth factors from cells encapsulated in alginate beads with bioactive glass, Biomaterials 26(19) (2005) 4171-9.
[589] Q. Zeng, Y. Han, H. Li, J. Chang, Bioglass/alginate composite hydrogel beads as cell carriers for bone regeneration, J Biomed Mater Res B Appl Biomater 102(1) (2014) 42-51.
[590] Q. Zeng, Y. Han, H. Li, J. Chang, Design of a thermosensitive bioglass/agarose-alginate composite hydrogel for chronic wound healing, J Mater Chem B 3(45) (2015) 8856-8864.
[591] U. Rottensteiner-Brandl, R. Detsch, B. Sarker, L. Lingens, K. Kohn, U. Kneser, A.K. Bosserhoff, R.E. Horch, A.R. Boccaccini, A. Arkudas, Encapsulation of Rat Bone Marrow Derived Mesenchymal Stem Cells in Alginate Dialdehyde/Gelatin Microbeads with and without Nanoscaled Bioactive Glass for In Vivo Bone Tissue Engineering, Materials (Basel) 11(10) (2018) 1880.
[592] R. Detsch, P. Stoor, A. Grunewald, J.A. Roether, N.C. Lindfors, A.R. Boccaccini, Increase in VEGF secretion from human fibroblast cells by bioactive glass S53P4 to stimulate angiogenesis in bone, J Biomed Mater Res A 102(11) (2014) 4055-61.
[593] D.R. Li, G.L. Jiao, W. Zhang, X.F. Chen, R.J. Ning, C. Du, Hybrid scaffolding strategy for dermal tissue reconstruction: a bioactive glass/chitosan/silk fibroin composite, Rsc Advances 6(24) (2016) 19887-19896.
[594] J. Li, F. Lv, H. Xu, Y. Zhang, J. Wang, Z. Yi, J. Yin, J. Chang, C. Wu, A patterned nanocomposite membrane for high-efficiency healing of diabetic wound, J Mater Chem B 5(10) (2017) 1926-1934.
[595] R. Nunez-Toldra, S. Montori, B. Bosch, L. Hupa, M. Atari, S. Miettinen, S53P4 Bioactive Glass Inorganic Ions for Vascularized Bone Tissue Engineering by Dental Pulp Pluripotent-Like Stem Cell Cocultures, Tissue Eng Part A 25(17-18) (2019) 1213-1224.
[596] M. Handel, T.R. Hammer, P. Nooeaid, A.R. Boccaccini, D. Hoefer, 45S5-Bioglass((R))-based 3D-scaffolds seeded with human adipose tissue-derived stem cells induce in vivo vascularization in the CAM angiogenesis assay, Tissue Eng Part A 19(23-24) (2013) 2703-12.
[597] S.B. Jung, D.E. Day, Wound care, Google Patents, 2013.
[598] A.A. Gorustovich, J.A. Roether, A.R. Boccaccini, Effect of bioactive glasses on angiogenesis: a review of in vitro and in vivo evidences, Tissue Eng Part B Rev 16(2) (2010) 199-207.
[599] W. Zhai, H. Lu, L. Chen, X. Lin, Y. Huang, K. Dai, K. Naoki, G. Chen, J. Chang, Silicate bioceramics induce angiogenesis during bone regeneration, Acta Biomaterialia 8(1) (2012) 341-349.
[600] H. Li, J. Chang, Bioactive silicate materials stimulate angiogenesis in fibroblast and endothelial cell co-culture system through paracrine effect, Acta Biomaterialia 9(6) (2013) 6981-6991.
[601] W. Zhai, H. Lu, L. Chen, X. Lin, Y. Huang, K. Dai, K. Naoki, G. Chen, J. Chang, Silicate bioceramics induce angiogenesis during bone regeneration, Acta Biomater 8(1) (2012) 341-9.
[602] K. Dashnyam, G.Z. Jin, J.H. Kim, R. Perez, J.H. Jang, H.W. Kim, Promoting angiogenesis with mesoporous microcarriers through a synergistic action of delivered silicon ion and VEGF, Biomaterials 116 (2017) 145-157.

[603] M.A. Saghiri, A. Asatourian, J. Orangi, C.M. Sorenson, N. Sheibani, Functional role of inorganic trace elements in angiogenesis-Part II: Cr, Si, Zn, Cu, and S, Crit Rev Oncol Hematol 96(1) (2015) 143-55.
[604] U. Forstermann, T. Munzel, Endothelial nitric oxide synthase in vascular disease: from marvel to menace, Circulation 113(13) (2006) 1708-1714.
[605] L. Munaron, A. Fiorio Pla, Calcium influx induced by activation of tyrosine kinase receptors in cultured bovine aortic endothelial cells, J Cell Physiol 185(3) (2000) 454-63.
[606] L. Munaron, C. Distasi, V. Carabelli, F.M. Baccino, G. Bonelli, D. Lovisolo, Sustained calcium influx activated by basic fibroblast growth factor in Balb-c 3T3 fibroblasts, J Physiol 484 (Pt 3)(3) (1995) 557-66.
[607] M. Estacion, L.J. Mordan, Competence induction by PDGF requires sustained calcium influx by a mechanism distinct from storage-dependent calcium influx, Cell Calcium 14(6) (1993) 439-54.
[608] A. Parenti, L. Morbidelli, X.L. Cui, J.G. Douglas, J.D. Hood, H.J. Granger, F. Ledda, M. Ziche, Nitric oxide is an upstream signal of vascular endothelial growth factor-induced extracellular signal-regulated kinase(1/2) activation in postcapillary endothelium, Journal of Biological Chemistry 273(7) (1998) 4220-4226.
[609] H.M. Wu, Y. Yuan, D.C. Zawieja, J. Tinsley, H.J. Granger, Role of phospholipase C, protein kinase C, and calcium in VEGF-induced venular hyperpermeability, Am J Physiol 276(2) (1999) H535-42.
[610] M.A. Saghiri, A. Asatourian, J. Orangi, C.M. Sorenson, N. Sheibani, Functional role of inorganic trace elements in angiogenesis-Part I: N, Fe, Se, P, Au, and Ca, Critical Reviews in Oncology Hematology 96(1) (2015) 129-142.
[611] M. Dzondo-Gadet, R. Mayap-Nzietchueng, K. Hess, P. Nabet, F. Belleville, B. Dousset, Action of boron at the molecular level - Effects on transcription and translation in an acellular system, Biological Trace Element Research 85(1) (2002) 23-33.
[612] S.G. Penn, H. Hu, P.H. Brown, C.B. Lebrilla, Direct analysis of sugar alcohol borate complexes in plant extracts by matrix-assisted laser desorption/ionization Fourier transform mass spectrometry, Analytical chemistry 69(13) (1997) 2471-2477.
[613] P. Rico, A. Rodrigo-Navarro, M. de la Pena, V. Moulisova, M. Costell, M. Salmeron-Sanchez, Simultaneous Boron Ion-Channel/Growth Factor Receptor Activation for Enhanced Vascularization, Adv Biosyst 3(1) (2019) e1800220.
[614] M. Park, Q. Li, N. Shcheynikov, W. Zeng, S. Muallem, NaBC1 is a ubiquitous electrogenic Na+ -coupled borate transporter essential for cellular boron homeostasis and cell growth and proliferation, Mol Cell 16(3) (2004) 331-41.
[615] G. Augustine, M. Aarthy, H. Thiagarajan, S. Selvaraj, N.R. Kamini, G. Shanmugam, N. Ayyadurai, Self-Assembly and Mechanical Properties of Engineered Protein Based Multifunctional Nanofiber for Accelerated Wound Healing, Adv Healthc Mater 10(8) (2021) e2001832.
[616] S. Ahtzaz, T. Sher Waris, L. Shahzadi, A. Anwar Chaudhry, I. Ur Rehman, M. Yar, Boron for tissue regeneration-it's loading into chitosan/collagen hydrogels and testing on chorioallantoic membrane to study the effect on angiogenesis, International Journal of Polymeric Materials and Polymeric Biomaterials 69(8) (2020) 525-534.

[617] K. Li, X. Lu, I. Razanau, X. Wu, T. Hu, S. Liu, Y. Xie, L. Huang, X. Zheng, The enhanced angiogenic responses to ionic dissolution products from a boron-incorporated calcium silicate coating, Materials Science and Engineering: C 101 (2019) 513-520.
[618] L.A. Haro Durand, G.E. Vargas, N.M. Romero, R. Vera-Mesones, J.M. Porto-Lopez, A.R. Boccaccini, M.P. Zago, A. Baldi, A. Gorustovich, Angiogenic effects of ionic dissolution products released from a boron-doped 45S5 bioactive glass, J Mater Chem B 3(6) (2015) 1142-1148.
[619] L. Xia, W. Ma, Y. Zhou, Z. Gui, A. Yao, D. Wang, A. Takemura, M. Uemura, K. Lin, Y. Xu, Stimulatory Effects of Boron Containing Bioactive Glass on Osteogenesis and Angiogenesis of Polycaprolactone: In Vitro Study, Biomed Res Int 2019 (2019) 8961409.
[620] S.B. Jung, D.E. Day, Boron trioxide glass-based fibers and particles in dressings, sutures, surgical glue, and other wound care compositions, Google Patents, 2012.
[621] F. Westhauser, B. Widholz, Q. Nawaz, S. Tsitlakidis, S. Hagmann, A. Moghaddam, A.R. Boccaccini, Favorable angiogenic properties of the borosilicate bioactive glass 0106-B1 result in enhanced in vivo osteoid formation compared to 45S5 Bioglass, Biomater Sci 7(12) (2019) 5161-5176.
[622] P. Balasubramanian, L. Hupa, B. Jokic, R. Detsch, A. Grünewald, A.R. Boccaccini, Angiogenic potential of boron-containing bioactive glasses: in vitro study, Journal of Materials Science 52(15) (2016) 8785-8792.
[623] Z. Su, J. Li, X. Bai, F.R. Tay, M. Zhang, K. Liang, L. He, H. Yuan, J. Li, Borate bioactive glass prevents zoledronate-induced osteonecrosis of the jaw by restoring osteogenesis and angiogenesis, Oral Dis 26(8) (2020) 1706-1717.
[624] O.F. Vila, J.R. Bago, M. Navarro, M. Alieva, E. Aguilar, E. Engel, J. Planell, N. Rubio, J. Blanco, Calcium phosphate glass improves angiogenesis capacity of poly(lactic acid) scaffolds and stimulates differentiation of adipose tissue-derived mesenchymal stromal cells to the endothelial lineage, J Biomed Mater Res A 101(4) (2013) 932-41.
[625] G. Kaur, G. Pickrell, N. Sriranganathan, V. Kumar, D. Homa, Review and the state of the art: Sol-gel and melt quenched bioactive glasses for tissue engineering, J Biomed Mater Res B Appl Biomater 104(6) (2016) 1248-75.
[626] J. Massera, A. Kokkari, T. Narhi, L. Hupa, The influence of SrO and CaO in silicate and phosphate bioactive glasses on human gingival fibroblasts, J Mater Sci Mater Med 26(6) (2015) 196.
[627] C. Peticone, D. De Silva Thompson, G.J. Owens, H.W. Kim, M. Micheletti, J.C. Knowles, I. Wall, Towards modular bone tissue engineering using Ti-Co-doped phosphate glass microspheres: cytocompatibility and dynamic culture studies, J Biomater Appl 32(3) (2017) 295-310.
[628] C. Stahli, N. Muja, S.N. Nazhat, Controlled copper ion release from phosphate-based glasses improves human umbilical vein endothelial cell survival in a reduced nutrient environment, Tissue Eng Part A 19(3-4) (2013) 548-57.
[629] E.D. Harris, A requirement for copper in angiogenesis, Nutr Rev 62(2) (2004) 60-4.
[630] C. Gerard, L.J. Bordeleau, J. Barralet, C.J. Doillon, The stimulation of angiogenesis and collagen deposition by copper, Biomaterials 31(5) (2010) 824-31.
[631] L. Finney, S. Vogt, T. Fukai, D. Glesne, Copper and angiogenesis: unravelling a relationship key to cancer progression, Clin Exp Pharmacol Physiol 36(1) (2009) 88-94.

[632] S.A. Lowndes, A.L. Harris, The role of copper in tumour angiogenesis, J Mammary Gland Biol Neoplasia 10(4) (2005) 299-310.
[633] W. He, Y. James Kang, Ischemia-induced copper loss and suppression of angiogenesis in the pathogenesis of myocardial infarction, Cardiovasc Toxicol 13(1) (2013) 1-8.
[634] G. Mavria, Y. Vercoulen, M. Yeo, H. Paterson, M. Karasarides, R. Marais, D. Bird, C.J. Marshall, ERK-MAPK signaling opposes Rho-kinase to promote endothelial cell survival and sprouting during angiogenesis, Cancer Cell 9(1) (2006) 33-44.
[635] T.F. Lane, M.L. Iruelaarispe, R.S. Johnson, E.H. Sage, Sparc Is a Source of Copper-Binding Peptides That Stimulate Angiogenesis, Journal of Cell Biology 125(4) (1994) 929-943.
[636] L. Bi, M.N. Rahaman, D.E. Day, Z. Brown, C. Samujh, X. Liu, A. Mohammadkhah, V. Dusevich, J.D. Eick, L.F. Bonewald, Effect of bioactive borate glass microstructure on bone regeneration, angiogenesis, and hydroxyapatite conversion in a rat calvarial defect model, Acta Biomater 9(8) (2013) 8015-26.
[637] H. Wang, S. Zhao, W. Xiao, J. Xue, Y. Shen, J. Zhou, W. Huang, M.N. Rahaman, C. Zhang, D. Wang, Influence of Cu doping in borosilicate bioactive glass and the properties of its derived scaffolds, Mater Sci Eng C Mater Biol Appl 58 (2016) 194-203.
[638] Y. Lin, W. Xiao, B.S. Bal, M.N. Rahaman, Effect of copper-doped silicate 13-93 bioactive glass scaffolds on the response of MC3T3-E1 cells in vitro and on bone regeneration and angiogenesis in rat calvarial defects in vivo, Mater Sci Eng C Mater Biol Appl 67 (2016) 440-452.
[639] G. Bührer, U. Rottensteiner, A. Hoppe, R. Detsch, D. Dafinova, T. Fey, P. Greil, C. Weis, J.P. Beier, A.R. Boccacini, Evaluation of in vivo angiogenetic effects of copper doped bioactive glass scaffolds in the AV loop model, Biomedical glasses 1(open-issue) (2016).
[640] C. Stahli, M. James-Bhasin, A. Hoppe, A.R. Boccaccini, S.N. Nazhat, Effect of ion release from Cu-doped 45S5 Bioglass(R) on 3D endothelial cell morphogenesis, Acta Biomater 19 (2015) 15-22.
[641] E.J. Ryan, A.J. Ryan, A. Gonzalez-Vazquez, A. Philippart, F.E. Ciraldo, C. Hobbs, V. Nicolosi, A.R. Boccaccini, C.J. Kearney, F.J. O'Brien, Collagen scaffolds functionalised with copper-eluting bioactive glass reduce infection and enhance osteogenesis and angiogenesis both in vitro and in vivo, Biomaterials 197 (2019) 405-416.
[642] L. Weng, S.K. Boda, H. Wang, M.J. Teusink, F.D. Shuler, J. Xie, Novel 3D Hybrid Nanofiber Aerogels Coupled with BMP-2 Peptides for Cranial Bone Regeneration, Adv Healthc Mater 7(10) (2018) e1701415.
[643] J. Li, D. Zhai, F. Lv, Q. Yu, H. Ma, J. Yin, Z. Yi, M. Liu, J. Chang, C. Wu, Preparation of copper-containing bioactive glass/eggshell membrane nanocomposites for improving angiogenesis, antibacterial activity and wound healing, Acta Biomater 36 (2016) 254-66.
[644] R.J. Watters, R.F. Brown, D.E. Day, Angiogenic Effect of Bioactive Borate Glass Microfibers and Beads in the Hairless Mouse, Biomedical glasses 1(1) (2015).
[645] L. Weng, S.K. Boda, M.J. Teusink, F.D. Shuler, X. Li, J. Xie, Binary Doping of Strontium and Copper Enhancing Osteogenesis and Angiogenesis of Bioactive Glass Nanofibers while Suppressing Osteoclast Activity, ACS Appl Mater Interfaces 9(29) (2017) 24484-24496.
[646] S. Ahtzaz, M. Nasir, L. Shahzadi, W. Amir, A. Anjum, R. Arshad, F. Iqbal, A.A. Chaudhry, M. Yar, I.U. Rehman, A study on the effect of zinc oxide and zinc peroxide nanoparticles to enhance

angiogenesis-pro-angiogenic grafts for tissue regeneration applications, Materials & Design 132 (2017) 409-418.
[647] Y. Hanai, H. Tokuda, E. Yasuda, T. Noda, T. Ohta, S. Takai, O. Kozawa, Up-regulation by zinc of FGF-2-induced VEGF release throughenhancing p44/p42 MAP kinase activation in osteoblasts, Life sciences 80(3) (2006) 230-234.
[648] A.K. Barui, V. Veeriah, S. Mukherjee, J. Manna, A.K. Patel, S. Patra, K. Pal, S. Murali, R.K. Rana, S. Chatterjee, C.R. Patra, Zinc oxide nanoflowers make new blood vessels, Nanoscale 4(24) (2012) 7861-9.
[649] Y. Zhang, M. Chang, F. Bao, M. Xing, E. Wang, Q. Xu, Z. Huan, F. Guo, J. Chang, Multifunctional Zn doped hollow mesoporous silica/polycaprolactone electrospun membranes with enhanced hair follicle regeneration and antibacterial activity for wound healing, Nanoscale 11(13) (2019) 6315-6333.
[650] A. Rahmani, S. Hashemi-Najafabadi, M.B. Eslaminejad, F. Bagheri, F.A. Sayahpour, The effect of modified electrospun PCL-nHA-nZnO scaffolds on osteogenesis and angiogenesis, J Biomed Mater Res A 107(9) (2019) 2040-2052.
[651] H. Chhabra, R. Deshpande, M. Kanitkar, A. Jaiswal, V.P. Kale, J.R. Bellare, A nano zinc oxide doped electrospun scaffold improves wound healing in a rodent model, Rsc Advances 6(2) (2016) 1428-1439.
[652] G. Hallmans, J. Lasek, The effect of topical zinc absorption from wounds on growth and the wound healing process in zinc-deficient rats, Scand J Plast Reconstr Surg 19(2) (1985) 119-25.
[653] T. Boehm, S. O'Reilly M, K. Keough, J. Shiloach, R. Shapiro, J. Folkman, Zinc-binding of endostatin is essential for its antiangiogenic activity, Biochem Biophys Res Commun 252(1) (1998) 190-4.
[654] C.H. Kim, J.H. Kim, J. Lee, C.Y. Hsu, Y.S. Ahn, Thiol antioxidant reversal of pyrrolidine dithiocarbamate-induced reciprocal regulation of AP-1 and NF-kappaB, Biol Chem 384(1) (2003) 143-50.
[655] S.T. Huang, R.C. Yang, H.T. Wu, C.N. Wang, J.H. Pang, Zinc-chelation contributes to the anti-angiogenic effect of ellagic acid on inhibiting MMP-2 activity, cell migration and tube formation, PLoS One 6(5) (2011) e18986.
[656] J. Bejarano, R. Detsch, A.R. Boccaccini, H. Palza, PDLLA scaffolds with Cu- and Zn-doped bioactive glasses having multifunctional properties for bone regeneration, J Biomed Mater Res A 105(3) (2017) 746-756.
[657] Z.T. Birgani, N. Gharraee, A. Malhotra, C.A. van Blitterswijk, P. Habibovic, Combinatorial incorporation of fluoride and cobalt ions into calcium phosphates to stimulate osteogenesis and angiogenesis, Biomedical Materials 11(1) (2016) 015020.
[658] Z. Deng, B. Lin, Z. Jiang, W. Huang, J. Li, X. Zeng, H. Wang, D. Wang, Y. Zhang, Hypoxia-Mimicking Cobalt-Doped Borosilicate Bioactive Glass Scaffolds with Enhanced Angiogenic and Osteogenic Capacity for Bone Regeneration, Int J Biol Sci 15(6) (2019) 1113-1124.
[659] A. Hoppe, B. Jokic, D. Janackovic, T. Fey, P. Greil, S. Romeis, J. Schmidt, W. Peukert, J. Lao, E. Jallot, A.R. Boccaccini, Cobalt-releasing 1393 bioactive glass-derived scaffolds for bone tissue engineering applications, ACS Appl Mater Interfaces 6(4) (2014) 2865-77.
[660] K. Rychli, C. Kaun, P.J. Hohensinner, A.J. Dorfner, S. Pfaffenberger, A. Niessner, M. Bauer, W. Dietl, B.K. Podesser, G. Maurer, K. Huber, J. Wojta, The anti-angiogenic factor PEDF is present in

the human heart and is regulated by anoxia in cardiac myocytes and fibroblasts, Journal of Cellular and Molecular Medicine 14(1-2) (2010) 198-205.
[661] J.K. Li, F. Lv, J.X. Li, Y.X. Li, J.D. Gao, J. Luo, F. Xue, Q.F. Ke, H. Xu, Cobalt-based metal-organic framework as a dual cooperative controllable release system for accelerating diabetic wound healing, Nano Research 13(8) (2020) 2268-2279.
[662] Q. Shi, X. Luo, Z. Huang, A.C. Midgley, B. Wang, R. Liu, D. Zhi, T. Wei, X. Zhou, M. Qiao, J. Zhang, D. Kong, K. Wang, Cobalt-mediated multi-functional dressings promote bacteria-infected wound healing, Acta Biomater 86 (2019) 465-479.
[663] K. Peters, H. Schmidt, R.E. Unger, G. Kamp, F. Prols, B.J. Berger, C.J. Kirkpatrick, Paradoxical effects of hypoxia-mimicking divalent cobalt ions in human endothelial cells in vitro, Mol Cell Biochem 270(1-2) (2005) 157-66.
[664] N. Fani, M. Farokhi, M. Azami, A. Kamali, N.L. Bakhshaiesh, S. Ebrahimi-Barough, J. Ai, M.B. Eslaminejad, Endothelial and Osteoblast Differentiation of Adipose-Derived Mesenchymal Stem Cells Using a Cobalt-Doped CaP/Silk Fibroin Scaffold, Acs Biomaterials Science & Engineering 5(5) (2019) 2134-2146.
[665] J. Zhao, Y. Liu, J. Sun, H. Zhu, Y. Chen, T. Dong, R. Sang, X. Gao, W. Yang, Y. Deng, Magnetic targeting cobalt nanowire-based multifunctional therapeutic system for anticancer treatment and angiogenesis, Colloids Surf B Biointerfaces 194 (2020) 111217.
[666] S. Arab-Ahmadi, S. Irani, H. Bakhshi, F. Atyabi, B. Ghalandari, Immobilization of cobalt-loaded laponite/carboxymethyl chitosan on polycaprolactone nanofiber for improving osteogenesis and angiogenesis activities, Polymers for Advanced Technologies (2021).
[667] H. Zhang, Y.Y. Zhao, Y. Zhang, R.Y. Hang, X.H. Yao, R.Q. Hang, Exosomes derived from macrophages upon cobalt ion stimulation promote angiogenesis, Colloids and Surfaces B-Biointerfaces 203 (2021) 111742.
[668] G.Q. Liu, X.S. Wang, X. Zhou, L.J. Zhang, J.M. Mi, Z.J. Shan, B.X. Huang, Z.F. Chen, Z.T. Chen, Modulating the cobalt dose range to manipulate multisystem cooperation in bone environment: a strategy to resolve the controversies about cobalt use for orthopedic applications, Theranostics 10(3) (2020) 1074-1089.
[669] A. Hoppe, A. Brandl, O. Bleiziffer, A. Arkudas, R.E. Horch, B. Jokic, D. Janackovic, A.R. Boccaccini, In vitro cell response to Co-containing 1,393 bioactive glass, Mater Sci Eng C Mater Biol Appl 57 (2015) 157-63.
[670] B.R. Barrioni, E. Norris, J.R. Jones, M.D. Pereira, The influence of cobalt incorporation and cobalt precursor selection on the structure and bioactivity of sol-gel-derived bioactive glass, Journal of Sol-Gel Science and Technology 88(2) (2018) 309-321.
[671] S. Chen, M. Michalek, D. Galuskova, M. Michalkova, P. Svancarek, A. Talimian, H. Kankova, J. Kraxner, K. Zheng, L. Liverani, D. Galusek, A.R. Boccaccini, Multi-targeted B and Co co-doped 45S5 bioactive glasses with angiogenic potential for bone regeneration, Mater Sci Eng C Mater Biol Appl 112 (2020) 110909.
[672] B.R. Barrioni, A.G.S. de Laia, T.M. Valverde, T.M.D. Martins, M.V. Caliari, M.A. de Sa, A.M. de Goes, M.D. Pereira, Evaluation of in vitro and in vivo biocompatibility and structure of cobalt releasing sol-gel bioactive glass, Ceramics International 44(16) (2018) 20337-20347.
[673] S. Kargozar, N. Lotfibakhshaiesh, J. Ai, M. Mozafari, P. Brouki Milan, S. Hamzehlou, M. Barati, F. Baino, R.G. Hill, M.T. Joghataei, Strontium- and cobalt-substituted bioactive glasses seeded with

human umbilical cord perivascular cells to promote bone regeneration via enhanced osteogenic and angiogenic activities, Acta Biomater 58 (2017) 502-514.
[674] A.G.S. de Laia, T.M. Valverde, B.R. Barrioni, P.D.S. Cunha, A.M. de Goes, M.C. de Miranda, D.A. Gomes, C.M. Queiroz-Junior, M.A. de Sa, M. de Magalhaes Pereira, Cobalt-containing bioactive glass mimics vascular endothelial growth factor A and hypoxia inducible factor 1 function, J Biomed Mater Res A 109(7) (2021) 1051-1064.
[675] E. Quinlan, S. Partap, M.M. Azevedo, G. Jell, M.M. Stevens, F.J. O'Brien, Hypoxia-mimicking bioactive glass/collagen glycosaminoglycan composite scaffolds to enhance angiogenesis and bone repair, Biomaterials 52 (2015) 358-66.
[676] A.K. Solanki, F.V. Lali, H. Autefage, S. Agarwal, A. Nommeots-Nomm, A.D. Metcalfe, M.M. Stevens, J.R. Jones, Bioactive glasses and electrospun composites that release cobalt to stimulate the HIF pathway for wound healing applications, Biomaterials Research 25(1) (2021) 1-16.
[677] K.L. Lin, X.H. Wang, N. Zhang, Y.H. Shen, Strontium (Sr) strengthens the silicon (Si) upon osteoblast proliferation, osteogenic differentiation and angiogenic factor expression, Journal of Materials Chemistry B 4(21) (2016) 3632-3638.
[678] F. Liu, X. Zhang, X. Yu, Y. Xu, T. Feng, D. Ren, In vitro study in stimulating the secretion of angiogenic growth factors of strontium-doped calcium polyphosphate for bone tissue engineering, J Mater Sci Mater Med 22(3) (2011) 683-92.
[679] Z.P. Gu, H.X. Xie, C.C. Huang, H. Peng, H. Tan, L. Li, X.X. Yu, Effects of strontium-doped calcium polyphosphate on angiogenic growth factors expression of co-culturing system in vitro and of host cell in vivo, Rsc Advances 4(6) (2014) 2783-2792.
[680] X. Wu, Z. Tang, K. Wu, Y. Bai, X. Lin, H. Yang, Q. Yang, Z. Wang, X. Ni, H. Liu, L. Yang, Strontium-calcium phosphate hybrid cement with enhanced osteogenic and angiogenic properties for vascularised bone regeneration, J Mater Chem B (2021).
[681] A. Udduttula, J. Li, P.-Y. Zhao, G.-C. Wang, J.V. Zhang, P.-G. Ren, Sol-gel derived nanosized Sr5(PO4)2SiO4 powder with enhanced in vitro osteogenesis and angiogenesis for bone regeneration applications, Ceramics International 45(3) (2019) 3148-3158.
[682] X. Wang, Y.P. Wang, L. Li, Z.P. Gu, H.X. Xie, X.X. Yu, Stimulations of strontium-doped calcium polyphosphate for bone tissue engineering to protein secretion and mRNA expression of the angiogenic growth factors from endothelial cells in vitro, Ceramics International 40(5) (2014) 6999-7005.
[683] Y.W. Chen, T. Feng, G.Q. Shi, Y.L. Ding, X.X. Yu, X.H. Zhang, Z.B. Zhang, C.X. Wan, Interaction of endothelial cells with biodegradable strontium-doped calcium polyphosphate for bone tissue engineering, Applied Surface Science 255(2) (2008) 331-335.
[684] Y. Chen, G. Shi, Y. Ding, X. Yu, X. Zhang, C. Zhao, C. Wan, In vitro study on the influence of strontium-doped calcium polyphosphate on the angiogenesis-related behaviors of HUVECs, Journal of Materials Science: Materials in Medicine 19(7) (2008) 2655-2662.
[685] Z. Gu, H. Xie, L. Li, X. Zhang, F. Liu, X. Yu, Application of strontium-doped calcium polyphosphate scaffold on angiogenesis for bone tissue engineering, Journal of Materials Science: Materials in Medicine 24(5) (2013) 1251-1260.
[686] S. Zhao, J. Zhang, M. Zhu, Y. Zhang, Z. Liu, C. Tao, Y. Zhu, C. Zhang, Three-dimensional printed strontium-containing mesoporous bioactive glass scaffolds for repairing rat critical-sized calvarial defects, Acta Biomater 12 (2015) 270-280.

[687] S.Z. Jalise, N. Baheiraei, F. Bagheri, The effects of strontium incorporation on a novel gelatin/bioactive glass bone graft: In vitro and in vivo characterization, Ceramics International 44(12) (2018) 14217-14227.
[688] L.A. Strobel, N. Hild, D. Mohn, W.J. Stark, A. Hoppe, U. Gbureck, R.E. Horch, U. Kneser, A.R. Boccaccini, Novel strontium-doped bioactive glass nanoparticles enhance proliferation and osteogenic differentiation of human bone marrow stromal cells, Journal of Nanoparticle Research 15(7) (2013).
[689] M. Luo, F. Zhao, L. Liu, Z. Yang, T. Tian, X. Chen, X. Cao, D. Chen, X. Chen, IFN-gamma/SrBG composite scaffolds promote osteogenesis by sequential regulation of macrophages from M1 to M2, J Mater Chem B 9(7) (2021) 1867-1876.
[690] C.D. Mao, P. Hoang, P.E. DiCorleto, Lithium inhibits cell cycle progression and induces stabilization of p53 in bovine aortic endothelial cells, J Biol Chem 276(28) (2001) 26180-8.
[691] Y. Takada, X. Fang, M.S. Jamaluddin, D.D. Boyd, B.B. Aggarwal, Genetic deletion of glycogen synthase kinase-3beta abrogates activation of IkappaBalpha kinase, JNK, Akt, and p44/p42 MAPK but potentiates apoptosis induced by tumor necrosis factor, J Biol Chem 279(38) (2004) 39541-54.
[692] Z.H. Németh, E.A. Deitch, C. Szabó, Z. Fekete, C.J. Hauser, G. Haskó, Lithium induces NF-κB activation and interleukin-8 production in human intestinal epithelial cells, Journal of Biological Chemistry 277(10) (2002) 7713-7719.
[693] I.T. Struewing, S.N. Durham, C.D. Barnett, C.D. Mao, Enhanced endothelial cell senescence by lithium-induced matrix metalloproteinase-1 expression, J Biol Chem 284(26) (2009) 17595-606.
[694] M.A. Saghiri, J. Orangi, A. Asatourian, C.M. Sorenson, N. Sheibani, Functional role of inorganic trace elements in angiogenesis part III: (Ti, Li, Ce, As, Hg, Va, Nb and Pb), Critical Reviews in Oncology Hematology 98 (2016) 290-301.
[695] L.A. Haro Durand, G.E. Vargas, R. Vera-Mesones, A. Baldi, M.P. Zago, M.A. Fanovich, A.R. Boccaccini, A. Gorustovich, In Vitro Human Umbilical Vein Endothelial Cells Response to Ionic Dissolution Products from Lithium-Containing 45S5 Bioactive Glass, Materials (Basel) 10(7) (2017).
[696] L. Liu, Y. Liu, C. Feng, J. Chang, R. Fu, T. Wu, F. Yu, X. Wang, L. Xia, C. Wu, B. Fang, Lithium-containing biomaterials stimulate bone marrow stromal cell-derived exosomal miR-130a secretion to promote angiogenesis, Biomaterials 192 (2019) 523-536.
[697] L.F. Zeilbeck, B. Muller, V. Knobloch, E.R. Tamm, A. Ohlmann, Differential angiogenic properties of lithium chloride in vitro and in vivo, PLoS One 9(4) (2014) e95546.
[698] C. Mao, X. Chen, G. Miao, C. Lin, Angiogenesis stimulated by novel nanoscale bioactive glasses, Biomed Mater 10(2) (2015) 025005.
[699] J.J. Kim, A. El-Fiqi, H.W. Kim, Synergetic Cues of Bioactive Nanoparticles and Nanofibrous Structure in Bone Scaffolds to Stimulate Osteogenesis and Angiogenesis, ACS Appl Mater Interfaces 9(3) (2017) 2059-2073.
[700] M.S. Kang, N.H. Lee, R.K. Singh, N. Mandakhbayar, R.A. Perez, J.H. Lee, H.W. Kim, Nanocements produced from mesoporous bioactive glass nanoparticles, Biomaterials 162 (2018) 183-199.

[701] L.B. Romero-Sanchez, M. Mari-Beffa, P. Carrillo, M.A. Medina, A. Diaz-Cuenca, Copper-containing mesoporous bioactive glass promotes angiogenesis in an in vivo zebrafish model, Acta Biomater 68 (2018) 272-285.
[702] C. Wu, Y. Zhou, W. Fan, P. Han, J. Chang, J. Yuen, M. Zhang, Y. Xiao, Hypoxia-mimicking mesoporous bioactive glass scaffolds with controllable cobalt ion release for bone tissue engineering, Biomaterials 33(7) (2012) 2076-85.
[703] F. Kermani, S. Mollazadeh Beidokhti, F. Baino, Z. Gholamzadeh-Virany, M. Mozafari, S. Kargozar, Strontium- and Cobalt-Doped Multicomponent Mesoporous Bioactive Glasses (MBGs) for Potential Use in Bone Tissue Engineering Applications, Materials (Basel) 13(6) (2020).
[704] A.J. Leite, A.I. Goncalves, M.T. Rodrigues, M.E. Gomes, J.F. Mano, Strontium-Doped Bioactive Glass Nanoparticles in Osteogenic Commitment, ACS Appl Mater Interfaces 10(27) (2018) 23311-23320.
[705] V. Miguez-Pacheco, D. de Ligny, J. Schmidt, R. Detsch, A.R. Boccaccini, Development and characterization of niobium-releasing silicate bioactive glasses for tissue engineering applications, Journal of the European Ceramic Society 38(3) (2018) 871-876.
[706] E.D. Wang, X.F. Li, Y. Zhang, L.L. Ma, Q. Xu, Y.Z. Yue, W.Z. Wang, Q. Li, J.D. Yu, J. Chang, Multi-Functional Black Bioactive Glasses Prepared via Containerless Melting Process for Tumor Therapy and Tissue Regeneration, Advanced Functional Materials 31(24) (2021) 2101505.
[707] A. Dreanca, M. Muresan-Pop, M. Taulescu, Z.R. Toth, S. Bogdan, C. Pestean, S. Oren, C. Toma, A. Popescu, E. Pall, B. Sevastre, L. Baia, K. Magyari, Bioactive glass-biopolymersgold nanoparticle based composites for tissue engineering applications, Mater Sci Eng C Mater Biol Appl 123 (2021) 112006.
[708] Z. Lei, F.H. Li, X.H. Chen, F.M. Mo, X.J. Chen, The in vitro osteogenic and angiogenic effects of sodium-free fluoride-containing bioactive glasses, Materials Letters 248 (2019) 138-142.
[709] A.M. Deliormanlı, Electrospun cerium and gallium-containing silicate based 13-93 bioactive glass fibers for biomedical applications, Ceramics International 42(1) (2016) 897-906.
[710] Y.H. Chen, Z.F. Rao, Y.J. Liu, X.S. Liu, Y.F. Liu, L.J. Xu, Z.Q. Wang, J.Y. Guo, L. Zhang, Y.S. Dong, C.X. Qi, C. Yang, S.F. Wang, Multifunctional Injectable Hydrogel Loaded with Cerium-Containing Bioactive Glass Nanoparticles for Diabetic Wound Healing, Biomolecules 11(5) (2021) 702.
[711] B.O. Cetinkaya, G.C. Keles, B. Ayas, O. Aydin, T. Kirtiloglu, G. Acikgoz, Comparison of the proliferative activity in gingival epithelium after surgical treatments of intrabony defects with bioactive glass and bioabsorbable membrane, Clin Oral Investig 11(1) (2007) 61-8.
[712] S.R. Moosvi, R.M. Day, Bioactive glass modulation of intestinal epithelial cell restitution, Acta Biomater 5(1) (2009) 76-83.
[713] H. Hennings, D. Michael, C. Cheng, P. Steinert, K. Holbrook, S.H. Yuspa, Calcium regulation of growth and differentiation of mouse epidermal cells in culture, Cell 19(1) (1980) 245-54.
[714] D.D. Bikle, S. Pillai, Vitamin D, calcium, and epidermal differentiation, Endocr Rev 14(1) (1993) 3-19.
[715] P.M. Elias, S.K. Ahn, M. Denda, B.E. Brown, D. Crumrine, L.K. Kimutai, L. Komuves, S.H. Lee, K.R. Feingold, Modulations in epidermal calcium regulate the expression of differentiation-specific markers, J Invest Dermatol 119(5) (2002) 1128-36.
[716] C.L. Tu, Y. Oda, L. Komuves, D.D. Bikle, The role of the calcium-sensing receptor in epidermal differentiation, Cell Calcium 35(3) (2004) 265-73.

[717] G.K. Menon, K.R. Feingold, P.M. Elias, Lamellar body secretory response to barrier disruption, J Invest Dermatol 98(3) (1992) 279-89.
[718] K. Helgeland, J. Leirskar, Silicate cement in a cell culture system, Scand J Dent Res 81(3) (1973) 251-9.
[719] C.A. Vaiana, M.K. Leonard, L.F. Drummy, K.M. Singh, A. Bubulya, R.A. Vaia, R.R. Naik, M.P. Kadakia, Epidermal growth factor: layered silicate nanocomposites for tissue regeneration, Biomacromolecules 12(9) (2011) 3139-46.
[720] S.J. Wong, H.P. Wang, Colon Obstruction Caused by Diaphragmatic Hernia Following Esophagectomy, Am J Gastroenterol 111(5) (2016) 596.
[721] F. Tang, J. Li, W. Xie, Y. Mo, L. Ouyang, F. Zhao, X. Fu, X. Chen, Bioactive glass promotes the barrier functional behaviors of keratinocytes and improves the Re-epithelialization in wound healing in diabetic rats, Bioact Mater 6(10) (2021) 3496-3506.
[722] C. Zihni, C. Mills, K. Matter, M.S. Balda, Tight junctions: from simple barriers to multifunctional molecular gates, Nat Rev Mol Cell Biol 17(9) (2016) 564-80.
[723] C. Lin, C. Mao, J. Zhang, Y. Li, X. Chen, Healing effect of bioactive glass ointment on full-thickness skin wounds, Biomedical Materials 7(4) (2012) 045017.
[724] T. Zhou, B. Sui, X. Mo, J. Sun, Multifunctional and biomimetic fish collagen/bioactive glass nanofibers: fabrication, antibacterial activity and inducing skin regeneration in vitro and in vivo, Int J Nanomedicine 12 (2017) 3495-3507.
[725] W. Gao, W. Jin, Y. Li, L. Wan, C. Wang, C. Lin, X. Chen, B. Lei, C. Mao, A highly bioactive bone extracellular matrix-biomimetic nanofibrous system with rapid angiogenesis promotes diabetic wound healing, J Mater Chem B 5(35) (2017) 7285-7296.
[726] L. Zhou, Y.W. Xi, Y.M. Xue, M. Wang, Y.L. Liu, Y. Guo, B. Lei, Injectable Self-Healing Antibacterial Bioactive Polypeptide-Based Hybrid Nanosystems for Efficiently Treating Multidrug Resistant Infection, Skin-Tumor Therapy, and Enhancing Wound Healing, Advanced Functional Materials 29(22) (2019).
[727] L. Yao, H. Gao, Z. Lin, Q. Dai, S. Zhu, S. Li, C. Liu, Q. Feng, Q. Li, G. Wang, A shape memory and antibacterial cryogel with rapid hemostasis for noncompressible hemorrhage and wound healing, Chemical Engineering Journal (2021) 131005.
[728] N. Chebassier, H. Ouijja el, I. Viegas, B. Dreno, Stimulatory effect of boron and manganese salts on keratinocyte migration, Acta Derm Venereol 84(3) (2004) 191-4.
[729] I. Tenaud, S. Leroy, N. Chebassier, B. Dreno, Zinc, copper and manganese enhanced keratinocyte migration through a functional modulation of keratinocyte integrins, Experimental dermatology 9(6) (2000) 407-416.
[730] Y.A. Kang, H.R. Choi, J.I. Na, C.H. Huh, M.J. Kim, S.W. Youn, K.H. Kim, K.C. Park, Copper-GHK increases integrin expression and p63 positivity by keratinocytes, Arch Dermatol Res 301(4) (2009) 301-6.
[731] S. Frank, H. Kampfer, M. Podda, R. Kaufmann, J. Pfeilschifter, Identification of copper/zinc superoxide dismutase as a nitric oxide-regulated gene in human (HaCaT) keratinocytes: implications for keratinocyte proliferation, Biochemical Journal 346(3) (2000) 719-728.
[732] J.Q. Yang, S. Li, F.E. Domann, G.R. Buettner, L.W. Oberley, Superoxide generation in v-Ha-ras-transduced human keratinocyte HaCaT cells, Mol Carcinog 26(3) (1999) 180-8.

[733] H. Sasaki, H. Akamatsu, T. Horio, Protective role of copper, zinc superoxide dismutase against UVB-induced injury of the human keratinocyte cell line HaCaT, J Invest Dermatol 114(3) (2000) 502-7.
[734] C.-Y. Tsai, J.C. Finley, S.S. Ali, H.H. Patel, S.B. Howell, Copper influx transporter 1 is required for FGF, PDGF and EGF-induced MAPK signaling, Biochemical pharmacology 84(8) (2012) 1007-1013.
[735] Y. Li, T. Xu, Z. Tu, W. Dai, Y. Xue, C. Tang, W. Gao, C. Mao, B. Lei, C. Lin, Bioactive antibacterial silica-based nanocomposites hydrogel scaffolds with high angiogenesis for promoting diabetic wound healing and skin repair, Theranostics 10(11) (2020) 4929-4943.
[736] H. Hu, Y. Tang, L. Pang, C. Lin, W. Huang, D. Wang, W. Jia, Angiogenesis and Full-Thickness Wound Healing Efficiency of a Copper-Doped Borate Bioactive Glass/Poly(lactic- co-glycolic acid) Dressing Loaded with Vitamin E in Vivo and in Vitro, ACS Appl Mater Interfaces 10(27) (2018) 22939-22950.
[737] I. Tenaud, I. Sainte-Marie, O. Jumbou, P. Litoux, B. Dreno, In vitro modulation of keratinocyte wound healing integrins by zinc, copper and manganese, Br J Dermatol 140(1) (1999) 26-34.
[738] B.H. Bin, J. Bhin, M. Takaishi, K.E. Toyoshima, S. Kawamata, K. Ito, T. Hara, T. Watanabe, T. Irie, T. Takagishi, S.H. Lee, H.S. Jung, S. Rho, J. Seo, D.H. Choi, D. Hwang, H. Koseki, O. Ohara, S. Sano, T. Tsuji, K. Mishima, T. Fukada, Requirement of zinc transporter ZIP10 for epidermal development: Implication of the ZIP10-p63 axis in epithelial homeostasis, Proc Natl Acad Sci U S A 114(46) (2017) 12243-12248.
[739] Y. Inoue, S. Hasegawa, S. Ban, T. Yamada, Y. Date, H. Mizutani, S. Nakata, M. Tanaka, N. Hirashima, ZIP2 Protein, a Zinc Transporter, Is Associated with Keratinocyte Differentiation, Journal of Biological Chemistry 289(31) (2014) 21451-21462.
[740] A. Ali, B.N. Singh, S.K. Hira, S.P. Singh, R. Pyare, ZnO modified 1393 bioactive scaffolds with enhanced cytocompatibility and mechanical performance, Ceramics International 46(5) (2020) 6703-6713.
[741] K. Magyari, Z. Pap, Z.R. Toth, Z. Kasa, E. Licarete, D.C. Vodnar, K. Hernadi, L. Baia, The impact of copper oxide nanoparticles on the structure and applicability of bioactive glasses, Journal of Sol-Gel Science and Technology 91(3) (2019) 634-643.
[742] P. Tarnow, M. Agren, H. Steenfos, J.O. Jansson, Topical zinc oxide treatment increases endogenous gene expression of insulin-like growth factor-1 in granulation tissue from porcine wounds, Scand J Plast Reconstr Surg Hand Surg 28(4) (1994) 255-9.
[743] W.B. Ma, X.Y. Yang, L. Ma, X.G. Wang, L. Zhang, G.J. Yang, C.M. Han, Z.R. Gou, Fabrication of bioactive glass-introduced nanofibrous membranes with multifunctions for potential wound dressing, Rsc Advances 4(104) (2014) 60114-60122.
[744] S. Naseri, G. Griffanti, W.C. Lepry, V.B. Maisuria, N. Tufenkji, S.N. Nazhat, Silver-doped sol-gel borate glasses: Dose-dependent effect on Pseudomonas aeruginosa biofilms and keratinocyte function, Journal of the American Ceramic Society (2021).
[745] S.I. Jinga, C.C. Costea, A.I. Zamfirescu, A. Banciu, D.D. Banciu, C. Busuioc, Composite Fiber Networks Based on Polycaprolactone and Bioactive Glass-Ceramics for Tissue Engineering Applications, Polymers (Basel) 12(8) (2020) 1806.

[746] S. Chen, D. Galuskova, H. Kankova, K. Zheng, M. Michalek, L. Liverani, D. Galusek, A.R. Boccaccini, Electrospun PCL Fiber Mats Incorporating Multi-Targeted B and Co Co-Doped Bioactive Glass Nanoparticles for Angiogenesis, Materials (Basel) 13(18) (2020) 4010.
[747] R. Sergi, D. Bellucci, V. Cannillo, A Comprehensive Review of Bioactive Glass Coatings: State of the Art, Challenges and Future Perspectives, Coatings 10(8) (2020) 757.
[748] L. Kong, Z. Wu, H. Zhao, H. Cui, J. Shen, J. Chang, H. Li, Y. He, Bioactive Injectable Hydrogels Containing Desferrioxamine and Bioglass for Diabetic Wound Healing, ACS Appl Mater Interfaces 10(36) (2018) 30103-30114.
[749] Y. Hu, B. Wu, Y. Xiong, R. Tao, A.C. Panayi, L. Chen, W. Tian, H. Xue, L. Shi, X. Zhang, Cryogenic 3D Printed Hydrogel Scaffolds Loading Exosomes Accelerate Diabetic Wound Healing, Chemical Engineering Journal (2021) 130634.
[750] P. Valerio, M.M. Pereira, A.M. Goes, M.F. Leite, The effect of ionic products from bioactive glass dissolution on osteoblast proliferation and collagen production, Biomaterials 25(15) (2004) 2941-8.
[751] M.M. Azevedo, O. Tsigkou, R. Nair, J.R. Jones, G. Jell, M.M. Stevens, Hypoxia inducible factor-stabilizing bioactive glasses for directing mesenchymal stem cell behavior, Tissue Eng Part A 21(1-2) (2015) 382-9.
[752] C. Wu, R. Miron, A. Sculean, S. Kaskel, T. Doert, R. Schulze, Y. Zhang, Proliferation, differentiation and gene expression of osteoblasts in boron-containing associated with dexamethasone deliver from mesoporous bioactive glass scaffolds, Biomaterials 32(29) (2011) 7068-78.
[753] J.R. Jones, O. Tsigkou, E.E. Coates, M.M. Stevens, J.M. Polak, L.L. Hench, Extracellular matrix formation and mineralization on a phosphate-free porous bioactive glass scaffold using primary human osteoblast (HOB) cells, Biomaterials 28(9) (2007) 1653-63.
[754] P. Naruphontjirakul, O. Tsigkou, S.W. Li, A.E. Porter, J.R. Jones, Human mesenchymal stem cells differentiate into an osteogenic lineage in presence of strontium containing bioactive glass nanoparticles, Acta Biomater 90 (2019) 373-392.
[755] P. Naruphontjirakul, A.E. Porter, J.R. Jones, In vitro osteogenesis by intracellular uptake of strontium containing bioactive glass nanoparticles, Acta Biomater 66 (2018) 67-80.
[756] K. Gunhan, S. Bariskan, U. Uz, S. Vatansever, M. Kivanc, 13-93B3 Bioactive Glass: a New Scaffold for Transplantation of Stem Cell-Derived Chondrocytes, J Craniofac Surg 29(1) (2018) 233-236.
[757] S. Li, A.L.B. Macon, M. Jacquemin, M.M. Stevens, J.R. Jones, Sol-gel derived lithium-releasing glass for cartilage regeneration, J Biomater Appl 32(1) (2017) 104-113.
[758] W. Xie, X. Chen, G. Miao, J. Tang, X. Fu, Regulation of cellular behaviors of fibroblasts related to wound healing by sol-gel derived bioactive glass particles, J Biomed Mater Res A 104(10) (2016) 2420-9.
[759] M. Laczka, K. Cholewa-Kowalska, A. Laczka-Osyczka, M. Tworzydlo, B. Turyna, Gel-derived materials of a CaO-P2O5-SiO2 system modified by boron, sodium, magnesium, aluminum, and fluorine compounds, Journal of Biomedical Materials Research 52(4) (2000) 601-612.
[760] L. Bi, S. Jung, D. Day, K. Neidig, V. Dusevich, D. Eick, L. Bonewald, Evaluation of bone regeneration, angiogenesis, and hydroxyapatite conversion in critical-sized rat calvarial defects implanted with bioactive glass scaffolds, J Biomed Mater Res A 100(12) (2012) 3267-75.

[761] T.E. Henson, J. Navratilova, A.H. Tennant, K.D. Bradham, K.R. Rogers, M.F. Hughes, In vitro intestinal toxicity of copper oxide nanoparticles in rat and human cell models, Nanotoxicology 13(6) (2019) 795-811.
[762] S. Zhao, H. Wang, Y. Zhang, W. Huang, M.N. Rahaman, Z. Liu, D. Wang, C. Zhang, Copper-doped borosilicate bioactive glass scaffolds with improved angiogenic and osteogenic capacity for repairing osseous defects, Acta Biomater 14 (2015) 185-96.
[763] E.D. Harris, J.K. Rayton, J.E. Balthrop, R.A. DiSilvestro, M. Garcia-de-Quevedo, Copper and the synthesis of elastin and collagen, Ciba Foundation Symposium, 1980, pp. 163-182.
[764] R.B. Rucker, H.E. Parker, J.C. Rogler, The effects of copper on collagen cross-linking, Biochem Biophys Res Commun 34(1) (1969) 28-33.
[765] W. Opsahl, H. Zeronian, M. Ellison, D. Lewis, R.B. Rucker, R.S. Riggins, Role of copper in collagen cross-linking and its influence on selected mechanical properties of chick bone and tendon, J Nutr 112(4) (1982) 708-16.
[766] R.B. Rucker, H.E. Parker, J.C. Rogler, Effect of copper deficiency on chick bone collagen and selected bone enzymes, J Nutr 98(1) (1969) 57-63.
[767] Z. Ahmed, B.D. Idowu, R.A. Brown, Stabilization of fibronectin mats with micromolar concentrations of copper, Biomaterials 20(3) (1999) 201-9.
[768] Z. Ahmed, A. Briden, S. Hall, R.A. Brown, Stabilisation of cables of fibronectin with micromolar concentrations of copper: in vitro cell substrate properties, Biomaterials 25(5) (2004) 803-12.
[769] M. Graille, M. Pagano, T. Rose, M.R. Ravaux, H. van Tilbeurgh, Zinc induces structural reorganization of gelatin binding domain from human fibronectin and affects collagen binding, Structure 18(6) (2010) 710-8.
[770] R. Osorio, M. Yamauti, E. Osorio, M.E. Ruiz-Requena, D.H. Pashley, F.R. Tay, M. Toledano, Zinc reduces collagen degradation in demineralized human dentin explants, J Dent 39(2) (2011) 148-53.
[771] M. Yamaguchi, H. Oishi, Y. Suketa, Stimulatory effect of zinc on bone formation in tissue culture, Biochem Pharmacol 36(22) (1987) 4007-12.
[772] E.H. Alcantara, R.A.R. Lomeda, J. Feldmann, G.F. Nixon, J.H. Beattie, I.S. Kwun, Zinc deprivation inhibits extracellular matrix calcification through decreased synthesis of matrix proteins in osteoblasts, Molecular Nutrition & Food Research 55(10) (2011) 1552-1560.
[773] B.C. Starcher, C.H. Hill, J.G. Madaras, Effect of zinc deficiency on bone collagenase and collagen turnover, J Nutr 110(10) (1980) 2095-102.
[774] M.J. Schoeninger, Trophic level effects on 15N/14N and 13C/12C ratios in bone collagen and strontium levels in bone mineral, Journal of human evolution 14(5) (1985) 515-525.
[775] M. Quade, M. Schumacher, A. Bernhardt, A. Lode, M. Kampschulte, A. Voss, P. Simon, O. Uckermann, M. Kirsch, M. Gelinsky, Strontium-modification of porous scaffolds from mineralized collagen for potential use in bone defect therapy, Materials Science & Engineering C-Materials for Biological Applications 84 (2018) 159-167.
[776] J. Zhang, S. Zhao, Y. Zhu, Y. Huang, M. Zhu, C. Tao, C. Zhang, Three-dimensional printing of strontium-containing mesoporous bioactive glass scaffolds for bone regeneration, Acta Biomater 10(5) (2014) 2269-81.

[777] S. Fiorilli, G. Molino, C. Pontremoli, G. Iviglia, E. Torre, C. Cassinelli, M. Morra, C. Vitale-Brovarone, The Incorporation of Strontium to Improve Bone-Regeneration Ability of Mesoporous Bioactive Glasses, Materials (Basel) 11(5) (2018) 678.
[778] M. Bellantone, H.D. Williams, L.L. Hench, Broad-spectrum bactericidal activity of Ag(2)O-doped bioactive glass, Antimicrob Agents Chemother 46(6) (2002) 1940-5.
[779] M. Bellantone, N.J. Coleman, L.L. Hench, Silver-containing, sol/gel derived bioglass compositions, Google Patents, 2002.
[780] G.F. Hu, Copper stimulates proliferation of human endothelial cells under culture, J Cell Biochem 69(3) (1998) 326-35.
[781] A. Thit, H. Selck, H.F. Bjerregaard, Toxicity of CuO nanoparticles and Cu ions to tight epithelial cells from Xenopus laevis (A6): effects on proliferation, cell cycle progression and cell death, Toxicol In Vitro 27(5) (2013) 1596-601.
[782] M. Gren, U. Mirastschijski, The release of zinc ions from and cytocompatibility of two zinc oxide dressings, Journal of wound care 13(9) (2004) 367-369.
[783] G. Paasche, P. Ceschi, M. Lobler, C. Rosl, P. Gomes, A. Hahn, H.W. Rohm, K. Sternberg, T. Lenarz, K.P. Schmitz, S. Barcikowski, T. Stover, Effects of metal ions on fibroblasts and spiral ganglion cells, J Neurosci Res 89(4) (2011) 611-7.
[784] J. Wu, K. Zheng, X. Huang, J. Liu, H. Liu, A.R. Boccaccini, Y. Wan, X. Guo, Z. Shao, Thermally triggered injectable chitosan/silk fibroin/bioactive glass nanoparticle hydrogels for in-situ bone formation in rat calvarial bone defects, Acta Biomater 91 (2019) 60-71.
[785] F. Bao, G. Pei, Z.C. Wu, H. Zhuang, Z.W.B. Zhang, Z.G. Huan, C.T. Wu, J. Chang, Bioactive Self-Pumping Composite Wound Dressings with Micropore Array Modified Janus Membrane for Enhanced Diabetic Wound Healing, Advanced Functional Materials 30(49) (2020) 2005422.
[786] L.L. Sheng, Z.W.B. Zhang, Y. Zhang, E.D. Wang, B. Ma, Q. Xu, L.L. Ma, M. Zhang, G. Pei, J. Chang, A novel "hot spring"-mimetic hydrogel with excellent angiogenic properties for chronic wound healing, Biomaterials 264 (2021) 120414.
[787] R. An, Y. Zhang, Y. Qiao, L. Song, H. Wang, X. Dong, Adipose stem cells isolated from diabetic mice improve cutaneous wound healing in streptozotocin-induced diabetic mice, Stem cell research & therapy 11(1) (2020) 1-11.
[788] A.J.F. King, The use of animal models in diabetes research, British Journal of Pharmacology 166(3) (2012) 877-894.
[789] A. Al-Awar, K. Kupai, M. Veszelka, G. Szucs, Z. Attieh, Z. Murlasits, S. Torok, A. Posa, C. Varga, Experimental Diabetes Mellitus in Different Animal Models, J Diabetes Res 2016 (2016) 9051426.
[790] T. Szkudelski, The mechanism of alloxan and streptozotocin action in B cells of the rat pancreas, Physiol Res 50(6) (2001) 537-46.
[791] L.G. Jin, H.X. Cheng, X.P. Xie, X.Y. Chen, G.Q. Tian, Z.L. Zhu, S.H. Wang, H.B. Xin, X.L. Wang, Dual-Effective Chronic Wounds Management System through a Monoglyceride Binary Blend Matrix Based Thermal-Responsive Phase-Transition Substrate, Advanced Healthcare Materials 10(8) (2021) 2001966.
[792] K. Srinivasan, P. Ramarao, Animal models in type 2 diabetes research: An overview, Indian Journal of Medical Research 125(3) (2007) 451-472.

[793] H. Zhao, J. Huang, Y. Li, X. Lv, H. Zhou, H. Wang, Y. Xu, C. Wang, J. Wang, Z. Liu, ROS-scavenging hydrogel to promote healing of bacteria infected diabetic wounds, Biomaterials 258 (2020) 120286.
[794] R.D. Lovchik, D. Taylor, G. Kaigala, Rapid micro-immunohistochemistry, Microsystems & nanoengineering 6(1) (2020) 1-10.
[795] B. Hennig, M. Toborek, C.J. McClain, Antiatherogenic properties of zinc: implications in endothelial cell metabolism, Nutrition 12(10) (1996) 711-717.
[796] B. Hennig, P. Meerarani, M. Toborek, C.J. McClain, Antioxidant-like properties of zinc in activated endothelial cells, Journal of the American College of Nutrition 18(2) (1999) 152-158.
[797] P.M. Plonka, B. Handjiski, M. Popik, D. Michalczyk, R. Paus, Zinc as an ambivalent but potent modulator of murine hair growth in vivo–preliminary observations, Experimental dermatology 14(11) (2005) 844-853.
[798] R.A. Wallace, Z. Misulovin, The role of zinc and follicle cells in insulin-initiated meiotic maturation of Xenopus laevis oocytes, Science 210(4472) (1980) 928-929.
[799] D. Li, Y. Xia, Electrospinning of Nanofibers: Reinventing the Wheel?, Advanced Materials 16(14) (2004) 1151-1170.
[800] X.-X. He, J. Zheng, G.-F. Yu, M.-H. You, M. Yu, X. Ning, Y.-Z. Long, Near-field electrospinning: progress and applications, The Journal of Physical Chemistry C 121(16) (2017) 8663-8678.
[801] D. Sun, C. Chang, S. Li, L. Lin, Near-field electrospinning, Nano letters 6(4) (2006) 839-842.
[802] A.L.B. Macon, S.H. Lee, G. Poologasundarampillai, T. Kasuga, J.R. Jones, Synthesis and dissolution behaviour of CaO/SrO-containing sol-gel-derived 58S glasses, Journal of Materials Science 52(15) (2017) 8858-8870.
[803] X. Li, H. Yang, H. Huang, T. Zhu, CELLCOUNTER: novel open-source software for counting cell migration and invasion in vitro, Biomed Res Int 2014 (2014) 863564.
[804] A.C. Mohan, B. Renjanadevi, Preparation of Zinc Oxide Nanoparticles and its Characterization Using Scanning Electron Microscopy (SEM) and X-Ray Diffraction(XRD), International Conference on Emerging Trends in Engineering, Science and Technology (Icetest - 2015) 24 (2016) 761-766.
[805] C. Heras, J. Jimenez-Holguin, A.L. Doadrio, M. Vallet-Regi, S. Sanchez-Salcedo, A.J. Salinas, Multifunctional antibiotic- and zinc-containing mesoporous bioactive glass scaffolds to fight bone infection, Acta Biomaterialia 114 (2020) 395-406.
[806] C. Heras, S. Sanchez-Salcedo, D. Lozano, J. Pena, P. Esbrit, M. Vallet-Regi, A.J. Salinas, Osteostatin potentiates the bioactivity of mesoporous glass scaffolds containing Zn(2+) ions in human mesenchymal stem cells, Acta Biomater 89 (2019) 359-371.
[807] Z. Nescakova, K. Zheng, L. Liverani, Q. Nawaz, D. Galuskova, H. Kankova, M. Michalek, D. Galusek, A.R. Boccaccini, Multifunctional zinc ion doped sol - gel derived mesoporous bioactive glass nanoparticles for biomedical applications, Bioact Mater 4 (2019) 312-321.
[808] K. Zheng, X. Dai, M. Lu, N. Huser, N. Taccardi, A.R. Boccaccini, Synthesis of copper-containing bioactive glass nanoparticles using a modified Stober method for biomedical applications, Colloids Surf B Biointerfaces 150 (2017) 159-167.
[809] M.M. Babu, P.V. Rao, R.K. Singh, H.-W. Kim, N. Veeraiah, M. Özcan, P.S. Prasad, ZnO incorporated high phosphate bioactive glasses for guided bone regeneration implants:

enhancement of in vitro bioactivity and antibacterial activity, Journal of Materials Research and Technology 15 (2021) 633-646.
[810] L.S. Connell, F. Romer, M. Suarez, E.M. Valliant, Z. Zhang, P.D. Lee, M.E. Smith, J.V. Hanna, J.R. Jones, Chemical characterisation and fabrication of chitosan-silica hybrid scaffolds with 3-glycidoxypropyl trimethoxysilane, J Mater Chem B 2(6) (2014) 668-680.
[811] M.F. Kulesz-Martin, D. Fabian, J.S. Bertram, Differential calcium requirements for growth of mouse skin epithelial and fibroblast cells, Cell Tissue Kinet 17(5) (1984) 525-33.
[812] E.M. Carlisle, Silicon: a requirement in bone formation independent of vitamin D1, Calcif Tissue Int 33(1) (1981) 27-34.
[813] E.M. Carlisle, Silicon: a possible factor in bone calcification, Science 167(3916) (1970) 279-80.
[814] S. Quignard, T. Coradin, J.J. Powell, R. Jugdaohsingh, Silica nanoparticles as sources of silicic acid favoring wound healing in vitro, Colloids Surf B Biointerfaces 155 (2017) 530-537.
[815] F. Monte, T. Cebe, D. Ripperger, F. Ighani, H.V. Kojouharov, B.M. Chen, H.K.W. Kim, P.B. Aswath, V.G. Varanasi, Ionic silicon improves endothelial cells' survival under toxic oxidative stress by overexpressing angiogenic markers and antioxidant enzymes, J Tissue Eng Regen Med 12(11) (2018) 2203-2220.
[816] N.L. Allbritton, C.R. Verret, R.C. Wolley, H.N. Eisen, Calcium ion concentrations and DNA fragmentation in target cell destruction by murine cloned cytotoxic T lymphocytes, J Exp Med 167(2) (1988) 514-27.
[817] A.M. Al-Ani, A.G. Messenger, J. Lawry, S.S. Bleehen, S. MacNeil, Calcium/calmodulin regulation of the proliferation of human epidermal keratinocytes, dermal fibroblasts and mouse B16 melanoma cells in culture, Br J Dermatol 119(3) (1988) 295-306.
[818] M.H. Gail, C.W. Boone, C.S. Thompson, A calcium requirement for fibroblast motility and prolifertion, Exp Cell Res 79(2) (1973) 386-90.
[819] B. Rokosova, J.P. Bentley, Effect of calcium on cell proliferation and extracellular matrix synthesis in arterial smooth muscle cells and dermal fibroblasts, Exp Mol Pathol 44(3) (1986) 307-17.
[820] H. Fujisaki, S. Futaki, M. Yamada, K. Sekiguchi, T. Hayashi, T. Ikejima, S. Hattori, Respective optimal calcium concentrations for proliferation on type I collagen fibrils in two keratinocyte line cells, HaCaT and FEPE1L-8, Regen Ther 8 (2018) 73-79.
[821] Y.-C. Huang, T.-W. Wang, J.-S. Sun, F.-H. Lin, Effect of Calcium Ion Concentration on Keratinocyte Behaviors in the Defined Media, Biomedical Engineering: Applications, Basis and Communications 18(01) (2012) 37-41.
[822] S. Garg, S. Thakur, A. Gupta, G. Kaur, O.P. Pandey, Antibacterial and anticancerous drug loading kinetics for (10-x)CuO-xZnO-20CaO-60SiO2-10P2O5 (2 </= x </= 8) mesoporous bioactive glasses, J Mater Sci Mater Med 28(1) (2017) 11.
[823] D. Zamani, F. Moztarzadeh, D. Bizari, Alginate-bioactive glass containing Zn and Mg composite scaffolds for bone tissue engineering, International journal of biological macromolecules 137 (2019) 1256-1267.
[824] N. Azizabadi, P.A. Azar, M.S. Tehrani, P. Derakhshi, Synthesis and characteristics of gel-derived SiO2-CaO-P2O5-SrO-Ag2O-ZnO bioactive glass: Bioactivity, biocompatibility, and antibacterial properties, Journal of Non-Crystalline Solids 556 (2021) 120568.

[825] M.-J. Lee, Y.-B. Seo, J.-Y. Seo, J.-H. Ryu, H.-J. Ahn, K.-M. Kim, J.-S. Kwon, S.-H. Choi, Development of a bioactive flowable resin composite containing a zinc-doped phosphate-based glass, Nanomaterials 10(11) (2020) 2311.
[826] F. Tsai, L. Wang, M. Chen, M. Lee, Y. Lin, C. Wang, Induction of Cell Proliferation and Cell Death in Human Follicle Dermal Papilla Cells by Zinc Chloride, Indian Journal of Pharmaceutical Sciences 81(4) (2019) 781-785.
[827] S. Ng, R. Karunanithy, W. Edirisinghe, A. Roy, P. Wong, S. Ratnam, Human follicular fluid levels of calcium, copper and zinc, Gynecologic and obstetric investigation 23(2) (1987) 129-132.
[828] B. Han, W.H. Fang, S. Zhao, Z. Yang, B.X. Hoang, Zinc sulfide nanoparticles improve skin regeneration, Nanomedicine: Nanotechnology, Biology and Medicine 29 (2020) 102263.
[829] N. Oliva, B.D. Almquist, Spatiotemporal delivery of bioactive molecules for wound healing using stimuli-responsive biomaterials, Advanced Drug Delivery Reviews 161 (2020) 22-41.
[830] S.L. Percival, S. McCarty, J.A. Hunt, E.J. Woods, The effects of pH on wound healing, biofilms, and antimicrobial efficacy, Wound Repair and Regeneration 22(2) (2014) 174-186.
[831] S. Maeno, Y. Niki, H. Matsumoto, H. Morioka, T. Yatabe, A. Funayama, Y. Toyama, T. Taguchi, J. Tanaka, The effect of calcium ion concentration on osteoblast viability, proliferation and differentiation in monolayer and 3D culture, Biomaterials 26(23) (2005) 4847-55.
[832] M.A. Bumke, D. Neri, G. Elia, Modulation of gene expression by extracellular pH variations in human fibroblasts: a transcriptomic and proteomic study, Proteomics 3(5) (2003) 675-88.
[833] M. Gioia, G.F. Fasciglione, S. Monaco, R. Iundusi, D. Sbardella, S. Marini, U. Tarantino, M. Coletta, pH dependence of the enzymatic processing of collagen I by MMP-1 (fibroblast collagenase), MMP-2 (gelatinase A), and MMP-14 ectodomain, J Biol Inorg Chem 15(8) (2010) 1219-32.
[834] G. Park, D.S. Oh, Y.U. Kim, M.K. Park, Acceleration of Collagen Breakdown by Extracellular Basic pH in Human Dermal Fibroblasts, Skin Pharmacol Physiol 29(4) (2016) 204-9.
[835] Y. Zhou, H. Li, K. Lin, W. Zhai, W. Gu, J. Chang, Effect of heat treatment on the properties of SiO2-CaO-MgO-P 2O 5 bioactive glasses, J Mater Sci Mater Med 23(9) (2012) 2101-8.
[836] H.C. Bae, H.J. Ryu, S.H. Jeong, E.Y. Lee, Y.-H. Park, K.G. Lee, B.H. Choi, E.H. Maeng, M.-K. Kim, S.W. Son, Oxidative stress and apoptosis induced by ZnO nanoparticles in HaCaT cells, Molecular & Cellular Toxicology 7(4) (2012) 333-337.
[837] J.S. Huang, J.J. Mukherjee, Z. Kiss, Ethanol potentiates the mitogenic effects of sphingosine 1-phosphate by a zinc- and calcium-dependent mechanism in fibroblasts, Arch Biochem Biophys 366(1) (1999) 131-8.
[838] J.S. Huang, J.J. Mukherjee, T. Chung, K.S. Crilly, Z. Kiss, Extracellular calcium stimulates DNA synthesis in synergism with zinc, insulin and insulin-like growth factor I in fibroblasts, Eur J Biochem 266(3) (1999) 943-51.
[839] B.L. O'Dell, J.D. Browning, Impaired Calcium Entry into Cells Is Associated with Pathological Signs of Zinc Deficiency, Advances in Nutrition 4(3) (2013) 287-293.
[840] B.L. O'Dell, J.D. Browning, Zinc Deprivation Impairs Growth Factor-Stimulated Calcium Influx into Murine 3T3 cells Associated with Decreased Cell Proliferation, Journal of Nutrition 141(6) (2011) 1036-1040.
[841] E.J. Battegay, J. Rupp, L. Iruela-Arispe, E.H. Sage, M. Pech, PDGF-BB modulates endothelial proliferation and angiogenesis in vitro via PDGF beta-receptors, J Cell Biol 125(4) (1994) 917-28.

[842] I.F. Dunn, O. Heese, P.M. Black, Growth factors in glioma angiogenesis: FGFs, PDGF, EGF, and TGFs, J Neurooncol 50(1-2) (2000) 121-37.
[843] T. Paramasivam, S.K. Maiti, S. Palakkara, D. Mohan, H. Manjunthaachar, K. Karthik, N. Kumar, Effect of PDGF-B Gene-Activated Acellular Matrix and Mesenchymal Stem Cell Transplantation on Full Thickness Skin Burn Wound in Rat Model, Tissue Engineering and Regenerative Medicine 18(2) (2021) 235-251.
[844] M. Estacion, L. Mordan, Competence induction by PDGF requires sustained calcium influx by a mechanism distinct from storage-dependent calcium influx, Cell calcium 14(6) (1993) 439-454.
[845] R.W. Tucker, D.T. Chang, K. Meade-Cobun, Effects of platelet-derived growth factor and fibroblast growth factor on free intracellular calcium and mitogenesis, J Cell Biochem 39(2) (1989) 139-51.
[846] B.J. Faler, R.A. Macsata, D. Plummer, L. Mishra, A.N. Sidawy, Transforming growth factor-beta and wound healing, Perspect Vasc Surg Endovasc Ther 18(1) (2006) 55-62.
[847] S. O'Kane, M.W. Ferguson, Transforming growth factor βs and wound healing, The international journal of biochemistry & cell biology 29(1) (1997) 63-78.
[848] R.F. Baugh, C. Hougie, The chemistry of blood coagulation, Clin Haematol 8(1) (1979) 3-30.
[849] S. Mukherjee, M.R. Kolb, F. Duan, L.J. Janssen, Transforming growth factor-beta evokes Ca2+ waves and enhances gene expression in human pulmonary fibroblasts, Am J Respir Cell Mol Biol 46(6) (2012) 757-64.
[850] J. Yu, L. Xu, K. Li, N. Xie, Y. Xi, Y. Wang, X. Zheng, X. Chen, M. Wang, X. Ye, Zinc-modified calcium silicate coatings promote osteogenic differentiation through TGF-β/Smad pathway and osseointegration in osteopenic rabbits, Scientific reports 7(1) (2017) 1-13.
[851] J.E. Ziello, I.S. Jovin, Y. Huang, Hypoxia-Inducible Factor (HIF)-1 regulatory pathway and its potential for therapeutic intervention in malignancy and ischemia, The Yale journal of biology and medicine 80(2) (2007) 51.
[852] C.W. Pugh, P.J. Ratcliffe, Regulation of angiogenesis by hypoxia: role of the HIF system, Nat Med 9(6) (2003) 677-84.
[853] P. Carmeliet, Y. Dor, J.M. Herbert, D. Fukumura, K. Brusselmans, M. Dewerchin, M. Neeman, F. Bono, R. Abramovitch, P. Maxwell, C.J. Koch, P. Ratcliffe, L. Moons, R.K. Jain, D. Collen, E. Keshert, Role of HIF-1alpha in hypoxia-mediated apoptosis, cell proliferation and tumour angiogenesis, Nature 394(6692) (1998) 485-90.
[854] D. Mottet, G. Michel, P. Renard, N. Ninane, M. Raes, C. Michiels, Role of ERK and calcium in the hypoxia-induced activation of HIF-1, J Cell Physiol 194(1) (2003) 30-44.
[855] D. Mottet, G. Michel, P. Renard, N. Ninane, M. Raes, C. Michiels, ERK and calcium in activation of HIF-1, Ann N Y Acad Sci 973(1) (2002) 448-53.
[856] A.S. Hui, A.L. Bauer, J.B. Striet, P.O. Schnell, M.F. Czyzyk-Krzeska, Calcium signaling stimulates translation of HIF-alpha during hypoxia, FASEB J 20(3) (2006) 466-75.
[857] I. Azimi, The interplay between HIF-1 and calcium signalling in cancer, International Journal of Biochemistry & Cell Biology 97 (2018) 73-77.
[858] L. Nardinocchi, V. Pantisano, R. Puca, M. Porru, A. Aiello, A. Grasselli, C. Leonetti, M. Safran, G. Rechavi, D. Givol, A. Farsetti, G. D'Orazi, Zinc downregulates HIF-1alpha and inhibits its activity in tumor cells in vitro and in vivo, PLoS One 5(12) (2010) e15048.

[859] X.L. Zhang, D. Liang, J.Y. Fan, X. Lian, Y. Zhao, X.M. Wang, Z.H. Chi, P. Zhang, Zinc Attenuates Tubulointerstitial Fibrosis in Diabetic Nephropathy Via Inhibition of HIF Through PI-3K Signaling, Biological Trace Element Research 173(2) (2016) 372-383.
[860] Y.S. Chun, E. Choi, E.J. Yeo, J.H. Lee, M.S. Kim, J.W. Park, A new HIF-1 alpha variant induced by zinc ion suppresses HIF-1-mediated hypoxic responses, J Cell Sci 114(Pt 22) (2001) 4051-61.
[861] Y.S. Chun, E. Choi, G.T. Kim, M.J. Lee, M.J. Lee, S.E. Lee, M.S. Kim, J.W. Park, Zinc induces the accumulation of hypoxia-inducible factor (HIF)-1alpha, but inhibits the nuclear translocation of HIF-1beta, causing HIF-1 inactivation, Biochem Biophys Res Commun 268(2) (2000) 652-6.
[862] H.F. Dvorak, L.F. Brown, M. Detmar, A.M. Dvorak, Vascular permeability factor/vascular endothelial growth factor, microvascular hyperpermeability, and angiogenesis, The American journal of pathology 146(5) (1995) 1029.
[863] H. Dvorak, J. Nagy, D. Feng, L. Brown, A. Dvorak, Vascular permeability factor/vascular endothelial growth factor and the significance of microvascular hyperpermeability in angiogenesis, Vascular Growth Factors and Angiogenesis (1999) 97-132.
[864] M. Clauss, M. Gerlach, H. Gerlach, J. Brett, F. Wang, P. Familletti, Y. Pan, J. Olander, D. Connolly, D. Stern, Vascular permeability factor: a tumor-derived polypeptide that induces endothelial cell and monocyte procoagulant activity, and promotes monocyte migration, The Journal of experimental medicine 172(6) (1990) 1535-1545.
[865] H.E. Broxmeyer, S. Cooper, Z. Li, L. Lu, H. Song, B. Kwon, R.E. Warren, D.B. Donner, Myeloid progenitor cell regulatory effects of vascular endothelial cell growth factor, International journal of hematology 62(4) (1995) 203-215.
[866] Y. Yu, G. Jin, Y. Xue, D. Wang, X. Liu, J. Sun, Multifunctions of dual Zn/Mg ion co-implanted titanium on osteogenesis, angiogenesis and bacteria inhibition for dental implants, Acta Biomater 49 (2017) 590-603.
[867] D.B. Rifkin, D. Moscatelli, Recent developments in the cell biology of basic fibroblast growth factor, The Journal of cell biology 109(1) (1989) 1-6.
[868] M. Przybylski, A review of the current research on the role of bFGF and VEGF in angiogenesis, Journal of wound care 18(12) (2009) 516-519.
[869] H.-X. Shi, C. Lin, B.-B. Lin, Z.-G. Wang, H.-Y. Zhang, F.-Z. Wu, Y. Cheng, L.-J. Xiang, D.-J. Guo, X. Luo, The anti-scar effects of basic fibroblast growth factor on the wound repair in vitro and in vivo, PloS one 8(4) (2013) e59966.
[870] I. Ono, Y. Akasaka, R. Kikuchi, A. Sakemoto, T. Kamiya, T. Yamashita, K. Jimbow, Basic fibroblast growth factor reduces scar formation in acute incisional wounds, Wound Repair and Regeneration 15(5) (2007) 617-623.
[871] S. Akita, K. Akino, T. Imaizumi, A. Hirano, Basic fibroblast growth factor accelerates and improves second-degree burn wound healing, Wound repair and regeneration 16(5) (2008) 635-641.
[872] T. Kaji, Y. Fujiwara, C. Yamamoto, M. Sakamoto, H. Kozuka, Stimulation by zinc of cultured vascular endothelial cell proliferation: possible involvement of endogenous basic fibroblast growth factor, Life sciences 55(23) (1994) 1781-1787.
[873] S. Midha, W. van den Bergh, T.B. Kim, P.D. Lee, J.R. Jones, C.A. Mitchell, Bioactive glass foam scaffolds are remodelled by osteoclasts and support the formation of mineralized matrix and vascular networks in vitro, Adv Healthc Mater 2(3) (2013) 490-9.

[874] L. Lamalice, F. Le Boeuf, J. Huot, Endothelial cell migration during angiogenesis, Circ Res 100(6) (2007) 782-94.
[875] T.V. Byzova, C.K. Goldman, N. Pampori, K.A. Thomas, A. Bett, S.J. Shattil, E.F. Plow, A mechanism for modulation of cellular responses to VEGF: activation of the integrins, Mol Cell 6(4) (2000) 851-60.
[876] U.R. Michaelis, Mechanisms of endothelial cell migration, Cell Mol Life Sci 71(21) (2014) 4131-48.
[877] Q.K. Tran, K. Ohashi, H. Watanabe, Calcium signalling in endothelial cells, Cardiovasc Res 48(1) (2000) 13-22.
[878] C. Tiruppathi, R.D. Minshall, B.C. Paria, S.M. Vogel, A.B. Malik, Role of Ca2+ signaling in the regulation of endothelial permeability, Vascul Pharmacol 39(4-5) (2002) 173-85.
[879] S.M. Dudek, J.G. Garcia, Cytoskeletal regulation of pulmonary vascular permeability, J Appl Physiol (1985) 91(4) (2001) 1487-500.
[880] A. Filippini, A. D'Amore, A. D'Alessio, Calcium Mobilization in Endothelial Cell Functions, Int J Mol Sci 20(18) (2019) 4525.
[881] J.E. Fish, P.A. Marsden, Endothelial nitric oxide synthase: insight into cell-specific gene regulation in the vascular endothelium, Cellular and Molecular Life Sciences 63(2) (2006) 144-162.
[882] T. Murohara, B. Witzenbichler, I. Spyridopoulos, T. Asahara, B. Ding, A. Sullivan, D.W. Losordo, J.M. Isner, Role of endothelial nitric oxide synthase in endothelial cell migration, Arterioscler Thromb Vasc Biol 19(5) (1999) 1156-61.
[883] G. Garcia-Cardena, R. Fan, V. Shah, R. Sorrentino, G. Cirino, A. Papapetropoulos, W.C. Sessa, Dynamic activation of endothelial nitric oxide synthase by Hsp90, Nature 392(6678) (1998) 821-4.
[884] L.J. Ignarro, G. Cirino, A. Casini, C. Napoli, Nitric oxide as a signaling molecule in the vascular system: An overview, Journal of Cardiovascular Pharmacology 34(6) (1999) 879-886.
[885] A. Brouet, P. Sonveaux, C. Dessy, J.L. Balligand, O. Feron, Hsp90 ensures the transition from the early Ca2+-dependent to the late phosphorylation-dependent activation of the endothelial nitric-oxide synthase in vascular endothelial growth factor-exposed endothelial cells, J Biol Chem 276(35) (2001) 32663-9.
[886] S. Naseri, W.C. Lepry, V.B. Maisuria, N. Tufenkji, S.N. Nazhat, Development and characterization of silver-doped sol-gel-derived borate glasses with anti-bacterial activity, Journal of Non-Crystalline Solids 505 (2019) 438-446.
[887] W.C. Lepry, S.N. Nazhat, Highly Bioactive Sol-Gel-Derived Borate Glasses, Chemistry of Materials 27(13) (2015) 4821-4831.
[888] W.C. Lepry, S. Smith, S.N. Nazhat, Effect of sodium on bioactive sol-gel-derived borate glasses, Journal of Non-Crystalline Solids 500 (2018) 141-148.
[889] Q. Nawaz, A. de Pablos-Martín, J. Martins de Souza e Silva, K. Hurle, A.T.C. Jaimes, D.S. Brauer, A.R. Boccaccini, New insights into the crystallization process of sol-gel–derived 45S5 bioactive glass, Journal of the American Ceramic Society 103(8) (2020) 4234-4247.
[890] M. Erfani, E. Saion, N. Soltani, M. Hashim, W.S.B.W. Abdullah, M. Navasery, Facile synthesis of calcium borate nanoparticles and the annealing effect on their structure and size, International journal of molecular sciences 13(11) (2012) 14434-14445.

[891] X. Li, D. Jiang, J. Zhang, Q. Lin, Z. Chen, Z. Huang, The dispersion of boron carbide powder in aqueous media, Journal of the European Ceramic Society 33(10) (2013) 1655-1663.
[892] S.-H. Lee, J. Seo, K.-S. You, S.-Y. Nam, J.-W. Ahn, Calcium Ion Extraction from Blast Furnace Slags for the Synthesis of Pure Calcium Carbonate Polymorphs by Accelerated Carbonation, 5th Asian Particle Technology Symposium, Singapore, 2012.
[893] X. Liu, M.N. Rahaman, D.E. Day, Conversion of melt-derived microfibrous borate (13-93B3) and silicate (45S5) bioactive glass in a simulated body fluid, Journal of Materials Science: Materials in Medicine 24(3) (2013) 583-595.
[894] X. Liu, M.N. Rahaman, D.E. Day, In vitro degradation and conversion of melt-derived Microfibrous borate (13-93B3) bioactive glass doped with metal ions, Journal of the American Ceramic Society 97(11) (2014) 3501-3509.
[895] T. Rao, A.R. Kumar, K. Neeraja, N. Veeraiah, M.R. Reddy, Optical and structural investigation of Eu3+ ions in Nd3+ co-doped magnesium lead borosilicate glasses, Journal of alloys and compounds 557 (2013) 209-217.
[896] G. Shao, X. Wu, Y. Kong, S. Cui, X. Shen, C. Jiao, J. Jiao, Thermal shock behavior and infrared radiation property of integrative insulations consisting of MoSi2/borosilicate glass coating and fibrous ZrO2 ceramic substrate, Surface and Coatings Technology 270 (2015) 154-163.
[897] T. Edwards, T. Endo, J.H. Walton, S. Sen, Observation of the transition state for pressure-induced BO3→ BO4 conversion in glass, Science 345(6200) (2014) 1027-1029.
[898] T. Abe, Borosilicate glasses, Journal of the American Ceramic Society 35(11) (1952) 284-299.
[899] X. Liu, W. Huang, H. Fu, A. Yao, D. Wang, H. Pan, W.W. Lu, X. Jiang, X. Zhang, Bioactive borosilicate glass scaffolds: in vitro degradation and bioactivity behaviors, Journal of Materials Science: Materials in Medicine 20(6) (2009) 1237-1243.
[900] E. Erasmus, R. Sule, O. Johnson, J. Massera, I. Sigalas, In vitro evaluation of porous borosilicate, borophosphate and phosphate bioactive glasses scaffolds fabricated using foaming agent for bone regeneration, Scientific reports 8(1) (2018) 1-13.
[901] R. Moonesi Rad, E. Pazarceviren, E. Ece Akgün, Z. Evis, D. Keskin, S. Şahin, A. Tezcaner, In vitro performance of a nanobiocomposite scaffold containing boron-modified bioactive glass nanoparticles for dentin regeneration, Journal of biomaterials applications 33(6) (2019) 834-853.
[902] H. Yin, C. Yang, Y. Gao, C. Wang, M. Li, H. Guo, Q. Tong, Fabrication and characterization of strontium-doped borate-based bioactive glass scaffolds for bone tissue engineering, Journal of Alloys and Compounds 743 (2018) 564-569.
[903] H. Wang, S.C. Zhao, J. Zhou, Y.Q. Shen, W.H. Huang, C.Q. Zhang, M.N. Rahaman, D.P. Wang, Evaluation of borate bioactive glass scaffolds as a controlled delivery system for copper ions in stimulating osteogenesis and angiogenesis in bone healing, Journal of Materials Chemistry B 2(48) (2014) 8547-8557.
[904] S.S. Hakki, B.S. Bozkurt, E.E. Hakki, Boron regulates mineralized tissue-associated proteins in osteoblasts (MC3T3-E1), J Trace Elem Med Biol 24(4) (2010) 243-50.
[905] X. Zhang, W. Jia, Y. Gu, W. Xiao, X. Liu, D. Wang, C. Zhang, W. Huang, M.N. Rahaman, D.E. Day, N. Zhou, Teicoplanin-loaded borate bioactive glass implants for treating chronic bone infection in a rabbit tibia osteomyelitis model, Biomaterials 31(22) (2010) 5865-74.
[906] W.C. Lepry, G. Griffanti, S.N. Nazhat, Bioactive sol-gel borate glasses with magnesium, Journal of Non-Crystalline Solids 581 (2022) 121415.

[907] B. Li, X. Bian, W. Hu, X. Wang, Q. Li, F. Wang, M. Sun, K. Ma, C. Zhang, J. Chang, Regenerative and protective effects of calcium silicate on senescent fibroblasts induced by high glucose, Wound Repair and Regeneration 28(3) (2020) 315-325.
[908] D.S. Steinbrech, M.T. Longaker, B.J. Mehrara, P.B. Saadeh, G.S. Chin, R.P. Gerrets, D.C. Chau, N.M. Rowe, G.K. Gittes, Fibroblast response to hypoxia: the relationship between angiogenesis and matrix regulation, Journal of surgical Research 84(2) (1999) 127-133.
[909] A. Modarressi, G. Pietramaggiori, C. Godbout, E. Vigato, B. Pittet, B. Hinz, Hypoxia impairs skin myofibroblast differentiation and function, Journal of investigative dermatology 130(12) (2010) 2818-2827.
[910] R. Goldman, Growth factors and chronic wound healing: past, present, and future, Advances in skin & wound care 17(1) (2004) 24-35.
[911] J. Lepistö, M. Laato, J. Niinikoski, C. Lundberg, B. Gerdin, C.-H. Heldin, Effects of homodimeric isoforms of platelet-derived growth factor (PDGF-AA and PDGF-BB) on wound healing in rat, Journal of Surgical Research 53(6) (1992) 596-601.
[912] G.R. Grotendorst, G. Martin, D. Pencev, J. Sodek, A. Harvey, Stimulation of granulation tissue formation by platelet-derived growth factor in normal and diabetic rats, The Journal of clinical investigation 76(6) (1985) 2323-2329.
[913] J.M. Lemons, X.-J. Feng, B.D. Bennett, A. Legesse-Miller, E.L. Johnson, I. Raitman, E.A. Pollina, H.A. Rabitz, J.D. Rabinowitz, H.A. Coller, Quiescent fibroblasts exhibit high metabolic activity, PLoS biology 8(10) (2010) e1000514.
[914] W.N. Hozzein, G. Badr, A.A. Al Ghamdi, A. Sayed, N.S. Al-Waili, O. Garraud, Topical application of propolis enhances cutaneous wound healing by promoting TGF-beta/Smad-mediated collagen production in a streptozotocin-induced type I diabetic mouse model, Cellular Physiology and Biochemistry 37(3) (2015) 940-954.
[915] F. Xu, C. Zhang, D.T. Graves, Abnormal cell responses and role of TNF-in impaired diabetic wound healing, BioMed research international 2013 (2013).
[916] H. Thangarajah, I.N. Vial, R.H. Grogan, D. Yao, Y. Shi, M. Januszyk, R.D. Galiano, E.I. Chang, M.G. Galvez, J.P. Glotzbach, HIF-1α dysfunction in diabetes, Cell cycle 9(1) (2010) 75-79.
[917] C. Tchanque-Fossuo, S. Dahle, S. Buchman, R. Rivkah Isseroff, Deferoxamine: potential novel topical therapeutic for chronic wounds, (2017).
[918] I.R. Botusan, V.G. Sunkari, O. Savu, A.I. Catrina, J. Grünler, S. Lindberg, T. Pereira, S. Ylä-Herttuala, L. Poellinger, K. Brismar, Stabilization of HIF-1α is critical to improve wound healing in diabetic mice, Proceedings of the National Academy of Sciences 105(49) (2008) 19426-19431.
[919] L. Chen, P. Gajendrareddy, L. DiPietro, Differential expression of HIF-1α in skin and mucosal wounds, Journal of dental research 91(9) (2012) 871-876.
[920] B.S. Sørensen, J. Alsner, J. Overgaard, M.R. Horsman, Hypoxia induced expression of endogenous markers in vitro is highly influenced by pH, Radiotherapy and oncology 83(3) (2007) 362-366.
[921] B.S. Sørensen, J. Hao, J. Overgaard, H. Vorum, B. Honoré, J. Alsner, M.R. Horsman, Influence of oxygen concentration and pH on expression of hypoxia induced genes, Radiotherapy and oncology 76(2) (2005) 187-193.
[922] M.S. Wietecha, L.A. DiPietro, Therapeutic approaches to the regulation of wound angiogenesis, Advances in wound care 2(3) (2013) 81-86.

[923] N.N. Nissen, P. Polverini, A.E. Koch, M.V. Volin, R.L. Gamelli, L.A. DiPietro, Vascular endothelial growth factor mediates angiogenic activity during the proliferative phase of wound healing, The American journal of pathology 152(6) (1998) 1445.
[924] T. Danielsen, E.K. Rofstad, VEGF, bFGF and EGF in the angiogenesis of human melanoma xenografts, International journal of cancer 76(6) (1998) 836-841.
[925] S. Kazemi, D. Wenzel, E. Kolossov, N. Lenka, A. Raible, P. Sasse, J. Hescheler, K. Addicks, B.K. Fleischmann, W. Bloch, Differential role of bFGF and VEGF for vasculogenesis, Cellular Physiology and Biochemistry 12(2-3) (2002) 55-62.
[926] A. Polo-Montalvo, L. Casarrubios, M.C. Serrano, A. Sanvicente, M.J. Feito, D. Arcos, M.T. Portolés, Effective Actions of Ion Release from Mesoporous Bioactive Glass and Macrophage Mediators on the Differentiation of Osteoprogenitor and Endothelial Progenitor Cells, Pharmaceutics 13(8) (2021) 1152.
[927] T. Aftab, M. Khan, M. Idrees, M. Naeem, M. Ram, Boron induced oxidative stress, antioxidant defence response and changes in artemisinin content in Artemisia annua L, Journal of Agronomy and Crop Science 196(6) (2010) 423-430.
[928] S. Li, N.F. Huang, S. Hsu, Mechanotransduction in endothelial cell migration, Journal of cellular biochemistry 96(6) (2005) 1110-1126.
[929] R.L. Klemke, S. Cai, A.L. Giannini, P.J. Gallagher, P.d. Lanerolle, D.A. Cheresh, Regulation of cell motility by mitogen-activated protein kinase, The Journal of cell biology 137(2) (1997) 481-492.
[930] Y. Lin, R.F. Brown, S.B. Jung, D.E. Day, Angiogenic effects of borate glass microfibers in a rodent model, J Biomed Mater Res A 102(12) (2014) 4491-9.
[931] C. Kalirajan, T. Palanisamy, Bioengineered Hybrid Collagen Scaffold Tethered with Silver-Catechin Nanocomposite Modulates Angiogenesis and TGF-beta Toward Scarless Healing in Chronic Deep Second Degree Infected Burns, Adv Healthc Mater 9(12) (2020) e2000247.
[932] K.R. Sindhu, N. Bansode, M. Remy, C. Morel, R. Bareille, M. Hagedorn, B. Hinz, P. Barthelemy, O. Chassande, C. Boiziau, New injectable self-assembled hydrogels that promote angiogenesis through a bioactive degradation product, Acta Biomaterialia 115 (2020) 197-209.
[933] C.Y. Tong, X.H. Zhong, Y.J. Yang, X. Liu, G.W. Zhong, C. Xiao, B. Liu, W. Wang, X.P. Yang, PB@PDA@Ag nanosystem for synergistically eradicating MRSA and accelerating diabetic wound healing assisted with laser irradiation, Biomaterials 243 (2020) 119936.
[934] T.H. Kim, M.S. Kang, N. Mandakhbayar, A. El-Fiqi, H.W. Kim, Anti-inflammatory actions of folate-functionalized bioactive ion-releasing nanoparticles imply drug-free nanotherapy of inflamed tissues, Biomaterials 207 (2019) 23-38.
[935] R. Shimizu, F. Sakazaki, T. Okuno, K. Nakamuro, H. Ueno, Difference in glucose intolerance between C57BL/6J and ICR strain mice with streptozotocin/nicotinamide-induced diabetes, Biomedical Research 33(1) (2012) 63-66.
[936] Y. Dekel, Y. Glucksam, I. Elron-Gross, R. Margalit, Insights into modeling streptozotocin-induced diabetes in ICR mice, Lab Animal 38(2) (2009) 55-60.
[937] Y. Chen, Q. Yu, C.-B. Xu, A convenient method for quantifying collagen fibers in atherosclerotic lesions by ImageJ software, Int J Clin Exp Med 10(10) (2017) 14904-14910.
[938] V. Falanga, Wound healing and its impairment in the diabetic foot, Lancet 366(9498) (2005) 1736-43.

[939] W.J. Jeffcoate, K.G. Harding, Diabetic foot ulcers, Lancet 361(9368) (2003) 1545-51.
[940] R. Kapukaya, O. Ciloglu, Treatment of chronic wounds with polyurethane sponges impregnated with boric acid particles: A randomised controlled trial, International Wound Journal 17(5) (2020) 1159-1165.
[941] B.E. Tepedelen, E. Soya, M. Korkmaz, Boric acid reduces the formation of DNA double strand breaks and accelerates wound healing process, Biological trace element research 174(2) (2016) 309-318.
[942] S. Perez-Amodio, N. Rubio, O.F. Vila, C. Navarro-Requena, O. Castaño, A. Sanchez-Ferrero, J. Marti-Munoz, M. Alsina-Giber, J. Blanco, E. Engel, Polymeric Composite Dressings Containing Calcium-Releasing Nanoparticles Accelerate Wound Healing in Diabetic Mice, Advances in Wound Care 10(6) (2021) 301-316.
[943] C. Lin, C. Mao, J. Zhang, Y. Li, X. Chen, Healing effect of bioactive glass ointment on full-thickness skin wounds, Biomed Mater 7(4) (2012) 045017.
[944] C. Mao, C. Lin, X.F. Chen, Enhanced Healing of Full-thickness Diabetic Wounds Using Bioactive Glass and Yunnan Baiyao Ointments, Journal of Wuhan University of Technology-Materials Science Edition 29(5) (2014) 1063-1070.
[945] I. Darby, O. Skalli, G. Gabbiani, Alpha-smooth muscle actin is transiently expressed by myofibroblasts during experimental wound healing, Laboratory investigation; a journal of technical methods and pathology 63(1) (1990) 21-29.
[946] S. Cherng, J. Young, H. Ma, Alpha-smooth muscle actin (α-SMA), J Am Sci 4(4) (2008) 7-9.
[947] R.T. Chitturi, A.M. Balasubramaniam, R.A. Parameswar, G. Kesavan, K.M. Haris, K. Mohideen, The role of myofibroblasts in wound healing, contraction and its clinical implications in cleft palate repair, Journal of international oral health: JIOH 7(3) (2015) 75.
[948] J.J. Tomasek, G. Gabbiani, B. Hinz, C. Chaponnier, R.A. Brown, Myofibroblasts and mechano-regulation of connective tissue remodelling, Nature reviews Molecular cell biology 3(5) (2002) 349-363.
[949] I.A. Darby, B. Laverdet, F. Bonté, A. Desmoulière, Fibroblasts and myofibroblasts in wound healing, Clinical, cosmetic and investigational dermatology 7 (2014) 301.
[950] G. Gabbiani, The myofibroblast in wound healing and fibrocontractive diseases, The Journal of Pathology: A Journal of the Pathological Society of Great Britain and Ireland 200(4) (2003) 500-503.
[951] Y. Zhang, X. Niu, X. Dong, Y. Wang, H. Li, Bioglass enhanced wound healing ability of urine-derived stem cells through promoting paracrine effects between stem cells and recipient cells, Journal of tissue engineering and regenerative medicine 12(3) (2018) e1609-e1622.
[952] W. Paul, C.P. Sharma, Chitosan and alginate wound dressings: a short review, Trends Biomater Artif Organs 18(1) (2004) 18-23.
[953] B.P. Antunes, A.F. Moreira, V.M. Gaspar, I.J. Correia, Chitosan/arginine-chitosan polymer blends for assembly of nanofibrous membranes for wound regeneration, Carbohydr Polym 130 (2015) 104-12.
[954] Q. Chen, I. Ahmed, J.C. Knowles, S.N. Nazhat, A.R. Boccaccini, K. Rezwan, Collagen release kinetics of surface functionalized 45S5 Bioglass®-based porous scaffolds, Journal of Biomedical Materials Research Part A: An Official Journal of The Society for Biomaterials, The Japanese Society

for Biomaterials, and The Australian Society for Biomaterials and the Korean Society for Biomaterials 86(4) (2008) 987-995.
[955] O.M. Dragostin, S.K. Samal, M. Dash, F. Lupascu, A. Panzariu, C. Tuchilus, N. Ghetu, M. Danciu, P. Dubruel, D. Pieptu, C. Vasile, R. Tatia, L. Profire, New antimicrobial chitosan derivatives for wound dressing applications, Carbohydr Polym 141 (2016) 28-40.
[956] I. Baranov, D.Y. Dzhons, A. Budruev, A. Mochalova, L. Smirnova, A. Koryagin, Long-acting bioactive composition based on chitosan and taxifolin, Inorganic Materials: Applied Research 6(5) (2015) 479-484.
[957] S. Chen, S. Cui, J. Hu, Y. Zhou, Y. Liu, Pectinate nanofiber mat with high absorbency and antibacterial activity: A potential superior wound dressing to alginate and chitosan nanofiber mats, Carbohydr Polym 174 (2017) 591-600.
[958] A. Maged, A.A. Abdelkhalek, A.A. Mahmoud, S. Salah, M.M. Ammar, M.M. Ghorab, Mesenchymal stem cells associated with chitosan scaffolds loaded with rosuvastatin to improve wound healing, Eur J Pharm Sci 127 (2019) 185-198.
[959] E.A. Kamoun, E.S. Kenawy, X. Chen, A review on polymeric hydrogel membranes for wound dressing applications: PVA-based hydrogel dressings, J Adv Res 8(3) (2017) 217-233.